



JAEA-Conf
2008-006

**Proceedings of the 2006 Symposium on Nuclear Data
January 25-26, 2007, RICOTTI, Tokai, Japan**

(Eds.) Taira HAZAMA and Tokio FUKAHORI

Reactor Physics Analysis and Evaluation Group
Advanced Nuclear System Research and Development Directorate

September 2008

Japan Atomic Energy Agency

日本原子力研究開発機構

JAEA-Conf

本レポートは独立行政法人日本原子力研究開発機構が不定期に発行する成果報告書です。
本レポートの入手並びに著作権利用に関するお問い合わせは、下記あてにお問い合わせ下さい。
なお、本レポートの全文は日本原子力研究開発機構ホームページ (<http://www.jaea.go.jp>)
より発信されています。

独立行政法人日本原子力研究開発機構 研究技術情報部 研究技術情報課
〒319-1195 茨城県那珂郡東海村白方白根 2 番地 4
電話 029-282-6387, Fax 029-282-5920, E-mail:ird-support@jaea.go.jp

This report is issued irregularly by Japan Atomic Energy Agency
Inquiries about availability and/or copyright of this report should be addressed to
Intellectual Resources Section, Intellectual Resources Department,
Japan Atomic Energy Agency
2-4 Shirakata Shirane, Tokai-mura, Naka-gun, Ibaraki-ken 319-1195 Japan
Tel +81-29-282-6387, Fax +81-29-282-5920, E-mail:ird-support@jaea.go.jp

© Japan Atomic Energy Agency, 2008

Proceedings of the 2006 Symposium on Nuclear Data

January 25-26, 2007, RICOTTI, Tokai, Japan

(Eds.) Taira HAZAMA and Tokio FUKAHORI⁺

FBR System Technology Development Unit
Advanced Nuclear System Research and Development Directorate
Japan Atomic Energy Agency
Oarai-machi, Higashiibaraki-gun, Ibaraki-ken

(Received May 29, 2008)

The 2006 Symposium on Nuclear Data was held at RICOTTI at Tokai-mura, Ibaraki-ken, Japan, on 25th and 26th of January 2007, with about 80 participants. Nuclear Data Division of Atomic Energy Society of Japan organized this symposium with cooperation of North Kanto Branch of the society. In the oral sessions, presented were 6 papers on topics of nuclear data needs for the fission reactor developments and non-energy nuclear applications. In the poster session, presented were 16 papers concerning experiments, evaluations, benchmark tests, applications, and so on. Tutorials on nuclear data, which were for uses of covariance data and MVP code, were also done. Major part of those presented papers is compiled in this proceedings.

Keywords: Nuclear Data, Symposium, Proceedings, Nuclear Reaction, JENDL, Experiment, Evaluation, Benchmark Test, Cross Section, Nuclear Fuel Cycle

⁺ Division of Nuclear Data and Reactor Engineering, Nuclear Science and Engineering Directorate

2006 年度核データ研究会報文集

2007 年 1 月 25～26 日、テクノ交流館リコッティ、東海村

日本原子力研究開発機構

次世代原子力システム開発部門 FBR 要素技術ユニット

(編) 羽様 平、深堀 智生⁺

(2008 年 5 月 29 日受理)

2006 年度核データ研究会が 2007 年 1 月 25 日と 26 日の両日、東海村のテクノ交流館リコッティにおいて約 80 名の参加の下で開催された。この研究会は日本原子力学会核データ部会の主催、日本原子力学会北関東支部の協力により開催されたものである。

口頭発表では、原子炉設計における核データニーズや非エネルギー分野での核データの利用について 6 件報告された。ポスター発表では、核データの測定、評価や、ベンチマークテスト及び応用等について 16 件報告された。共分散データの利用や MVP についてのチュートリアルも実施された。本報文集はそれらの論文の一部をまとめたものである。

Program Committee

Tokio FUKAHORI (Chairman)	Japan Atomic Energy Agency
Masayuki IGASHIRA (Co-chairman)	Tokyo Institute of Technology
Mamoru BABA	Tohoku University
Kazumi IKEDA	Mitsubishi Heavy Industries Ltd.
Makoto ISHIKAWA	Japan Atomic Energy Agency
Nobuyuki IWAMOTO	Japan Atomic Energy Agency
Osamu IWAMOTO	Japan Atomic Energy Agency
Yosuke IWAMOTO	Japan Atomic Energy Agency
Shin-ya KOSAKA	TEPCO Systems Co. (TEPSYS)
Satoshi KUNIEDA	Japan Atomic Energy Agency
Tsuyoshi MISAWA	Kyoto University Research Reactor Institute
Hiroshi NAKASHIMA	Japan Atomic Energy Agency

プログラム委員会

深堀 智生 (委員長)	日本原子力研究開発機構
井頭 政之 (副委員長)	東京工業大学
馬場 護	東北大学
池田 一三	三菱重工業(株)
石川 眞	日本原子力研究開発機構
岩本 信之	日本原子力研究開発機構
岩元 洋介	日本原子力研究開発機構
岩本 修	日本原子力研究開発機構
小坂 進矢	テプコシステムズ(株)
国枝 賢	日本原子力研究開発機構
三沢 毅	京都大学原子炉実験所
中島 弘	日本原子力研究開発機構

This is a blank page.

Contents

1. Introduction	1
2. Papers Presented at Oral Sessions	5
2.1 Critical Role of Nuclear Data in Nuclear Astrophysics	7
Y. Nagai, T. Shima, A. Tomyo, H. Makii, K. Mishima, M. Segawa, H. Ueda, Y. Temma, T. Ohsaki, J. Nishiyama, M. Igashira	
2.2 Cosmic-ray Transport Simulation in the Atmosphere	13
T. Sato, K. Niita	
2.3 Nuclear Data Relevant to Single Event Upsets in Semiconductor Memories Induced by Cosmic-ray Neutrons and Protons	19
Y. Watanabe	
2.4 Nuclear Data Needs for Fast Reactors	26
G. Chiba	
2.5 Nuclear Data Needs for Advanced Reactors	32
T. Yoshida	
2.6 Needs of Nuclear Data for Advanced Light Water Reactor	36
M. Chaki	
3. Papers Presented at Poster Sessions	37
3.1 Recent Activities for MA Cross-Section Measurements	39
S. Nakamura, M. Ohta, H. Harada, T. Fujii, H. Yamana	
3.2 Measurement of Neutron Capture Cross Sections of ^{139}La , ^{152}Sm and $^{191,193}\text{Ir}$ at 55 and 144keV	40
V. H. Tan, T. T. Anh, N. C. Hai, P. N. Son, T. Fukahori	
3.3 Measurement of Charged-particle Emission DDX for Carbon with 14-MeV Incident Neutrons	46
K. Kondo, I. Murata, K. Ochiai, H. Miyamaru, N. Kubota, C. Konno, T. Nishitani	
3.4 Measurement of $^{\text{nat}}\text{Zr}$ (n,2n) Reaction Cross Section from the Angle- Correlated Neutron Spectrum with Pencil-beam DT Neutron Source	52
K. Shiken, S. Takaki, K. Kondo, M. Matsunaka H. Miyamaru, I. Murata, K.Ochiai, C.Konno, T. Nishitani	
3.5 Neutron-Production Double-Differential Cross Sections for 150 MeV Neutron-Incidence on Fe	58
H. Arakawa, T. Kajimoto, S. Noda, T. Watanabe, N. Shigyo, K. Ishibashi, S. Kunieda, R.C. Haight	
3.6 Calculation of Fission Yield by Macroscopic-Microscopic Method Based	

on Selective Channel Scission Model	67
M. Ohta, S. Nakamura	
3.7 Effect of Effective Interaction Potentials Used in Quantum Molecular Dynamics on Nucleon-induced Reactions	72
D.N. Kadrev, Y. Watanabe	
3.8 Nuclear Data Evaluation of ²⁰⁶ Pb for Proton- and Neutron-induced Reaction in Energy Region from 20 to 200 MeV	80
T. Kajimoto, N. Shigyo, K. Ishibashi, S. Kunieda, T. Fukahori	
3.9 Prompt Time Constants of a Reflected Reactor	86
T. Ye, C. Chen, W. Sun, B. Zhang, D. Tian	
3.10 Design of MA-loaded Core Experiments Using J-PARC	92
T. Sugawara, K. Sugino, T. Sasa	
3.11 Analyses of Benchmark Experiments at FNS with Recent Nuclear Data Libraries	104
K. Ochiai, S. Sato, M. Wada, C. Konno	
3.12 Development of Burn-up Calculation System for Fusion-Fission Hybrid Reactor	109
M. Matsunaka, S. Shido, K. Kondo, H. Miyamaru, I. Murata	
3.13 Nuclear Heating Calculation for the High Flux Test Module in IFMIF	117
D. Kaku, T. Ye, Y. Watanabe	
3.14 Sensitivity Analysis of Actinide Decay Heat Focused on Mixed Oxide Fuel	125
N. Hagura, T. Yoshida	
3.15 Neutron Multigroup Constant Sets of Moderator Materials for Design of Low-Energy Neutron Sources	129
Y. Abe, N. Morishima	
Appendix : Participants Lists	141

目次

1. はじめに	1
2. 口頭発表論文	5
2.1 宇宙核物理研究と核データ(元素合成について)	7
永井 泰樹 他	
2.2 核データを用いた大気中の宇宙線輸送計算	13
佐藤 達彦 他	
2.3 宇宙線中性子・陽子による半導体メモリのSEUに関連する核データ	19
渡辺 幸信	
2.4 高速炉における核データのニーズ	26
千葉 豪	
2.5 革新炉における核データのニーズ	32
吉田 正	
2.6 次世代軽水炉における核データのニーズ	36
茶木 雅夫	
3. ポスター発表論文	37
3.1 MA断面積測定の最近の活動	39
中村 詔司 他	
3.2 Measurement of Neutron Capture Cross Sections of ^{139}La , ^{152}Sm and $^{191,193}\text{Ir}$ at 55 and 144keV	40
Vuong Huu Tan 他	
3.3 14MeV中性子入射による炭素の荷電粒子放出二重微分断面積の測定	46
近藤 恵太郎 他	
3.4 ビーム状DT中性子源を使った角度相関中性子スペクトルからの $^{nat}\text{Zr}(n,2n)$ 反応微分断面積測定	52
四間 公章 他	
3.5 Feへの150MeV中性子入射に対する中性子生成二重微分断面積	58
荒川 弘之 他	
3.6 選択チャンネル核分裂モデルに基づく巨視的-微視的法による核分裂収率計算	67
太田 雅之 他	
3.7 Effect of effective interaction potentials used in quantum molecular dynamics on nucleon-induced reactions	72
D.N. Kadrev 他	
3.8 20MeVから200MeV以下の陽子および中性子入射の ^{206}Pb の核データ評価	80
梶本 剛 他	
3.9 Prompt Time Constants of a Reflected Reactor	86

Ye Tao 他	
3.10 J-PARCを用いたMA装荷炉心実験の設計	92
菅原 隆徳 他	
3.11 最近の核データライブラリーによるFNSベンチマーク実験の解析	104
落合 謙太郎 他	
3.12 核融合核分裂ハイブリッド炉燃焼計算システムの構築	109
松中 允亨 他	
3.13 国際核融合材料照射試験施設(IFMIF)の高中性子束テストモジュールに おける核発熱計算	117
加来 大輔 他	
3.14 使用済MOX燃料の崩壊熱に関する断面積感度解析	125
羽倉 尚人 他	
3.15 低エネルギー中性子源設計用群定数セットの開発	129
安部 豊 他	
付録:参加者リスト	141

1. Introduction

The 2006 Symposium on Nuclear Data was held at RICOTTI at Tokai-mura, Ibaraki-ken, Japan, on 25th and 26th of January 2007, with about 80 participants. Nuclear Data Division of Atomic Energy Society of Japan organized this symposium with cooperation of North Kanto Branch of the society.

The program of the symposium is listed below. In the oral sessions, presented were 6 papers on topics of nuclear data needs for the fission reactor developments and non-energy nuclear applications. In the poster session, presented were 16 papers concerning experiments, evaluations, benchmark tests, applications, and so on. Tutorials on nuclear data, which were for uses of covariance data and MVP code, were also done. Major part of those presented papers is compiled in this proceedings.

Program of Symposium on Nuclear Data 2006

Jan. 25(Thu.)

13:30-13:40

1. Opening Address

T.Yosiada (Musashi Inst. of Tech.)

13:40-17:20

2. Tutorial on Nuclear Data

2.1 Use of Covariance Data

M. Ishikawa (JAEA)

2.2 Use of MVP

T. Mori (JAEA)

Jan. 26(Fri.)

10:30-12:00

3. Nuclear Data Needs for Non-energy Applications

3.1 Critical Role of Nuclear Data in Nuclear Astrophysics

Y. Nagai (Osaka Univ.)

3.2 Cosmic-ray Transport Simulation in the Atmosphere

T. Sato (JAEA)

3.3 Nuclear Data Relevant to Single Event Upsets in Semiconductor Memories Induced by Cosmic-ray Neutrons and Protons

Y. Watanabe (Kyusyu Univ.)

13:00-14:30

Poster session

14:30-16:00

4. Nuclear Data Requirements from Core Design

4.1 Nuclear Data Needs for Fast Reactors

G. Chiba (JAEA)

4.2 Nuclear Data Needs for Advanced Reactors

T. Yoshida (Musashi Inst. of Tech.)

4.3 Needs of Nuclear Data for Advanced Light Water Reactor

M. Chaki (Hitachi Ltd.)

16:00-16:10

1. Closing Address

T. Fukahori (JAEA)

Poster Session

13:00-14:30

P1. Recent Activities for MA Cross-Section Measurements

S. Nakamura (JAEA)

P2. Measurement of Neutron Capture Cross Sections of ^{139}La , ^{152}Sm and $^{191,193}\text{Ir}$ at 55 and 144keV

Vuong Huu Tan (VAEC)

P3. Measurement of Charged-particle Emission DDX for Carbon with 14-MeV Incident Neutrons

K. Kondo (Osaka Univ.)

P4. Measurement of natZr (n,2n) Reaction Cross Section from the Angle Correlated Neutron Spectrum with Pencil-beam DT Neutron Source

K. Shiken (Osaka Univ.)

P5. Neutron-Production Double-Differential Cross Sections for 150 MeV Neutron-Incidence on Fe

H. Arakawa (Kyushu Univ.)

P6. Calculation of Fission Yield by Macroscopic-Microscopic Method Based on Selective Channel Scission Model

M. Ohta (JAEA)

P7. Analysis of the $^{24}\text{Mg}(t, p)$ reaction in the incident energy $E_t=1.5\text{-}3.5$ MeV

T. Murata (AITEL)

P8. Effect of Effective Interaction Potentials Used in Quantum Molecular Dynamics on Nucleon-induced Reactions

D.N. Kadrev (Kyushu Univ.)

P9. Nuclear Data Evaluation of ^{206}Pb for Proton- and Neutron-induced Reaction in Energy Region from 20 to 200 MeV

T. Kajimoto (Kyushu Univ.)

P10. Prompt Time Constants of a Reflected Reactor

T. Ye (Kyusyu Univ.)

P11. Design of MA-loaded Core Experiments Using J-PARC

T. Sugawara (JAEA)

P.12. Analyses of Benchmark Experiments at FNS with Recent Nuclear Data Libraries

K. Ochiai (JAEA)

P.13. Development of Burn-up Calculation System for Fusin-fission Hybrid Reactor

M. Matsunaka (Osaka Univ.)

P.14. Nuclear Heating Calculation for the High Flux Test Module in IFMIF

D. Kaku (Kyushu Univ.)

P.15. Sensitivity Analysis of Actinide Decay Heat Focused on Mixed Oxide Fuel

N. Hagura (Musashi Inst. of Tech.)

P.16. Neutron Multigroup Constant Sets of Moderator Materials for Design of Low-Energy Neutron Sources

Y. Abe (Kyoto Univ.)

This is a blank page.

2. Papers Presented at Oral Sessions

This is a blank page.

2.1 Critical Role of Nuclear Data in Nuclear Astrophysics

Y. Nagai, T. Shima, A. Tomyo, H. Makii, K. Mishima, M. Segawa, H. Ueda, Y. Temma

Research Center for Nuclear Physics, Osaka University, Ibaraki, Osaka 567-0047

e-mail:nagai@rcnp.osaka-u.ac.jp

T. Ohsaki, J. Nishiyama and M. Igashira

Laboratory for Nuclear Reactors, Tokyo Institute of Technology, Meguro, Tokyo 152-8552

Accurate data of the photon-, alpha-, and neutron-induced reaction cross sections of a nucleus at astrophysics relevant energy are necessary to construct stellar models of nucleosynthetic yields of stars to trace the history of Galaxy. The cross section measurements of the ${}^4\text{He}(\gamma, xny\text{p})$, ${}^{12}\text{C}({}^4\text{He}, \gamma){}^{16}\text{O}$, and ${}^{62}\text{Ni}(n, \gamma){}^{63}\text{Ni}$ reactions were carried out using a quasi-monoenergetic pulsed photon beam with a newly developed 4π time projection chamber, a pulsed intense alpha beam with a newly installed high efficiency NaI(Tl) spectrometer, and a pulsed keV neutron beam with a high sensitive anti-Compton NaI(Tl) spectrometer, respectively. The present results were compared to previous data, recent theoretical calculations, and their astrophysics impacts were discussed.

1. Introduction

The photodisintegration reaction and its inverse reaction on few body systems provide important information both on nuclear astrophysics and nuclear physics. In fact, the proton and/or neutron capture reactions and/or their reverse reactions on light nuclei at a temperature relevant to the primordial nucleosynthesis are key reactions in estimating the primordial light element abundance in the early universe, and the remaining uncertainties of these reaction cross sections give rise to the uncertainties in the estimated abundance mentioned [1]. From a point of view of nuclear physics, γ -ray transitions following radiative and/or inverse reactions relevant to the primordial nucleosynthesis such as $\text{p}(n, \gamma){}^2\text{H}$ and ${}^2\text{H}(n, \gamma){}^3\text{H}$ reactions are characterized as being hindered and/or forbidden transitions in an impulse approximation [2]. The ${}^2\text{H}(n, \gamma){}^3\text{H}$ cross section for thermal neutron is very small [3], 1/660 of that for proton, due to the nuclear structures of ${}^2\text{H}$ and ${}^3\text{H}$, and the electromagnetic transition proceeds via a small component of wave functions. The cross section has not ever been measured at keV energies, and therefore it is quite interesting to measure it to learn the role of sub-nucleonic degrees of freedom in the reaction process with increasing the neutron energy. The photodisintegration study of ${}^4\text{He}$ could provide

useful information on the scenario of the rapid process nucleosynthesis induced by neutrino driven wind from a nascent neutron star [4], and of the delayed supernovae explosion [5], where the neutrino heating by its interaction with ${}^4\text{He}$ would influence the explosion process [6]. Here, the neutrino-nucleus interaction is analogous to the electromagnetic interaction with a nucleus via an $E1$ transition [7]. In nuclear physics, the photodisintegration of ${}^4\text{He}$, the lightest self-conjugate nucleus with closed shell structure, has been a quite interesting subject, since the study could provide a testing ground for theory on NN , three-body forces and collective nuclear motion [8]. In addition, the cross section ratio of the ${}^4\text{He}(\gamma,p)$ to ${}^4\text{He}(\gamma,n)$ in the giant dipole region has been used to test the validity of the charge symmetry of the strong interaction in nuclei [9]. So far, the photodisintegration cross sections of ${}^4\text{He}$ were measured in the energy range from 20 to 215 MeV using quasi-monoenergetic photon beams and/or bremsstrahlung photon beams [10]. Although above 35-40 MeV most of the old ${}^4\text{He}(\gamma,p){}^3\text{H}$ and ${}^4\text{He}(\gamma,n){}^3\text{He}$ data agree with each other within their respective data sets, they are controversial especially in the peak region of 25-26 MeV, and show either a pronounced GDR peak or a fairly flat excitation function, requiring a new precise measurement. It should be mentioned that the systematic uncertainties of the old data seem to be much larger than the statistical uncertainties. Theoretical calculations also predict different cross sections in the region of the electric dipole resonance (25~26 MeV) [11].

The ${}^{12}\text{C}(\alpha,\gamma){}^{16}\text{O}$ reaction cross section at the center-of-mass energy $E_{\text{c.m.}}$ of 0.3 MeV, $\sigma_{\text{tot.}}(E_{\text{c.m.}}=300)$, plays an important role in determining the mass fraction of ${}^{12}\text{C}$ and ${}^{16}\text{O}$ after stellar helium burning, the abundance distribution of elements between carbon and iron, and the iron-core mass before super-nova explosion [12]. The direct measurement of the $\sigma_{\text{tot.}}(E_{\text{c.m.}}=300)$, however, is not possible using current experimental techniques, since the $\sigma_{\text{tot.}}(E_{\text{c.m.}}=300)$ is very small of $\sim 10^{-17}$ b [13]. Hence, $\sigma_{\text{tot.}}(E_{\text{c.m.}}=300)$ is derived by extrapolating a measured cross section at $E_{\text{c.m.}} \geq 1.0$ MeV into the range of the stellar temperature with use of theoretical calculations [14]. The $\sigma_{\text{tot.}}(E_{\text{c.m.}}=300)$ is considered to be dominated by direct electric dipole ($E1$) and electric quadrupole ($E2$) α -capture reactions into the ground state of ${}^{16}\text{O}$ [15]. Because of the different energy dependence of the $\sigma_{E1}(E_{\text{c.m.}})$ and $\sigma_{E2}(E_{\text{c.m.}})$ it is necessary to separately extrapolate the $\sigma_{E1}(E_{\text{c.m.}})$ and $\sigma_{E2}(E_{\text{c.m.}})$ to obtain the total cross section of the ${}^{12}\text{C}(\alpha,\gamma){}^{16}\text{O}$ reaction at $E_{\text{c.m.}}=0.3$ MeV, $\sigma_{\text{tot.}}(E_{\text{c.m.}}=300)$. Despite extensive studies of the angular distribution measurement, there remain significant uncertainties of $\sigma_{E1}(E_{\text{c.m.}})$ and $\sigma_{E2}(E_{\text{c.m.}})$ [16].

Comparison of observed elemental abundance of various metallic stars with calculated nucleosynthetic yields based on stellar nucleosynthetic models provides crucial information to finally construct models for chemical evolution of galaxies [17]. According to the recent estimation of the nucleosynthetic yields of massive stars, several isotopes such as ${}^{61}\text{Ni}$, ${}^{62}\text{Ni}$ and ${}^{64}\text{Ni}$ are overproduced, and one of the largest

overproductions is ^{62}Ni [18]. The origin of the overproduction is considered to be due to residual uncertainties in the stellar models and/or in the nuclear physics inputs used for the calculation such as the neutron capture cross-section of Ni isotopes.

Because of the nuclear astrophysics and nuclear physics interest we determined the cross sections of the $^4\text{He}(\gamma, xny)p$, $^{12}\text{C}(\alpha, \gamma)^{16}\text{O}$, $^2\text{H}(n, \gamma)^3\text{H}$, and $^{62}\text{Ni}(n, \gamma)^{63}\text{Ni}$ reactions with small systematic uncertainty by developing a new measurement system, as described below.

2. Experimental Method

2.1 Photodisintegrations of ^4He

The ^4He photodisintegration cross section was performed at the National Institute of Advanced Science and Technology at Tsukuba by using pulsed laser Compton backscattering (LCS) photons, and a newly constructed time projection chamber (TPC) with an active He target, which allowed to simultaneously measure the (γ, p) and (γ, n) reaction channels [19]. There are several key points in the present method to obtain real events with a large signal to noise ratio. Real events are only produced along the photon axis with a diameter of 2 mm, when a pulsed photon beam entered the TPC, we could obtain information on the track shape of a charged fragment, energy loss deposited by the fragment, and the reaction point, necessary to clearly identify the event, angular distribution of a fragment, using the TPC, and the solid angle is large, nearly 4π , and the detection efficiency is as high as 100% [20]. The photodisintegration cross section of ^4He is given as products of the reaction yield, the number of ^4He target, the incident LCS γ -ray flux, and the detection efficiency of the TPC. The target number was obtained by measuring the gas pressure and temperature in the TPC, and the efficiency was determined by using the ^{241}Am α -ray source. The reaction yield and the incident γ -ray flux were obtained by referring to the track shape of charged fragment from the reaction together with its pulse height, and by measuring the γ -ray spectrum by means of a BGO detector.

2.2 $^{12}\text{C}(\alpha, \gamma)^{16}\text{O}$ reaction

The differential cross sections of the $^{12}\text{C}(\alpha, \gamma)^{16}\text{O}$ reaction have been measured at center-of-mass energy of 1.4 and 1.6 MeV with a new measurement system installed at the 3.2 MV Pelletron accelerator laboratory of the Research Laboratory for Nuclear Reactors at Tokyo Institute of Technology [21]. We used an intense pulsed α -beam together with three anti-Compton NaI (TI) spectrometers. The spectrometer was heavily shielded against neutrons from the $^{13}\text{C}(\alpha, n)^{16}\text{O}$ reaction and background γ -rays produced by thermalized neutrons capture reaction by various materials in the measurement room. It was

essential to use a pulsed α -beam to get rid of neutron induced background from $^{13}\text{C}(\alpha,n)^{16}\text{O}$ from real events due to $^{12}\text{C}(\alpha,\gamma)^{16}\text{O}$ with a time-of-flight method [21]. Note that a small amount of ^{13}C is known to produce significant amounts of background since the cross section of the $^{13}\text{C}(\alpha,n)^{16}\text{O}$ reaction is about 10^7 times larger than that of the $^{12}\text{C}(\alpha,\gamma)^{16}\text{O}$ reaction. In addition, preparation of the enriched targets which could stand against an intense beam was crucial since we used an intense α -beam. We measured the Rutherford backscattering spectrum of α -particles from targets to obtain the flux of incident α -beam and monitor any change of the target thickness during measurements.

2.3 $^2\text{H}(n,\gamma)^3\text{H}$ and $^{62}\text{Ni}(n,\gamma)^{63}\text{Ni}$ reactions

The (n,γ) cross sections for ^2H [22] and ^{62}Ni [23] at keV energy were measured using pulsed neutrons at the 3.2 MV Pelletron accelerator at Tokyo Institute of Technology. A discrete γ -ray promptly emitted from the neutron capture reaction by deuteron was detected by means of an anti-Compton NaI(Tl) spectrometer [24]. Gold was used to normalize the neutron capture cross section of a sample, since the cross section of Au is well known within an uncertainty of 3 %.

3. Results

3.1 Cross section of the ^4He photodisintegration reactions

Using the reaction yield, the photon flux, the target number of ^4He , and the detection efficiency of the TPC mentioned above, we could obtain the photodisintegration cross section of ^4He . Here, in order to learn about any possible systematic uncertainty of the present experimental method, we measured the photodisintegration cross section of deuteron using CD_4 gas at $E_\gamma=22.3$ MeV. Note the reaction cross section has been well known with good accuracy. The obtained result is in good agreement with old data and with a theoretical value [25], confirming the validity of the new method including its analysis.

The thus obtained cross sections for the (γ,p) and (γ,n) reactions on ^4He are shown together with previous data and theoretical calculations in **Fig. 1** [20]. They increase monotonically with increasing the γ -ray energy up to 30 MeV, and do not show a prominent peak in the region of 25 ~26 MeV, contrary to several old data and a recent theoretical calculation [11]. The cross section ratio of the (γ,p) to the (γ,n) reactions derived from the present measurement agrees with the expected value assuming the charge conservation of the strong interaction in nuclei.

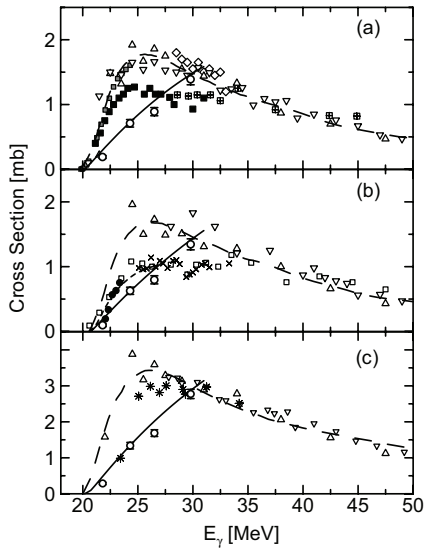


Fig. 1 ^4He photodisintegration cross sections. Open circles: present result. Solid curves: most probable cross sections obtained from the present data. Other symbols: previous data (see Ref. 20). (a) (γ, p) cross sections. (b) (γ, n) cross sections. (c) total photoabsorption cross sections.

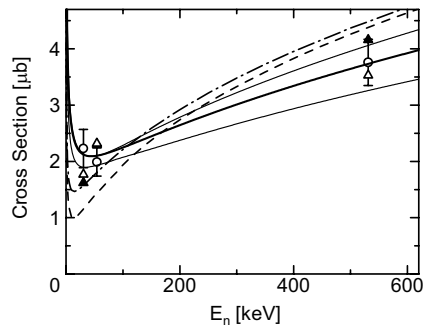


Fig. 2 Cross section of the $\text{D}(n, \gamma)^3\text{H}$ reaction vs. neutron energy (in the center-of-mass energy). Open circles: present results. Other symbols: calculated values see Ref. 22.

3.3 Cross sections of the $^2\text{H}(n, \gamma)^3\text{H}$ and $^{62}\text{Ni}(n, \gamma)^{63}\text{Ni}$ reactions

The present result of the $^2\text{H}(n, \gamma)^3\text{H}$ reaction is shown in **Fig. 2** together with theoretical calculations based on the Faddeev approach and the pionless effective field theory [22].

The cross section of the $^{62}\text{Ni}(n, \gamma)^{63}\text{Ni}$ reaction was precisely measured in the neutron energy range from 5.5 to 90 keV and obtained the MACS at 30 keV as being 37.5 ± 2.5 mbarn (preliminary), about 3 times larger than the value used for the nucleosynthetic yield estimation of massive stars [18]. This large MACS could solve the longstanding problem of the overproduction of ^{62}Ni in the yield estimation.

4. Summary

We have successfully measured the photodisintegration cross section of ^4He (in addition, ^2H and ^3He) by constructing a new measurement system with a small systematic uncertainty. The present studies for the direct simultaneous measurements of these nuclei solved a longstanding problem of the discrepancy of the existing ^4He two-body photodisintegration cross sections. Further theoretical developments are highly

required to get deeper insight of the obtained excitation function of the ^4He photodisintegration. We also succeeded to measure the γ -ray angular distribution from the $^{12}\text{C}(\alpha, \gamma)^{16}\text{O}$ reaction to the ground state of ^{16}O by installing also a new measurement system with use of an intense pulsed α -beam together with high sensitive anti-Compton NaI(Tl) spectrometers at $E_{\text{c.m.}}=1.4$ and 1.6 MeV. The neutron capture cross sections of ^2H and ^{62}Ni were measured at keV energies using a pulsed neutron beam with use of a prompt γ -ray detection method. These data are important in the nucleosynthetic yield estimation in the primordial nucleosynthesis and stellar nucleosynthesis. They also serve as a testing ground of various theoretical calculations.

References:

- [1] R.H. Cyburt, *Phys. Rev. D* 70, 023505 (2004).
- [2] L. I. Schiff, *Phys. Rev.* 52, 242 (1937), J. L. Friar, B. F. Gibson, & G. L. Payne, *Phys. Lett.* B251, 11 (1990), J. Carlson, et al., *Phys. Rev.* C42, 830 (1990).
- [3] L. Kaplan, G. R. Ringo, and K. E. Wilzbach, *Phys. Rev.* 87, 785 (1952), E. T. Jurney, P. T. Bendt, and J. C. Browne, *Phys. Rev.* C25, 2810 (1982)
- [4] S.E. Woosley, D.H. Hartmann, R.D. Hoffman, and W.C. Haxton, *Astrophys. J.* 356, 272 (1990).
- [5] H.A. Bethe, and J.R. Wilson, *Astrophys. J.* 295, 14 (1895).
- [6] K. Sumiyoshi, private communication.
- [7] W.Haxton, *Phys. Rev. Lett.* 60, 1999 (1988).
- [8] M. Unkelbach and H. M. Hofmann, *Nucl. Phys.* A549, 550 (1992).
- [9] F. C. Barker and A. K. Mann, *Philos. Mag.* 2, 5 (1957).
- [10] K. I. Hahn , C. R. Brune, and R. W. Kavanagh, *Phys. Rev.* C51, 1624 (1995), and references therein.
- [11] S. Quaglioni, W. Leidemann, G. Orlandini, N. Barnea, and V. D. Efros, *Phys. Rev.* C69, 044002 (2004), G. Ellerkmann, W. Sandhas, S. A. Sofianos, and H. Fiedeldey, *Phys. Rev.* C53, 2638 (1996).
- [12] T.A. Weaver and S.E.Woosley, *Phys. Rep.* 227, 65 (1993).
- [13] C. Rolfs and W.S. Rodney, "Caudrons in the Cosmos" (University of Chicago Press, 1988).
- [14] F.C. Barker, and T. Kajino, *Aust. J. Phys.* 44, 396 (1991), C. Angulo and P. Descouvemont, *Phys. Rev. C* 61, 064611 (2000).
- [15] L. Buchmann et al., *Phys. Rev. C* 54, 393 (1996).
- [16] M. Assuncao et al., *Phys. Rev. C* 73, 055801 (2006).
- [17] F.X.Timmes, S.E.Woosley, and T.A.Weaver, *Astrophys. J.* 98, 617 (1995)
- [18] T.Rauscher, A. Heger, R.D.Hoffman, and S.E.Woosley, *Astrophys. J.* 576, 323 (2002)
- [19] T. Kii, T. Shima, T. Baba and Y. Nagai, *Nucl. Instr. and Meth.* A 552, 329 (2005).
- [20] T. Shima et al., *Phys. Rev.* C72, 044004 (2005).
- [21] H.Makii et al., *Nucl. Instr. and Meth.* A547, 41 (2005).
- [22] Y. Nagai et al., *Phys. Rev. C* 74, 025804 (2006).
- [23] A.Tomyo et al., *Astrophys. J.* 623, L153 (2005).
- [24] T.Ohsaki et al., *Nucl. Instr. and Meth.* A506, 250 (1999), M. Igashira et al, *Proc. Conf. of the 8th. Int. Symp. on Capture Gamma-Ray and Related Topics*, World Scientific, Singapore, 992 (1993).
- [25] H. Arenhövel and M. Sanzone, "Photodisintegration of the Deuteron (Few-Body Systems Suppl. 3)" (Springer-Verlag, Wien, 1991).

2.2 Cosmic-ray Transport Simulation in the Atmosphere

T. Sato^{1*} and K. Niita²

¹Research Group for Radiation Protection, Division of Environment and Radiation Sciences,
Nuclear Science and Engineering Directorate, Japan Atomic Energy Agency,
Tokai, Ibaraki 319-1195, Japan

²Research Organization for Information Science and Technology, Tokai, Ibaraki, 319-1106, Japan
*E-mail: sato.tatsuhiko@jaea.go.jp

Abstract

Estimation of cosmic-ray neutron spectra in the atmosphere has been an essential issue in the evaluation of the aircrew doses and the soft-error rates of semiconductor devices. We therefore performed Monte Carlo simulations for estimating neutron spectra, using the PHITS code coupled with the nuclear data library JENDL-High-Energy (JENDL/HE) file or the intra-nuclear cascade (INC) model for simulating high-energy neutron and proton induced nuclear reactions. The calculated spectra based on JENDL/HE agree with measured data very much for a wide altitude range even at ground level. On the other hand, the calculation adopting INC generally overestimates the measured data, especially at lower altitudes. These tendencies indicate that JENDL/HE can play an important role not only in the cosmic-ray transport simulation, but also in the deep-penetration simulation for the shielding design of high-energy accelerator facilities, since the two simulations have a lot of similarities with respect to the source terms, shielding properties and so on. The incorporation of the pion-production channels into JENDL/HE will be very helpful in the future study of radiation protection dosimetry.

1. Introduction

In the last decade, radiation protection for aircrews against terrestrial cosmic-rays was one of the most intensively discussed dosimetric issues. Furthermore, increasing attention has been paid to the soft errors of semiconductor devices induced by the cosmic-rays even at the ground level, since the recent miniaturization of the devices causes a rapid decrease of their critical charges. These radiation effects are predominantly triggered by neutrons produced by nuclear reactions between the cosmic-rays and atmospheric components. Therefore, estimation of cosmic-ray neutron spectra in the atmosphere is an essential issue in the evaluation of the aircrew doses and the soft-error rates (SERs).

A number of studies have been devoted to the estimation of the neutron spectra¹⁻⁴⁾ by performing atmospheric propagation simulations of cosmic-rays. However, the cosmic-ray neutron spectra depend not only on the atmospheric depth, cut off rigidity and solar modulation (referred to here as global conditions) but also the structure of the aircraft⁵⁾ and the water density around the point of interest²⁾ (referred to here as local geometries) in an intricate manner, and none of the existing models are able to reproduce the measured neutron spectra at any location and time with satisfactory accuracy. One reason for causing the

difficulty in reproducing the measured data is that the atmospheric propagation simulation of cosmic-rays requires a very sophisticated nuclear reaction model for high-energy neutrons, since the atmosphere is very thick, approximately 1000 g/cm^2 , and even a slight inaccuracy in the calculated transparency of high-energy neutrons triggers a huge discrepancy of the neutron spectra at the end of the atmosphere *i.e.* sea level. For instance, it is known that the simulation employing a widely-used nuclear reaction model of the intra-nuclear cascade⁶⁾ (abbreviated to INC, hereafter) generally overestimates the cosmic-ray neutron spectra at sea level.

With these situations in mind, we have calculated the cosmic-ray neutron spectra by performing Monte Carlo particle transport simulation in the atmosphere based on the Particle and Heavy Ion Transport code System PHITS^{7,8)}, utilizing the latest version of the nuclear data library JENDL-High-Energy File^{9,10)} (abbreviated to JENDL/HE, hereafter). Similar simulation but employing INC instead of JENDL/HE was also performed in order to figure out the dependence of the cosmic-ray neutron spectra on the nuclear reaction model. Based on a comprehensive analysis of the simulation results, we proposed analytical functions to predict the cosmic-ray neutron spectra at any global condition at the altitudes below 20 km, considering the local geometry effect.

The details of the calculated results together with the derivation and verification of the analytical function had already been reported in our previous paper¹¹⁾. Hence, this paper focuses on the discussion about the role of the nuclear reaction models in the atmospheric-propagation simulation of cosmic-rays by comparing between the neutron spectra obtained by the simulations employing JENDL/HE and INC.

2. Simulation Procedure

The earth system virtually constructed in our simulation is depicted in Figure 1. The earth was represented as a sphere with the radius of 6378.14 km, and its composition was assumed to be 59.2% oxygen, 28.0% silicon, 10.6% aluminum and 2.2% hydrogen by mass. This constitution corresponds to 60% SiO₂, 20% Al₂O₃ and 20% H₂O by mass. The particles arriving at 1000 g/cm^2 below the ground level were discarded in the simulation for reducing the computational time, since there are few albedo neutrons from so deep underground to the atmosphere. The atmosphere was divided into 28 concentric spherical shells, and its maximum altitude was 86 km. The densities and temperatures of each shell were determined referring to the US-Standard-Atmosphere-1976. The atmosphere was assumed to be composed of 75.4% nitrogen, 23.3% oxygen and 1.3% argon by mass above the altitude of 2 km, and additionally, 0.06% hydrogen by mass below this altitude due to the existence of water vapor. Note that argon was replaced by the atom with the same mass number – calcium – in our simulation, since JENDL/HE does not yet include the data for argon.

In the simulation, cosmic-rays were incident on the earth system from the top of the atmosphere, *i.e.* from the altitude of 86 km. Proton, alpha and heavy ions with charges up to 28 (Ni) were considered as the source particles, although the contributions of heavy ions to the cosmic-ray neutron spectra are generally small. The incident cosmic-ray spectra for the 30 conditions – 15 geomagnetic fields with the vertical cut-off rigidities from 0.1 to 14 GV at the solar minimum and solar maximum periods, respectively – were considered in our simulation, and the spectra were calculated by the CREME96 code¹²⁾.

The atmospheric propagation of the incident cosmic-rays and their associated cascades was

simulated by the PHITS code, which can deal with the transports of all kinds of hadrons and heavy ions with energies up to 200 GeV/n. As mentioned before, the simulation was performed alternatively by employing JENDL/HE or INC for high-energy neutron and proton induced nuclear reactions. The reaction models adopted in each simulation are summarized in Figure 2. Note that the pion-production channels are excluded from the database of JENDL/HE used in the PHITS simulation, and hence, the transports of pions and the associated particles with their decay – muon, photon, electron and positron – were not considered in our simulation.

3. Results and Discussion

Figure 3 shows the comparisons of the calculated neutron spectra with the corresponding experimental data obtained by Goldhagen *et al.*¹³⁾ and Nakamura *et al.*¹⁴⁾. The statistical errors in the values obtained by the simulation are generally small – approximately less than 5% and 20% for the high altitude and ground level data, respectively, except for very high and low energies. The spectra predicted by the analytical functions based on the JENDL/HE data, which were proposed in our previous paper¹¹⁾, are also plotted in the figures.

Two peaks around 1 MeV and 100 MeV can be observed in every spectrum. The former is attributed to neutrons emitted by the evaporation process, while the latter is to those produced by the pre-equilibrium and intra-nuclear cascade processes. The peaks at the thermal energy can be found only in the spectra at the ground level, since they are predominantly composed of the earth's albedo neutrons.

It is evident from the figure that the simulation employing JENDL/HE can reproduce the experimental data for all the calculated conditions very well. On the other hand, the simulation adopting INC generally overestimates the measured data, especially for lower altitudes. This discrepancy is predominantly attributed to the tendency of INC to over-predict the yields of high energy secondary particles knocked out by nuclear reactions of light nuclei such as nitrogen and oxygen. As an example to show the difference between JENDL/HE and INC, the neutron and proton spectra produced from the 150 MeV neutron-induced nuclear reaction of oxygen calculated by the two models are plotted in Figure 4. It is obvious from the figure that INC gives larger values for both the neutron and proton yields at high energies than JENDL/HE does. This tendency causes the over-prediction of neutron fluences in deep-penetration calculations such as the cosmic-ray propagation simulation in the atmosphere.

It is also found from Fig. 3 that the analytical functions are substantially superior to the Monte Carlo simulation in reproducing experimental data at lower energies, although they were proposed based on the simulation data obtained by PHITS coupled with JENDL/HE. This is because the local geometry effect on the spectra is precisely considered in the analytical calculation, providing the water density in ground or the mass of aircraft to the functions. Using the analytical functions, we have developed EXcel-based Program for Calculating Cosmic-ray Spectrum (EXPACS), which can calculate not only cosmic-ray neutron spectrum but also the corresponding effective dose and ambient dose equivalent for any locations in the world. The software has been opened for public from its web site¹⁵⁾.

4. Conclusions

The cosmic-ray neutron spectra were calculated by performing the atmospheric-propagation

simulation by the PHITS code coupled with JENDL/HE or INC. The calculated spectra based on JENDL/HE agree with measured data very much for a wide altitude range even at ground level. On the other hand, the calculation adopting INC generally overestimates the measured data, especially at lower altitudes. These tendencies indicate that JENDL/HE can play an important role not only in the cosmic-ray transport simulation, but also in the deep-penetration simulation for the shielding design of high-energy accelerator facilities, since the two simulations have a lot of similarities with respect to the source terms, shielding properties and so on. In the future, we plan to calculate the photon and charged-particle spectra in the atmosphere, applying the Monte Carlo simulation technique established by this work.

Acknowledgements

We would like to thank Dr. Y. Watanabe and Dr. T. Fukahori for their support in incorporating JENDL/HE into PHITS. We also wish to thank technical staffs of the CCSE office of JAEA for their help in performing the Monte Carlo simulation.

References

- 1) K. O'Brien, W. Friedberg, H. H. Sauer and D. F. Smart, "Atmospheric cosmic rays and solar energetic particles at aircraft altitudes," *Environ. Int.* **22** (Suppl.1), S9-44 (1996).
- 2) S. Roesler, W. Heinrich and H. Schraube, "Calculation of radiation fields in the atmosphere and comparison to experimental data," *Radiat. Res.* **149**, 87-97 (1998).
- 3) A. Ferrari, M. Pelliccioni and T. Rancati, "Calculation of the radiation environment caused by galactic cosmic rays for determining air crew exposure," *Radiat. Prot. Dosim.* **93**, 101-114 (2001)
- 4) J. M. Clem, G. De Angelis, P. Goldhagen and J. W. Wilson, "New calculations of the atmospheric cosmic radiation field – results for neutron spectra," *Radiat. Prot. Dosim.* **110**, 423-428 (2004).
- 5) A. Ferrari, M. Pelliccioni and R. Villari, "Evaluation of the influence of aircraft shielding on the aircrew exposure through an aircraft mathematical model," *Radiat. Prot. Dosim.* **108**, 91-105 (2004).
- 6) H. W. Bertini, "Low-energy intranuclear cascade calculation," *Phys. Rev.* **131**, 1801-1821 (1963).
- 7) H. Iwase, K. Niita and T. Nakamura, "Development of a general-purpose particle and heavy ion transport Monte Carlo code," *J. Nuc. Sci. Technol.* **39**(11) 1142-1151 (2002).
- 8) K. Niita, T. Sato, H. Iwase, H. Nose, H. Nakashima and L. Sihver, "Particle and heavy ion transport code system; PHITS," *Radiat. Meas.* **41**(9-10), 1080-1090 (2006).
- 9) T. Fukahori, Y. Watanabe, N. Yoshizawa, F. Maekawa, S. Meigo, C. Konno, N. Yamano, A.Yu. Konobeyev and S. Chiba, "JENDL High Energy File," *J. Nucl. Sci. Technol.*, **Suppl. 2**, 25-30 (2002).
- 10) Y. Watanabe, T. Fukahori, K. Kosako, N. Shigyo, T. Murata, N. Yamano, T. Hino, K. Maki, H. Nakashima, N. Odano and S. Chiba, "Nuclear data evaluations for JENDL high-energy file," *Proceedings of International Conference on Nuclear Data for Science and Technology*, Santa Fe, USA, Sep.26-Oct.1, 2004; AIP CP769, p326-331 (2005).
- 11) T. Sato and K. Niita, "Analytical function to predict cosmic-ray neutron spectrum in the atmosphere," *Radiat. Res.* **166**, 544-555 (2006).
- 12) A. J. Tylka, J. H. Adams, Jr., P. R. Boberg, B. Brownstein, W. F. Dietrich, E. O. Flueckiger, E. L. Petersen, M. A. Shea, D. F. Smart and E. C. Smith, "CREME96: A revision of the cosmic ray effects

- on micro-electronics code,” *IEEE Transactions on Nuclear Science* **44**, 2150-2160 (1997).
- 13) P. Goldhagen, J. M. Clem and J. W. Wilson, “The energy spectrum of cosmic-ray induced neutrons measured on an airplane over a wide range of altitude and latitude,” *Radiat. Prot. Dosim.* **110**, 387-392 (2004).
 - 14) T. Nakamura, T. Nunomiya, S. Abe, K. Terunuma and H. Suzuki, “Sequential measurements of cosmic-ray neutron spectrum and dose rate at sea level in Sendai, Japan,” *J. Nucl. Sci. Technol.*, **42**, 843-853 (2005).
 - 15) <http://www3.tokai-sc.jaea.go.jp/rphpwww/radiation-protection/expacs/expacs.html>

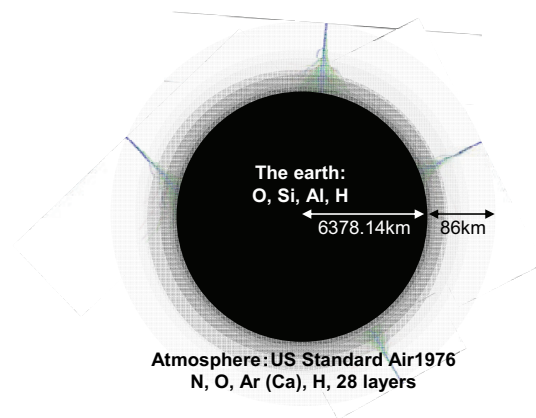


Figure 1 Earth system virtually constructed for the atmospheric-propagation simulation of cosmic-rays

		Simulation employing JENDL/HE						
		0.001eV	1MeV	20MeV	1GeV	2.5GeV	3.5GeV	100 GeV
Neutron		JENDL/HE				INC	JAM	
Proton		No Transport	JENDL/HE			INC	JAM	
Heavy Ions		No Transport	JQMD			JAMQMD		
		Simulation employing INC						
Neutron		JENDL3.2		INC		JAM		
Proton		No Transport	INC			JAM		
Heavy Ions		No Transport	JQMD			JAMQMD		
		0.001eV	1MeV	20MeV	1GeV	2.5GeV	3.5GeV	100 GeV

Figure 2 Nuclear reaction models employed in the atmospheric-propagation simulation of cosmic-rays

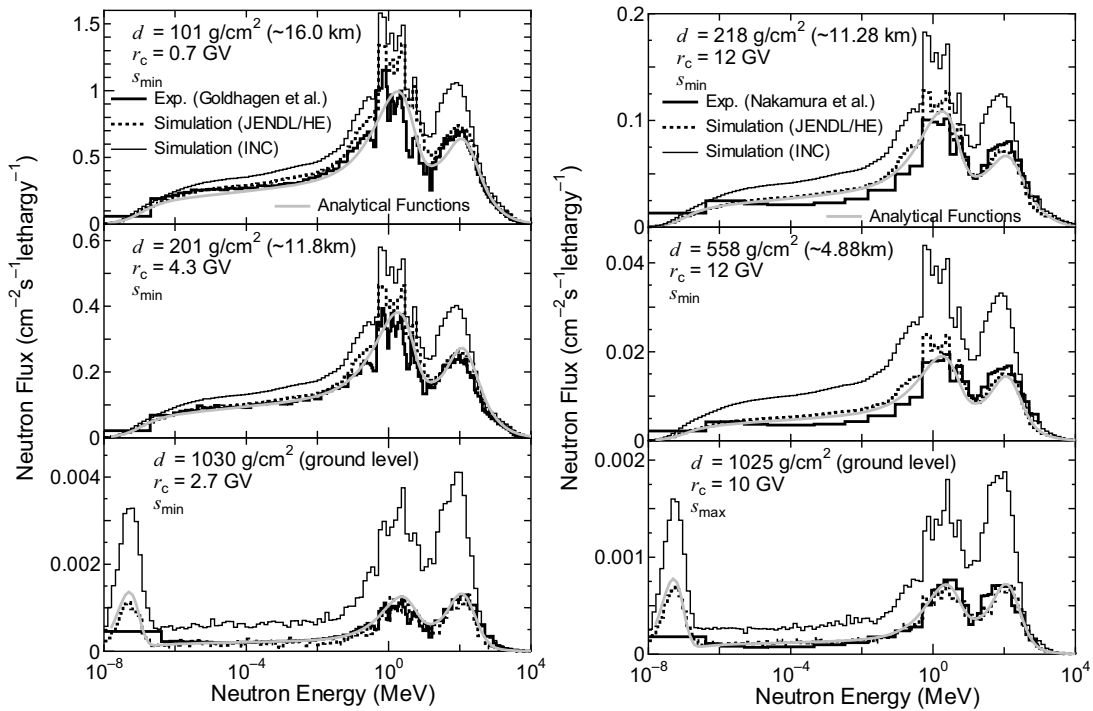


Figure 3 Calculated and measured neutron spectra in the atmosphere. The values of d and r_c are the atmospheric depth and the cut-off rigidity, respectively, while s_{min} and s_{max} indicate the solar minimum and maximum, respectively.

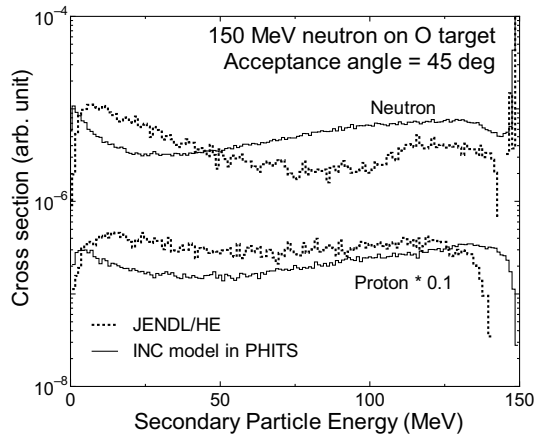


Figure 4 Neutron and proton spectra produced from the 150 MeV neutron-induced nuclear reaction of oxygen calculated by JENDL/HE and the INC model implemented in PHITS.

2.3 Nuclear data relevant to single event upsets in semiconductor memories induced by cosmic-ray neutrons and protons

Yukinobu Watanabe

*Department of Advanced Energy Engineering Science, Kyushu University,
Kasuga, Fukuoka 816-8580, Japan*

Corresponding email: watanabe@aes.kyushu-u.ac.jp

The role of nuclear data is examined in the study of single event upset (SEU) phenomena in semiconductor memories caused by cosmic-ray neutrons and protons. Neutron and proton SEU cross sections are calculated with a simplified semi-empirical model using experimental heavy-ion SEU cross-sections and a dedicated database of neutron and proton induced reactions on ^{28}Si . Some impacts of the nuclear reaction data on SEU simulation are analyzed by investigating relative contribution of secondary ions and neutron elastic scattering to SEU and influence of simultaneous multiple ions emission on SEU.

1. Introduction

In recent years, cosmic-rays induced single-event upsets (SEUs) have been recognized as a key reliability concern for microelectronic devices used not only in space but also at the ground level or in airplanes at higher altitude. The SEU is one of the transient radiation effects by which the memory state of a cell can be flipped from a 1 to a 0 or vice versa, resulting in malfunction. As illustrated schematically in Fig.1, the SEU is initiated by the interaction of incident cosmic-ray particles with materials in microelectronics devices. Then, light-charged particles and heavy recoils are generated via the nuclear reaction with a constituent atomic nucleus, mainly ^{28}Si , and then deposit the charge in a small sensitive volume (SV) of the device. The deposited charge is collected at one of the nodes keeping the memory information and the resulting transient current generates an SEU. Knowledge on nuclear physics and radiation physics is indispensable to understand well these elementary processes in the SEU phenomena. Particularly, nuclear reaction data play an essential role in estimating the SEU rate accurately, because the nuclear interaction takes place in the first stage of the SEU process.

So far, we have studied the SEU as one of the applications of high-energy nuclear data [1,2]. A dedicated nuclear reaction database was created using available nuclear data and theoretical model calculations, and was applied to calculations of nucleon-induced SEU cross sections using a semi-empirical model based on SV concept mentioned below. The results were compared with experimental SEU cross sections, and influences of nuclear data on the SEU simulation were investigated.

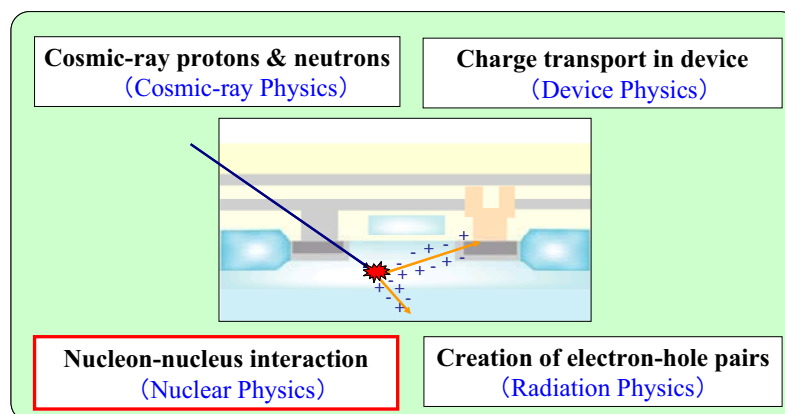


Fig.1 Schematic illustration of SEU phenomena

In this report, our recent work on SEU is summarized. The Monte Carlo simulation method is described

in sect. 2. In sect. 3, the calculated SEU cross sections are compared with experimental data. In sect. 4, we discuss the incident energy dependence of secondary-ion dependent SEU fraction and the effect of neutron elastic scattering and simultaneous multiple ions emission on SEU. Finally, a summary and future outlook is given in sect.5.

2. Monte Carlo simulator based on sensitive volume concept

Figure 2 illustrates a general flow chart of SEU simulation. Our calculation model [2] uses a well-known memory cell geometry having a sensitive volume (SV) of rectangular parallelepiped shape as shown schematically in Fig.3. The SV is defined as the volume containing all the charges deposited by secondary ions generated from the interaction between an incident nucleon and ^{28}Si , which are ultimately collected by a memory node and induce an SEU. One of the important physical quantities relevant to the SEU is the distribution function of the energy E_d deposited in the SV. It is hereinafter denoted by $f(E_{in}, E_d)$, where E_{in} is the incident energy. It is characterized by the nuclear reaction, particularly energy and angular distributions of the generated secondary ions, and ion penetration and linear energy transfer (LET) into the device. It should be noted that the deposited charge Q_d can be reduced to the deposited energy E_d using the relation, E_d (in MeV) = 0.0225 Q_d (in fC). Therefore, the quantity $f(E_{in}, E_d)$ corresponds to the initial charge deposition distribution.

In the present model, a semi-empirical approach using experimental heavy-ion SEU cross sections [3,4] is applied when one calculates nucleon-induced SEU cross section from the energy deposition distribution, $f(E_{in}, E_d)$, instead of charge transport and collection simulation. The nucleon-induced SEU cross section is expressed by

$$\sigma_{SEU}(E_{in}) = N_{Si} V_{int} \sigma_N(E_{in}) \int_0^\infty f(E_{in}, E_d) h(E_d) dE_d, \quad (1)$$

where N_{Si} is the number density of silicon atoms, V_{int} the volume size of the region (“interaction volume”) where nuclear reactions occur in the memory cell of interest, $\sigma_N(E_{in})$ the cross section to describe the interaction between an incident nucleon and ^{28}Si , which is given by the sum of elastic scattering cross section and total reaction cross section, $h(E_d)$ the normalized heavy-ion SEU cross section expressed by the following Weibull fitting function:

$$h(E_d) = \sigma_{HI}(E_d) / \sigma_{HI}^\infty = 1 - \exp\left\{-\left[\frac{E_d - E_0}{W}\right]^s\right\}, \quad (2)$$

where W and s are shape parameters, σ_{HI}^∞ is the saturation value of the heavy-ion SEU cross section and E_0 the SEU threshold. Since experimental heavy-ion SEU data are usually given as a function of LET, we need to convert it to the deposit energy using the relation, $E_d = d \times LET$, where d represents the sensitive depth. If we assume a step function $h(E_d) = \Theta(E_d - E_c)$, where E_c is called the critical energy required to cause an SEU, then Eq.(1) is given by

$$\sigma_{SEU}(E_{in}, E_c) = N_{Si} V_{int} \sigma_N(E_{in}) F(E_c), \quad (3)$$

where $F(E_c) = \int_{E_c}^\infty f(E_{in}, E_d) dE_d$.

The distribution function $f(E_{in}, E_d)$ is calculated by a Monte Carlo method using a nuclear reaction database and a range and energy loss database of secondary ions as illustrated in Fig.2. In the present work,

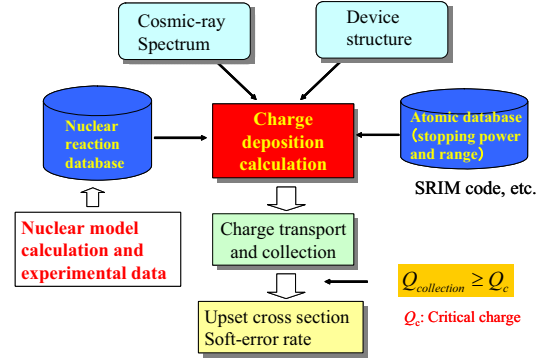


Fig. 2 Flow chart of SEU simulation

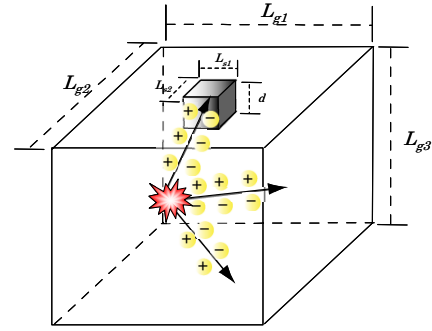


Fig. 3 Schematic illustration of memory cell geometry including the sensitive volume

two kinds of neutron and proton databases from 20 MeV to 1 GeV are prepared using the JQMD/GEM code [5,6]. One consists of so-called “inclusive” double-differential cross sections of all secondary ions including light ions. Another contains the “event-by-event” information, *i.e.*, the type of secondary ions and their emission energy and angle, so that simultaneous multiple ions emission can be correctly taken into account. Figure 4 shows a comparison of JQMD/GEM calculation with experimental data [7] for the p+Al reaction at 180 MeV, because there is no similar experimental data for Si. For production of heavy ions, the angle-dependent energy spectra are reproduced well by the JQMD/GEM calculation.

When the former “inclusive” database is used, a secondary ion j is firstly generated in a position chosen randomly in the interaction volume by sampling its energy and emission direction in terms of the double-differential cross sections. Then, the energy deposited by the ion in the SV is calculated numerically using the data of range and energy loss computed by the SRIM code [8]. In this case, $\sigma_N(E_{in})f(E_{in}, E)$ used in Eqs.(1) and (3) is replaced by $\sum_j \sigma_j(E_{in})f_j(E_{in}, E)$ where $\sigma_j(E_{in})$ is the production cross section of the ion of type j . Consequently, Eq.(3) can be re-written by

$$\sigma_{SEU}(E_{in}, E_c) = N_{Si} V_{int} \sum_j \sigma_j(E_{in}) F_j(E_c) = N_{Si} V_{int} \sum_j \int_{E_c}^{\infty} \sigma_j(E_{in}) f_j(E_{in}, E_d) dE_d, \quad (4)$$

It should be noted that Eq.(4) was used to calculate SEU cross sections in our earlier work [1].

In case of using the latter “event-by-event” database, a position where a nuclear reaction occurs is chosen randomly in the interaction volume shown in Fig.3. Then the total energy deposited in the SV by all secondary ions generated in a certain reaction event is calculated using the above-mentioned way.

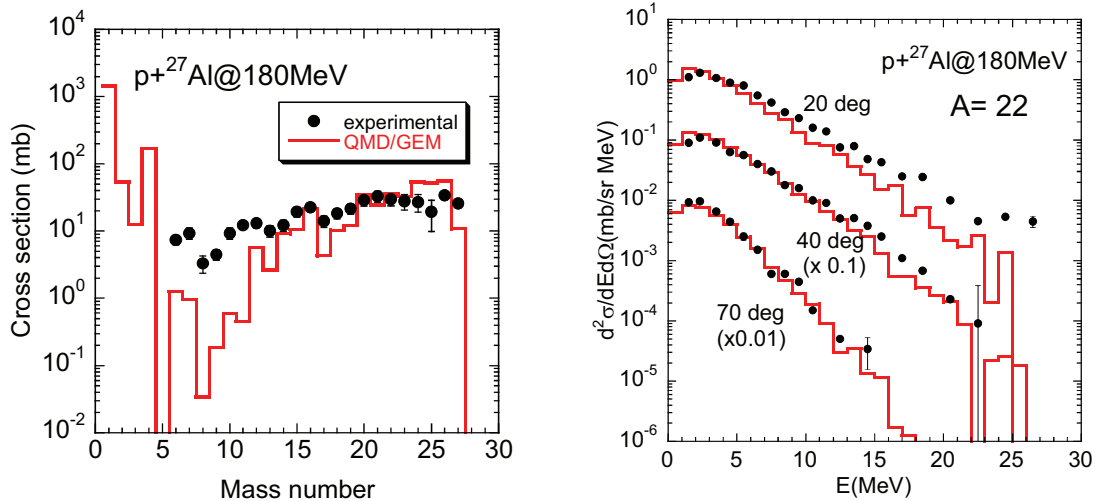


Fig.4 Comparison of JQMD/GEM calculation with experimental data of p+Al reaction at 180 MeV [7]

3. Comparison of calculated proton SEU cross-sections with experimental data

The present semi-empirical model is applied to calculations of proton induced SEU cross-sections for some memory devices at incident energies below 500 MeV. In the calculations, the “event-by-event” nuclear reaction data and the JENDL/HE-2004 data [9] for elastic scattering were used. In Fig.5, two examples of the results are presented with experimental data [10,11] for (a) 256Kb SRAM (HM62256) and (b) 4Mb SRAM (HM628512A), respectively. Other results are also shown in ref.[1]. The Weibull function parameters of heavy-ion SEU cross sections in Eq.(2) were determined by fitting of the experimental data for both devices [10,12]. The dimension of the SV was defined by the saturation cross section, σ_{HI}^{∞} , and the sensitive depth, d , which is a free parameter. The interaction volume surrounding the SV was taken to be so large that the calculated proton SEU cross-section was saturated.

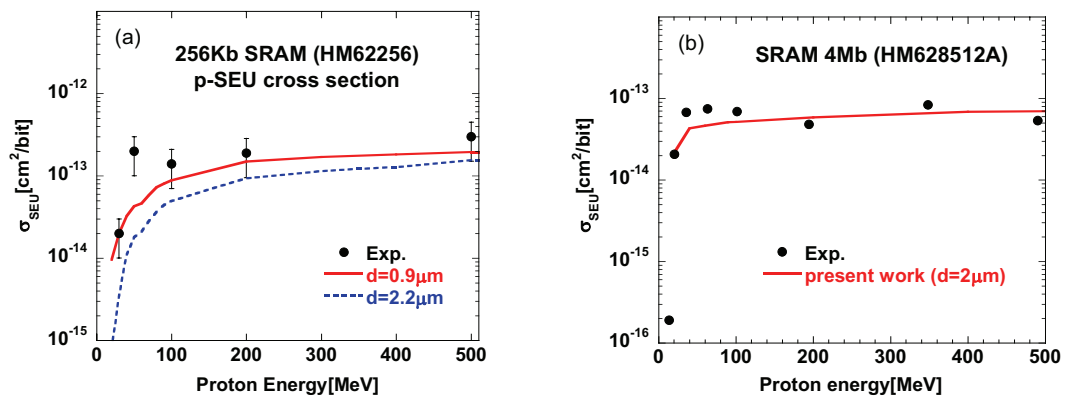


Fig.5 Comparison of calculated proton SEU cross-sections with experimental data [10,11]
 (a) 256Kb SRAM and (b) 4Mb SRAM

In Fig.5, our model calculation is generally in good agreement with the measured SEU cross sections in shape and magnitude. The proton SEU cross sections rise steeply at energies below 50 MeV and become nearly constant at energies higher than 100 MeV. The SV size is one of the key parameters in calculations of SEU cross-section using the models based on the SV concept. In Fig.5(a), the dependence of the sensitive depth ($d=0.9$ and $2.2 \mu\text{m}$ [13]) is shown. Our calculation supports the smaller d value. However, further investigation will be necessary for reliable determination of the sensitive depth.

4. Discussion

4.1 Relative contribution of secondary-ion on SEU

We have examined relative contribution of secondary ions to SEU cross section for two different Q_c values: (a) $Q_c = 50\text{fC}$ and (b) 10fC . It is calculated using Eq. (4) as functions of incident energy and critical charge for a device having the sensitive volume $V_s = 1 \times 1 \times 1 \mu\text{m}^3$, and the “inclusive” reaction data (without elastic scattering) are used. As can be seen in Fig.6, heavier ions (Na, Mg, and Al) are dominant at lower incident energies, while lighter ions (C, N, and O) contribute as the incident energy increases. As Q_c become smaller, there appears the contribution from lighter ions with atomic mass less than Be, particularly He. Since these light ions have smaller LET than heavy ions, SEU may take place for smaller Q_c . It should be noted that the QMD calculation underestimates the production of secondary ions with $A=6$ to 12 as shown in Fig.4. Further improvement of the reaction model will be necessary because Q_c is expected to decrease more and more in the future.

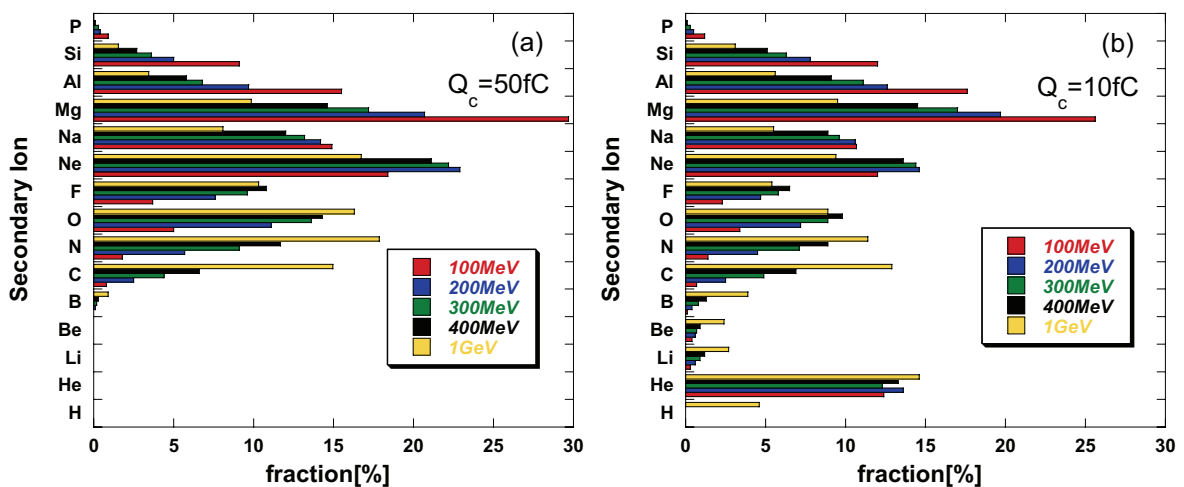


Fig.6 Relative contribution of each secondary ion to SEU cross section: (a) $Q_c = 50\text{fC}$ and (b) 10fC

4.2 Neutron elastic scattering

The influence of neutron elastic scattering on SEU was examined using JENDL/HE-2004 data [2], because the elastic scattering is not included in the QMD calculation. As shown in Fig.7, the elastic cross section is much larger than the reaction cross section in the incident energy range between 20 and 120 MeV. Therefore, it is of importance to know how the elastic scattering influences on SEU in the incident energy range of interest.

Relative contribution of the elastic scattering to SEU is calculated as functions of incident energy and critical charge for a device having the sensitive volume $V_s = 1 \times 1 \times 1 \mu\text{m}^3$. The ratio of the elastic SEU cross-section to the total SEU cross section is plotted as a function of incident neutron energy in Fig.8. Paying attention to the energy range above 20 MeV, one can find that the contribution of the elastic scattering increases as the critical charge is reduced and the maximum fraction is at most 20 % near 20 MeV. Less important role of the elastic scattering can be explained by the fact that the average kinetic energy of the recoiled ^{28}Si becomes smaller than other heavy recoils as seen in Fig.9. On the other hand, the ratio increases suddenly up to unity at a certain energy corresponding to the SEU threshold energy below 10 MeV except at $Q_c=50$ fC. In this energy range, the elastic scattering is the most dominant nuclear process as seen in Fig.7 and the other reaction channels are suppressed. Thus, the elastic scattering is expected to play an essential role near the SEU threshold energy for the memory devices with small Q_c .

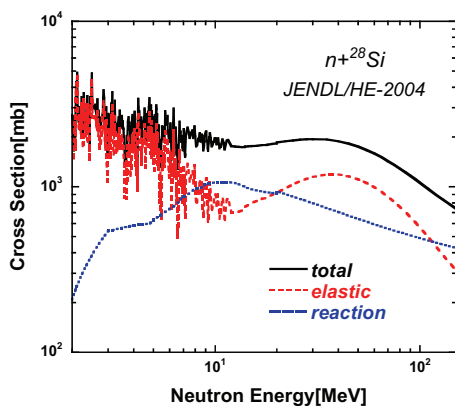


Fig.7 Neutron total, elastic, and reaction cross-section of ^{28}Si taken from JENDL/HE-2004

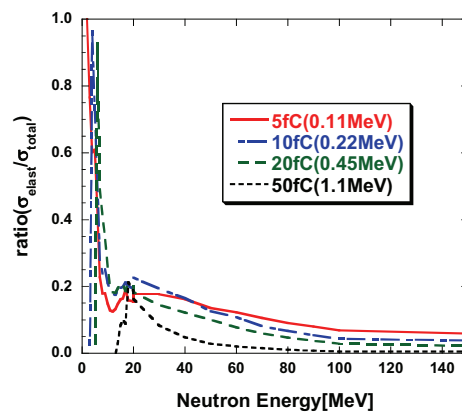


Fig.8 Ratio of the elastic SEU cross section to the total SEU cross section

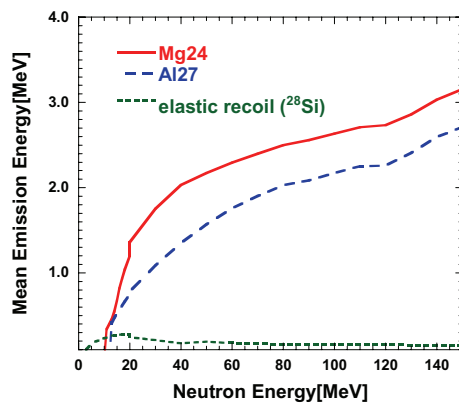


Fig.9 Averaged emission energy for elastic recoil (^{28}Si), ^{27}Al and ^{24}Mg

4.3 Simultaneous multiple ions emission

The effect of simultaneous multiple ions emission on SEU was investigated by comparing the SEU cross sections calculated using the above-mentioned two different nuclear reaction databases consisting of the “inclusive” data (denoted hereinafter Cal. 1) and the “event-by-event” data (Cal.2), respectively [2].

In Fig. 10(a), the SEU cross sections calculated by Eq. (3) are plotted as a function of E_c for the case of a small sensitive volume with $V_s = 1 \times 1 \times 1 \mu\text{m}^3$. There is no obvious difference between two calculations with different nuclear reaction data sets. This implies that simultaneous multiple ions emission has

negligible influence on SEU if the size of SV is small. To see the reason, the mean number of emitted ions was examined as functions of the atomic number of generated ions and the incident neutron energy. Secondary light ions, particularly protons and deuterons, are mainly included in the simultaneous multiple ions emission and the total fraction of heavy nuclides is nearly equal to unity. Even if many light ions are generated by a certain nuclear reaction, the energy deposited in the small SV is negligibly small because of their low LET. Also, a geometrical consideration suggests that the probability that more than one ion passes through the SV simultaneously is reduced as the size of SV becomes small. The present analysis indicates that it is a quite good approximation to use the “inclusive” nuclear data in the calculation of SEU rates for a device having as small SV as this case.

Figure 10(b) shows the result for a larger SV size ($V_s = 20 \times 20 \times 2 \mu\text{m}^3$) than that used in Fig.10(a). In this case, there is an appreciable difference between two calculations as the critical energy is over 2 MeV corresponding to $Q_c=89$ fC. Also, a significant difference is seen near $E_c=0$. Since the sensitive area is much wider than the above case, light ions emitted in the lateral direction can deposit considerable energy along the path in spite of low LET. Thus, the emitted light-ions become involved in SEU as well. If one uses the “inclusive” data, contributions from these light ions are added incoherently, which results in larger value at very small E_c than Cal.2. In the calculation with the “event-by-event” data, the total energy deposited by all the ions generated in a reaction event is tallied. This leads to enhancement at larger E_c compared to the result of Cal.1.

Through this investigation, we draw a conclusion that the simultaneous multiple ions emission does not influence seriously on SEUs for the devices having the small SV size. However, such multiple-ions emission is expected to have some sorts of effects on multiple bits upsets (MBUs) [14].

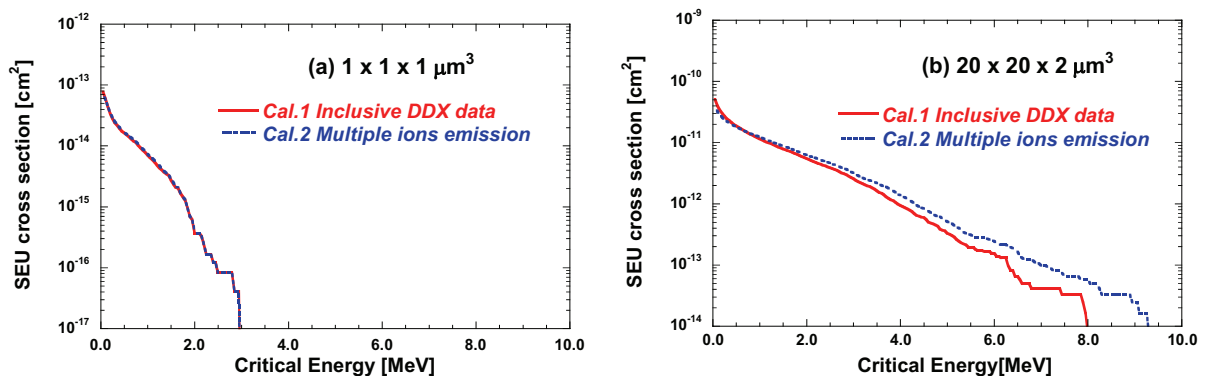


Fig.10 Calculated neutron SEU cross section as a function of critical energy E_c for the following sensitive volume: (a) $V_s = 1 \times 1 \times 1 \mu\text{m}^3$ and (b) $V_s = 20 \times 20 \times 2 \mu\text{m}^3$

5. Summary and outlook

The results of our recent work on nucleon-induced SEUs were presented from the point of view of the nuclear reaction data relevant to SEUs. The proton SEU cross sections calculated using the semi-empirical model with the “event-by-event” nuclear reaction data and the JENDL/HE-2004 for the elastic scattering reproduced generally well the incident energy dependence of experimental proton SEU cross sections in both shape and magnitude. This indicates that the present semi-empirical model based on the sensitive volume concept has a capability of predicting nucleon-induced SEU cross sections reasonably well if one can obtain available heavy-ion SEU data and reliable information about the sensitive depth.

Some quantitative analyses were performed in order to investigate the crucial impact of nuclear reaction data on SEU simulation. The relative contribution of secondary ions to proton SEU cross section was investigated. As a result, it was found that secondary heavy ions has a larger contribution at low incident energies than light ions, while the latter has a large fraction as the incident energy increases and the critical charge decreases. The analysis indicates that the relative importance of elastic scattering is enhanced when the critical charge is small, because the averaged kinetic energy of the recoil nucleus, ^{28}Si , is smaller than the other heavy recoils. Our calculation for the memory devices with the small SV shows that its fraction becomes at most 20% for $Q_c = 5$ fC. In addition, the simultaneous multiple ions emission was found to have negligible effects in the case where the sensitive volume (SV) size is sufficiently small because the

light ions having low LET are primarily produced in the process. However, it is likely that multiple ions production has some impact on multiple-bit upsets (MBUs) for devices with low Q_c [14].

The critical charge in SRAMs is expected to decrease more and more with progress in high integration in the future [15]. As shown in Fig. 6, our analysis suggests a possibility that light-ion production such as alpha will have a large effect on SEU. The present QMD/GEM model underestimates preequilibrium components for light composite particle emission. This will require further refinement in order to provide more reliable nuclear reaction data for microscopic simulation of SEUs. The present status of the related nuclear data measurements is not satisfactory. Therefore, experimental double-differential cross sections of all secondary ions will be strongly requested to benchmark the nuclear data and/or nuclear model calculations used in SEU simulations.

Acknowledgement

The author is grateful to Akihiro Kodama and Kouta Nishijima for their full cooperation on this work.

References

- [1] Y. Watanabe et al., Proc. of Int. Conf. on Nuclear Data for Science and Technology, Santa Fe, USA, Sept. 26-Oct. 1, 2004; AIP Conference Proceedings Vol. 769, pp. 1646-1649, (2005).
- [2] A. Kodama, K. Nishijima, and Y. Watanabe, Proc. of the 2005 Symp. on Nuclear Data, Feb. 2-3, 2006, JAEA, Tokai, Japan; JAEA-Conf 2006-009, p. 151-156 (2006).
- [3] J. Barak et al., IEEE Trans. Nucl. Sci., **43**, No.3, 979-984 (1996).
- [4] E.L. Petersen, IEEE Trans. Nucl. Sci., **43**, No. 6, 952-959 (1996); *ibid*, 2805-2813 (1996).
- [5] K. Niita et al., Phys. Rev. C, **52**, 2620 (1995); JQMD code, JAERI-Data/Code 99-042 (1999).
- [6] S. Furihata, Nucl. Inst. Method in Phys. Res. B **171**, 251 (2000).
- [7] K. Kwiatkowski et al., Phys. Rev. Lett. **50**, 1648 (1983).
- [8] J.F. Ziegler, SRIM-2000 code, URL <http://www.srim.org/>
- [9] Y. Watanabe et al., Proc. of Int. Conf. on Nuclear Data for Science and Technology, Santa Fe, USA, Sept. 26-Oct. 1, 2004; AIP Conference Proceedings Vol. 769, pp. 326-331, (2005).
- [10] R. Harboe-Sorensen et al., IEEE Trans. Nucl. Sci. **40**, No.6, 1498 (1993).
- [11] C.S. Dyer, et al., IEEE Trans. on Nucl. Sci, **51**, No.5, 2817 (2004).
- [12] C. Infuimbert, et al., IEEE Trans. on Nucl. Sci, **49**, No.3, 1480 (2002).
- [13] P.D. Bradley and E. Normand, IEEE Trans. on Nucl. Sci, **45**, No.6, 2929 (1998).
- [14] F. Wrobel et al., IEEE Trans. Nucl. Sci., **48**, No.6, 1946-1952 (2000).
- [15] P. Shivakumar et al., Proc. of 2002 Int. Conf. on Dependable Systems and Networks, 389-398 (2002).

2.4 Nuclear Data Needs for Fast Reactors

Go Chiba

Japan Atomic Energy Agency

e-mail:chiba.go@jaea.go.jp

In the present paper, we show that the neutronics parameter uncertainties expected in current design studies of fast reactors are reasonable when both differential data and integral data are taken into consideration. This conclusion is based on an assumption that cross section covariance is properly evaluated. We attempt to verify the cross section covariance of JENDL-3.3 with the integral data, which were obtained at critical assemblies at Los Alamos National Laboratory. As a result, we suggest that uncertainty of P1 coefficient of elastic scattering cross sections of U-238 seems to be underestimated.

I Introduction

Various researches on nuclear data for fast reactor applications have been carried out until now. Currently, targets of nuclear data researches for fast reactor applications shift to improvement of the nuclear data quality of minor actinides and fission products. In the present paper, we will discuss necessities of nuclear data researches for fast reactor applications except for those on minor actinides and fission products, and attempt to obtain its conclusion.

II Nuclear data needs for fast reactors

‘Nuclear data needs for fast reactors’ are motivations to improve the prediction accuracies for neutronics parameters of fast reactors. **Table 1** shows uncertainties in neutronics parameters with 1σ reliability, which are expected in the current design studies for fast reactors. These uncertainties are composed of uncertainties induced by nuclear data and numerical simulations for neutron transport.

Before we discuss a necessity to reduce these uncertainties, we have to show that these uncertainties are reasonable. This is the main target of the present paper. The necessity to reduce uncertainties is a future topic.

Neutronics parameter uncertainties induced by nuclear data uncertainties can be estimated using covariance data given in nuclear data files and sensitivity coefficients. **Table 2** shows an example of this estimation for a 1,500MWe fast reactor⁽¹⁾. This result shows

Table 1: Neutronics parameter uncertainties expected in fast reactor design studies

	Uncertainties (%)
Criticality	0.4
Sodium-voided reactivity	7.5
Doppler reactivity	7.5

that the current nuclear data satisfies the expectation for prediction accuracies of the sodium-voided reactivity and the Doppler reactivity. However, uncertainty in criticality is much larger than the expectation. **Table 3** shows the component-wise uncertainties in criticality. It is desirable to improve nuclear data for such nuclide and reaction, if possible.

It has been shown above that we cannot satisfy the expectation of prediction accuracies of neutronics parameters in the current design studies only with the differential data, which are information on evaluated nuclear data files. Hence, we have utilized also the integral data, which are, for example, multiplication factor or spectrum indices obtained at critical assemblies or power reactors via the cross section adjustment technique based on the Bayesian theory. **Table 4** shows neutronics parameter uncertainties when using both the differential and integral data. It is shown that the expectation in the design studies is satisfied using these information.

We have shown above that the uncertainties expected in the current design studies are reasonable. However, it should be noted that the above conclusion is based on the following assumptions:

- Uncertainties induced by numerical simulations for neutron transport are ‘properly’ estimated.
- Covariance data for nuclear data are ‘properly’ estimated.

The current numerical simulations for neutron transport are based on the deterministic

Table 2: Nuclear data-induced neutronics parameter uncertainties

	Uncertainties (%)
Criticality	1.0
Sodium-voided reactivity	6.0
Doppler reactivity	8.0

Table 3: Nuclide- and reaction-wise uncertainties in criticality

	Uncertainties (%)
Pu-239, χ	0.4
Pu-239, (n,f)	0.5
U-238, (n,n')	0.3
Fe, (n,n')	0.5

Table 4: Nuclear data-induced neutronics parameter uncertainties with differential and integral data

	Uncertainties (%)
Criticality	0.26
Sodium-voided reactivity	4.0
Doppler reactivity	7.0

theory. Hence, it is not easy to quantify uncertainties induced by numerical simulations. Especially, it is difficult to quantify a correlation between the uncertainties for critical assemblies and those for power reactors since the structure of unit lattice (fuel assembly) is totally different from each other. If it is possible to utilize the Monte-Carlo method for neutronics simulations, the uncertainties induced by numerical simulations may be easily estimated.

Since evaluated nuclear data is ‘evaluated’ by a person, evaluated nuclear data depend on the person. The evaluated nuclear data is verified through its application into integral data. This procedure can be also applied to covariance of nuclear data. In the next chapter, we will show an example to verify the covariance data with integral measurement data.

III Verification of evaluated covariance data with integral measurement data

In this chapter, we will utilize experimental data obtained at fast critical assemblies in Los Alamos National Laboratory. The features of these assemblies are shown in **table 5**.

Table 5: Features of critical assemblies

Name	Fuel	U-reflector	Radius (cm)	Exp. error ($\Delta k/kk'$)
JEZEBEL	Pu	No	6.3849	0.002
JEZEBEL-240	Degraded Pu	No	6.6595	0.002
GODIVA	U	No	8.7407	0.001
FLATTOP-Pu	Pu	Yes	24.142 (Fuel:4.5332)	0.003
FLATTOP-25	U	Yes	24.1242 (Fuel:6.1156)	0.003

Figure 1 shows C/E values of criticalities of these assemblies with the latest nuclear data files. The error bars in this figure refer to 1σ uncertainties of measurement data. These neutron transport calculations are carried out with the continuous-energy Monte-Carlo code.

The nuclear data-induced uncertainties in these criticalities, V_k , can be estimated as

$$V_k = \vec{G} \vec{M} \vec{G}^t \quad (1)$$

where \vec{G} is sensitivities of nuclear data to k_{eff} and \vec{M} is covariance matrix of nuclear data. In the present study, we calculate \vec{G} with the discrete ordinates transport method and use covariance data given in JENDL-3.3. The calculated uncertainties, *i.e.*, standard deviations and correlation matrix, are shown in **table 6** and **7**.

To verify deviations of these C/Es from 1.0 and uncertainties in C/Es, we calculate χ^2 value defined as

$$\chi^2 = (\vec{C}E - \vec{1.0}) \vec{V}^{-1} (\vec{C}E - \vec{1.0})^t \quad (2)$$

where $\vec{C}E$ refers to a vector of C/E values, $\vec{1.0}$ a vector whose elements are 1.0 and \vec{V} covariance matrix defined as

$$\vec{V} = \vec{V}_k + \vec{V}_e + \vec{V}_m \quad (3)$$

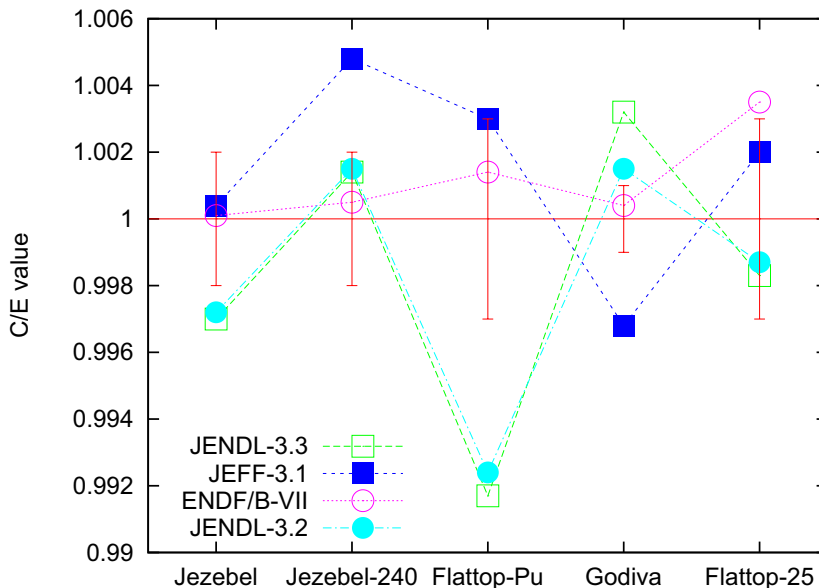


Figure 1: C/E values of criticalities of LANL small-sized fast critical assemblies

Table 6: Standard deviations in criticalities induced by nuclear data uncertainties

Core	Standard deviation	C/E
JEZEBEL	0.0054	0.9970
JEZEBEL-240	0.0057	1.0014
FLATTOP-Pu	0.0064	0.9917
FLATTOP-25	0.0052	0.9984
GODIVA	0.0041	1.0032

Table 7: Correlation matrix in criticalities induced by nuclear data uncertainties

	JEZ	JEZ240	FLAT-Pu	FLAT-25	GODIVA
JEZ	1.00	0.98	0.85	0.07	0.09
JEZ240		1.00	0.85	0.05	0.07
FLAT-Pu			1.00	0.31	0.08
FLAT-25				1.00	0.77
GODIVA					1.00

where \vec{V}_e corresponds to uncertainties in experimental data and \vec{V}_m statistical errors in calculated values. We obtain 6.8 of this χ^2 value in the present case. A value, that χ^2 is divided by the degree of freedom (5 in this case), becomes about 1.4. This result suggests that nuclear data covariance, or uncertainty in experimental data or statistical errors in Monte-Carlo calculations are slightly underestimated.

In the results obtained with JENDL-3.3, C/E values for U-reflected assemblies (FLATTOP-

Pu and FLATTOP-25) are much smaller than those of bare assemblies (JEZEBEL and GODIVA). However, as shown in table 7, nuclear data-induced uncertainties of JEZEBEL and FLATTOP-Pu (GODIVA and FLATTOP-25 also) have strong correlations to each other. Hence, it is difficult to describe this ‘reflector-bias’ with nuclear data uncertainty.

This bias is not observed in the ENDF-VII result at all. Through sensitivity analyses, this difference is caused by a difference in the P_1 coefficients of elastic scattering cross sections of U-238. **Figure 2** shows this coefficient. **Figure 3** shows differences of the P_1

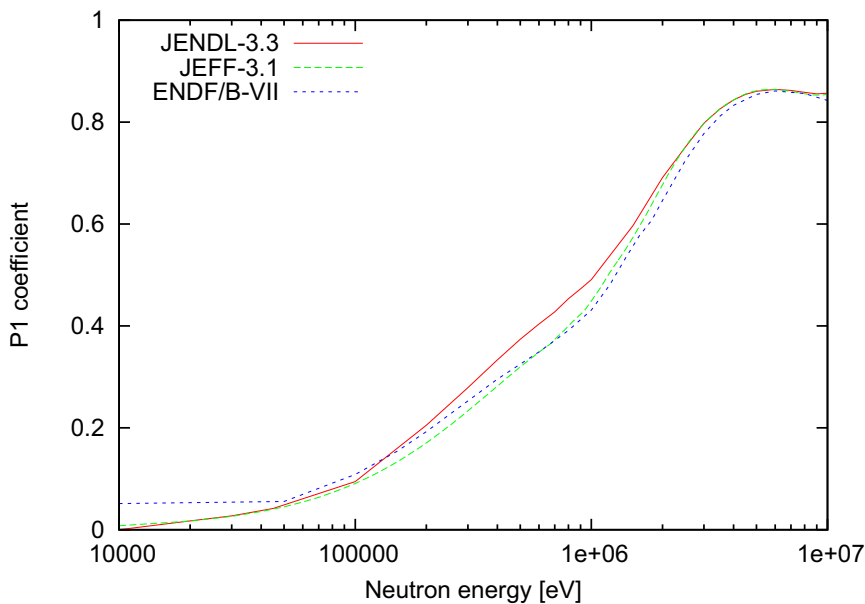


Figure 2: P_1 coefficients of elastic scattering cross sections of U-238

coefficients of ENDF/B-VII and JEFF-3.1 to that of JENDL-3.3. JENDL-3.3 evaluates this cross section larger about 10% systematically than the other data files.

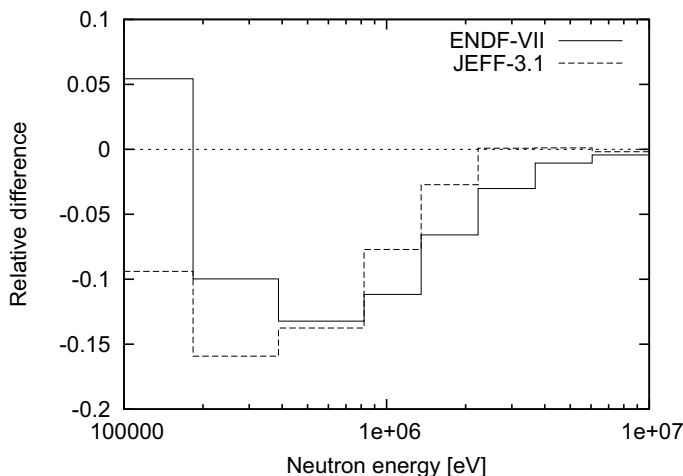


Figure 3: Difference in P_1 elastic scattering cross sections of U-238 to JENDL-3.3

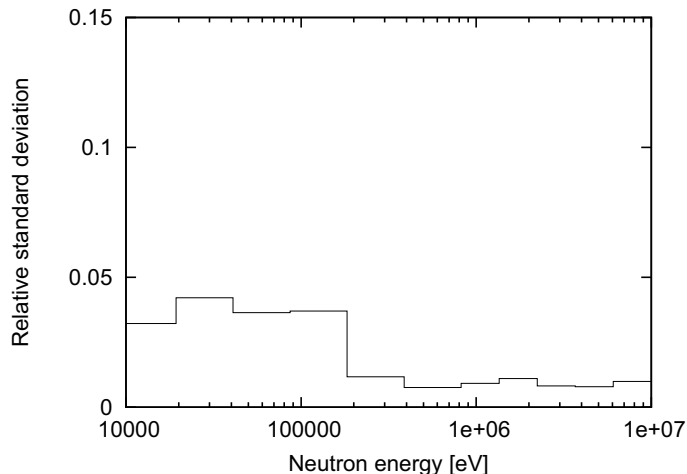


Figure 4: Standard deviation of P1 elastic scattering cross sections of U-238

Figure 4 shows standard deviations of this cross section based on JENDL-3.3. This uncertainty is much smaller than the difference between different nuclear data files.

With this comparison and the reflector-bias observed in the JENDL-3.3 results, it can be said that the uncertainty for P1 coefficients of elastic scattering cross sections of U-238 seem to be underestimated in JENDL-3.3 evaluations.

IV Conclusion

We have shown that the neutronics parameter uncertainties expected in the current design studies of fast reactors are reasonable when both differential and integral data are taken into consideration. We also pointed out that this conclusion is based on an assumption that cross section covariance is properly evaluated. We have attempted to verify the evaluated cross section covariance with the integral data.

References

- [1] T.Hazama, *et al.*, ‘Development of the unified cross-section set ADJ2000R for fast reactor analysis,’ JNC TN9400 2002-064 (2002) [in Japanese].

2.5 Nuclear Data Needs for Advanced Reactors

Tadashi Yoshida

Musashi Institute of Technology, Tamazutsumi 1-28-1, Setagaya-ku Tokyo 158-8557, Japan

A wide spectrum of advanced reactor concepts are being envisaged around the world. The Generation IV reactors selected by International Forum in the early 2000's cover 6 new categories of advanced reactors. Apart from the Gen-VI reactors, introduction of Inert Matrix Fuel in order to burn plutonium effectively is extensively studied. These new reactor concepts and new materials used therein create new needs for nuclear data.

1. Introduction

In the course of time, scientific and technology fields which are in keen needs of the nuclear data are expanding from conventional reactor applications to astronomy, electronics, particle accelerators, ADS and so on. Accordingly the required data spread from the neutron data less than, for instance, 20MeV to much higher energy up to several GeV including the charged particle and the photon reaction data. In this report, however, we confine the survey within the advanced fission-reactor applications. When we consider about the future advanced reactors, it seems appropriate to cite, first of all, the Generation IV reactors, which are expected to be deployed in 2030's. They are ; 1) Supercritical Water-cooled Reactor (SCWR), 2) Sodium-cooled Fast Reactor (SFR), 3) Lead-cooled Fast Reactor (LFR), 4) Gas-cooled Fast Reactor (GFR), 5) Very High Temperature Reactor (VHTR), and Molten Salt Reactor (MSR). In order to discuss the nuclear data needs for analysis and design of these reactors, Workshop on Nuclear Data Needs for Generation-IV System was held on 5 ~ 7 April 2005 in Antwerp [1]. Discussion there can be summarized from two view-points, namely, the quality and the variety of nuclear data. As for the quality, most speakers stressed the urgent necessity for the covariance matrices. As for the variety, the needs come from the non-conventional materials

introduced into the core of the Gen-IV reactors. On the other hand, the concepts of the Inert Matrix Fuels under study worl-wide can be realized by introducing exotic materials, in the sense of neutronics, into their cores. In this paper we preview the nuclear data which become necessary in feasibility study and design of those advanced fission reactors.

In advance of the Antwerp Workshop, another workshop on Gen-IV nuclear data was also held in the US domestically. The conclusions and the recommendations from this US/CSEWG Workshop were summarized by Taiwo and Khalil [2] at the begining of Antwerp Workshop.

II. Covariance Data

Aliberti *et al.* [3] made a sensitivity analysis and evaluated the present uncertainty in various reactor characteristics ranging from k_{eff} to decay heat. They used two independent sets of covariance matrices. One is an ANL “home made” covariance set and another is a set available from the NEA Data Bank, which are the selection from JENDL3.3, IRDF-2002 ENDF/B-V, -VI and JEFF3. The systems they studied are SFR, LFR, GER, VHTR and, in addition, EFR (European Fast Reactor). Roughly speaking, the inclusion of the off-diagonal elements of the covariance matrices increases the estimated uncertainty by 60 ~ 70% though only the energy-energy correlations are taken into account. Hagura *et al.*, concluded that 10 ~ 30% increase in the uncertainty comes from the inclusion of the energy correlation in their error analysis of the actinide decay heat from spent LWR fuels [4].

Apart from the off-diagonal elements, it should be kept in mind that the standard deviation, the square roots of the diagonal elements of the covariance matrix, varies drastically from set to set. Taking fission as an example, SD differs by factor of more than ten in 10 ~ 100 eV for ^{241}Pu , and 50 ~ 100 % for ^{241}Am less than 100 keV. It is clear from these examples that consistent and reasonable uncertainty for each nuclide should be given prior to the off-diagonal elements. The importance of covariance data, however, does never diminish as many authors discuss in Ref. [1].

III. Gen-IV Reactors

As any fully exotic materials are not introduced in the Generation-IV reactors from the neutronic

point of view, the data needs may not change drastically from the case of conventional reactors. Although the significant accumulation of minor actinides (MA) will result from the increase of extended burnup in advanced reactors, MA data do not always play any decisive role with some exceptions according to the analysis made in Ref.[3]. On the other hand the data for Pu-isotopes become more and more important. For example, the dominant path leading to MA nuclides runs through the neutron capture in ^{240}Pu and therefore the uncertainty of the $^{240}\text{Pu}(n, \gamma)$ cross section must be diminished. The standard deviation in JENDL-3.3 for this reaction is less than 2 %, except the energy range from 10 to 20 eV where the SD reaches 10%. This might be too small when we consider the fact that even the ^{235}U resonance capture is now to be revisited as one of the activities of WPEC[5]. In reality Rimpault stressed the present inconsistency in $^{240}\text{Pu}(n, \gamma)$ between JEF2.2 and new evaluation, and further its large impact on the CAPRA PuN core design [6].

Importance of the nuclear data for non-conventional materials were stressed in the GEN-IV nuclear data workshop [1] as well as the enhanced importance of the Pu-isotopes. These new materials are lead and bismuth in LFR, silicon and zirconium in GFR, Th and ^{233}U in MSR and so on. Especially the inelastic scattering cross section for Pb attracted attention in the Antwerp Workshop.

III. Actinide Burner and Inert Matrix Fuel

In order to manage the surplus of the world inventory of plutonium, the inert matrix fuel (IMF) is studied world wide [7]. In addition to this, U-free fuels are also envisaged in transmuting the minor actinides [8]. Table I taken from Ref. [7] shows the candidates of IMF materials. As seen here, magnesium, aluminum, zirconium, yttrium are among the well-suited elements for IMF and the nuclear data for these elements will be required along with the progress of the IMF study.

IV. Concluding remarks

Nuclear data needs do not change fundamentally by placing advanced reactors in the scope, although non-conventional materials such as lead or silicon will be introduced to the core. We have already the nuclear data for most of these materials in the major data libraries. Much more reliability,

however, will surely be required for these materials along with the development of the design study. On the other hand, the persistent needs for qualified nuclear data for actinides, especially Pu isotopes, will surely continue because the highly extended burnup is anticipated in the advanced reactors.

Table I Example of Inert Matrix Fuel Materials (taken from ref. 7)

Inert Matrix Type	Inert Matrix Formula
Elements	C, Mg, Al, Si, Cr, V, Zr, Mo, W
Inter-metals	AlSi, AlZr, ZrSi
Alloys	stainless steel, zirconium alloys
Carbides	$^{11}\text{B}_4\text{C}$, SiC, TiC, ZrC
Nitride	AlN, TiN, ZrN, CeN
Binary oxides	MgO, Y_2O_3 , ZrO_2 , CeO_2
Ternary oxides	MgAl_2O_4 , $\text{Y}_3\text{Al}_5\text{O}_{12}$, ZrSiO_4
Oxide solid solutions	$\text{Y}_y\text{Zr}_{1-y}\text{O}_{2-y/2}$, $\text{Mg}_{(1-x)}\text{Al}_{(2+x)}\text{O}_{(4-x)}$

Referenes

[1] P. Rullhusen (ed.) “*Nuclear Data Needs For Generation IV Nuclear Energy Systems.*” Proceedings of the International Workshop, (2006) World Scientific Publishing

[2] T.A.Taiwo and H.S.Khalil, *ibid.*, pp.8~17

[3] G. Aliberti, G.Palmiotti, M.Salvatores, T.K.Kim, T.A.Taiwo, I.Kodeli, E.Sartori, J.C.Bosq, and J.Tommasi, *ibid.*, pp.81~100

[4] N.Hagura, T.Yoshida, M.Nakagawa, Int. Conf. on Nucl. Data for Science and Technol., Nice (2007)

[5] WPEC SubGroup 29, <http://www.nea.fr/html/science/wpec/index.html>

[6] G.Rimpault, Proc. International Workshop on Nuclear Data Needs For Generation IV Nuclear Energy Systems, (2006) pp.18~31

[7] C.Deguelldre, H.Akie, P.Boczar, N.Chauvin, M.Meyer, V.Troyanov, Global 2003, pp.1967~1973

[8] D.Haas, A.Fernandez, J.Somers, Proc. International Workshop on Nuclear Data Needs For Generation IV Nuclear Energy Systems, (2006) pp.64~69

2.6 Needs of Nuclear Data for Advanced Light Water Reactor

Masao Chaki

Hitachi, Ltd. Power Systems
Power & Industrial Systems R & D Laboratory

Hitachi has been developing medium sized ABWRs as a power source that features flexibility to meet various market needs, such as minimizing capital risks, providing a timely return on capital investments, etc. Basic design concepts of the medium sized ABWRs are 1) using the current ABWR design which has accumulated favorable construction and operation histories as a starting point; 2) utilizing standard BWR fuels which have been fabricated by proven technology; 3) achieving a rationalized design by suitably utilizing key components developed for large sized reactors. Development of the medium sized ABWRs has proceeded in a systematic, stepwise manner. The first step was to design an output scale for the 600MWe class reactor (ABWR-600), and the next step was to develop an uprating concept to extend this output scale to the 900MWe class reactor (ABWR-900) based on the rationalized technology of the ABWR-600 for further cost savings [1]. In addition, Hitachi and MHI developed an ultra small reactor, "Package-Reactor" [2].

About the nuclear data, for the purpose of verification of the nuclear analysis method of BWR for mixed oxide (MOX) cores, UO₂ and MOX fuel critical experiments EPICURE and MISTRAL were analyzed using nuclear design codes HINES and CERES with ENDF/B nuclear data file. The critical keffs of the absorber worth experiments, the water hole worth experiments and the 2D void worth experiments agreed with those of the reference experiments within about 0.1%Δk. The root mean square differences of radial power distributions between calculation and measurement were almost less than 2.0%. The calculated reactivity worth values of the absorbers, the water hole and the 2D void agreed with the measured values within nearly experimental uncertainties. These results indicate that the nuclear analysis method of BWR in the present paper [3] give the same accuracy for the UO₂ cores and the MOX cores.

[1] Development of Medium Sized ABWRs (ABWR-600, ABWR-900),

Proceedings of GLOBAL 2005Tsukuba, Japan, Oct 9-13, 2005, Paper No. 417

[2] Development of the Package-Reactor, *Trans. At. Energy Soc. Japan, Vol.5, No. 4, pp. 257-267, 2006 (in Japanese)*

[3] Analysis of Mixed Oxide Fuel Critical Experiments EPICURE and MISTRAL with Nuclear Analysis Code for BWR, *Trans. At. Energy Soc. Japan, Vol.5, No. 1, pp. 34-44, 2006 (in Japanese)*

3. Papers Presented at Poster Sessions

This is a blank page.

3.1 Recent Activities for MA Cross-Section Measurements

Shoji NAKAMURA*¹⁾, Masayuki OHTA¹⁾, Hideo HARADA¹⁾,
Toshiyuki FUJII²⁾ and Hajimu YAMANA²⁾

1) Japan Atomic Energy Agency, 2-4 Shirane, Shirakata, Tokai-mura, Naka-gun, Ibaraki-ken 319-1195

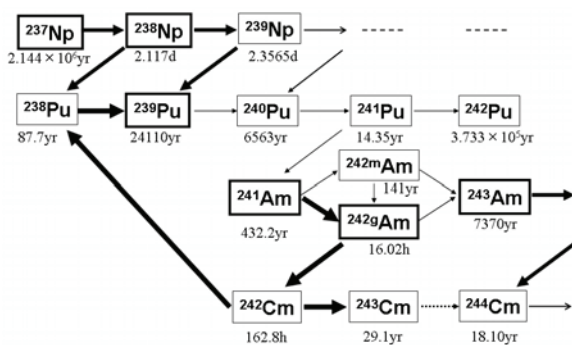
2) Kyoto University Research Reactor Institute, Kumatori-cho Sennan-gun, Osaka 590-0494

*E-mail: nakamura.shoji@jaea.go.jp

The social acceptability of nuclear power reactors is related to the waste management of long-lived fission products (LLFPs) and minor actinides (MAs) existing in spent nuclear fuels. The MAs (²³⁷Np, ²⁴¹Am, ²⁴³Am) are important in the nuclear waste management, because the presence of these nuclides induces long-term radiotoxicity because of their extremely long half-lives. **Figure 1** illustrates the section of the chart of the nuclides displaying the relevant reactions and decays. Neptunium-237 is one of the most important MAs because of its relatively large abundance in spent nuclear fuels of nuclear power reactors. As seen in Fig.1, ²³⁷Np is one of the nuclides that contribute to the breeding of ²³⁹Pu. Neptunium-238 also participates in the process. The Am isotopes generate the higher actinides as the Cm isotopes through neutron capture reactions. Since ²⁴²Cm generated by the ²⁴¹Am(n,γ) reaction has a relatively short half-life, the presence of ²⁴²Cm induces a problem of decay-heat in the reprocessing of spent nuclear fuels.

The transmutation is one of the solutions to reduce the radiotoxicity of nuclear wastes. In the transmutation study of MAs, the accurate data of neutron capture cross-sections are necessary to evaluate reaction rates by reactor neutrons. In this view point, the cross-section measurements have been made by an activation method. However, there are discrepancies among the reported data for the thermal-neutron capture cross-sections for these nuclides. The discrepancies reach to 10 - 20%. Therefore, our concern was focused to measure the cross-sections for these MAs. In the session, our recent activities, particularly for cross-section measurements of MAs (See **Table 1**), will be reported together with the details of experiments. Furthermore, a news flash for cross-sections of LLFPs will be presented on this occasion.

Table 1 Recent results for MA cross-sections



Nuclide	Half-life	Past Data (Author, Year)	JAEA Data
²³⁷ Np	2.14 × 10 ⁶ yr	σ ₀ = 158 ± 3 b I ₀ = 652 ± 24 b (Kobayashi 1994) σ ₀ = 180 ± 5 b (Letourneau 2004)	σ ₀ = 141.7 ± 5.4 b I ₀ = 862 ± 51 b (2003) [1] σ ₀ = 169 ± 6 b (2006) [2]
²³⁸ Np	2.1 day	No Data!	σ _{eff} = 479 ± 24 b (2004) [3]
²⁴³ Am	7370 yr	σ _{0m} = 80 b, σ _{0g} = 4.3 b σ _{0m+g} = 84.3 b (Ice 1966)	σ _{eff} = 174.0 ± 5.3 b (2006) [4]
²⁴¹ Am	432 yr	σ _{0g} = 768 ± 58 b I _{0g} = 1694 ± 146 b (Shinohara 1997)	σ _{0g} = 628 ± 22 b I _{0g} = 3.9 ± 0.3 kb (Tentative) [5]

Fig. 1 The section of the chart of the nuclides

[1] Katoh *et al.*, *JNST*, **40**, 559(2003). [2] Harada *et al.*, *JNST*, **43**, 1289(2006). [3] Harada *et al.*, *JNST*, **41**, 1(2004).
[4] Ohta *et al.*, *JNST*, **43**, 1441(2006). [5] Nakamura *et al.*, *JNST*, to be submitted.

3.2 Measurement of Neutron Capture Cross Sections of ^{139}La , ^{152}Sm and $^{191,193}\text{Ir}$ at 55 and 144keV

Vuong Huu Tan

Vietnam Atomic Energy Commission
59-Ly Thuong Kiet, Hanoi, Vietnam

Tran Tuan Anh, Nguyen Canh Hai and Pham Ngoc Son

Dalat Nuclear Research Institute
01-Nguyen Tu Luc, Dalat, Vietnam

Tokio Fukahori

Nuclear Data Center, Nuclear Science and Engineering Directorate
Japan Atomic Energy Agency
Tokai-mura, Naka-gun, Ibaraki-ken, 319-1195, Japan

The neutron capture cross sections of ^{139}La , ^{152}Sm and $^{191,193}\text{Ir}$ at average energies of 55keV and 144keV have been measured relative to the standard capture cross sections of ^{197}Au by means of the activation method. The neutron beams were derived by filtered techniques from the horizontal channel No.4 of the research reactor at the Dalat Nuclear Research Institute, Vietnam. A fast-digital gamma-ray spectroscopy in compacted with a 58% efficient HPGe detector has been used for measurements of gamma-ray spectra from the activated samples. The correction factors for multi-scattering, self-shielding and resonance capture effects of neutron in the irradiating samples were calculated by Monte-Carlo technique. The present results have been compared with the previous measurements, and the evaluated data from JENDL-3.3 and ENDF/B-VI.8 libraries.

Key words: *neutron, capture cross section, nuclear reaction data, filtered neutron beam, resonance neutron capture, correction*

1. Introduction

Accurate measurements of neutron capture cross sections for most of nuclides are currently necessary for the calculations of neutron transport, the assessments of the reactor safety, the investigations of high-burn-up core characteristics, the decay heat power predictions, and for the nuclear transmutation study. In keV energy region, the (n,γ) cross sections of the nuclides at or near magic neutron number, $N=50$, 82 and 126 are special important for the study on the s-process reaction chain for nucleosynthesis. However, the present status of experimental data for capture cross sections is still inadequate both in quality and in quantity. Therefore, it is important to perform the precisely measurements of capture cross sections for those nuclides, particular in keV energy region [1-6].

In the present experiment, we performed the measurements of capture cross section of ^{139}La , ^{152}Sm and $^{191,193}\text{Ir}$ on the filtered neutron beams of 55keV and 144keV, relative to the standard capture cross section of ^{197}Au by the activation method. The neutron beams were derived from the horizontal channel No.4 of the research reactor at the Dalat Nuclear Research Institute (DNRI), by using the filtered compositions of $98\text{cmSi} + 35\text{g/cm}^2\text{S} + 0.2\text{g/cm}^2\text{B}^{10}$ and $98\text{cmSi} + 1\text{cmTi} + 0.2\text{g/cm}^2\text{B}^{10}$ for 55keV and 144keV respectively [6,7]. The neutron energy resolution, FWHM, is 8keV at 55keV peak, and 22keV at 144keV peak [7].

Beside determining the corrections for neutron multi-scattering and self-shielding in irradiated samples, it is important to concern that the large resonance capture cross sections of the standards and samples, in the slow neutron background region above the Cd-Cutoff energy, strongly contribute to the

uncertainty of experimental results. Therefore, the correction factors for slow neutron resonance capture in the present experiments were also calculated by the general least square method for strong resonance captures at 4.92eV of ¹⁹⁷Au, 8.06eV of ¹⁵²Sm, 1.3eV of ¹⁹³Ir, 0.67eV, 5,38eV and 6.15eV of ¹⁹¹Ir, and 72.3eV of ¹³⁹La. Furthermore, a low background and fast-digital spectroscopy with a high efficiency, 58%, HPGe detector has been used for detection of gamma-ray spectrum from the irradiated samples, and the statistical uncertainties are expected to be less than 1%.

2. Experiments

The measurements for neutron capture cross sections of ¹³⁹La, ¹⁵²Sm and ^{191,193}Ir at the energies of 55keV and 144keV were performed on the filtered neutron beams of DNRI. The neutron beams were collimated to 3cm in diameter by using the usual materials of LiF, Cd, B₄C, Pb and borated paraffin. The physical properties of these beams are given in Table 1. Since the neutron spectra had been experimentally measured before with a recoil-proton counter [6], in this work, the neutron transport and unfolding methods [8,9] were applied to obtain the exact spectra, shown in Fig. 1 and 2, which have been used for calculation of the average quantities and of the correction factors.

The samples were prepared from the natural oxide powders, 99.99% purity, of La₂O₃, Sm₂O₃ and IrO₂. In order to diminish the effect of water on the samples [10], each collected amount of the powders was dried up at about 105°C for several hours before weighting and pressing into pellets. Then the pellets were covered by thin polyethylene foils. The standard gold foils with 2.54cm in diameter and 0.01mm in thickness were used as the neutron flux monitors. Each sample was sandwiched between two gold disks, and the sample groups were wrapped in Cd covers with 0.5mm in thickness with aim to reject most of thermal neutron background. The irradiation time was 70 hours for every sample group.

The specific activities of the samples and the gold disks were measured by using the fast-digital spectroscopy system and with the high efficiency HPGe detector. The system was calibrated by using standard radioisotope sources and a multi-nuclides standard solution, supported by IAEA. Each of irradiated samples, standards and calibrated sources was measured under the same conditions.

Table 1 The properties of the filtered neutron beams [6]

Neutron energy (keV)	Filter combination	Flux density (n/cm ² /s)	FWHM
55	98cmSi + 35g/cm ² S + 0.2g/cm ² B ¹⁰	5.61 x 10 ⁵	8 keV
144	98cmSi + 1cmTi + 0.2g/cm ² B ¹⁰	2.14 x 10 ⁶	22 keV

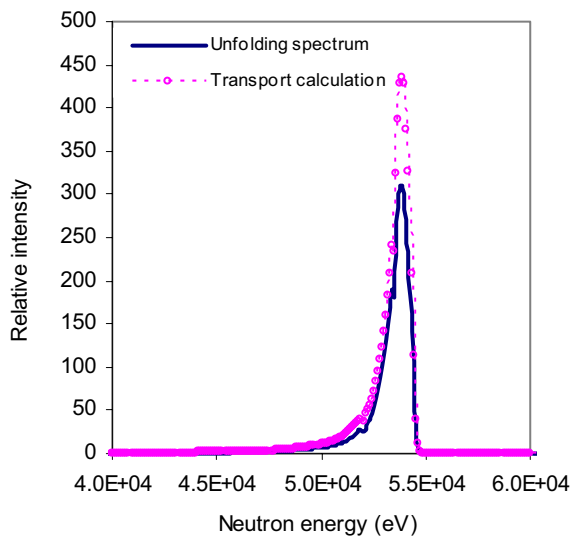


Fig. 1 Neutron spectrum of the 55keV filtered beam

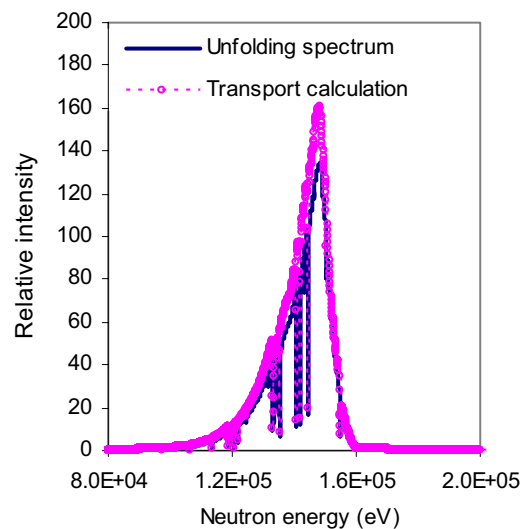


Fig. 2 Neutron spectrum of the 144keV filtered beam

3. Data Analysis

During irradiation in the neutron beam with energy spectrum $\Phi(E)$, the reaction rate, R , of samples is defined as follows:

$$R = N \int \Phi(E) \sigma_a(E) dE \quad (1)$$

where N is the number of nuclei in sample, and $\sigma_a(E)$ is the neutron capture cross section at energy E . The average neutron capture cross section, $\langle \sigma_a \rangle$, and neutron flux, $\langle \Phi \rangle$, are defined as following:

$$\langle \sigma_a \rangle = \int \sigma_a(E) \Phi(E) dE / \int \Phi(E) dE \quad ; \quad \langle \Phi \rangle = \int \Phi(E) dE \quad .$$

Applying these average quantities, the integrating equation (1) can be rewritten:

$$R = N \langle \sigma_a \rangle \langle \Phi \rangle \quad (2)$$

The activity, A , of the sample at the end of neutron irradiation is given by expressions:

$$A = R(1 - \exp(-\lambda t_1)) \quad (3)$$

$$A = \frac{C f_c \lambda}{\varepsilon_\gamma I_\gamma \exp(-\lambda t_2) (1 - \exp(-\lambda t_3))} \quad (4)$$

where C denotes the net counts of the corresponding gamma peak, and t_1 , t_2 and t_3 are irradiating, cooling and measuring times, respectively. λ is the decay constant of the product nucleus, ε_γ the detection efficiency of detector, I_γ the intensity of interesting γ -ray line and f_c is the correction factors. Finally, from equations (2), (3) and (4), the average capture cross sections, $\langle \sigma_a \rangle^x$, for the samples at average neutron spectrum $\langle \Phi \rangle$ can be obtained relative to that of ^{197}Au standard by the following relations:

$$\langle \sigma_a \rangle^x = \frac{C^x f(\lambda, t)^x f_c^x I_\gamma^{Au} \varepsilon_\gamma^{Au} N^{Au} \langle \sigma_a \rangle^{Au}}{C^{Au} f(\lambda, t)^{Au} f_c^{Au} I_\gamma^x \varepsilon_\gamma^x N^x} \quad (5)$$

$$f(\lambda, t) = \frac{\lambda}{(1 - \exp(-\lambda t_1)) \exp(-\lambda t_2) (1 - \exp(-\lambda t_3))} \quad (6)$$

where the superscript 'x' denotes the nucleus of sample. Calculating from the ENDF/B-VI.8 data library, the average standard capture cross section of ^{197}Au respects to the 55keV beam's spectrum is 414.61mb, and for that to the 144keV beam's spectrum is 277.21mb. The relevant decay data of product nuclei, used in this work, are given in Table 2.

Table 2 Decay properties of the product nuclei [11]

Product nucleus	Half-life	γ -ray energy (keV)	Intensity per decay (%)
^{198}Au	2.6952±0.0002 d	411.8	95.6±0.1
^{140}La	1.6781±0.0003 d	487.02	45.5±0.6
^{153}Sm	46.50±0.21 h	103.2	29.3±0.1
^{192}Ir	73.827±0.013 d	316.5	82.7±0.2
^{194}Ir	19.28±0.13 h	328.45	13.1±1.7

The correction factors for the neutron self-shielding, multi-scattering and the effects of strong resonance capture of samples with slow neutron background were calculated by Monte-Carlo method [9, 12]. In which, the effect of isotopic impurities and oxygen in the samples and the loss energy by scattering of neutron were taken into account. In the resonance capture corrections, the background spectra of neutron beams were measured by unfolding method and resonance thin-foil activation technique. The data used for the correction calculation were taken from JENDL-3.3 [13] and ENDF/B-VI.8 [14]. The calculated correction factors are given in Table 3.

Table 3 Correction factors for multi-scattering, self-shielding and background resonance capture of neutron in the samples

Nuclides	55keV region			144keV region		
	Self-shielding	Multi-scattering	Resonance capture	Self-shielding	Multi-scattering	Resonance capture
Au-197	0.9985	0.9901	0.4269	0.9988	0.9929	0.5338
La-139	0.9962	0.9785	0.6227	0.9986	0.982	0.7531
Sm-152	0.9988	0.9856	0.2816	0.9991	0.9917	0.4890
Ir-191	0.9959	0.9782	0.4937	0.9968	0.9828	0.6593
Ir-193	0.9959	0.9774	0.5214	0.9968	0.9826	0.6944

4. Results and Discussion

In the present work, the new values of average neutron capture cross sections of ^{139}La , ^{152}Sm and $^{191,193}\text{Ir}$ at incident neutron energies of 55keV and 144keV are reported with errors about 5-6.5%. The results are given in Table 4. The uncertainties in the present measurements are mainly due to the statistical errors (0.1-2%), the uncertainties of γ -ray detection efficiency (3.5%), the reference cross section (~3%) and the correction factors for neutron resonance capture, self-shielding and multi-scattering effects (~3%). In comparisons with the previous measurements and the evaluated data, The present results are seem to be good agreement with the previous measurements of Musgrove [15], Wisshak [16], Duamet [17], Macklin [18] and with the evaluated data of JENDL-3.3 and ENDF/B-VI.8 within the experimental uncertainties. The comparisons results are shown in Figs.3-6.

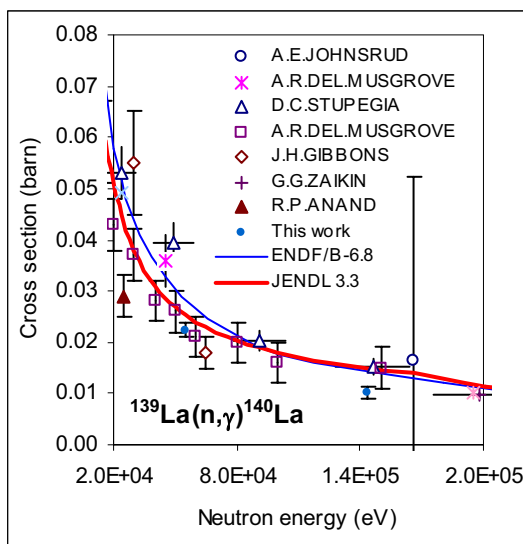


Fig. 3 Neutron capture cross section of ^{139}La in keV region

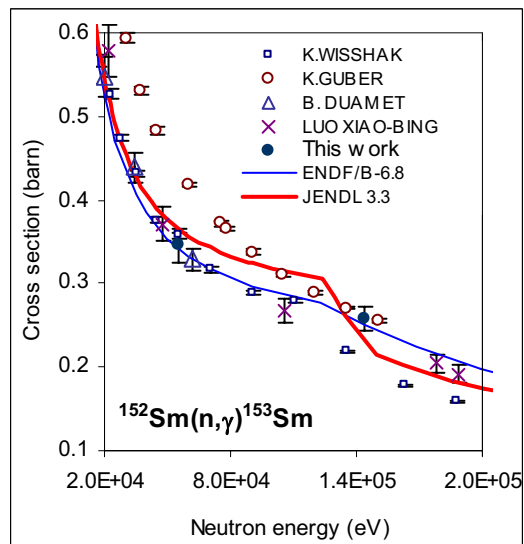


Fig. 4 Neutron capture cross section of ^{152}Sm in keV region

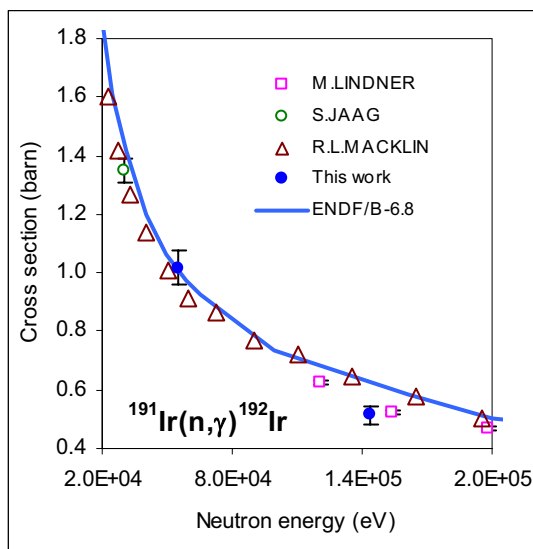


Fig. 5 Neutron capture cross section of ^{191}Ir in keV region

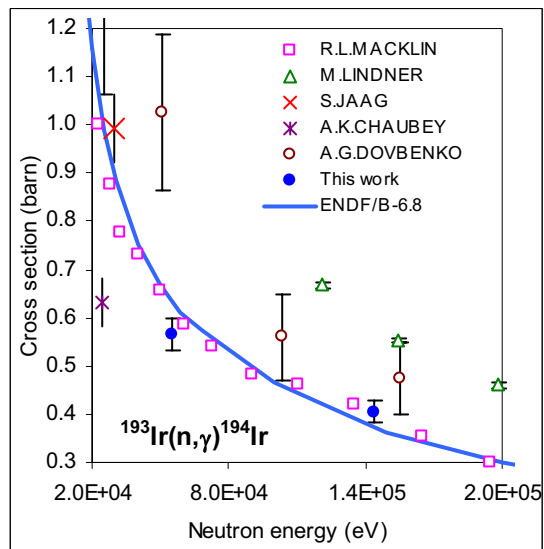


Fig. 6 Neutron capture cross section of ^{193}Ir in keV region

Table 4 The neutron capture cross sections of ^{139}La , ^{152}Sm and $^{191, 193}\text{Ir}$ obtained in the present study

Average neutron energy [Energy range] (keV)	$\langle\sigma_a\rangle_{\text{La-139}}$ (mb)	$\langle\sigma_a\rangle_{\text{Sm-152}}$ (mb)	$\langle\sigma_a\rangle_{\text{Ir-191}}$ (mb)	$\langle\sigma_a\rangle_{\text{Ir-193}}$ (mb)
55 [51-59]	22.4 ± 1.2	345.5 ± 19.4	1016.5 ± 57.2	566.7 ± 32.6
144 [133-155]	12.01 ± 0.58	258.7 ± 14.5	514 ± 29.4	404.5 ± 22.8

5. Conclusion

The neutron capture cross section of ^{139}La , ^{152}Sm and $^{191, 193}\text{Ir}$ at average incident neutron energies of 55keV and 144keV have been measured by means of the activation method, using the filtered neutron beams at DNRI. The results, with uncertainties of 5-6.5%, were obtained relative to the standard capture cross sections of ^{197}Au . The energy ranges of the filtered neutron beams are 14 and 15% for 55keV and 144keV beams, respectively. Although the slow neutron background existing in the filtered neutron beam is quite low, the effects of strong resonance capture cross sections of the samples and standards should be taken into account to improve the accuracy of the experimental results.

Acknowledgments

We would like to express our thanks to the Vietnam Atomic Energy Commission (VAEC) and the Dalat Nuclear Research Institute (DNRI) for their great encouragement and helpful in creating an advantage research condition for this work. The present study was sponsored by the Fundamental Research Program of VAEC under the subproject No. 409706. The advanced gamma-ray spectroscopy system used in the experiments was supported by IAEA. We also wish to express our deep gratitude to the members of the Nuclear Data Center of JAEA for their helpful reference data and materials.

References

- [1] K. H. Guber, et al., Neutron Cross Section Measurements at the Spallation Neutron Source, Int. Conf. on Nuclear Data for Science and Technology, Tsukuba (JP), 7-12, P. 281, Oct. 2001.

- [2] Stefano Marrone, Measurement of the $^{139}\text{La}(n,\gamma)$ Cross Section at n_TOF, 12th Conference on Capture Gamma-Ray Spectroscopy and Related Topics, CGS12, 4-9 (2005).
- [3] S. O'Brien et al., Neutron capture cross section of ^{139}La , Phys. Rev. C68, 035801 (2003).
- [4] Z. Y. Bao, H. Beer, F. Kappeler, F. Voss, And K. Wisshak, Neutron Cross Sections for Nucleosynthesis Studies, Atomic Data and Nuclear Data Tables **76**, 70–154 (2000).
- [5] Kazuya OHGAMA, et al., Measurement of keV-Neutron Capture Cross Sections and Capture Gamma-Ray Spectra of $^{91,92}\text{Zr}$, J. Nuclear Science and Technology, Vol. 42, P. 333 (April 2005).
- [6] P. Z. Hien, V. H. Tan, N. C. Hai. Radiative capture cross section measurements for U-238 on the 55 keV and 144 keV filtered neutron beams, KC-09-08, Dalat (1995), P. 117.
- [7] V. P. Vertebnyj, et al., Filtered Medium and Thermal Neutron Beams and Their Use, "Properties of Neutron Sources", IAEA-TECDOC-401, (1986).
- [8] O. O. Gritzay, et al., Neutron Filters at Kyiv Research Reactor, KIRN-01-6 (2001).
- [9] K. Senoo, Y. Nagai, T. Shima, T. Ohsaki, A Monte Carlo code for multiple neutron scattering events in a thick sample for (n, γ) experiments, Nucl. Instr. and Meth. A339 (1994) 556-563.
- [10] Motoharu Mizumoto and Masayoshi Sugimoto, The Influence of Water Absorption in Samples for Neutron Capture Cross Section Measurements, Nucl. Instr. and Meth., A282 (1989) 324.
- [11] Nudat 2.2 Database, <http://www.nndc.bnl.gov/nudat2/>
- [12] Oleg Shcherbakov and Hideo Harada, Resonance Self-Shielding Corrections for Activation Cross Section Measurements, J. Nucl. Sci. Tech., Vol. 39, No. 5, P. 548 (2002).
- [13] K. Shibata, T. Kawano, T. Nakagawa, O. Iwamoto, J. Katakura, T. Fukahori, S. Chiba, A. Hasegawa, T. Murata, H. Matsunobu, T. Ohsawa, Y. Nakajima, T. Yoshida, A. Zukeran, M. Kawai, M. Baba, M. Ishikawa, T. Asami, T. Watanabe, Y. Watanabe, M. Igashira, N. Yamamuro, H. Kitazawa, N. Yamano and H. Takano: "Japanese Evaluated Nuclear Data Library Version 3 Revision-3: JENDL-3.3," *J. Nucl. Sci. Technol.* **39**, 1125 (2002).
- [14] V. McLane and Members of the Cross Section Evaluation Working Group, "ENDF/B-VI Summary Documentation (ENDF-201)", BNL-NCS-17541, Brookhaven National Laboratory (1996).
- [15] A. R. de L. Musgrove, B. J. Allen, R. L. Macklin, Resonance Neutron Capture in ^{139}La , Aust. J. Phys., 30, 599-604 (1977).
- [16] K. Wisshak, et al., Neutron Capture in $^{148,150}\text{Sm}$: A Sensitive Probe of the S-Process Neutron Density, Phys. Rev. C48, 3, (1993).
- [17] B. Duamet, et al. Measurement of keV-Neutron Capture Cross Sections and Capture Gamma-Ray Spectra of $^{147,148,149,150,152,154}\text{Sm}$, J. Nucl. Sci. Tech., Vol. 36, p. 865-876 1999).
- [18] R. L. Macklin, D. M. Darke and J. J. Malanify, Fast Neutron Capture Cross Section of ^{169}Tm , ^{191}Ir , ^{193}Ir , ^{175}Lu for En from 3-2000 keV, LA-7479-MS, Aug. 1978.

3.3 Measurement of charged-particle emission DDX for carbon with 14-MeV incident neutrons

Keitaro Kondo¹, Isao Murata¹, Kentaro Ochiai², Hiroyuki Miyamaru¹,
Naoyoshi Kubota^{2†}, Chikara Konno² and Takeo Nishitani²

¹ *Division of Electrical, Electronic and Information Engineering, Graduate School of Engineering, Osaka University, Yamada-oka 2-1, Suita, Osaka 565-0871, Japan*

² *Japan Atomic Energy Agency,*

Shirakata Shirane 2-4, Tokai-mura, Naka-gun, Ibaraki, 319-1195, Japan

[†] *Present address: Materials Characterization Laboratory, Nippon Steel Corporation*

e-mail: ktaro@ef.eie.eng.osaka-u.ac.jp

A preliminary measurement of charged-particle emission double differential cross-section (DDX) for carbon with 14-MeV incident neutrons was carried out. In the measurement, a superior S/N ratio, fine energy and angular resolution were realized with a pencil-beam neutron source and a counter telescope consisting of a pair of silicon surface barrier detectors, ΔE and E. Minimum detection energy of 1.0 MeV for α -particles was achieved by utilizing an anticoincidence spectrum of the ΔE detector. The agreement of our measurement with a previous data measured by Haight et al. was fairly well in the higher energy part of DDX, while a discrepancy was observed below 3 MeV. In order to investigate the mechanism of the $^{12}\text{C}(n,n'+3\alpha)$ reaction, we tried to calculate energy distributions of emitted particles by the Monte Carlo method considering reaction kinematics of a lot of channels which contribute to the reaction. As a results, the contribution of the $^9\text{Be}^*_{(4.7\text{ MeV})}$ channel was suggested and the estimated branching ratio for the $^{12}\text{C}(n,\alpha)^9\text{Be}^*_{(\geq 2.43\text{ MeV})}$ channels was more than 30%.

1. Introduction

In fusion reactor development, double-differential cross-section (DDX) for charged-particle emission reaction induced with 14-MeV neutrons is needed to calculate nuclear heating and fundamental values to evaluate material damages, i.e. primary knock-on atom (PKA) spectra, amount of gas production and displacement per atom (DPA) cross-sections. The particularly important charged-particle emission DDX is of nuclides contained in the first wall and blanket materials highly exposed to 14-MeV incident neutrons. We recently developed an improved measurement system for secondary emitted charged particles using a pencil-beam neutron source furnished in the Fusion Neutronics Source (FNS) in Japan Atomic Energy Agency (JAEA) [1]. Systematic measurements are being carried out for light nuclei of which the measurement has not yet been performed sufficiently so far [2]. In this paper, a preliminary result of measurement for carbon is presented. Carbon is one of the important nuclides for organic materials. Regarding the fusion reactor

development, carbon is proposed for an alternative first wall and contained in SiC, which would be an advanced material for various devices. Detailed measurement is also important from an aspect of nuclear physics because of the complex mechanism of the $^{12}\text{C}(n,n'+3\alpha)$ reaction. We tried to reproduce energy spectra of emitted particles from the reaction by Monte Carlo calculations considering reaction kinematics. The reaction mechanism was investigated through the calculation and analysis.

2. Experimental

2.1 Charged-particle spectrometer using a pencil-beam neutron source

All the present measurements of DDX were carried out with the pencil-beam DT neutron source available at FNS/JAEA. A schematic view of the facility and the experimental setup is shown in **Figure 1**. In the facility, a deuteron beam of 350 keV and 20mA at the maximum bombards a large tritium target. Generated DT neutrons are collimated by a 2 m thick shielding structure with a narrow hole of 2 cm in diameter. The mean neutron energy is 14.2 MeV. A vacuum chamber was set at the outlet of the neutron beam, and a sample material was fixed at the center of the chamber. The sample material used in the present study is a self-supported carbon foil of 5 μm thickness (1033 $\mu\text{g}/\text{cm}^2$). A counter-telescope system with a pair of silicon surface barrier detectors, one for ΔE (thickness of 9.6 μm) and the other for E (thickness of 760 μm), was employed in order to distinguish kinds of emitted charged particles. The minimum detectable energy of the telescope, which depends on the thickness of the ΔE detector, is 2.5 MeV for α -particles. In order to extend the detectable energy range for α -particles as much as possible, we attempted to use an anticoincidence spectrum of the ΔE detector. When the ΔE detector of 9.6 μm thickness is used, the threshold energy beyond which the ΔE detector can be penetrated is around 700 keV for protons and around 1.0 MeV for tritons. The anticoincidence spectrum above those threshold energies for protons and tritons hence originates only from α -particles or particles heavier than α -particles. In the present measurement, recoiling carbon and ^9Be particles emitted via the $^{12}\text{C}(n,\alpha_0)^9\text{Be}$ reaction cannot be negligible and their contributions were calculated and subtracted. As a result, the measurement of α -particles with a minimum energy of around 1 MeV was successfully realized.

2.2 Data analysis

In order to obtain an actual energy spectrum of emitted charged particles, the measured spectrum must be corrected for energy loss in the sample. A relationship between the actual spectrum and the measured spectrum was calculated by the Monte Carlo code SRIM-2003 [3] combined with the processing codes we made. Then the spectrum unfolding was carried out with our original code based on the spectrum type Bayes estimation method [4] to obtain the actual spectrum. For a standard cross section, 122.0 mb for the $^{27}\text{Al}(n,\alpha)$ reaction evaluated in JENDL-3.3 [5] was used.

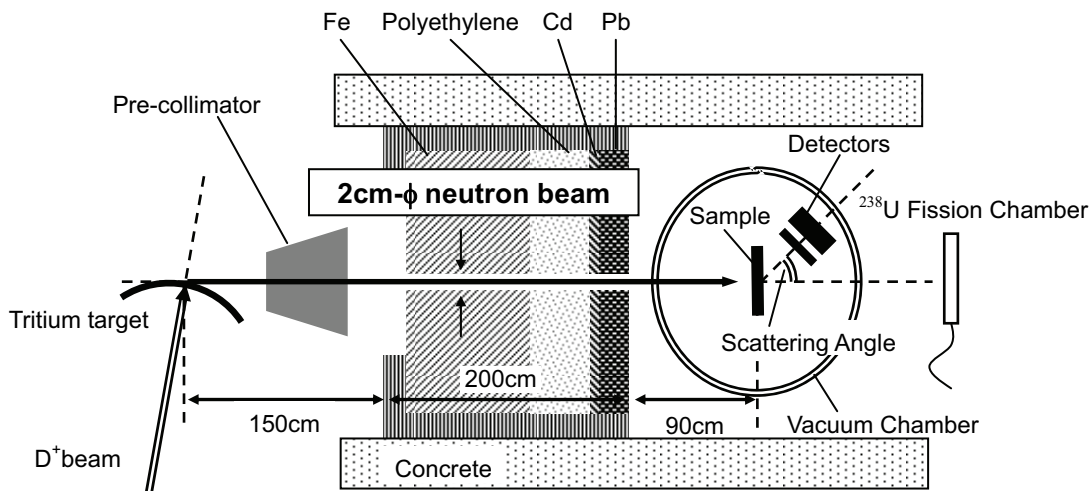


Figure 1 Experimental arrangement.

3. Results and discussion

3.1 Measured double-differential cross-section for α -particles

Up to now, DDX for α -particles has been obtained for only 30 degrees of emission angle in our measurement and further measurements are still in progress. **Figure 2** shows the obtained DDX and the previously measured DDX by R. C. Haight *et al.* [6] at the emission angle of 30 deg.. In our DDX, the contribution from the $^{12}\text{C}(n,\alpha)^9\text{Be}$ was clearly identified. The obvious structures according to $^9\text{Be}_{(\text{Ground State})}$ and $^9\text{Be}^*_{(2.43 \text{ MeV})}$ appeared. Also the contribution of $^9\text{Be}^*_{(4.7 \text{ MeV})}$ might exist. Between the both measurements, the agreement of the higher energy part of DDX is fairly well, while a slight discrepancy was observed below 3 MeV.

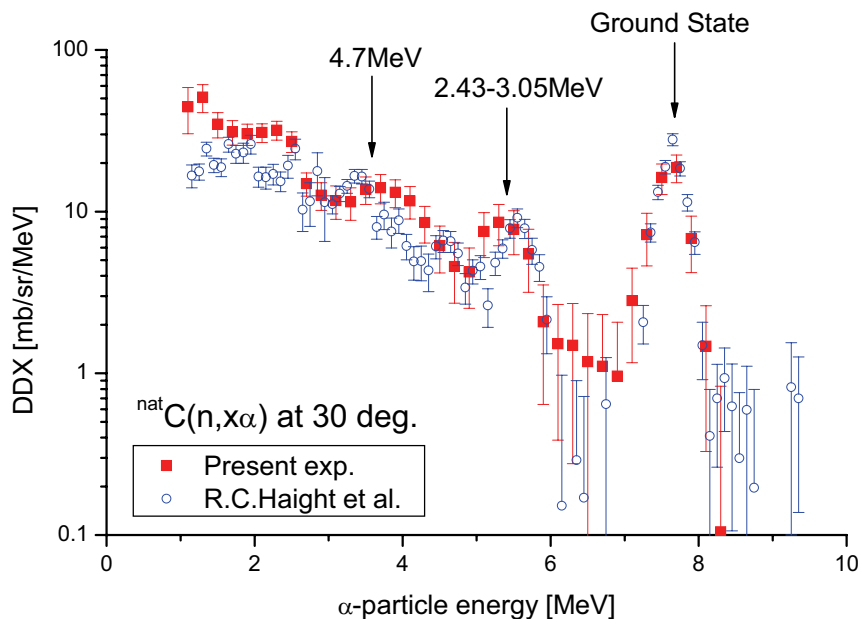
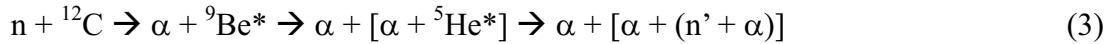
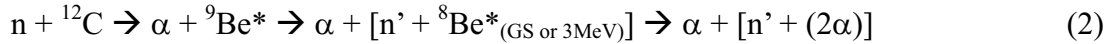
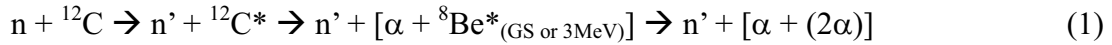


Figure 2 Our obtained DDX and previously measured DDX at the emission angle of 30 deg.

3.2 Monte Carlo calculation and analysis

The mechanism of the $^{12}\text{C}(n,n'+3\alpha)$ reaction is complex, because a lot of reaction channels can contribute to formation of 4-body final state of $n'+3\alpha$. In order to investigate the reaction mechanism, we tried to calculate energy distribution of emitted particles for each channel which contributes to the reaction and determine the branching ratio to the channels so as to reproduce the experimental result well. This analysis is also useful to examine the cause of the large discrepancy in Fig. 2 in the lower energy part of DDX, which would make a large impact on the evaluation of the total α -particle production cross-section. The emitted energy distributions both for α -particles and neutrons were calculated by the Monte Carlo method based on reaction kinematics. The calculation scheme was entirely adopted from Ref. [7]. The contributed channels for the $^{12}\text{C}(n, n'+3\alpha)$ reaction were considerably identified by Antolković *et al.*, who carried out a kinematical analysis for the reaction using nuclear emulsions [8]. In the present calculation, simply 2-body sequential decays, which reach to the final states of $n'+3\alpha$, via excited states of ^{12}C and ^9Be were considered based on their analysis. The decay schemes are as follows:



Decay modes of the intermediate nuclei, $^8\text{Be}^*$ and $^5\text{He}^*$, were adopted according to literatures [8, 9, 10]. For all the intermediate states, the density-of-states function was given by a Breit-Wigner distribution with constant level widths [9, 10]. The angular distributions for the inelastic scattering of neutrons were extracted from the neutron emission DDX measured by Takahashi *et al.* [11] for the excited states of ^{12}C at 7.65 and 9.64 MeV. For the other excited states of ^{12}C , the isotropic distribution in center-of-mass system was assumed. In other 2-body decays, also the isotropic distribution in center-of-mass system was assumed.

The calculated spectra were fitted into our obtained DDX for α -particles and DDX for neutrons measured by Takahashi *et al.* [11], and the branching ratio for the contributed channels was estimated. **Figure 3** shows the best fitted result of the DDX both for emitted α -particles and neutrons at the emission angle of 30 deg.. The continuum in lower energy of the neutron DDX is reproduced fairly well. In the present estimation, a large contribution of the $^9\text{Be}^*_{(4.7\text{ MeV})}$ channel plays an important role, although its validity should be confirmed by some theoretical analyses. The estimated branching ratio for the $^{12}\text{C}(n,\alpha)^9\text{Be}^*_{(\geq 2.43\text{ MeV})}$ channels was more than 30%. Such a large contribution of the $^9\text{Be}^*$ channels might suggest importance of the α -particle knock-on or stripping process. This supposition will be confirmed by further detailed measurement of the angular distribution of emitted α -particles. The measurement is also needed in order to estimate the total α -production cross-section.

From the present analysis, it was found that the lower energy part of our measured DDX would be reasonable when the assumed reaction channels contribute to the reaction.

To examine the cause of the discrepancy with the Haight's result precisely, further measurements for other angles than 30 deg. are indispensable.

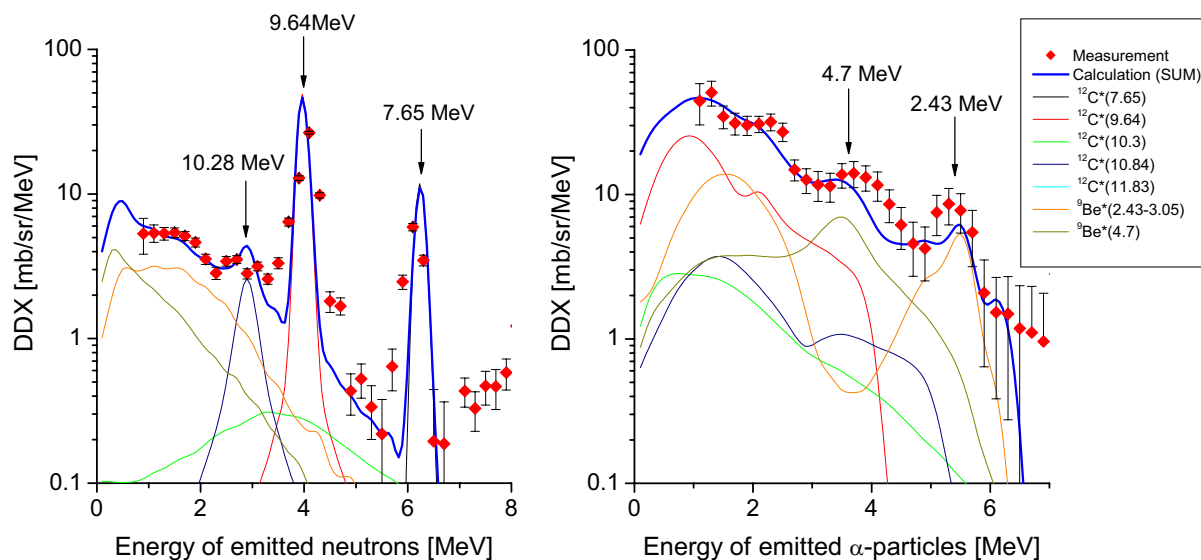


Figure 3 Best fitted result of the DDX calculation for both emitted α -particles and neutrons at the emission angles of 30 deg.

4. Conclusion

Measurement of the α -particle emission double differential cross-section (DDX) for carbon with 14-MeV incident neutrons is being carried out and a preliminary result was described in this paper. The agreement of our obtained DDX at the emission angle of 30 deg. with a previous data measured by Haight *et al.* was fairly well in the higher energy part, while a slight discrepancy was observed below 3 MeV. In order to investigate the mechanism of the $^{12}\text{C}(n,n'+3\alpha)$ reaction, we tried to calculate the energy spectra of emitted particles by the Monte Carlo method considering reaction kinematics of a lot of channels which contribute to the reaction. As a results, the contribution of $^9\text{Be}^*_{(4.7\text{ MeV})}$ was suggested and it was found that rather large contribution of the $^{12}\text{C}(n,\alpha)^9\text{Be}^*_{(\geq 2.43\text{ MeV})}$ channels had to be assumed to reproduce the experimental results well. The assumed ratio to the total α -particle production was more than 30%. Such a large contribution of the $^9\text{Be}^*$ channels might suggest importance of the direct reaction process. More detailed measurement and analysis of the angular distribution of emitted α -particles are needed to reveal the mechanism of the $^{12}\text{C}(n,n'+3\alpha)$ reaction. Further measurement is also needed in order to estimate the total α -production cross-section.

Acknowledgements

The authors wish to acknowledge the FNS staff for their excellent operation of the FNS accelerator: Messrs. C. Kutsukake, S. Tanaka, Y. Abe, M. Seki, Y. Oginuma and M. Kawabe. The support and encouragement provided by K. Okada, K. Takakura, S. Takagi and S. Shido are also greatly appreciated.

References

- 1) K. Kondo, I. Murata, K. Ochiai, *et al.*, “Charged-particle spectrometry using pencil-beam DT neutron source for double-differential cross-section measurement,” *Nucl. Instrum. Methods A* **568**, 723 (2006).
- 2) K. Kondo, S. Takagi, I. Murata, *et al.*, “New approach to measure double-differential charged-particle emission cross section of several materials for a fusion reactor,” *Fusion Eng. Des.* **81**, 1527 (2006).
- 3) J. F. Ziegler and J. P. Biersack, *The Stopping Power and Ranges of Ions in Matter*, Pergamon, New York (1985) ; Computer code “SRIM-2003”, <http://www.srim.org/>.
- 4) S. Iwasaki, “A new approach for unfolding PHA problems based only on the Bayes Theorem,” *Reactor Dosimetry*, H.A. Abderrahim, P. D’hondt, B. Osmera (Eds.), World Scientific Publishing Co. Pte. Ltd., Singapore, 245 (1998).
- 5) K. Shibata T. Kawano, T. Nakagawa, *et al.*, “Japanese Evaluated Nuclear Data Library Version 3 Revision-3: JENDL-3.3,” *J. Nucl. Sci. Technol.* **39** 1125 (2002).
- 6) R. C. Haight, S. M. Grimes, R. G. Johnson and H. H. Barschallet al., “The $^{12}\text{C}(n,\alpha)$ reaction and the Kerma Factor for Carbon at $E_n=14.1$ MeV,” *Nucl. Sci. Eng.* **87**, 41 (1984).
- 7) S. T. Perkins, E. F. Plechaty and R. J. Howerton, “A reevaluation of the $^9\text{Be}(n,2n)$ reaction and its effect on neutron multiplication in fusion blanket applications,” *Nucl. Sci. Eng.* **90**, 83 (1985).
- 8) B. Antolković and Z. Dolenc, “The neutron-induced $^{12}\text{C}(n,n')3\alpha$ reaction at 14.4 MeV in a kinematically complete experiment,” *Nucl. Phys.* **A237**, 235 (1975).
- 9) D. R. Tilley, J. H. Kelley, J. L. Godwin, *et al.*, “Energy levels of light nuclei $A=8,9,10$,” *Nucl. Phys.* **A745**, 155 (2004).
- 10) F. Ajzenberg-Selove, “Energy levels of light nuclei $A = 11-12$,” *Nucl. Phys.* **A506**, 1 (1990).
- 11) A. Takahashi, E. Ichimura, Y. Sasaki and H. Sugimoto, *Double and single differential neutron emission cross sections at 14.1 MeV —Volume-I—*, OKTAVIAN Report, A-87-03, Osaka University, Japan (1987).

3.4 Measurement of ^{nat}Zr (n,2n) Reaction Cross Section from the Angle-Correlated Neutron Spectrum with Pencil-beam DT Neutron Source

K. Shiken, S. Takaki, K. Kondo, M. Matsunaka H. Miyamaru, I. Murata,
K.Ochiai* C.konno*T. Nishitani*

Department of Electric, Information Systems and Energy Engineering
Graduate School of Engineering, Osaka University, Suita, Japan

*Japan Atomic Energy Agency, Tokai-mura, Ibaraki, Japan

e-mail: shiken@ef.eie.eng.osaka-u.ac.jp

Angle-correlated differential cross-section for ^{nat}Zr (n,2n) reaction has been measured with the coincidence detection technique and a pencil-beam DT neutron source at FNS, JAEA. Energy spectra of two emitted neutrons were obtained for azimuthal and polar direction independently.

1. Introduction

The (n,2n) reaction is a neutron multiplication reaction, the cross-section data of which are crucial information to design a fusion reactor. The ^{nat}Zr (n,2n) reaction cross-section is very important because Li_2ZrO_3 is one of the fusion blanket candidate materials. However, in the previous benchmark studies it was pointed out that agreement between experiment and evaluation was not acceptable as shown in Figs.1 and 2. In the case of ^{nat}Zr (n,2n) reaction cross section measurement, the conventional foil activation method cannot be applied, because suitable radioisotopes cannot be produced by the reaction. In the present study, two neutrons simultaneously emitted by the (n,2n) reaction were detected directly by two detectors.

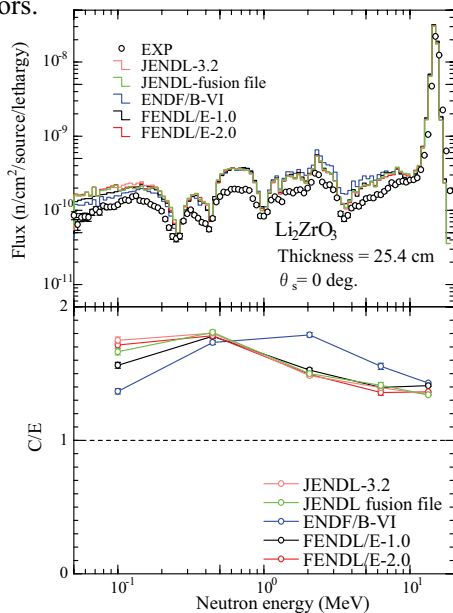


Fig.1 Comparison of measured and calculated leakage neutron spectra at 0° for 25.4 cm thick Li_2ZrO_3 assembly

I. Murata et al. Fus. Eng. Des., 51-52(2000) p.821.

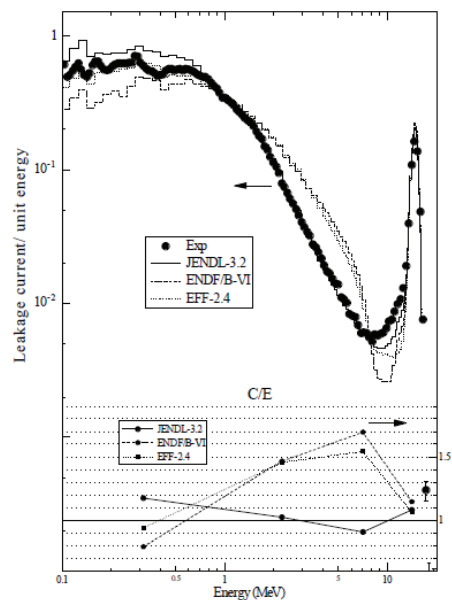


Fig.2 Measured and calculated neutron leakage spectra from the Zr pile

C. Ichihara et al. J. Nucl. Sci. Tech., 40 (2003) p.417.

2. Experimental procedure

In present experiment, we used a pencil-beam DT neutron source of Fusion Neutronics Source (FNS) in Japan Atomic Energy Agency (JAEA). It is the only existing pencil-beam DT neutron source in the world, which supplies an excellent experimental condition, i.e., 10^5 n/cm²/sec inside the beam and very low neutron flux of several hundred n/cm²/sec outside the beam.

The schematic experimental arrangement around detectors is shown in Fig.3. The distance between the neutron source and a zirconium sample (2.4cm in diameter, 2cm long) was 550cm. Two spherical NE213 (4cm in diameter) detectors to detect neutrons emitted simultaneously by the (n,2n) reaction were located at 18.8cm from the zirconium sample. An ²³⁸U fission chamber was set up on the beam line behind the sample to monitor the neutron flux. As shown in Fig.4, three angle parameter (θ_0, θ, ϕ) with respect to the detector position were defined in which θ_0 and θ are the polar angles of emitted two neutrons and ϕ is the azimuthal angle of detector 2 from detector 1. Measurement points were determined by the combination of these angle parameters.

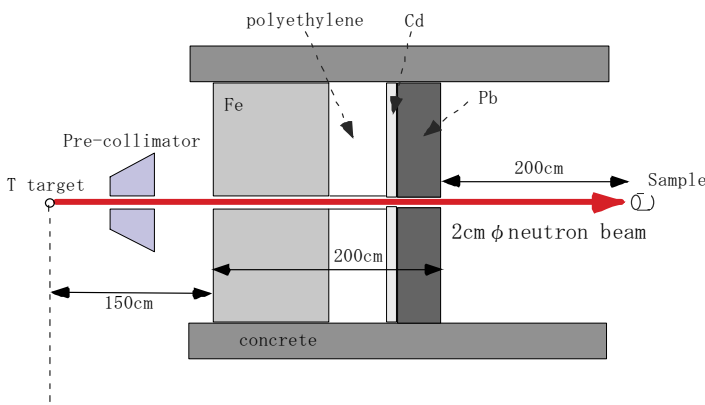


Fig.3 Schematic experimental arrangement

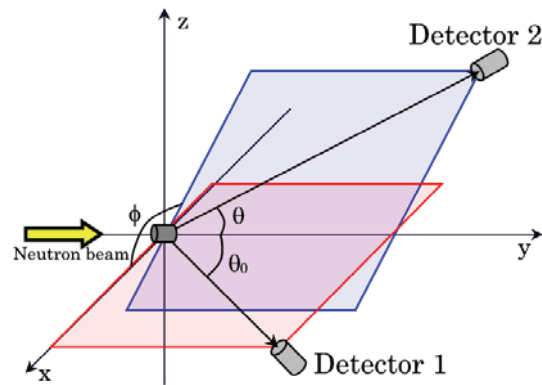


Fig.4 Arrangement around sample and detectors

Because two detectors are positioned very close with each other, there exists a neutron, which can be detected in both detectors by passing through them in turn. This is a troublesome background called “inter-detector scattering” in this paper. A polyethylene shielding brick up to 10.16cm in thickness was thus arranged between two detectors to prevent the inter-detector scattering components.

Because NE213 detectors are sensitive also to gamma ray, n/ γ discrimination was carried out by the pulse shape discrimination technique. Two amplifiers with different gains were used to cover a wider measurable energy range from 800 keV to around 10 MeV. Time difference spectrum of anode signals of the two detectors was used to extract the coincidence signals. The region including the peak was gated and defined as Foreground (FG), and the flat region of time-independent signals was defined as Background (BG). Eight pulse height spectra were measured for one case considering two detectors (1/2), two gains (high/low) and FG and BG. Details of the electric circuit of the measurement is described in Ref.[1].

3. Data processing

Obtained pulse height spectra were transformed into light output spectra. Examples of measured pulse height spectra are shown in Fig.5. The position of Compton edge made by 1.275MeV gamma ray emitted from ^{22}Na and 0.834MeV gamma ray emitted from ^{54}Mn was used in the light unit calibration. The BG spectrum (y_{BG}) was subtracted from the FG spectrum (y_{FG}) to derive the net FG spectrum by the following equation.

$$y = y_{FG} - \alpha y_{BG} \quad (1)$$

where α is the ratio of the gate widths between FG and BG spectra.

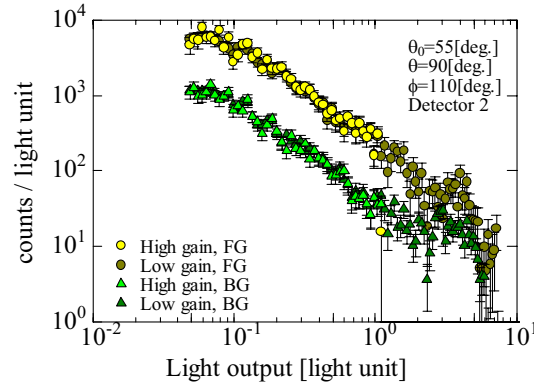


Fig.5 Measured light output spectra.

The net light output spectra were unfolded using FORIST^[2] unfolding code. Necessary response function was calculated with SCINFUL^[3]. And the energy and angle differential cross sections were obtained by the following equations,

$$y(\theta_0, \theta, \phi, E) = R \cdot x(\theta_0, \theta, \phi, E) \quad (2)$$

$$\sigma_i(\theta_0, \theta, \phi, E) = \frac{x_i(\theta_0, \theta, \phi, E)}{N \cdot FC \cdot C \cdot d\Omega_i \cdot d\Omega_j \cdot f_j} \quad (3)$$

where subscripts in Eq.(3) represent either detector 1 or detector 2, R is the response matrix of the NE213 detector, x_i is the unfolded spectrum, σ_i is the obtained energy and angle differential cross section, N is the number of nuclei of the sample, FC is the integrated counts of the fission chamber, C is the conversion factor of FC into the neutron flux at the sample, $d\Omega_i$, $d\Omega_j$ is the solid angle of each detector, f_j is the efficiency of detector j . The efficiency of the other detector was considered in the response matrix. The conversion factor C was determined by the activation method using aluminum foil. As for the correction of the inter-detector scattering, the detection rate of inter-detector scattering was estimated by Monte Carlo calculation with MCNP^[4] taking into account precise model of each experimental arrangement.

4. Results and discussion

Figure 6 shows the obtained energy spectra. This is a triple-differential cross section, i.e., double-angle and single energy differential cross section, called TDX. Hence, there are no evaluated data, which can be compared with the present measured data. The spectra seem to be an evaporation spectrum. Estimated error contains statistical error and unfolding process error evaluated by FORIST. Figure 7 shows the detection ratio between the inter-detector scattering component of a neutron and the coincident signal of two neutrons emitted from (n,2n) reaction calculated by MCNP. The results were used to evaluate correction factors. The ratio increases as the distance between two detectors becomes closer. A 10 cm polyethylene shield, arranged between the detectors, effectively suppressed the inter-detector scattering.

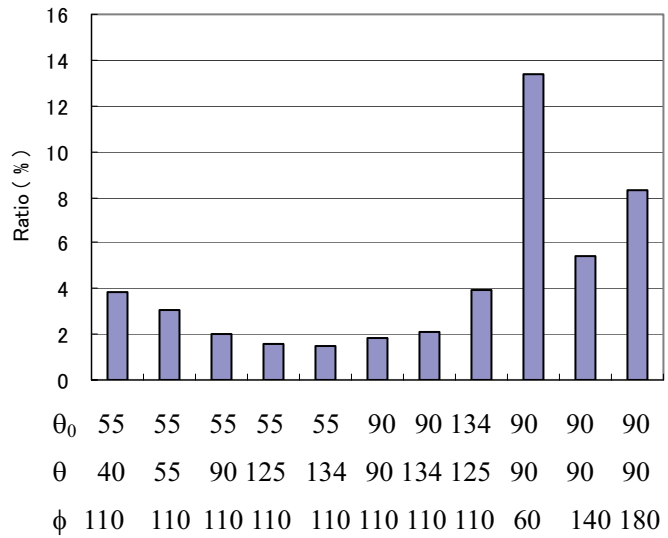
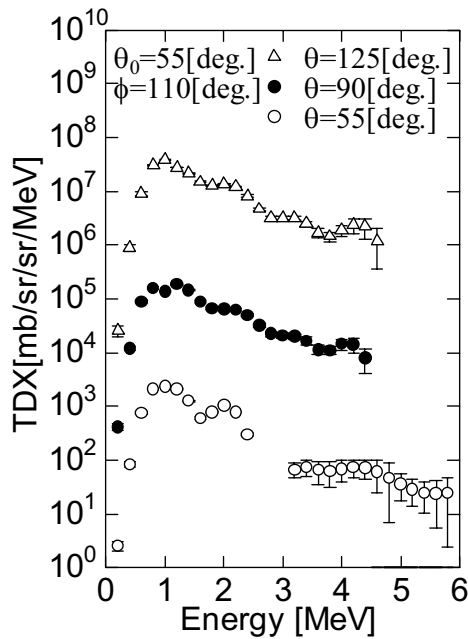


Fig.6 Measured energy spectra at each angle. Fig.7 Ratio of inter-detector scattering component at each angle.

By integrating TDX over energy, two kind of angular distributions named ADDX are obtained, i.e., one is as a function of azimuthal angle (Fig. 8) and the other is for polar angle (Fig. 9). It seems no angular dependence azimuthally within the error bar as shown in Fig. 8. A gentle forward oriented polar distribution was observed for axial ADDX as in Fig. 9. The ADX is obtained by integrating ADDX over angle. It shows also a slight forward peaked distribution. The obtained total cross-section (TOX) over the minimum measurable energy of 800 keV was fairly larger than the one evaluated in JENDL-3.3 as described in Table 1. Unexpectedly, the result shows an opposite trend to the suggestion pointed out by the previous benchmark studies.

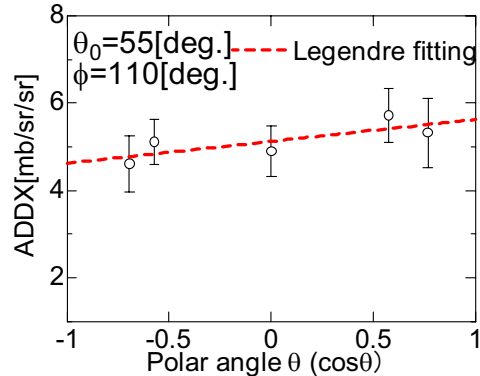
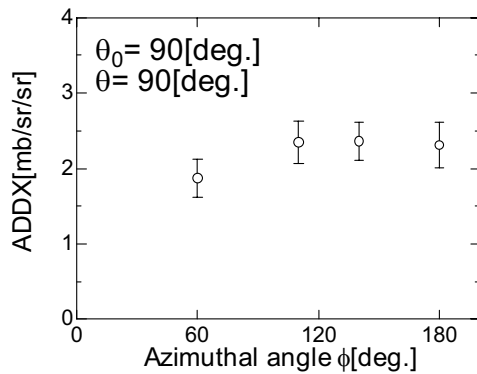


Fig.8 The azimuthal distribution of ^{nat}Zr (n,2n) reaction cross-section. Fig.9 Example of the polar distribution of ^{nat}Zr (n,2n) reaction cross-section.

Table.1 Comparison of the obtained total cross-section (TOX) of ^{nat}Zr (n,2n) reaction

	ADX at 55 deg. [mb/sr] ($E_n > 800$ keV)	TOX. [mb] ($E_n > 800$ keV)
Present Exp.	64 ± 3	745 ± 23
JENDL-3.3	44.9	538.2

Next, to discuss the unexpected discrepancy of the total (n,2n) reaction cross section mentioned above, extrapolation of spectrum for energies below 800 keV was carried out with an evaporation spectrum. The nuclear temperature preferred is 1 MeV in the present study, because the evaporation spectrum for 1 MeV would fit our spectrum very smoothly. The value is the same as the one evaluated in RIPL-2. Nuclear temperatures stored in JENDL-3.3 and ENDF/B-VI are also used as references. The results are summarized in Table 2 below.

Table.2 Comparison of total cross-sections for ^{nat}Zr (n,2n) reaction, estimated by extrapolation of the measured energy spectrum below 800 keV with different evaporation spectra for several nuclear temperatures.

Nuclear temperature [MeV]	0.65 (assumed in JENDL evaluation)	1.0 (used also in RIPL-2 library)	1.73 (assumed in ENDF evaluation)
Preliminary TOX [mb]	1095 ± 30	997 ± 27	919 ± 26

The result shows the agreement with JENDL-3.3 is acceptable for the total cross-section of ^{nat}Zr (n,2n) reaction obtained by extrapolating the measured energy spectrum down to zero energy. Our estimation agrees very well with the only existing measured data of Frehaut et. al., (946 ± 67 mb at $E_n=14.3$ MeV). As a result, it is suggested that the discrepancy seen in the previous benchmark studies may be caused, not by the problem of absolute value, but by the problem of energy spectrum shape determined by the nuclear temperature. For JENDL-3.3, the absolute value is more or less acceptable, but the nuclear temperature used

may be a little small, meaning a little underestimation is seen in larger energy region and overestimation in lower energy region. For ENDF/B-VI, a slight underestimation is seen as a whole. However, from the present result and the previous benchmark study, the nuclear temperature used may be a little too high. The above results suggest examination of nuclear temperature used in the nuclear data library is worth being carried out.

5. conclusion

Using the pencil-beam DT neutron source and the coincidence detection technique, angle-correlated energy differential cross-section for ^{nat}Zr (n,2n) reaction was measured successfully. The obtained total cross-section above the emitted neutron energy of 800 keV was fairly larger than the one evaluated in JENDL-3.3. The total cross-section of ^{nat}Zr (n,2n) reaction was estimated by extrapolating the spectrum down to zero energy taking into account the nuclear temperature. The estimated value was between those of JENDL-3.3 and ENDF/B-VI. It is suggested that the disagreement pointed out in the previous benchmark studies may be due to inappropriate nuclear temperature used in the evaluation of ^{nat}Zr (n,2n) reaction cross section.

References

- [1] I. Murata et al., *J. Nucl. Sci. Technol.*, Sup. 2, p. 433-436 (2002)
- [2] R. H. Johnson: 'FORIST:Neutron Spectrum UnfoldingCode - Iterative Smoothing Technique', PSR-92, ORNL/RSIC (1975).
- [3] J. K. Dickens: 'A Monte Carlo Based Computer Program to Determine a Scintillator Full Energy Response to Neutron Detector for En Between 0.1 and 80 MeV:User's Manual and FORTRAN Program Listing', ORNL-6462 (1988).
- [4] J. F. Briesmeister, Ed.: "MCNP – A General Monte Carlo N-Particle Transport Code, Version 4C", LA-13709-M (2000).

3.5

Neutron-Production Double-Differential Cross Sections for 150 MeV Neutron-Incidence on Fe

Hiroyuki Arakawa¹, Tsuyoshi Kajimoto¹, Shusaku Noda¹, Takehito Watanabe¹,
Nobuhiro Shigyo¹, Kenji Ishibashi¹, Satoshi Kunieda², Robert C. Haight³,

¹ Kyushu University, 744, Motoooka, Nishi-ku, Fukuoka 819-0395 Japan

² Japan Atomic Energy Agency, Tokai, Naka, Ibaraki 319-1195 Japan

³ Los Alamos National Laboratory, Los Alamos, NM 87545 USA

The neutron-production double-differential cross sections for the neutron-induced reaction were measured on Fe at 140 – 160 MeV. Neutrons produced by a 800 MeV proton-bombarded spallation target were used as incident particles. The results are compared with calculated data.

1 Introduction

High-energy neutron production double-differential cross sections are important for realization of accelerator driven systems (ADS) and radiotherapy. Proton-induced neutron-production double-differential cross sections have been measured up to 3 GeV. However, data of neutron-induced neutron-production double-differential cross sections above 100 MeV are insufficient because of neutron measurement difficulties and a few quasi-monochromatic neutron sources. Utilization of a continuous energy neutron source by spallation reaction enables us to measure cross section for various incident energies at a time.

The purpose of this study is to measure the neutron-production double-differential cross sections at 150 MeV on Fe using a continuous energy neutron source.

2 Experiments

Experiments were performed at the Weapons Neutron Research (WNR) facility in Los Alamos Neutron Science Center (LANSCE)¹ which has an 800 MeV proton linear accelerator. Neutrons generated at a tungsten spallation target (Target-4) were used as incident particles. The neutron energies cover a wide energy range up to 750 MeV. The distance between the spallation target and the experimental room is about 90 m. The geometry of the WNR facility is illustrated in Fig. 1.

Experiments consist of 2 parts. One part was the measurement of response functions of neutron detectors. The energy spectra of emitted neutrons were derived from unfolding their deposition-energy spectra with the responses of the detectors. These response functions were measured by using the spallation neutrons which were collimated to 2 mm in diameter. The alignment of the experiment is in Fig. 2. The response function of each NE213 liquid organic scintillator 12.7 cm thick and 12.7 cm in diameter was measured by irradiating neutrons from the Target-4. The time-of-flight (TOF) between the spallation target and a neutron detector and the charge spectrum from the photomultiplier connected with the NE213 scintillator were measured.

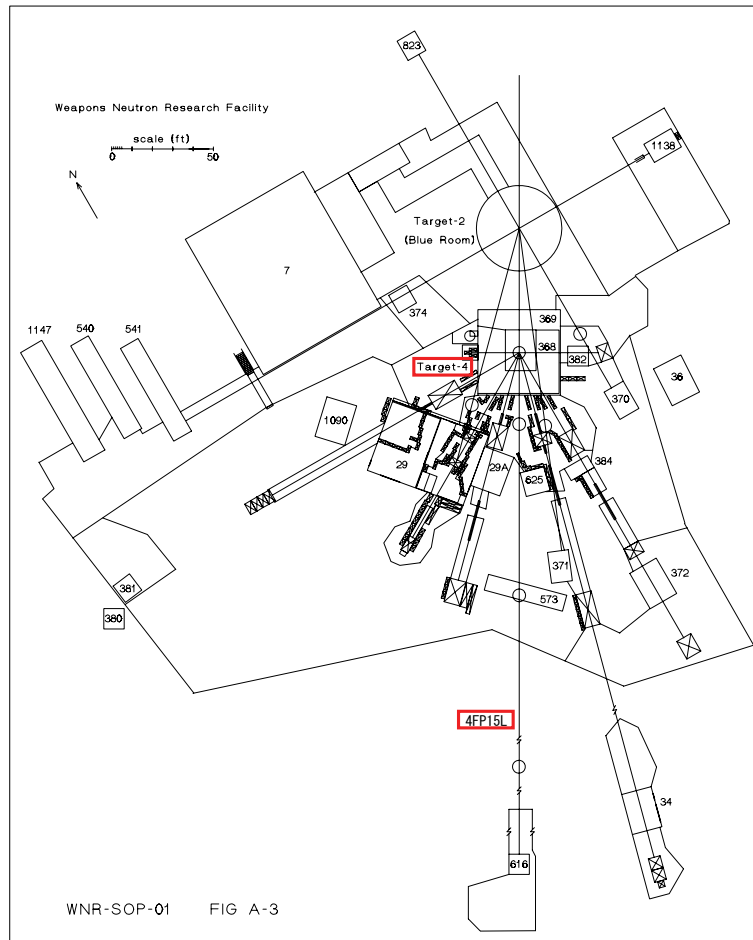


Fig. 1. Schematic view of the beam line at the WNR facility²⁾

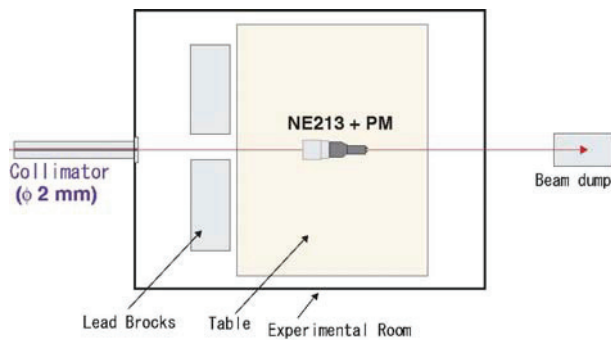


Fig. 2. Arrangement of the measurement for response function

Another part of the experiment was the measurement of double-differential cross sections. Setup of the measurement are shown in Fig. 3.

Six NE213 scintillators were employed to detect neutrons emitted from an Fe sample (10 mm thick, $\phi 50$ mm) and placed at 15° , 30° , 60° , 90° , 120° and 150° . The distance between the sample and the detectors were about 0.7 m. A fission ionization chamber³⁾ was set to know the incident-neutron flux. A 10 mm thick NE102A plastic

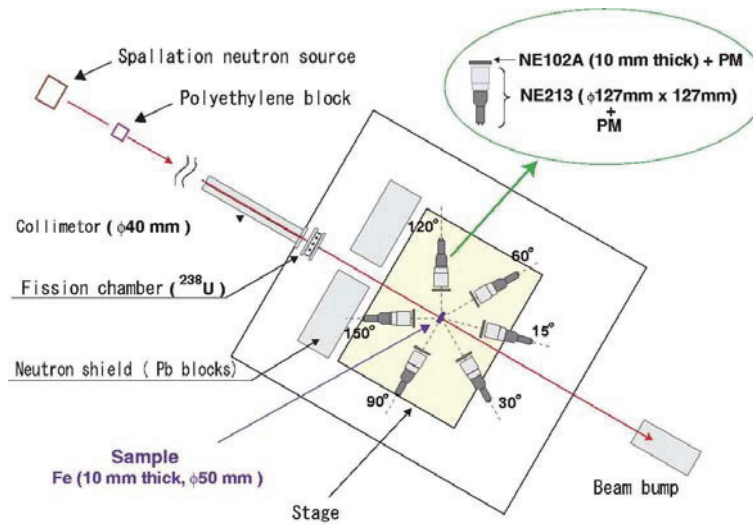


Fig. 3. Set up of the measurement for deposition-energy spectra

scintillator as a veto detector was set in front of each NE213 scintillator. The beam size was adjusted to 36 mm in diameter.

3 Analysis

3.1 Elimination of charged particles and gamma rays

Charged particle events were eliminated by discrimination of signals from an NE102A scintillator plastic scintillators because charged particles gave larger energy in an NE213 scintillator than neutrons and gamma-rays. An example of ADC spectra by an NE102A plastic scintillator is shown in Fig. 4.

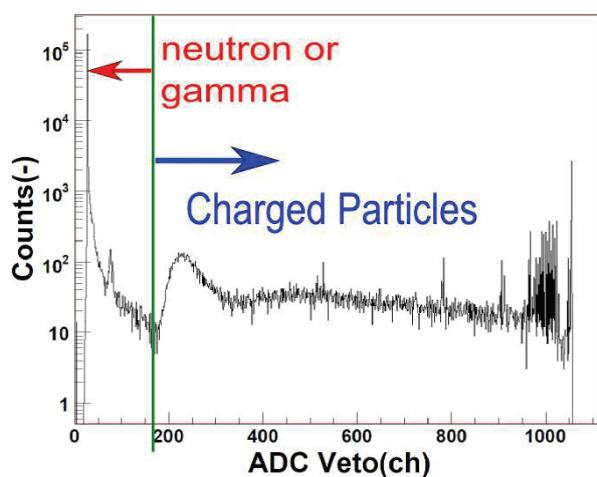


Fig. 4. An example of ADC spectrum of a veto detector

Gamma-ray events were discriminated using the two gate integration method⁴⁾ since NE213 liquid organic scintillators were sensitive to not only neutrons but also gamma rays. Fig. 5 stands for schematic view of the gate

integration method. Comparison between ADC spectrum with the prompt-gate and that with the delayed-gate enables to discriminate between neutron events and gamma ray ones. Fig. 6 illustrates an example of the 2D-plot of the ADC spectra with the prompt gate and the delayed one.

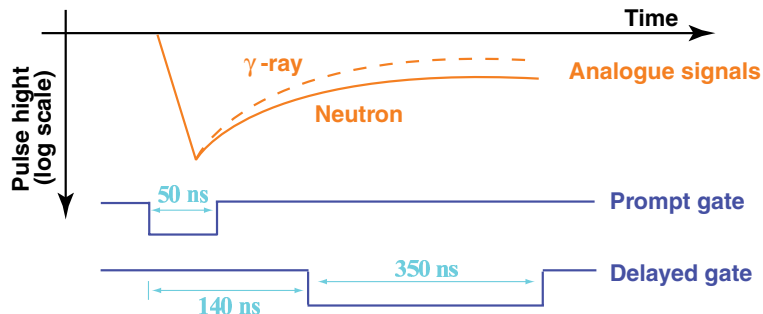


Fig. 5. Schematic view of gate integration method

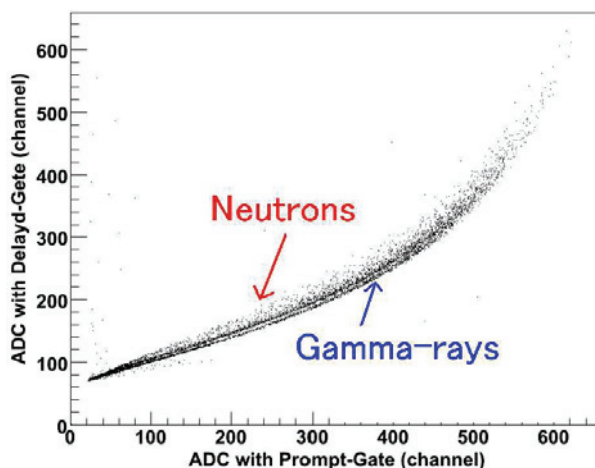


Fig. 6. Discrimination of neutrons and gamma rays

3.2 Incident neutron energy

Incident neutron energies were obtained by neutron flight times between Target-4 and NE213 scintillators. Because the distance between Target-4 and the sample were much longer than those between the sample and the detectors, the flight time of the latter was negligible. Fig. 7 shows a schematic view of the TOF measurement alignment. The timing of flash gamma-rays from the spallation target was used as the time base of TOF analysis. Fig. 8 shows one of TOF spectra.

3.3 Incident neutron flux

The number of incident neutrons was possible to be gotten by the equation

$$\phi_{\mu p}(E_n)\Delta E_n = \frac{n_f(E_n)\Delta E_n}{\sigma(E_n) \times \epsilon_{eff} \times \rho_f} \times \frac{1}{n_{\mu p} \times S_{beam}} \quad (1)$$

where $\phi_{\mu p}(E_n)$, $n_f(E_n)$, and $\sigma(E_n)$ are the number of incident neutron flux, the number of fission events detected by the fission chamber, and the fission cross sections of ^{238}U for corresponding neutron energy E_n ⁵⁾, respectively.

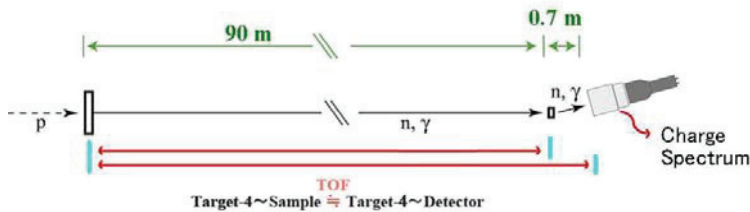


Fig. 7. Schematic view of the TOF measurement alignment

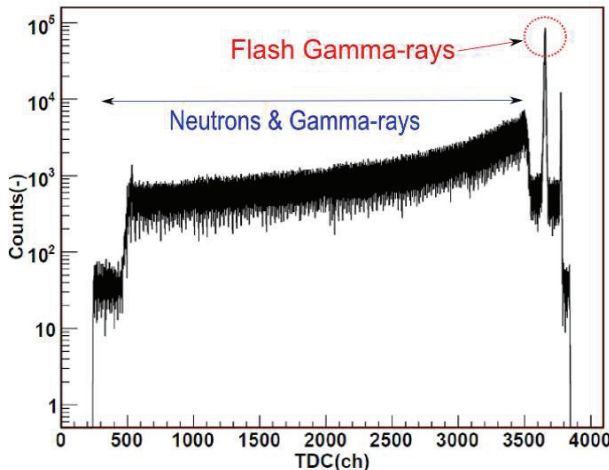


Fig. 8. TOF spectrum between the spallation target and a neutron detector

ϵ_{eff} is the detection efficiency of the fission chamber, and ρ_f is the arial density of the number of atoms of fissile material on the foil in chamber. S_{beam} is the cross section of the beam.

3.4 Calibration

Charge-integration spectra were calibrated to get corresponding electron-equivalent light-output for all neutron detectos. The gamma-ray Compton edges of ^{60}Co and Pu-Be sealed sources were converted into light-unit with the semi-empirical formula by Dietze et al.⁶⁾ for low-energy (a few MeV) parts. For the calibrations of higher-energy, neutron energies were identified by the TOF between the spallation target and neutron detectors and were converted into light-unit by the empirical equation by Cecil et al.⁷⁾

$$T_e = 0.83T_p - 2.82[1.0 - \exp(-0.25T_p0.93)] \quad (2)$$

where T_p , T_e are proton and electron energy in an NE213 scintillator, respectively. The maximum channel of the ADC spectrum was used as corresponding charge-integration values. The relationship between charge-integrations and electron-equivalent light-outputs for the NE213 scintillator used at 90° is shown in Fig. 9

3.5 Response functions and Deposition-energy spectra

Response functions normalized by the number of incident-neutrons were shown in Fig. 10. In this experiment, the SCINFUL-QMD⁸⁾ calculations adjusted to reproduce experimental data with light attenuation were used as

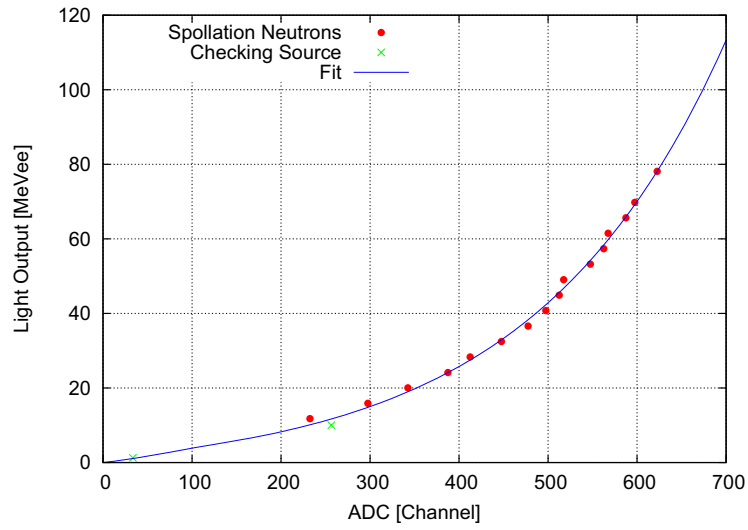


Fig. 9. Relationship between integrated charge and light output for 60° detector

response matrix elements below 30 MeV incident energy for all neutron detectors since there are no experimental data below 30 MeV incident energies.

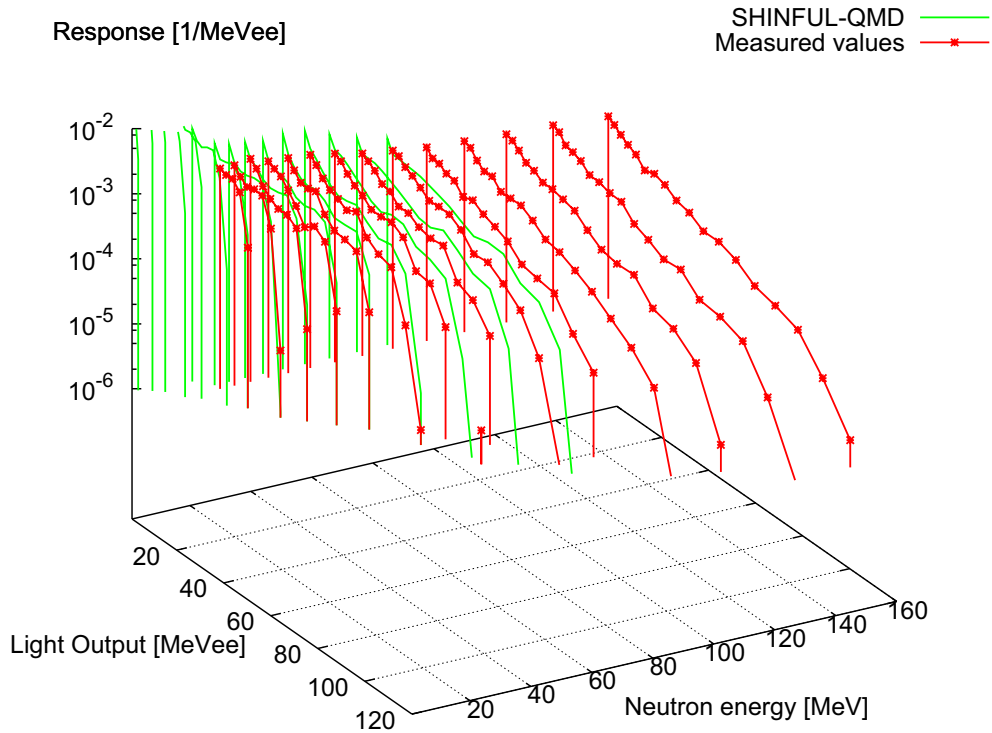


Fig. 10. Response functions of the NE213 scintillator at 60°

Deposition-energy spectra at 140 – 160 MeV normalized by the number of incident-neutrons and subtracted

background (sample-out) spectra are shown in Fig. 11.

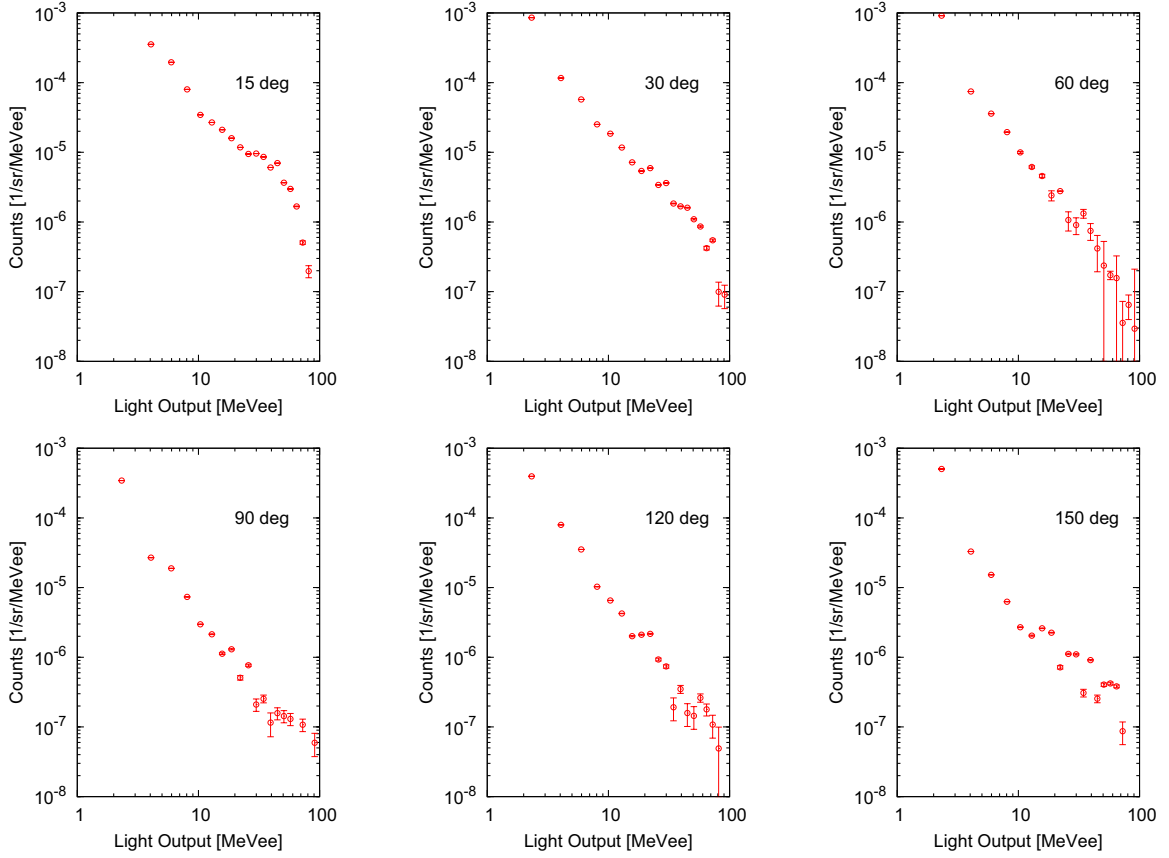


Fig. 11. Deposition energy spectra at 140 – 160 MeV neutron incident energy

3.6 Unfolding

The energy spectra of emitted neutrons were derived by unfolding their deposition-energy spectra with the responses of the detectors. In this experiment, elastic scattering component was considered separately from the other reaction ones. The determinant of this experiment was

$$\begin{pmatrix} \vdots \\ y_{\xi} \\ \vdots \end{pmatrix} = \begin{pmatrix} \ddots & \vdots & \vdots \\ \vdots & a_{\xi,E} & \vdots \\ \vdots & \vdots & \ddots \end{pmatrix} \cdot \begin{pmatrix} \vdots \\ x_E \\ \vdots \end{pmatrix} \cdot k + \begin{pmatrix} \vdots \\ a_{\xi,E_{in}} \\ \vdots \end{pmatrix} \cdot x_{el} \cdot k \quad (3)$$

where y_{ξ} , a_{ξ} , E , and x_E were deposition-energy spectra, response function, outgoing energy spectra (unfolding results), respectively. x_{el} was elastic scattering factor. k was matting factor for absolute value of response functions with deposition-energy spectra. $x_E (=x(E, \theta))$ was assumed to conform following equation.

$$\left(\frac{d^2\sigma}{dE d\Omega} \right) \frac{x(E, \theta)}{\rho \Delta E} = \sum_{i=1}^3 p A_i \exp \left\{ - \left(\frac{E + m - p \beta_i \cos \theta}{\sqrt{1 - \beta_i^2}} - m \right) \right\} \quad (4)$$

where E and p is the kinetic energy (MeV) and the momentum (MeV/c) of an emitted neutron in the laboratory frame and m the neutron mass (MeV), respectively. The quantities of A , β , and T are called amplitude, velocity

and temperature parameters, respectively. Three components of $i = 1$ to 3 correspond to individual processes of the cascade, the preequilibrium and the evaporation. In the process of unfolding these deposition-energy spectra, neutron-induced neutron-production double-differential cross sections were parameterized with moving source model by SALS code⁹⁾ as a least mean square approximation program.

4 Results

The provisional parameterized double-differential cross sections by the moving source model with it's elements as experimental results for 140 – 160 MeV neutron incident energy are shown in Fig. 12. These results were compared with the PHITS¹⁰⁾ calculation data, the evaluated value of LA150¹¹⁾(GNASH¹²⁾+ Kalbach and Mann's systematics¹³⁾) and JENDL-HE¹⁴⁾. The experimental results show that under 50 MeV neutron emission energy are approximately good agreement with calculated data except for 15° and 30° results. 15° and 30° experimental results overestimate calculation data from 5 MeV to 100 MeV neutron emission energy and underestimated above that. For backward angles of experimental results over 50 MeV neutron emission energy have some discrepancies with calculation data.

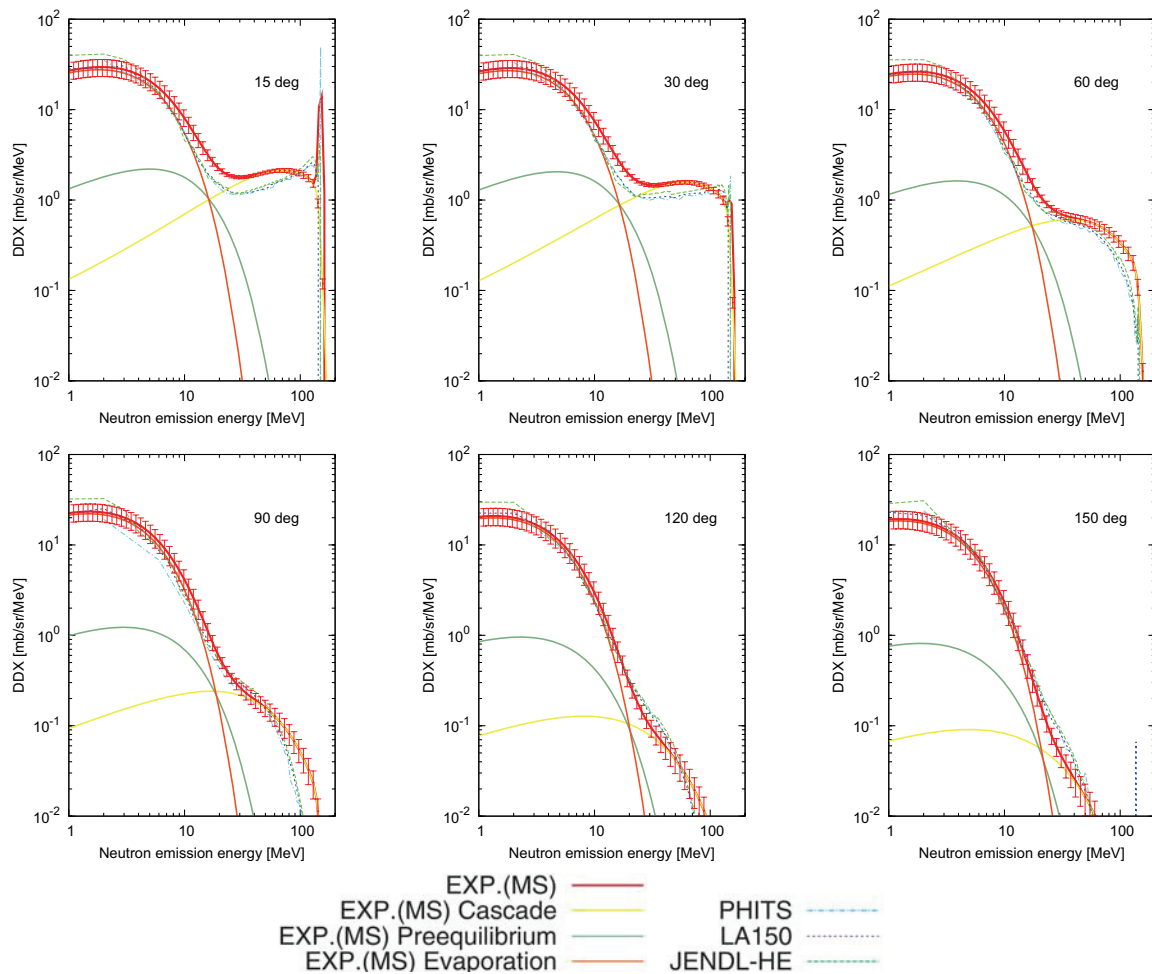


Fig. 12. Double-Differential Cross Sections for 140 – 160 MeV neutron incident energy with calculated data

5 Conclusion

The neutron-production double-differential cross sections at 150 MeV on Fe are measured using a continuous energy neutron source. The double-differential cross sections were parameterized by moving source model. The experimental results have some discrepancies with calculated data. To understanding these discrepancies, for more detailed analysis are needed.

References

- 1) P.W. Lisowski, C.D. Bowman, G.J. Russell, and S.A. Wender. *J. Nucl. Sci. Eng.*, 106:208, 1990.
- 2) Weapons neutron research facility (WNR). <http://wnr.lanl.gov/>.
- 3) S.A. Wender, S. Balestrini, A. Brown, R.C. Haight, C.M. Laymon, T.M. Lee, P.W. Lisowski, W. MacCokle, R.O. Nelson, W. Parker, and N.W. Hill. *J. Nucl. Instrum. Methods Phys. Res.*, A336:226, 1993.
- 4) M. Moszynsky and et al. *J. Nucl. Instrum. Methods.*, A343:563, 1994.
- 5) P.W. Lisowski, A. Gavron, W.E. Parker, J.L. Ullmann, S.J. Balestrini, A.D. Carlson, O.A. Wasson, and N.W. Hill. Fission cross sections in the intermediate energy region. *Specialists meeting on neutron cross section standards for the energy region above 20 MeV*, 21:23, 1991.
- 6) G. Dietze and H. Klein. *J. Nucl. Instrum. Methods.*, 193:549, 1982.
- 7) R.A. Cecil, B.D. Anderson, and R. Madey. *Nucl. Instr. Meth.*, 161:439, 1979.
- 8) D. Satoh, N. Shigyo, Y. Iwamoto, H. Kitsuki, and K. Ishibashi. *IEEE Trans. Nucl.Sci.*, 48:1165 – 1167, 2001.
- 9) T. Nakagawa and Y. Oyanagi. *Recent Developments in Statistical Inference and Data Analysis "Program system SALS for nonlinear least-squares fitting in experimental science" (K. Matsusita, ed.)*, page 221. NorthHolland. Publ. Amsterdam, 1980.
- 10) H. Iwase and et al. *J. Nucl. Sci. Technol.*, 39:1142, 2002.
- 11) M.B. Chadwick, P.G. Young, S. Chiba, S.C. Frankle, G.M. Hale, H.G. Hughes, A.J. Koning, R.C. Little, R.E. MacFarlane, R.E. Prael, and L.S. Walter. *Nucl. Sci. Eng.*, 131:293 – 328, 1999.
- 12) P.G. Young, E.D. Arthur, and M.B. Chadwick. *LA-6947 (1997) ; LAUR-88-382 (1988)*.
- 13) C. Kalbach and F.M. Mann. *Phys. Rev.*, C23:112, 1981.
- 14) Y. Watanabe, T. Fukahori, K. Kosako, N. Shigyo, T. Murata, N.Yamano, T. Hino, K. Maki, H. Nakashima, N.Odano, and S.Chiba. Nuclear data evaluation for jendl high - energy file. *Proceedings of International Conference on Nuclear Data for Science and Technology ,Santa Fe, New Mexico, USA, 1:326, Sep.26 - Oct.1 2004*.

3.6 Calculation of Fission Yield by Macroscopic-Microscopic Method Based on Selective Channel Scission Model

Masayuki OHTA and Shoji NAKAMURA

Japan Atomic Energy Agency

2-4 Shirakata-Shirane, Tokai-mura, Naka-gun, Ibaraki, 319-1195, Japan

E-mail: ohta.masayuki@jaea.go.jp

The mass-distributions of fission yields for neutron-induced fissions of U-235 were calculated by a macroscopic-microscopic method based on the selective channel scission model. The present result was compared with the previous result from the aspect of fission modes.

1. Introduction

The selective channel scission (SCS) model has been proposed and developed to calculate fission yields for any nuclei [1-3]. The SCS model deals with the fission process for each channel. The fission yield is obtained from the penetrability of the “channel-dependent” fission barrier. In previous analysis [3], mass-distributions of fission yields were calculated on simple assumptions about the channel-dependent fission barriers. This calculation method is applicable to wide range of fissionable nuclei without adjustable parameters. However, there were discrepancies between the calculated results and experimental data of fission yield in the mass regions of $A = 85-95$ and $A = 140-150$.

In this work, the channel-dependent fission potentials were calculated by a macroscopic-microscopic method based on the idea of SCS. The mass-distribution of fission yield was calculated for the neutron-induced fission of U-235.

2. SCS Model and Calculation of Fission Potential

The SCS model deals with the fission process for each channel. The fission yields are calculated from the penetrabilities of the “channel-dependent” fission barriers E_f .

The basic definition of nuclear shape is given by

$$R(\theta) = \lambda^{-1} R_0 \left(1 + \sum_{n=1}^N \alpha_n P_n(\cos \theta) \right), \quad (1)$$

where λ^{-1} is the volume conservation, R_0 is the radius of spherical nucleus, α_n is the deformation parameter and P_n is Legendre polynomial.

A macroscopic-microscopic method is commonly used for the calculation of fission potential.

The total potential energy E of a deformed nucleus is defined as the summation of the liquid-drop energy E_{LDM} as a macroscopic term and the shell correction energy E_{shell} as a microscopic term in this method.

$$E = E_{\text{LDM}} + E_{\text{shell}}. \quad (2)$$

The E_{LDM} is derived from the surface energy E_S and the Coulomb energy E_C of the deformed nucleus.

$$E_{\text{LDM}} = E_S + E_C. \quad (3)$$

The channel-dependent fission potentials were calculated by a macroscopic-microscopic method based on the idea of SCS. The surface energy E_S in the macroscopic term was obtained from an equation whose form was proportional to the surface area S of the deformed nucleus [4].

$$E_S = \gamma S, \quad (4)$$

$$\gamma = \frac{1}{4\pi r_0^2} a_2 \left[1 - \kappa \left(\frac{N-Z}{A} \right)^2 \right].$$

The Coulomb energy E_C also in the macroscopic term was obtained by the Monte-Carlo integral of the Coulomb energy between differential volumes which were taken at random all over the region of the deformed nucleus (see **Fig.1**). Mersenne Twister [5] was used as a random number generator.

$$E_C = \frac{1}{2} \iint \frac{1}{4\pi \epsilon_0} \frac{\rho_i \rho_j}{r_{ij}} d^3 r_i d^3 r_j \quad (5)$$

$$= \frac{Ze^2}{4\pi \epsilon_0} \frac{1}{2N^2} \sum_{i \neq j}^N \frac{\rho_i \rho_j}{\rho^2} \frac{1}{r_{ij}}.$$

The shell energy E_{shell} in the microscopic term was calculated approximately as follows. The two fission fragments (FP1 and FP2) were assigned to the shape of the deformed nucleus for a channel (see **Fig. 2**). The whole shell energy was calculated from the sum of the shell energies of the two deformed fission fragments assigned to the deformed nucleus (E_{sh1} and E_{sh2}).

$$E_{\text{shell}} = E_{\text{sh1}} + E_{\text{sh2}}. \quad (6)$$

A calculation code [6] was used for the calculation of shell energy for each fission fragment.

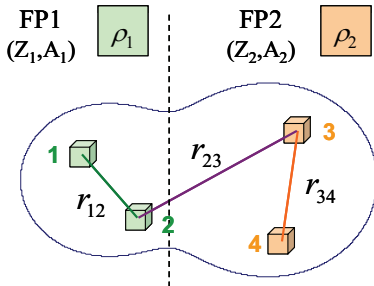


Fig. 1 Differential volumes taken in the deformed nucleus

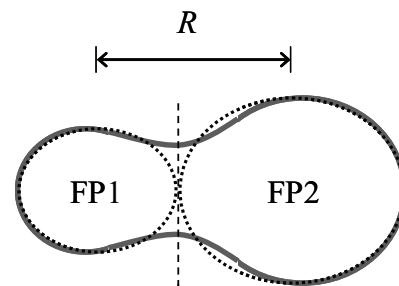


Fig. 2 Assignment of the two fragments to the deformed nucleus

The potential near the saddle point is approximated by the inverted parabola and the curvatures α is assumed as a constant for all humps, for simplicity. The tunnel probability P_i for the saddle point i is reduced as

$$P_i \approx \frac{1}{1 + \exp[0.218\alpha\sqrt{\mu} \Delta E_i]}, \quad (7)$$

in MeV and fm units, where $\mu = A_1 A_2 / (A_1 + A_2)$, $\Delta E_i = E_{fi} - E_x$ and A_1 and A_2 are the mass number of FP1 and FP2, respectively. In case of a two-humped potential, the probability P is deduced from tunnel probabilities for the two humps (P_A and P_B).

$$P = \frac{P_A P_B}{P_A + P_B}. \quad (8)$$

The fission yields are obtained by summing up these probabilities all over fission channels.

3. Results and Discussions

Figure 3-(a) shows an example of calculated fission potential for a channel. These potential calculations were carried out for about 230 channels that have high fission yields. The tunnel probability P was obtained for an excitation energy (e.g. $E_x = 0$), as shown in **Fig. 3-(b)**. The parameters α_2 at inner and outer saddle points were shown in **Figs. 3-(c)** and **3-(d)**, respectively.

Fission yields for the thermal neutron-induced fissions of U-235 were obtained as shown in **Fig. 3-(e)**. The α was taken as 0.2 in Eq. (7). Prompt neutron emission was not considered in the calculated fission yield. Meanwhile, the prompt neutron emission is considered for JENDL-3.3 data. It is known that the neutron multiplicity against mass number of fragment shows a saw-tooth curve [7]. Then, the calculated fission yield showed qualitative consistency with the data of JENDL-3.3. There were discrepancies in mass regions of $A = 85-95$ and $A = 140-150$ in previous analysis [3]. Although there were not such discrepancies in present result, fission yields were underestimated in mass regions above $A = 150$ and below $A = 90$.

The shape elongation factor η was obtained at the saddle point deduced from JENDL-3.3 data in a previous analysis [2]. The η changed the trend at mass of fragments $A \sim 130$. The similar behavior appeared in the deformation parameter a_2 in Fig. 3-(c). The α_2 contributes significantly to the deformation of nucleus. It might depend on the existence of symmetric and asymmetric fissions.

4. Conclusions

The channel-dependent fission potentials were calculated for the neutron-induced fission of U-235 by a macroscopic-microscopic method based on the selective channel scission model. The mass-distribution of fission yield was obtained for thermal neutron-induced fission of U-235.

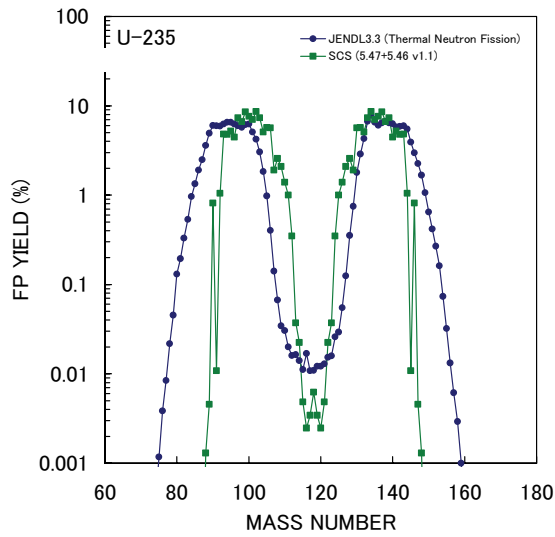
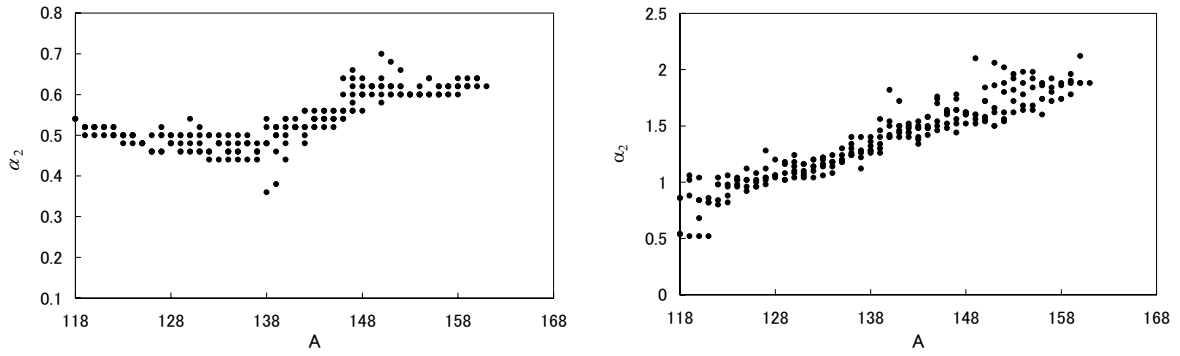
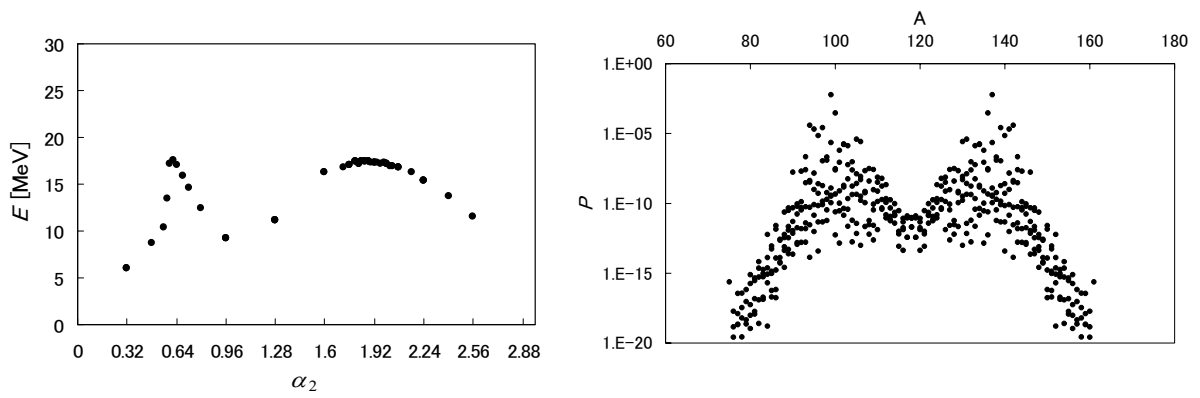


Fig. 3 Results for $n+^{235}\text{U}$

Acknowledgement

The computations were carried out with Fujitsu PRIMEPOWER HPC2500 at Japan Atomic Energy Agency (JAEA).

References

- [1] A. Takahashi *et al.*, *Jpn. J. Appl. Phys.*, **40** (2001) 7031.
- [2] M. Ohta *et al.*, *Jpn. J. Appl. Phys.*, **45** (2006) 6431.
- [3] M. Ohta *et al.*, *Proc. 2005 Symp. Nucl. Data*, JAEA-Conf 2006-009 (2006) p. 145.
- [4] W.D. Myers and W.J. Swiatecki, *Nucl. Phys.*, **81** (1966) 1.
- [5] M. Matsumoto and T. Nishimura, *ACM Trans. on Modeling and Computer Simulation*, **8** (1998) 3.
- [6] F. Garcia *et al.*, *Comp. Phys. Comm.*, **120** (1999) 57.
- [7] For example, *The New Encyclopaedia Britannica*, Encyclopaedia Britannica, Chicago, 1980 15th ed., Vol. 13, p. 301.

3.7 Effect of effective interaction potentials used in quantum molecular dynamics on nucleon-induced reactions

D. N. Kadrev^{1,2} and Y. Watanabe¹

¹*Department of Advanced Energy Engineering Science, Kyushu University, Kasuga, Fukuoka 816-8580, Japan*

²*Institute for Nuclear Research and Nuclear Energy, Bulgarian Academy of Sciences, Sofia 1784, Bulgaria*

A quantum molecular dynamics (QMD) model is applied to investigate the light-ion production in nucleon-induced reactions. The JQMD code is employed and the generalized evaporation model (GEM) is used to account for statistical decay processes after the QMD stage. In order to improve the ground state properties of the created nucleus other important effective interaction potentials, such as Pauli, momentum-dependent and Yukawa are added to the JQMD. The effect of the newly added effective interactions on the total reaction cross sections and differential cross sections of light-ion production in nucleon-induced reactions is also investigated.

1 Introduction

Various applications involving fast neutrons with energies over several tens of MeV have recently been developed, e.g., dosimetry at commercial aircraft altitudes, radiation therapy of cancer, soft-error estimation in microelectronic devices, accelerator-driven transmutation of nuclear waste, etc. Elementary interaction of a neutron with matter occurs via only a nuclear reaction because it has no charge. As a result, the kinetic energy is transferred into matter by light ions (p, d, t, ³He and ⁴He) and recoils produced by the nuclear reaction. As the incident neutron energy increases, it is known that emission of light ions with relatively high energy in the forward direction through direct and preequilibrium processes becomes important. Thus, it is necessary to enhance our understanding of these mechanisms and to establish a reliable model predicting accurately the energy and angular distributions of produced light ions from both viewpoints of fundamental nuclear physics and the above-mentioned applications.

To meet the needs, we have chosen the quantum molecular dynamics (QMD) model [1, 2] as one of the models describing the preequilibrium light-ion production in nucleon-induced reactions, and examined the applicability of the JAERI QMD (JQMD) code [2]. It has been found that the JQMD calculation can reproduce preequilibrium nucleon emission fairly well [2, 3], while it underestimates remarkably preequilibrium emission of light clusters (d, t, ³He and ⁴He) [4, 5]. More recent work [5] has suggested that implementation of a phenomenological surface coalescence model into the QMD leads to a reasonable description of preequilibrium light-cluster production in neutron-induced reactions. For further refinement, it is important to investigate how the model parameters used in the QMD calculations have an impact on the nucleon-induced light-cluster production.

It is well known that the usage of realistic initial ground state configuration in the QMD model is essential for the high predictable ability of the studied reactions. It has been found that the JQMD model can reproduce satisfactorily ground state properties of nuclei, e.g. the binding energy, root-mean-square radii, density and momentum distributions. The results show

overestimation of the root-mean-square radii in comparison with the experimental data, underestimation of the density in the center of the nucleus and its increase in the surface region and cannot reproduce experimentally observed high-momentum component of the total momentum distribution. One of the reasons for this is expected to be the simple effective interaction used in the JQMD model. It includes an attractive 2-body and repulsive 3-body simple Skyrme interactions, Coulomb and symmetry terms. The total wave function is a direct product of single-particle wave functions and is not antisymmetric. The fermionic properties of nucleons are taken into account only by checking the Pauli principle in the ground state and by the Pauli blocking effect in the collision process. It has been demonstrated [6] that it is possible to devise a Pauli potential so that the fermionic nature of the nucleons in a semiclassical manner could be reproduced, and this potential could yield an effect similar to that of the antisymmetrization of the total wave function.

In order to improve the ground state properties we modify the JQMD model by introducing the Pauli potential and also other important interactions such as momentum-dependent and Yukawa. The effects of these interactions on the total reaction cross sections and differential cross sections of light-ion production in nucleon-induced reactions are investigated.

2 The QMD model

The JQMD model is described in details in Ref. [2]. In this section we give only some basic equations and ingredients which are changed or added to the JQMD.

The QMD model is a semi-classical simulation model in which each nucleon state is represented by a Gaussian wave function of width L

$$\phi_i(\mathbf{r}) = \frac{1}{(2\pi L)^{3/4}} \exp \left[-\frac{(\mathbf{r} - \mathbf{R}_i)^2}{4L} + \frac{i}{\hbar} \mathbf{r} \cdot \mathbf{P}_i \right], \quad (1)$$

where R_i and P_i are the centers of position and momentum of the i -th nucleon, respectively. The total wave function is assumed to be a direct product of these wave functions.

The one-body distribution function is obtained by the Wigner transform of the wave function,

$$f(\mathbf{r}, \mathbf{p}) = \sum_i f_i(\mathbf{r}, \mathbf{p}), \quad f_i(\mathbf{r}, \mathbf{p}) = 8 \exp \left[-\frac{(\mathbf{r} - \mathbf{R}_i)^2}{2L} - \frac{2L(\mathbf{p} - \mathbf{P}_i)^2}{\hbar^2} \right]. \quad (2)$$

The equation of motion of nucleons is given by the Newtonian equations

$$\dot{\mathbf{R}}_i = \frac{\partial H}{\partial \mathbf{P}_i}, \quad \dot{\mathbf{P}}_i = -\frac{\partial H}{\partial \mathbf{R}_i}, \quad (3)$$

and the stochastic two-body collision term.

The Hamiltonian H in the present work consists of the kinetic energy and the energy of two-body effective interactions

$$H = T + V_{\text{local}} + V_{\text{Pauli}} + V_{\text{MD}} + V_{\text{Yukawa}}, \quad (4)$$

where $T = \sum_i \sqrt{m_i^2 + \mathbf{P}_i^2}$ is the kinetic energy including the mass term. V_{local} , V_{Pauli} , V_{MD} and V_{Yukawa} are the local potential, the Pauli potential, the momentum-dependent (MD) potential and the Yukawa potential parts, respectively.

For the local potential part we adopt the effective interaction used in the JQMD model. It contains the Skyrme type, the Coulomb and the symmetry terms,

$$V_{\text{local}} = \frac{A}{2\rho_0} \sum_i \rho_i + \frac{B}{\rho_0^\tau(1+\tau)} \sum_i \rho_i^\tau + \frac{e^2}{2} \sum_{i,j(\neq i)} \frac{c_i c_j}{|\mathbf{R}_i - \mathbf{R}_j|} \text{erf} \left(\frac{|\mathbf{R}_i - \mathbf{R}_j|}{4L} \right) + \frac{C_s}{2\rho_0} \sum_{i,j(\neq i)} (1 - 2c_i - c_j) \rho_{ij}, \quad (5)$$

where erf denotes the error function, c_i is 1 for protons and 0 for neutrons and ρ_i is an overlap of density with other nucleons defined as

$$\rho_i = \sum_{j \neq i} \rho_{ij} = \sum_{j \neq i} \int d\mathbf{r} \rho_i(\mathbf{r}) \rho_j(\mathbf{r}) = \sum_{j \neq i} (4\pi L)^{-3/2} \exp \left[-(\mathbf{R}_i - \mathbf{R}_j)^2 / 4L \right], \quad (6)$$

with

$$\rho_i(\mathbf{r}) = \int \frac{d\mathbf{p}}{(2\pi\hbar)^3} f_i(\mathbf{r}, \mathbf{p}) = (2\pi L)^{-3/2} \exp \left[-(\mathbf{r} - \mathbf{R}_i)^2 / 2L \right]. \quad (7)$$

In addition to the JQMD effective interaction we include also Pauli potential, momentum-dependent term and Yukawa potential.

The Pauli potential [6, 7] is introduced for the sake of simulating fermionic properties of nucleons in a semiclassical way. This phenomenological potential prohibits nucleons of the same spin σ and isospin τ from coming close to each other in the phase space. Here we employ the Gaussian form of the Pauli potential

$$V_{\text{Pauli}} = \frac{C_P}{2} \left(\frac{\hbar}{q_0 p_0} \right)^3 \sum_{i,j(\neq i)} \exp \left[-\frac{(\mathbf{R}_i - \mathbf{R}_j)^2}{2q_0^2} - \frac{(\mathbf{P}_i - \mathbf{P}_j)^2}{2p_0^2} \right] \delta_{\tau_i \tau_j} \delta_{\sigma_i \sigma_j}. \quad (8)$$

The momentum-dependent term [7] is introduced as a Fock term of the Yukawa-type interaction. It is divided into two ranges so as to fit the effective mass and the energy dependence of the real part of the optical potential, as

$$V_{\text{MD}} = \frac{C_{\text{ex}}^{(1)}}{2\rho_0} \sum_{i,j(\neq i)} \frac{1}{1 + [(\mathbf{P}_i - \mathbf{P}_j)/\mu_1]^2} \rho_{ij} + \frac{C_{\text{ex}}^{(2)}}{2\rho_0} \sum_{i,j(\neq i)} \frac{1}{1 + [(\mathbf{P}_i - \mathbf{P}_j)/\mu_2]^2} \rho_{ij}. \quad (9)$$

The Yukawa potential [6, 8] has the form

$$V_{\text{Yukawa}} = \frac{C_Y}{2} \sum_{i,j(\neq i)} \frac{\exp(L/\gamma_Y^2)}{2|\mathbf{R}_i - \mathbf{R}_j|} \left\{ \exp\left(-\frac{|\mathbf{R}_i - \mathbf{R}_j|}{\gamma_Y}\right) \left[1 - \text{erf} \left(\frac{2L/\gamma_Y - |\mathbf{R}_i - \mathbf{R}_j|}{4L} \right) \right] - \exp\left(\frac{|\mathbf{R}_i - \mathbf{R}_j|}{\gamma_Y}\right) \left[1 - \text{erf} \left(\frac{2L/\gamma_Y + |\mathbf{R}_i - \mathbf{R}_j|}{4L} \right) \right] \right\}. \quad (10)$$

Two sampling methods are employed in the JQMD model for creation of the ground state, random packing and frictional cooling. The random packing method accepts initial configurations which binding energy per nucleon lies within 0.5 MeV interval of the liquid-drop model value. The frictional cooling method cool or heat the system to adjust the binding energy to the liquid-drop model value. We also use the Metropolis sampling method [9], which give possibility to obtain a ground state at certain temperature, and so to examine the thermostatic properties of nuclei.

The QMD simulations of nucleon-induced reactions are performed up to certain time (100–150 fm/c in our case) and then at the end of dynamical stage we switch to statistical decay calculations. The generalized evaporation model (GEM) [10] is used to account for the decay processes.

3 Results and Discussion

The modified QMD model has been used to explore the effect of the different effective interactions on the ground state properties of nuclei, reaction cross sections and light-ion production in nucleon-induced reactions. Calculations have been done for several nuclei of interest, such as ^{12}C , ^{16}O , ^{27}Al , and ^{28}Si .

We use two parameter sets, which take into account different effective interactions. They are listed in Table 1 along with the JQMD one. The first of them (denoted as P&MD) in addition to the JQMD interaction includes Pauli and momentum-dependent potentials and is taken from Ref. [11], the other one (Yukawa) with Pauli and Yukawa potentials is from [12]. We use the

Table 1: Parameters of the model for the different interactions.

	JQMD	P&MD	Yukawa
A (MeV)	-219.4	-127.86	-163.0
B (MeV)	165.3	204.28	125.95
L (fm ²)	2.0	1.75	1.0
τ	1.33	1.33	1.67
C_P (MeV)		140	30
q_0 (fm)		1.644	5.81
p_0 (MeV)		120	400
$C_{\text{ex}}^{(1)}$ (MeV)		-258.54	
$C_{\text{ex}}^{(1)}$ (MeV)		-375.60	
μ_1 (MeV)		2.35	
μ_2 (MeV)		0.4	
C_Y (MeV fm)			-0.498
γ_Y			1.4

JQMD values for the saturation density $\rho_0 = 0.168 \text{ fm}^{-3}$ and the symmetry energy parameter $C_s = 25 \text{ MeV}$.

The ground state in the JQMD and with the P&MD parameter set is generated by the frictional cooling method. In order to investigate the thermostatic properties of the ground state and to check the effect of the temperature on the reaction cross section, the ground state for the P&MD parameter set is created also using the Metropolis sampling method at temperature $T = 3 \text{ MeV}$. For the Yukawa parameter set we use random packing because of difficulties in the creation of stable ground state by means of the frictional cooling and adjustment of the binding energy.

In Fig. 1 we show the density $\rho(r)$ and momentum $n(p)$ distributions of the ground state of ^{12}C and ^{28}Si nuclei calculated with different parameter sets. The corresponding root-mean-square radii are listed in Table 2. The QMD simulations are performed up to $150 \text{ fm}/c$ and the averaged quantities over 1000 events are plotted. The results are compared with the empirical density distribution of Negele [13] and with “experimental” total momentum distribution deduces by y -scaling analysis [14] of inclusive electron-scattering data. The results of both parameter sets show improvement of the ground state properties in comparison with the JQMD ones. We have higher density in the center of nucleus and not so wide surface shape, root-mean-square radii are smaller and closer to the experimental ones, and the momentum distributions develop a high-momentum component. The inclusion of the Pauli and momentum-dependent potentials shows, for the ^{12}C case, fair agreement of the density distribution and root-mean-

square radius with the empirical ones. Increasing of the temperature of the system leads to rearrangement of the nucleons from the center to the periphery. The momentum distribution of ^{12}C calculated with Yukawa parameter set is in better agreement with the experimental data.

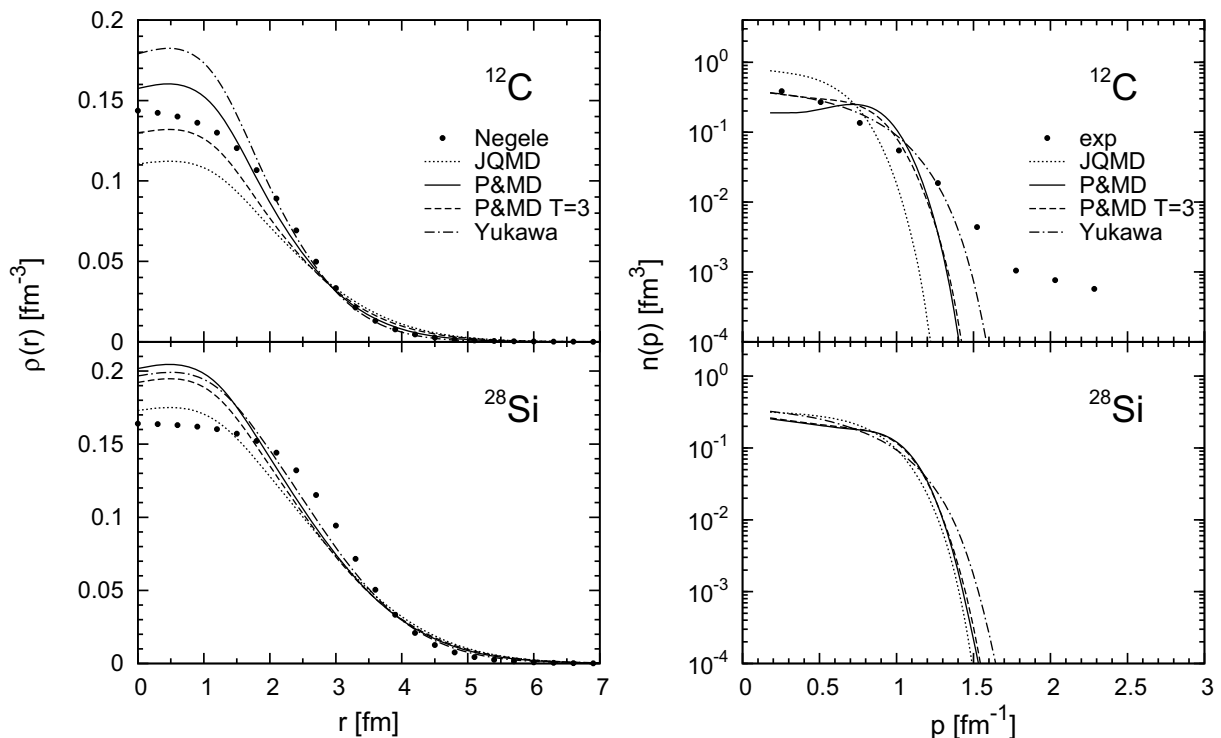


Figure 1: Density (left) and momentum (right) distributions of the ground state of ^{12}C and ^{28}Si obtained with different parameter sets.

Table 2: Root-mean-square radii (in fm) of ^{12}C and ^{28}Si obtained with different parameter sets.

Nucleus	JQMD	P&MD	P&MD $T = 3$ MeV	Yukawa	Negele
^{12}C	3.082	2.771	2.987	2.555	2.707
^{28}Si	3.488	3.413	3.447	3.265	3.165

A comparison between QMD calculations of the total reaction cross section for the proton-induced reaction on ^{12}C is shown in Fig. 2. The results are averaged quantities over time evolution up to 100 fm/c and over 10^4 events. The experimental data are taken from Ref. [15]. The JQMD model describes satisfactorily the reaction cross section, especially at high energies. The QMD calculations with the Pauli and momentum-dependent parameter set underestimate the experimental cross section for whole energy spectrum, but reproduce very well the energy dependence. We can improve the results by increasing the temperature of the ground state. The calculations with the Yukawa parameter set show good agreement with the experimental data. Similar results have been obtained for the ^{27}Al nucleus.

The results with the P&MD parameter set for angle-integrated energy spectra of light-ion production for ^{28}Si in neutron-induced reaction at incident energy 96 MeV are presented in Fig. 3. The QMD simulations are performed with 10^6 events and up to 100 fm/c. It can be seen that the JQMD results reproduce very well the proton production, but show large underestimation

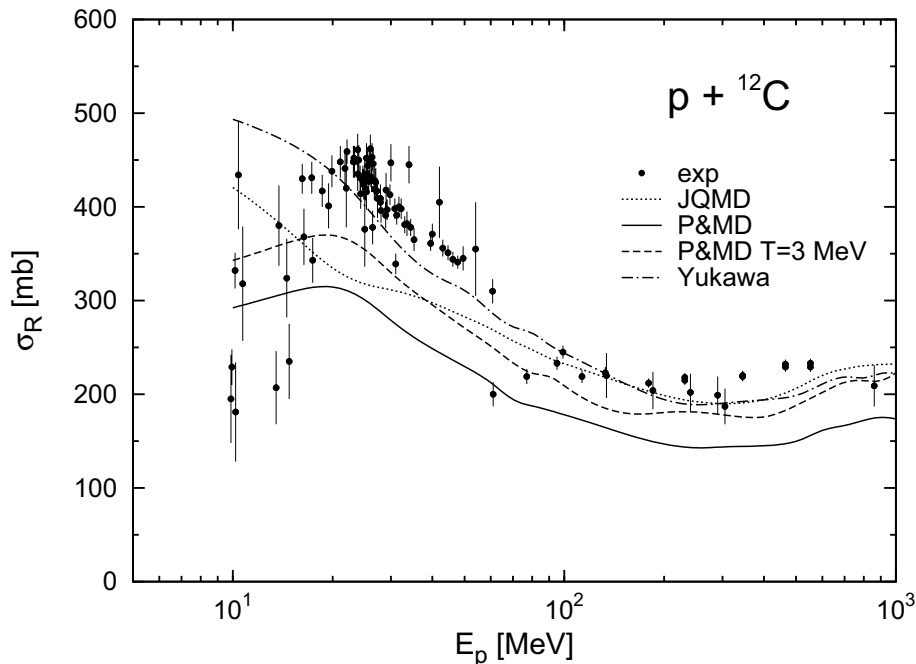


Figure 2: Total reaction cross section of ^{12}C for incident proton.

for other light clusters. The introduction of Pauli and momentum-dependent potentials with present parameters doesn't change significantly the description of light-ion emission. The proton cross sections are slightly reduced, while for the cross sections of other light clusters we have small enhancement. The results for the double-differential cross sections are similar. Thus, the present work indicates that the effective interaction potentials used in QMD calculations have little influence on preequilibrium light-cluster production in neutron-induced reactions. It should be noted that agreement with the experimental data is fairly improved by implementation of a phenomenological coalescence model into the QMD calculation as shown in our recent work [5].

4 Conclusions

The JQMD model is used to explore the preequilibrium light-cluster production in nucleon-induced reactions at intermediate energies. In order to improve ground state properties of nuclei, new effective interactions, for instance Pauli, momentum-dependent and Yukawa, are added to the nuclear Hamiltonian. Two parameter sets are used, the first one includes the Pauli and momentum-dependent potentials, the second one – the Pauli and Yukawa potentials.

The inclusion of the Pauli potential and momentum-dependent interaction leads to enhancement of the density distribution and the root-mean-square radii of nuclei. Calculations show underestimation of the proton-induced total reaction cross section but the energy dependence is reproduced rather well. Increasing of the temperature of the system leads to enhancement of the results.

The introduction of the Yukawa potential improves the nucleon momentum distribution, it develops a high-momentum component in accordance to the experimental data. The proton-induced total reaction cross section is reproduced rather well.

Newly added interactions with present parameter sets don't affect significantly the JQMD description of the light-cluster emission in nucleon-induced reactions.

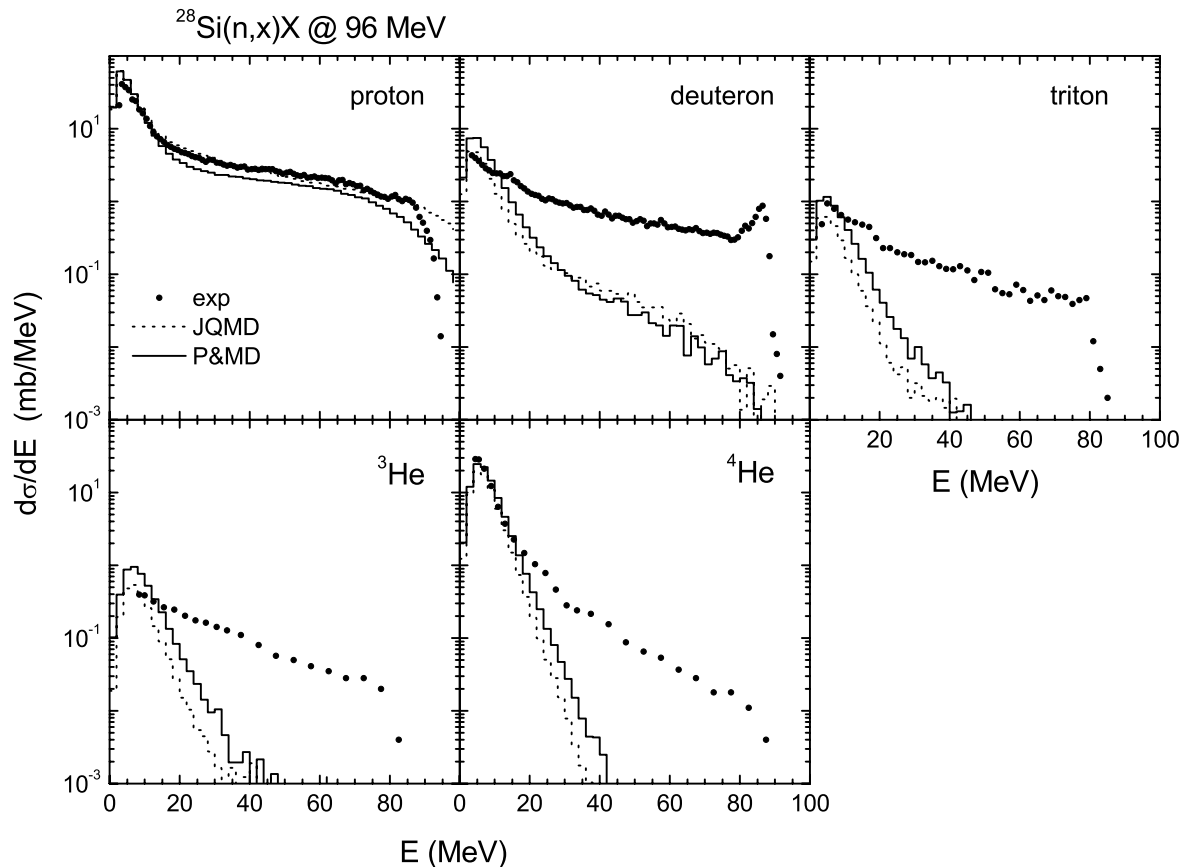


Figure 3: Angle-integrated energy spectra of light ions produced from neutron-induced reaction on ^{28}Si at 96 MeV. The experimental data are taken from [16].

Acknowledgments

The authors would like to thank Drs. K. Niita and S. Chiba for valuable comments on this work. D.N.K. is grateful to the Japan Society for the Promotion of Science (JSPS) for a postdoctoral fellowship. This work is partly supported by the Grants-in-Aid (No.17-05374) for Scientific Research from JSPS.

References

- [1] J. Aichelin, Phys. Rep. **202**, 233 (1991) and references therein.
- [2] K. Niita, S. Chiba, T. Maruyama, T. Maruyama, H. Takada, T. Fukahori, Y. Nakahara, and A. Iwamoto, Phys. Rev. C **52**, 2620 (1995).
- [3] S. Chiba, O. Iwamoto, T. Fukahori, K. Niita, T. Maruyama, T. Maruyama, and A. Iwamoto, Phys. Rev. C **54**, 285 (1996).
- [4] Y. Watanabe, in *Perspectives on Nuclear Data for the Next Decade*, Workshop Proceedings, Bruyères-le-Châtel, France, 26-28 September 2005, edited by E. Bauge (OECD Nuclear Energy Agency, Paris, 2006), p. 95.
- [5] Y. Watanabe and D. N. Kadrev, in *Proceedings of the Tenth International Symposium on Neutron Dosimetry*, Uppsala, Sweden, 2006, Radiat. Prot. Dosim. (to be published).

- [6] G. Peilert, J. Konopka, H. Stöcker, W. Greiner, M. Blann, and M. G. Mustafa, *Phys. Rev. C* **46**, 1457 (1992).
- [7] T. Maruyama, K. Niita, K. Oyamatsu, T. Maruyama, S. Chiba, and A. Iwamoto, *Phys. Rev. C* **57**, 655 (1998).
- [8] S. A. Bass *et al.*, *Prog. Part. Nucl. Phys.* **41**, 225 (1998).
- [9] N. Metropolis, A. W. Rosenbluth, M. N. Rosenbluth, A. H. Teller, and E. Teller, *J. Chem. Phys. C* **21**, 1087 (1953).
- [10] S. Furihata, *Nucl. Instrum. Methods Phys. Res. B* **171**, 251 (2000).
- [11] S. Chiba, K. Niita, T. Fukahori, T. Maruyama, T. Maruyama, and A. Iwamoto, in *Nucleon-nucleus optical model up to 200 MeV*, Proceedings of a Specialists Meeting, 13-15 November 1996, Bruyères-le-Châtel, France (OECD Nuclear Energy Agency, Paris, 1997), p. 49.
- [12] Khaled Abdel-Waged, *Phys. Rev. C* **74**, 034601 (2006).
- [13] J. W. Negele, *Phys. Rev. C* **1**, 1260 (1970).
- [14] C. Ciofi degli Atti, E. Pace, and G. Salmè, *Phys. Rev. C* **43**, 1155 (1991).
- [15] R. F. Carlson, *At. Data Nucl. Data Tables* **63**, 93 (1996).
- [16] U. Tippawan *et al.*, *Phys. Rev. C* **69**, 064609 (2004).

3.8 Nuclear data evaluation of ^{206}Pb for proton- and neutron-induced reaction in energy region from 20 to 200 MeV

Tsuyoshi Kajimoto¹, Nobuhiro Shigyo¹, Kenji Ishibashi¹, Satoshi Kunieda²,
and Tokio Fukahori²

¹*Kyushu University, 744 Nishi-ku, Motoooka, Fukuoka 819-0395 Japan*

²*Japan Atomic Energy Agency, Tokai, Naka, Ibaraki 319-1195, Japan*

Nuclear data evaluation was carried out for ^{206}Pb for proton and neutron incidence in the energy range from 20 to 200 MeV by using the ECIS-96 and the GNASH code. Evaluated cross sections were compared with measurement data and the LA150 evaluations.

1 Introduction

The evaluated nuclear data in the intermediate energy range for various nuclei are required such technologies as spallation neutron sources, accelerator shielding design, radiation therapy, and space developments. The program for completion of the JENDL High Energy File (JENDL-HE)¹ is now ongoing under the Japanese Nuclear Data Committee to meet these needs. The 2007 version of JENDL-HE will be published this year.

In the shielding design of high energy accelerators, lead is one of the important shield element. Evaluating nuclear data for lead is necessary to the recent and the future nuclear technologies. In this work, the evaluation of neutron and proton induced nuclear data for ^{206}Pb was performed using the GNASH code system. The evaluations for neutron incidence were started at 20 MeV that was the upper limit of existing data files for fission and fusion reactors.

The optical model analysis was carried out as the initial approach. The ECIS-96 code² was adopted for the optical model calculation. It was also applied to obtain transmission coefficients of induced- and outgoing-particles which were required for the statistical model calculations, and to evaluate elastic- and inelastic- scattering, total and total-reaction cross sections. The GNASH code³ was used in order to calculate light particle spectra and isotope-production cross sections. The code employed the Hauser-Feshbach model for statistical decay process, and the exciton model for pre-equilibrium processes.

We made evaluations for such values of total, total-reaction, angular-differential elastic-scattering, energy-differential particle-production, and double-differential particle-production cross sections. The validities of calculated excitation functions for isotope-production cross sections were also investigated. Present results were compared with the LA150⁴ evaluations.

2 Optical model calculation

The optical model is one of the most efficient method to calculate angular-differential elastic-scattering, total and total reaction cross sections. In the model calculation, the optical model potential (OMP) parameters were essential to be optimized. They are also

important values to provide transmission coefficient required in the statical model calculation. Therefore, the optical potential was searched for so as to obtain good descriptions of measured data. In this work, we assumed the OMP could be described with following functional forms.

$$V_R = \left(V_R^0 + V_R^1 E^\dagger + V_R^2 E^{\dagger 2} + V_R^{DISP} e^{-\lambda_R E^\dagger} \right) \left[1 + \frac{1}{V_R^0 + V_R^{DISP}} (-1)^{Z'+1} C_{viso} \frac{N-Z}{A} \right] + C_{coul} \frac{ZZ'}{A^{1/3}} \rho_{coul} (E^\dagger), \quad (1)$$

$$W_V = W_V^{DISP} \frac{E^{\dagger 2}}{E^{\dagger 2} + WID_V^2}, \quad (2)$$

$$W_D = \left[W_D^{DISP} + (-1)^{Z'+1} C_{viso} \frac{N-Z}{A} \right] e^{-\lambda_D E^\dagger} \frac{E^{\dagger 2}}{E^{\dagger 2} + WID_D^2}, \quad (3)$$

$$V_{SO} = V_{SO}^0 e^{-\lambda_{SO} E^\dagger}, \quad (4)$$

$$W_{SO} = W_{SO}^{DISP} \frac{E^{\dagger 2}}{E^{\dagger 2} + WID_{SO}^2}. \quad (5)$$

The functions were proposed by Soukhovitskii et al.⁵⁾ The symbols V_R , W_V , W_D , V_{SO} and W_{SO} correspond to real volume, imaginary volume, imaginary surface, real and imaginary spin-orbit terms of potential depths in MeV, respectively. The spin-orbit parameters were taken from those of Koning and Delaroche.⁶⁾ The parameters A , Z , N and Z' are the numbers of nucleon, proton, neutron in target nucleus and charge-number of projectile particle, respectively. The E^\dagger expresses the relative projectile-energy to the Fermi energy E_f . The ρ_{coul} stands for the Coulomb term which is written as follows.

$$\rho_{coul} = \left(\lambda_R V_R^{DISP} e^{-\lambda_R E^\dagger} - V_R^1 - 2V_R^2 E^\dagger \right) \left[1 + \frac{1}{V_R^0 + V_R^{DISP}} (-1)^{Z'+1} C_{viso} \frac{N-Z}{A} \right]. \quad (6)$$

The Woods-Saxon form $f_{R,D,V,SO}$ was utilized to described geometries of the optical potential. The optical potential is described as,

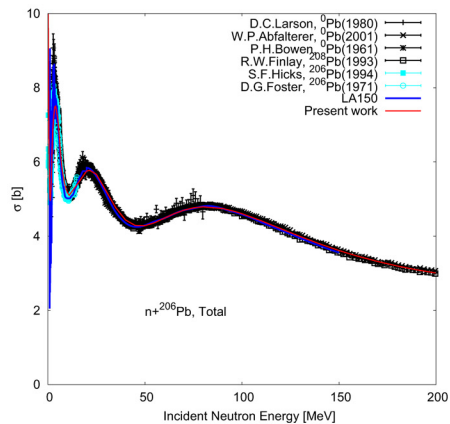
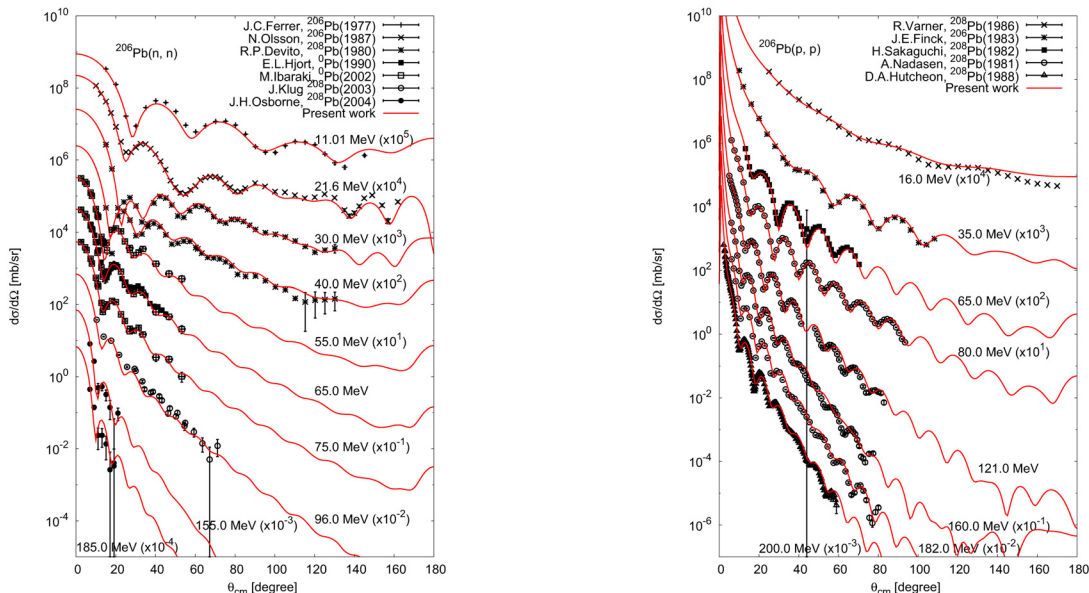
$$V(r) = -V_R f_R(r) + i \left[4W_D a_D \frac{d}{dr} f_D(r) - W_V f_V(r) \right] + \left(\frac{\hbar}{m_\pi c} \right)^2 (V_{SO} + iW_{SO}) \frac{1}{r} \frac{d}{dr} f_{SO}(r) \mathbf{L} \cdot \boldsymbol{\sigma} + V_{Coul}(r). \quad (7)$$

The symbols \mathbf{L} and $\boldsymbol{\sigma}$ stand for the orbital angular-momentum for the relative motion and the Pauli matrices of projectile. The $V_{Coul}(r)$ indicates the Coulomb potential.

At first, the OMP parameters were searched for the neutron-incidence interactions. The initial OMP parameters were taken from the local parameter set proposed by Kunieda et al.⁷⁾ Parameters $V_R^{0-2,DISP}$, $\lambda_{R,D}$, W_D^{DISP} , and $WID_{D,V}$ were adjusted so as to obtain accurate descriptions of measured total and elastic scattering differential cross sections. The determined OMP parameters are listed in **Table 1**. The evaluated total and angular-differential elastic-scattering cross sections are shown together with experimental data in **Figs. 1** and **2**, respectively. The characteristic of proton and neutron is analogous except for the Coulomb effects. Therefore, the OMP parameters for proton were determined by modifying those for neutron. The determined OMP parameters for proton are also listed in Table 1. Figure 2 gives evaluated proton-induced angular-differential elastic-scattering cross sections together with measured data. Good agreements were seen between calculated and experiment data.

Table 1: OMP parameters used in evaluation of ^{206}Pb .

	neutron	proton
V_R^0	-35.3	-39.5
V_R^1	0.02	0.03
V_R^2	0.000145	0.000125
V_R^{DISP}	93.28	99.18
λ_R	0.0045	0.00445
W_D^{DISP}	16.5	15.0
WID_D	16.0	9.0
λ_D	0.0185	0.0155
W_V^{DISP}	18.0	17.0
WID_V	110.0	105.0
a	0.671	0.671
E_f	-8.09	-7.25


 Fig. 1: Present evaluation and measured data⁹⁾ for neutron-induced total cross sections on ^{206}Pb .

 Fig. 2: Present evaluations and measured data⁹⁾ for neutron- and proton-induced angular-differential elastic-scattering cross sections on ^{206}Pb .

3 The GNASH calculations

The GNASH code was utilized for calculating energy-differential cross sections for the productions of light-particles (neutron, proton, deuteron, triton, ^3He and α -particle) and isotope-production cross sections. The code was basically the same one employed in the LA150 evaluations. In the Monte Carlo simulations for high energy applications, the angular distributions of emission particles are important. Therefore, double-differential cross sections were also calculated for the emitted particles by using the Kalbach angular-distribution systematics.⁸⁾

The exciton model has some adjustable parameters such as the single-particle state

density parameter g and the average squared matrix element M^2 . The evaluation of double-differential cross sections was implemented by adjusting these parameters. The results deduced in the laboratory frame are compared with available experimental data and the LA150 evaluations in **Fig. 3** for (n, xp) and **Fig. 4** for (p, xn) and (p, xp) . The evaluations of isotope-production cross sections are presented together with experimental data and the LA150 evaluations in **Figs. 5** and **6**. These results show that the evaluated cross sections give good agreements with experimental data. However, there was large discrepancy between evaluated and experimental isotope-production cross sections for some residual nuclei. One of the reasons might be due to some imperfect descriptions of the level density parameters.

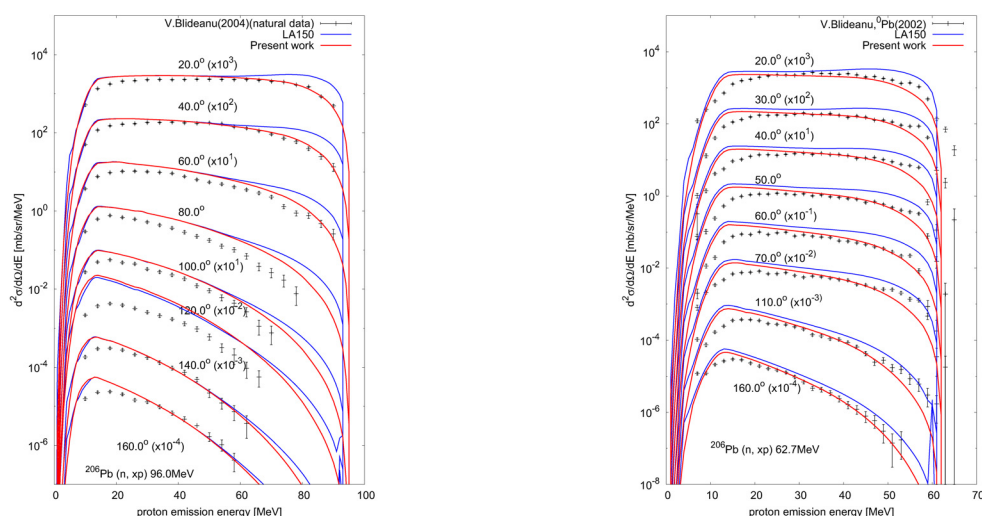


Fig. 3: Present evaluations and experimental data⁹⁾ of double-differential cross sections for (n, xp) reactions on ^{206}Pb at 96 MeV, and 62.7 MeV.

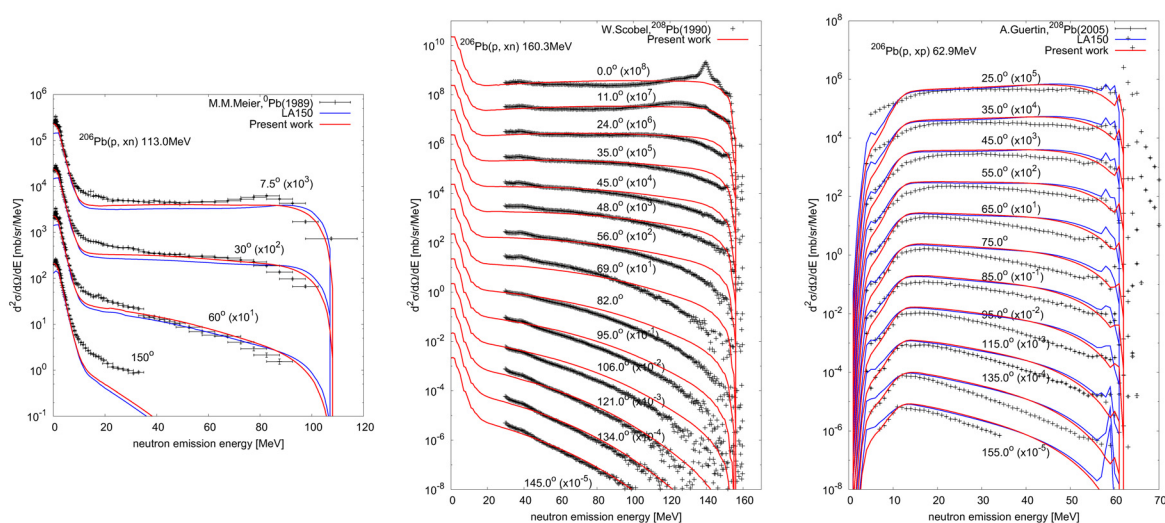


Fig. 4: Present evaluations and experimental data⁹⁾ of double-differential cross sections for (p, xn) and (p, xp) reactions on ^{206}Pb at 113 MeV, 160.3 MeV, and 62.9 MeV.

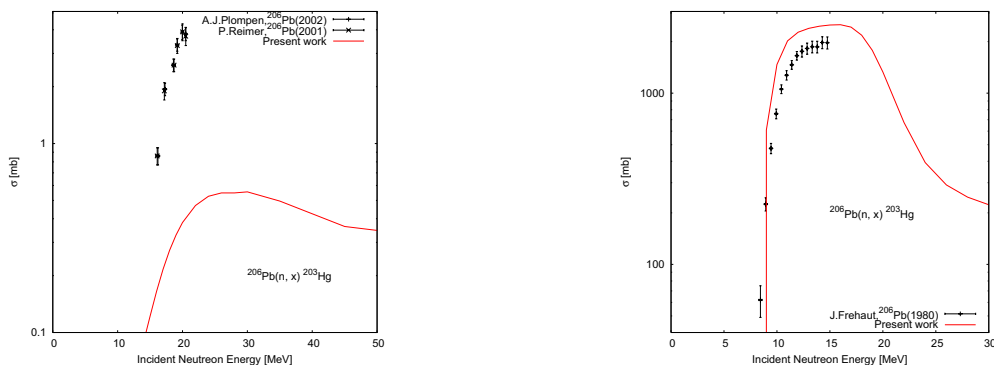


Fig. 5: Present evaluations, experimental data⁹⁾ of isotope-production cross sections for neutron incidence.

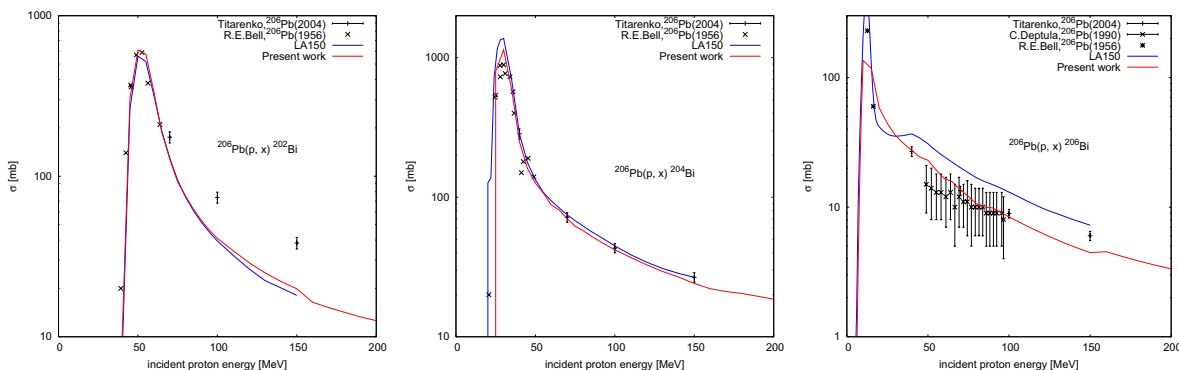


Fig. 6: Present evaluations, experimental data⁹⁾ and LA150 evaluations of isotope-production cross sections for proton incidence.

4 Summary

The evaluation of cross sections for ^{206}Pb was performed for neutron- and proton-induced reactions by using the ECIS-96 and the GNASH code. The energy range of evaluation was from 20 to 200 MeV. The global optical potentials were adopted to allow the continuous evaluation for the incident energy. The optical model potential parameters were determined to give good agreements with experimental data of total and angular-differential elastic scattering cross sections. The GNASH code was used for evaluations of energy-differential particle-production cross sections and isotope-production cross sections. Double-differential cross-sections of the emitted particles were calculated on the basis of the Kalbach systematics. Present evaluations were compared with the available experimental data and LA150. Good overall agreements were obtained. However, there was large discrepancy between evaluated and experimental isotope-production cross sections for some residual nuclei.

Acknowledgments

The authors would like to appreciate technical supports for all the members of Nuclear Data Center at Japan Atomic Energy Agency.

References

- 1) T. Fukahori, Y. Watanabe, N. Yoshizawa, F. Maekawa, S. Meigo, C. Konno, N. Yamano, AY Konobeyev, and S. Chiba, *J. Nucl. Sci. Technol. Suppl.*, **2**, 25, (2002).
- 2) J. Raynal, Notes on ECIS94, Report CEA-N-2772, Centre d'Etude de Saclay CEA, Saclay, France (1994).
- 3) P. G. Young, E. D. Arthur, M. B. Chadwick, in: Workshop on Nuclear Reaction Data and Nuclear Reactors, Trieste, Italy, 15 April-17 May 1996, p. 227.
- 4) M. B. Chadwick, P. G. Young, S. Chiba, S. C. Frankle, G. M. Hale, H. G. Hughes, A. J. Koning, R. C. Little, R. E. MacFarlane, R. E. Prael, *et al.*, *Nucl. Sci. Eng.*, **131**, 293 (1999).
- 5) E. Sh. Soukhovitskii, S. Chiba, O Iwamoto, *et al.*, JAERI-Data/Code 2005-002 (2005).
- 6) A. J. Koning, J. P. Delaroche, *Nucl. Phys.*, **A713**, 231 (2003).
- 7) S. Kunieda, S. Chiba, K. Shibata, A. Ichihara, Efrem Sh. Sukhovitskii, published to *J. Nucl. Sci. Technol.*, **44**.
- 8) C. Kalbach, *Phys. Rev. C*, **37**, 2350 (1988).
- 9) EXFOR cross section data online at <http://www.nea.fr/html/dbdata/x4/welcome.htm>

3.9 Prompt Time Constants of a Reflected Reactor

*Tao Ye Chaobin Chen Weili Sun Benai Zhang Dongfeng Tian
Institute of Applied Physics and Computational Mathematics, Beijing, 100088, China

**E-mail: yetao@aees.kyushu-u.ac.jp*

Based on G. D. Spriggs' two-region kinetics model, a two-group point reactor kinetics model is developed. With the help of MCNP code, the modified model calculates prompt time decay constants of one benchmark reactor, PU-MET-FAST-024. The results of fundamental and secondary modes agree well with MCNP time fitting results in different subcritical reactivities.

1. INTRODUCTION

Time eigenvalue of transportation equation, alpha, is defined to describe all neutrons' time behavior (increasing or decreasing) in a nuclear reactor. Its number reflects the criticality also. The time constant, especially prompt time constant, had been studied for 60 years. Lots of reflected reactor's experimental data *cannot be satisfactorily explained using the standard point kinetic model*¹. And multiple decay modes near delayed critical were also observed, which of course cannot be described by standard point kinetic model.

The existing numerical transportation codes, such as MCNP4C² and TART^{3,4}, can do the job well with only the fundamental mode calculated. By using alpha static criticality method, MCNP4C is a good tool if k_{eff} is close 1, which means the reactor is near delayed critical. But MCNP4C's calculation may be very difficult and time-consuming if the reactor has more negative reactivity or reflector contains hydrogen, or both.

In the region of analytical method, many works contains too much mathematics, which are not easy to calculate and compare with experimental data. G. D. Spriggs' one-group, two-region kinetic model based on Avery-Cohn model is simple, calculable. The model introduces *simple probability relationships essential to calculating the coupling parameters between core and reflector*,¹ and derives the reflected-core inhour equation which contains multiple decay modes. However, Spriggs model cannot well describe multiple time constants of the thermal reflected reactor. In this kind of reactor, thermal neutrons with long lifetime contribute much to the time constant. Because of importance of thermal neutrons in such fast-thermal reactor, we present a simplified two-group, two-region kinetic model (2G2R) based on Spriggs model, and rewrite the reflected-core inhour equation. With the help of MCNP code, we calculated the coupling parameters, neutron lifetimes and first and secondary time constant of a spherical benchmark reactor, PU-MET-FAST-024.⁶ Because we don't have experimental data, the results of time constants are also compare with 3 different models, MCNP time fitting method, alpha static method (MCNP4C), and Spriggs model. The results of 2G2R model agree well with MCNP time fitting method which can be thought as an experiment in computer.

2. ALPHA STATIC CRITICALITY METHOD

MCNP4C code introduced a new feature to calculate the fundamental mode of prompt time eigenvalue². It is based on alpha static criticality method. In subcritical condition, the equation is

$$\begin{aligned} \nu\Omega \cdot \nabla N + \left(\sigma_t + \frac{|\alpha|}{\nu} \right) \cdot \nu N = & \iint d\Omega' dE' \left(\sigma_s' \nu' N' + 2 \frac{|\alpha|}{\nu} \cdot \nu' N' \delta(\Omega' - \Omega) \delta(E' - E) \right) \\ & + \frac{1}{k'} \iint d\Omega' dE' (\nu \sigma_f \nu' N') \end{aligned} \quad (1)$$

The calculation procedures are to get $k' \approx 1$ by searching proper alpha. Then equation becomes

$$\begin{aligned} \nu\Omega \cdot \nabla N + \left(\sigma_t + \frac{|\alpha|}{\nu} \right) \cdot \nu N = & \iint d\Omega' dE' \left(\sigma_s' \nu' N' + 2 \frac{|\alpha|}{\nu} \cdot \nu' N' \delta(\Omega' - \Omega) \delta(E' - E) \right) \\ & + \iint d\Omega' dE' (\nu \sigma_f \nu' N') \end{aligned} \quad (1')$$

which is the alpha eigenequation.

If a reactor has more negative reactivity or reflector contains hydrogen, or both, the ratio between (α/ν) term and σ_t term can be very large, which will results non-physical high particle weight and stops the calculation. We add an adjusting parameter to lower the ratio. The modified equation is

$$\begin{aligned} \nu\Omega \cdot \nabla N + \left(\sigma_t + \eta \frac{|\alpha|}{\nu} \right) \cdot \nu N = & \iint d\Omega' dE' \left(\sigma_s' \nu' N' + (1 + \eta) \frac{|\alpha|}{\nu} \cdot \nu' N' \delta(\Omega' - \Omega) \delta(E' - E) \right) \\ & + \frac{1}{k'} \iint d\Omega' dE' (\nu \sigma_f \nu' N') \end{aligned} \quad (2)$$

The modification can only weaken the tendency of getting huge particle weight, and restrictedly extend the usage of MCNP4C. The k' intends to converge to a number larger than unit if reactor is in a deeper subcriticality, which means calculated alpha is smaller than true value in number axis. The determination of adjusting parameter is a little arbitrary based on various calculation conditions. Once confirmed, it shall not change in the running.

3. MCNP TIME FITTING

In time dependant transportation equation, neutron density or flux has the formal solution,⁵

$$N(\vec{r}, \vec{\Omega}, E, t) = \sum_{j=0} N_j(\vec{r}, \vec{\Omega}, E) \times e^{\alpha_j t} \quad (3)$$

In a subcritical system, all α_j values are negative. We assume α_j 's absolute values increase with increasing j . And α_0 is the largest one, the fundamental time constant. If we add a pulse source at zero time, the neutron's time distribution will start a buildup in the beginning, then drop to multiple decay mode which has nothing to do with source anymore.

By integrating volume, solid angle and energy, the current term becomes leakage term. But its time behavior still follows formula (3). which means we can use MCNP's tally option, F1, to count leakage neutrons' time distribution as system's time distribution. Then, we use formula (3) to fit time distribution to get multiple time constants. The fitting coefficients are time-independent flux corresponding to each decay mode. However, the coefficient, N_j , is not concerned in this work.

With enough neutron source particles (NPS) and adequate time, MCNP F1 tally can explain Rossi- α measurement well in the vicinity of delayed critical. At this point, MCNP F1 tally is doing the same thing

as Rossi- α does. The difference is Rossi- α has background term, which is not easy to get rid of from experimental counts, and will conceal the lower decay modes, especially α_0 , in a deeper subcritical system with a thermal reflector. To the contrary, MCNP F1 tally can display all lower decay modes without interference of background term. So, MCNP F1 tally can be seen as an imaginary Rossi- α measurement in computer.

4. 2G2R MODEL

We adopt the conventional diffusion approximation to deal with a two-region system consisting of a core surrounded by a non-multiplying, source-free reflector.¹ The simplified model can be described as the following set of two-group coupled differential equations.

$$\begin{pmatrix} \frac{d\phi_{1c}}{\nu_{1c} dt} \\ \frac{d\phi_{2c}}{\nu_{2c} dt} \\ \frac{d\phi_{1r}}{\nu_{1r} dt} \\ \frac{d\phi_{2r}}{\nu_{2r} dt} \end{pmatrix} = \begin{pmatrix} -B_c^2 D_{1c} + (1 - \beta_{eff}) \nu \Sigma_{f_{1c}} - \Sigma_{r_{1c}} & (1 - \beta_{eff}) \nu \Sigma_{f_{2c}} & B_r^2 D_{1r} f_{rc_{11}} & 0 \\ \Sigma_{s_{12c}} & -B_c^2 D_{2c} - \Sigma_{a_{2c}} & 0 & B_r^2 D_{2r} f_{rc_{22}} \\ B_c^2 D_{1c} f_{cr_{11}} & 0 & -B_r^2 D_{1r} - \Sigma_{r_{1r}} & 0 \\ 0 & B_c^2 D_{2c} f_{cr_{22}} & \Sigma_{s_{12r}} & -B_r^2 D_{2r} - \Sigma_{a_{2r}} \end{pmatrix} \begin{pmatrix} \phi_{1c} \\ \phi_{2c} \\ \phi_{1r} \\ \phi_{2r} \end{pmatrix} \quad (4)$$

Where subscript 1 represents the fast group ($E > 1eV$), and 2 represents thermal group ($E < 1eV$). c means core, and r means reflector. For simplification, we only include effective fraction of delayed neutrons, β_{eff} , in set of equations.

After Laplace transformation, we can get inhour equation,

$$\left[(\omega l_{1c} + 1 - k_{1c} (1 - \beta_{eff})) (\omega l_{1r} + 1) - f_{11} \right] \times \left[(\omega l_{2c} + 1) (\omega l_{2r} + 1) - f_{22} \right] - k_{2c} (1 - \beta_{eff}) [(\omega l_{1r} + 1) (\omega l_{2r} + 1) k_{s_{12c}} + f_{12}] = 0 \quad (5)$$

In most reflected systems, the thermal neutron's number is a few orders smaller than fast neutron's number, which leads to a neglectable $f_{22} (\approx 0)$. And average thermal neutron's lifetime is sufficiently small such that $\omega_j l_{2c} \ll 1$ for all possible j roots. Introducing the definition of reactivity, the inhour equation can be rewritten as

$$\omega \frac{l_{1c}}{k_c + \Delta} - \omega \frac{f_{11} l_{1r}}{(\omega l_{1r} + 1)(k_c + \Delta)} - \frac{f_{12} k_{2c} (1 - \beta_{eff})}{k_c + \Delta} \left[1 - \frac{1}{(\omega l_{1r} + 1)(\omega l_{2r} + 1)} \right] = 1 - \beta_{eff} - \frac{1 - f_{11}}{k_c + \Delta} = \rho - \beta_{eff} \quad (6)$$

In many cases, f_{22} and $k_{s_{12c}}$ can be neglected and l_{2r} is very large such that $\omega_j l_{2r} \gg 1$, then the inhour equation is back to Spriggs model shape with one feedback constant, and only describe fast neutron's time constant. But we will lose a root related with l_{2r} by this simplification. It is better to resolve cubic equation

$$\left[(\omega l_{1c} + 1 - k_{1c} (1 - \beta_{eff})) (\omega l_{1r} + 1) - f_{11} \right] \times (\omega l_{2r} + 1) - k_{2c} (1 - \beta_{eff}) f_{12} = 0 \quad (7)$$

with determined coefficients calculated by MCNP code.

5. MODEL CALCULATIONS

Because we don't have experimental data to test the 2G2R model, a benchmark model, PU-MET-FAST-024,⁶ is chosen as preliminary test. A summary of the reactor is given in Table I. And 3 different models do the same calculations for comparison between them. One model, MCNP time fitting, is regarded as imaginary experiment because of similarity with Rossi- α measurement. All results are listed below.

Table I: Simplified *PUT-MET-FAST-024* Reactor Description ⁶

Region/Dimension	Material	Atom Density($\times 10^{-24}$) cm^{-3}
Core (spherical) 6cm radius	²³⁹ Pu	3.6620×10^{-2}
	²⁴⁰ Pu	6.6944×10^{-4}
	Ga	2.1962×10^{-3}
	Fe	1.4126×10^4
	O	2.8972×10^{-4}
	Ni	1.9748×10^{-3}
Reflector (spherical shell) 1.55cm thick	C	3.8814×10^{-2}
	H	7.7616×10^{-2}
	D	1.1644×10^{-5}

Table II: Integral Quantities with different reflector thick

Model / Reflector's thick	0cm Bare Reactor	0.6cm	1.0cm	1.55cm
k_{eff}				
MCNP	0.92311	0.95323	0.97277	0.99823
Fundamental Time Constant, α_0 (μs^{-1})				
Alpha Static Method	-25.88	-2.372	-0.45	-0.035
MCNP Time Fitting	-29.48	-1.23	-0.53	-0.038
Spriggs Model ^a	-22.43	-10.0	-3.68	-0.16
2G2R Model ^a	-22.40	-0.57	-0.26	-0.20
Secondary Time Constant, α_1 (μs^{-1})				
MCNP Time Fitting	—	-8.26	-5.10	-0.37
2G2R Model	—	-10.21	-4.55	-0.82

a— $\beta_{eff}=0.0023$ is taken.

Figures a to d display the MCNP time fitting results. Fig. a is for bare system, and Fig. d is for critical system. In Fig. b and c, neutron counts shows a sharp drop of 2 orders in a few microseconds and still do not enter the fundamental decay mode. Rossi- α measurement will be difficult to get the fundamental mode for such reactors, because secondary decay mode is dominant and background neutrons cover and destroy the fundamental decay mode.

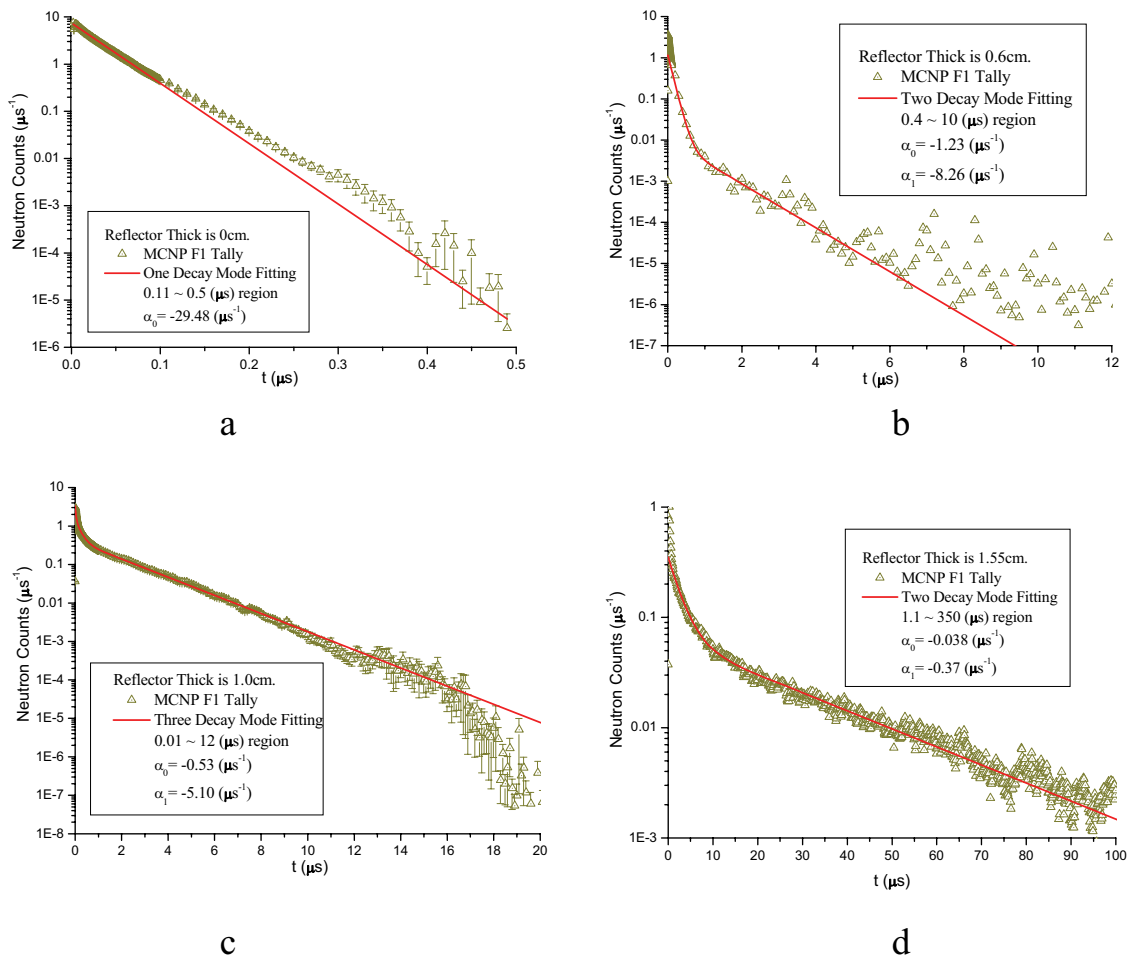


Fig. a. Leakage neutron time distribution and its fitting with 0cm-thick reflector.
 Fig. b. Leakage neutron time distribution and its fitting with 0.6cm-thick reflector.
 Fig. c. Leakage neutron time distribution and its fitting with 1.0cm-thick reflector.
 Fig. d. Leakage neutron time distribution and its fitting with 1.55cm-thick reflector.

6. DISCUSSION

Comparing the results given in Table II, we can see that all 2 time constants of 2G2R model are close to MCNP time fitting method, the imaginary experiments. Two reasons contribute much to this. Firstly, two-group calculation is included in 2G2R model. Second, all coupling parameters from Spriggs model are determined by MCNP running.

At the same time, fundamental time constants calculated by Spriggs model results are close to MCNP time fitting for critical and bare system, and are not for two systems in the middle. Two middle systems' results are close to MCNP time fitting's secondary time constant. These two features can be explained that Spriggs model's time constant reflect the dominant time decay behavior which may not be the fundamental decay mode.

Though alpha static method (MCNP4C) 's results are close to MCNP time fitting, the convergence of k' in alpha static equation (1) or (2) is departure from unit with a few percent error for two middle systems, which strongly lowers the results of alpha static method.

According to the discussion above, 2G2R model provides a simple way to analyze multiple time decay modes quantitatively.

REFERENCES

- [1]. G. D. Spriggs et al., “Two-Region Kinetic Model for Reflected Reactor”, *Ann. Nucl. Energy*, **24**, 205, (1997).
- [2]. Judith F. Briesmeister, “MCNPTM-A General Monte Carlo N – Particle Transport Code”, LA-13709-M, Arpi. 10, (2001).
- [3]. Dermott E. Cullen, “TART 2002: A Coupled Neutron-Photon 3-D Combinatorial Geometry, Time Dependent Monte Carlo Transport Code”, UCRL-ID-126455, Rev. 4, June (2003).
- [4]. Dermott E. Cullen et al., “Static and Dynamic Criticality: Are They Different?”, UCRL-TR-201506, Nov. 22, (2003).
- [5]. G. I. Bell, S. Glasstone, *Nuclear Reactor Theory*, Van Nostrand, Princeton, N. J., (1970).
- [6]. M. V. Gorbatenko et al., “Polyethylene-Reflected Spherical Assembly of ²³⁹PU(δ , 98%)”, Vol. I, NEA/NSC/DOC/(95).

APPENDIX Effective multiplication factor, k_{eff}

To calculate effective multiplication factor, k_{eff} , we resolve the set of equations below,

$$\begin{vmatrix} -B_c^2 D_{1c} + \frac{1}{k_{eff}}(1 - \beta_{eff})\nu\Sigma_{f_{1c}} - \Sigma_{r_{1c}} & \frac{1}{k_{eff}}(1 - \beta_{eff})\nu\Sigma_{f_{2c}} & B_r^2 D_{1r} f_{rc_{11}} & 0 \\ \Sigma_{s_{12c}} & -B_c^2 D_{2c} - \Sigma_{a_{2c}} & 0 & B_r^2 D_{2r} f_{rc_{22}} \\ B_c^2 D_{1c} f_{cr_{11}} & 0 & -B_r^2 D_{1r} - \Sigma_{r_{1r}} & 0 \\ 0 & B_c^2 D_{2c} f_{cr_{22}} & \Sigma_{s_{12r}} & -B_r^2 D_{2r} - \Sigma_{a_{2r}} \end{vmatrix} = 0 \quad (A1)$$

The effective multiplication factor, k_{eff} and k_c are,

$$\begin{aligned} k_{eff} &= \frac{1}{(1 - f_{11})} \left[\frac{\nu\Sigma_{f_{1c}}/\Sigma_{r_{1c}}}{1 + \tau_1 B_c^2} + \frac{\nu\Sigma_{f_{2c}}/\Sigma_{a_{2c}}}{(1 + \tau_2 B_c^2)(1 - f_{22})} \left(\frac{\Sigma_{s_{12c}}/\Sigma_{r_{1c}}}{1 + \tau_1 B_c^2} + f_{12} \right) \right] \\ &= \frac{1}{(1 - f_{11})} \left[k_{1c} + \frac{k_{2c}(k_{s_{12c}} + f_{12})}{(1 - f_{22})} \right] \approx \frac{k_c + \Delta}{(1 - f_{11})} \end{aligned} \quad (A2)$$

$$k_c = k_{1c} + k_{2c} k_{s_{12c}} = \frac{\nu\Sigma_{f_{1c}}/\Sigma_{r_{1c}}}{1 + \tau_1 B_c^2} + \frac{\nu\Sigma_{f_{2c}}/\Sigma_{a_{2c}}}{1 + \tau_2 B_c^2} \frac{\Sigma_{s_{12c}}/\Sigma_{r_{1c}}}{1 + \tau_1 B_c^2} \quad (A3)$$

3.10 Design of MA-loaded Core Experiments using J-PARC

Takanori SUGAWARA^{*1}, Kazuteru SUGINO² and Toshinobu SASA¹

¹ Nuclear Transmutation Technology Group, Japan Atomic Energy Agency,
Shirakata Shirane 2-4, Tokai-mura, Naka-gun, Ibaraki, Japan

² Reactor Physics Analysis and Evaluation Group, Japan Atomic Energy Agency,
Narita-machi 4002, Oarai, Ibaraki, Japan

* E-mail: sugawara.takanori@jaea.go.jp

Uncertainties of the current minor actinide (MA) nuclear data are larger than those of other major nuclides. Therefore, analyzed neutronic properties of MA-loaded fast reactor (FR) and accelerator driven system (ADS) have much larger design margins in comparison with those of conventional FR. To improve the reliability, safety and economical efficiency of these systems, it is required to increase the accuracy of the nuclear data of MA by the experimental data taken by adequate experimental conditions.

In this study, error analyses were performed to estimate “How much would the error caused by the MA nuclear data decrease if the MA-loaded core experiments were performed”. TEF-P (Transmutation Physics Experimental Facility), which is being planned to carry out basic experiments for MA-loaded systems in JAEA, was employed to simulate hypothetical MA-loaded core experiments. For the estimation, the cross section adjustment procedure was employed.

These analysis results showed that the errors caused by the nuclear data were improved by considering existing 233 integral data and 7 hypothetical results simulating TEF-P experiments. As a typical result, the errors (the confidence level is 1σ) for the coolant void reactivity were improved from 2.4% to 1.4% for MA-loaded FR and from 5.8% to 3.0% for ADS designed by JAEA.

1. Introduction

Research and development (R&D) for minor actinide (MA) transmutation technologies by using Fast Reactor (FR) and Accelerator Driven System (ADS) have been performed at Japan Atomic Energy Agency (JAEA). Improvement on the neutronic design accuracy of the MA-loaded core is one of the most important issues in the MA transmutation technology. Uncertainties of the current MA nuclear data are larger than those of other major nuclides. Therefore, analyzed neutronic properties of MA-loaded FR and ADS have much larger design margins in comparison with those of conventional FR. To improve the reliability, safety and economical efficiency of these systems, it is required to increase the accuracy of the nuclear data of MA by the experimental data taken by adequate experimental conditions.

JAEA plans a construction of “TEF-P” (Transmutation Physics Experimental Facility) in the second

phase of the “J-PARC” (Japan Proton Accelerator Research Complex) project. TEF-P is a plate-type fuelled critical assembly which is able to accept a proton beam (400MeV, 10W) delivered from a LINAC of J-PARC. Various experiments are available in a critical condition or a sub-critical state driven by spallation neutrons. Furthermore, the experiments using pin-type MA fuel, which must be handled with remote devices, are planned to simulate the MA-loaded systems.

In this study, error analyses were performed to estimate “How much would the error caused by the MA nuclear data decrease if the MA-loaded core experiments at TEF-P were performed”. In this estimation, the cross-section adjustment procedure was employed.

2. Procedure to estimate Errors caused by Nuclear Data

The error analyses were performed by the cross-section adjustment procedure [1]. This procedure adjusts the nuclear data to reduce the errors caused by the nuclear data and makes it possible to estimate the errors quantitatively. Figure 1 shows a simplified schematic of this procedure (details are described in the reference [1]). Existing nuclear data (cross section \mathbf{T} and covariance data \mathbf{M}) such as JENDL-3.3 are adjusted by the Bayesian theorem by using sensitivity \mathbf{G} , analytical modeling error \mathbf{V}_m and experimental error \mathbf{V}_e for 233 integral data [1]. The adjusted nuclear data \mathbf{T}' and \mathbf{M}' are calculated as an output.

In this theory, the errors caused by the nuclear data are defined as \mathbf{GMG}^t (t means a transpose). So, it is available to compare the errors before the adjustment (\mathbf{GMG}^t) and after the adjustment by the 233 integral data ($\mathbf{GM}'\mathbf{G}^t$). This procedure also enables to assess the effect of hypothetical experiments. In this study, seven hypothetical MA experiment data at TEF-P were added to the 233 integral data to estimate “How much would the error caused by the MA nuclear data decrease”. New adjusted nuclear data \mathbf{T}'' and \mathbf{M}'' were calculated and the error caused by the new data ($\mathbf{GM}''\mathbf{G}^t$) was estimated.

3. Calculation Conditions

(1) Hypothetical MA experiments

To simulate hypothetical MA experiments, the FCA XVII-1 core [2] which was a mock-up of a MOX fuelled fast reactor was referred. Figure 2 shows the RZ calculation model of the TEF-P core. The characteristic and difference against the FCA core of the TEF-P are that it is available to treat the pin-type MA fuel. The MA fuel pin was loaded in the TEST region. In this study, a MA-loaded FR and an ADS were treated for the error analyses. For the FR analysis, U/Pu/MA(=77.4/17.6/5.0 wt%) oxide fuel pin surrounded by Na was set to the TEST region. Pu/MA(31/69 wt%) nitride fuel surrounded by Pb-Bi was set to the TEST region for the ADS analysis. The composition of MAs was Np-237/Am-241/Am-243/Cm-244 = 11.1/44.4/22.2/22.2 wt% through this study.

In these calculations, the sensitivity was calculated by the SAGEP code [3] with 18 energy group structure. Seven calculation cases shown in Table 1 were performed; for a criticality, for a coolant void reactivity and a Doppler reactivity. The analytical modeling error and the experimental errors were determined based on the FCA XVII-1 experiments described in the reference [1].

(2) Object of estimation

In this study, the errors included in neutronic designs of the MA-loaded FR and the ADS were estimated. The 1600MWt sodium cooled FR core studied in the feasibility study [4] was employed as a typical FR. Figure 3 shows the RZ calculation model of the FR core. 5 wt% MAs were added to the inner and outer core region. The 800MWt LBE (lead bismuth eutectic) cooled ADS designed by JAEA [5] was employed as a typical ADS core (Fig. 4). The sensitivities for the criticality, the coolant void reactivity (coolant volume fraction at the driver region was changed to 0%) and the Doppler reactivity ($\Delta T=500\text{K}$ at the driver region) were calculated for both cores by SAGEP code.

(3) Nuclides and reactions for adjustment

In this study, nuclides and reactions whose covariance data were prepared in JENDL-3.3 were treated for the adjustment. Table 2 and Table 3 show the nuclides and reactions which were adjusted for the FR and the ADS, respectively. As shown in these tables, covariance data for elastic and inelastic reactions of MAs are not prepared in JENDL-3.3. Additionally, many covariance data which are important to analyze the errors of the ADS are not prepared; such as capture and elastic reactions for Pb isotopes and Bi-209, capture and inelastic reactions for N-15. In the present study, these nuclides and reactions which were not prepared in JENDL-3.3 were not considered; in other words, errors caused by these nuclides and reactions were not included in present results.

4. Results and Discussion

The errors caused by the nuclear data are summarized in Table 4 for the FR and Table 5 for the ADS. Figure 5-10 show the contributions of the nuclides and the reactions to the errors caused by the nuclear data for each case. For the FR, the effect of the TEF-P experiments was shown as the improvement of the error for Am-241 and Cm-244 capture reaction mainly though the changes (from 233 to 240) of the total error were small for all cases.

For the ADS, the total error was decreased by the TEF-P experiments from 0.74% to 0.68% (from 233 to 240) for the criticality, from 3.8% to 3.0 for the coolant void reactivity and from 4.0% to 2.8% for the Doppler reactivity. For the criticality, the changes of the errors for Am-241 capture reaction, N-15 elastic reaction and inelastic reactions of the Pb isotopes and Bi-209 were prominent (Fig. 6). For the coolant void, the changes of the errors for Am-241 and Am-243 capture reactions, N-15 elastic reaction and inelastic reactions of the Pb isotopes and Bi-209 were significant (Fig. 8). For the Doppler reactivity, the changes of the errors for Am-241 and Am-243 capture reactions, N-15 elastic reaction and capture reactions of Fe and Zr-40 were impressive (Fig. 10).

However, the results for the ADS are not exact since the covariance data of many nuclides and reactions, such as elastic and inelastic reactions for MAs, capture and elastic reactions for the Pb isotopes and Bi-209 and capture and inelastic reactions for N-15 (Table 3), are not prepared as described above. To perform more correct estimations, more experiments and estimations for MAs and other nuclides should be carried out and an expansion of the covariance data is important.

5. Conclusion

The error analyses were performed to estimate “How much would the error caused by the MA nuclear data decrease if the MA-loaded core experiments at TEF-P were performed”. In this estimation, the cross-section adjustment procedure was employed for the FR and the ADS. The seven hypothetical TEF-P experiments were calculated and the sensitivities were used in the cross-section adjustment procedure.

These results showed that the TEF-P experiments with MA fuel were effective to improve the accuracy of the neutronic design for MA-loaded systems. For the ADS, the errors caused by the nuclear data were changed from 0.74% to 0.68% for the criticality, from 3.8% to 3.0% for the coolant void reactivity and from 4.0% to 2.8% for the Doppler reactivity (from 233 to 240 int. data). On the other hand, these results were unable to reduce the margins in the neutronic designs for the MA-loaded systems since the covariance data for elastic and inelastic reactions for MAs were not considered. For the present ADS design, the covariance data for capture and elastic reactions of Pb isotopes and Bi-209, capture and inelastic reactions of N-15 and all reactions for Zr isotopes were also required since the quantities of these nuclides were very large in the present design. More experiments for MAs and other nuclides are important, and the expansion of the covariance data is also necessary.

References

- [1] T. Hazama, G. Chiba, K. Numata and W. Sato, *Development of the Unified Cross-section Set ADJ2000R for Fast Reactor Analysis*, JNC TN9400 2002-064, Japan Nuclear Cycle Development Institute (JNC), (2002), (In Japanese).
- [2] H. Oigawa, S. Iijima, T. Sakurai, *et al.*, “A Proposal of Benchmark Calculation on Reactor Physics for Metallic Fueled and MOX Fueled LMFBR Based upon Mock-up Experiment at FCA”, *J. Nucl. Sci. and Technol.*, **37**[2], 186, (2000).
- [3] A. Hara, T. Takeda and Y. Kikuchi, *SAGEP: Two-Dimensional Sensitivity Analysis Code Based on Generalized Perturbation Theory*, JAERI-M 84-027, Japan Atomic Energy Research Institute (JAERI), (1984), (In Japanese).
- [4] JAEA, *Feasibility Study on Commercialized Fast Reactor Cycle Systems - (1) Fast Reactor Plant Systems -*, JAEA-Research 2006-042, Japan Atomic Energy Agency (JAEA), (2006), (In Japanese).
- [5] K. Tsujimoto, T. Sasa, K. Nishihara, *et al.*, “Neutronics Design for Lead-Bismuth Cooled Accelerator-Driven System for Transmutation of Minor Actinide”, *J. Nucl. Sci. and Technol.*, **41**[1], 21, (2004).

Table 1: Calculation cases for hypothetical MA experiments at TEF-P

Cases	Analytical modeling error $V'm$ [%]	Experimental error $V'e$ [%]
Criticality	0.04	0.2
Void reactivity (1-3z)	1.0	5.0
Void reactivity (1-6z)	2.0	5.0
Void reactivity (1-9z)	3.0	10.0
Doppler reactivity (573K)	3.0	3.5
Doppler reactivity (823K)	3.0	4.0
Doppler reactivity (1073K)	3.0	4.5

Table 2: Nuclides and reactions for adjustment (FR)

Nuclide	Capture	Fission ν	Elastic	Inelastic χ	μ	-bar
U-235	○	○	○	○	○	○
U-238	○	○	○	○	○	○
Pu-238	○	○	○	○	○	○
Pu-239	○	○	○	○	○	○
Pu-240	○	○	○	○	○	○
Pu-241	○	○	○	○	○	○
Pu-242	○	○	○	○	○	○
Np-237	○	○	○	○	○	○
Am-241	○	○	○	○	○	○
Am-243	○	○	○	○	○	○
Cm-244	○	○	○	○	○	○
O	○	-	-	○	○	-
Fe	○	-	-	○	○	-
Cr	○	-	-	○	○	-
Ni	○	-	-	○	○	-
Na	○	-	-	○	○	-

Table 3: Nuclides and reactions for adjustment (ADS)

Nuclide	Capture	Fission ν	Elastic	Inelastic χ	μ	-bar
Pu-238	○	○	○	○	○	○
Pu-239	○	○	○	○	○	○
Pu-240	○	○	○	○	○	○
Pu-241	○	○	○	○	○	○
Pu-242	○	○	○	○	○	○
Np-237	○	○	○	○	○	○
Am-241	○	○	○	○	○	○
Am-242m	○	○	○	○	○	○
Am-243	○	○	○	○	○	○
Cm-244	○	○	○	○	○	○
N-15	○	-	-	○	-	-
Fe	○	-	-	○	○	-
Cr	○	-	-	○	○	-
Ni	○	-	-	○	○	-
Zr-40	○	-	-	○	-	-
Pb-206	○	-	-	○	-	-
Pb-207	○	-	-	○	-	-
Pb-208	○	-	-	○	-	-
Bi-209	○	-	-	○	-	-

Table 4: Errors caused by nuclear data (FR)

unit [%]	Before Adjustment	After Adjustment by 233 int. data	After Adjustment by 240 (233+TEF-P) int. data
Criticality	1.06	0.30	0.27
Coolant Void Reactivity	2.43	1.57	1.36
Doppler Reactivity	3.76	2.16	1.71

Table 5: Errors caused by nuclear data (ADS)

unit [%]	Before Adjustment	After Adjustment by 233 int. data	After Adjustment by 240 (233+TEF-P) int. data
Criticality	1.08	0.74	0.68
Coolant Void Reactivity	5.80	3.82	2.98
Doppler Reactivity	4.92	3.99	2.77

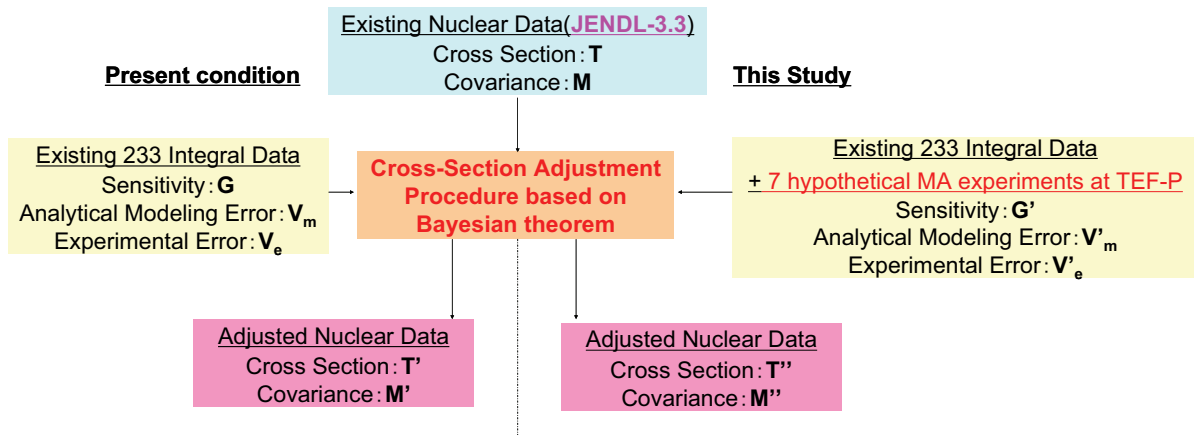


Fig. 1: Procedure to estimate errors caused by nuclear data

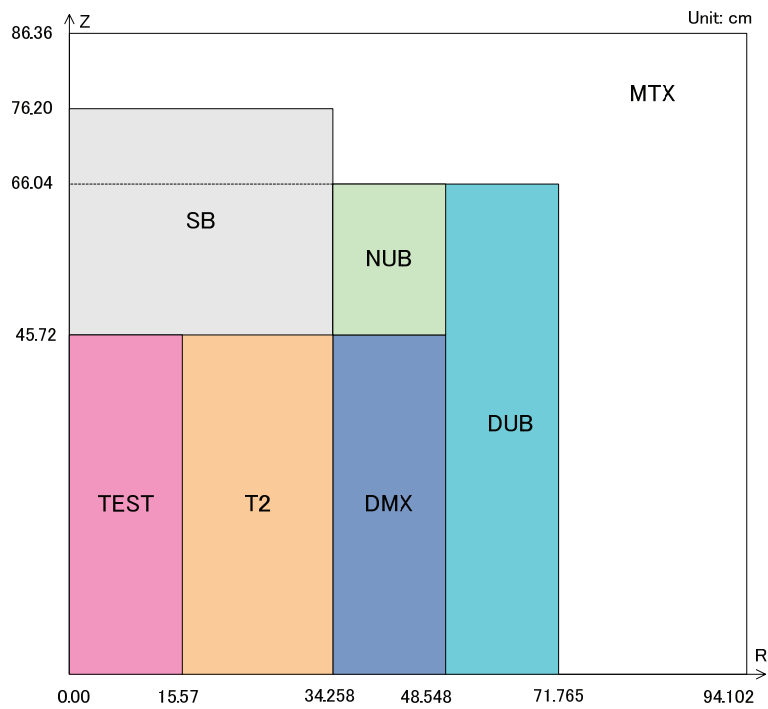


Fig. 2: RZ model of TEF-P core

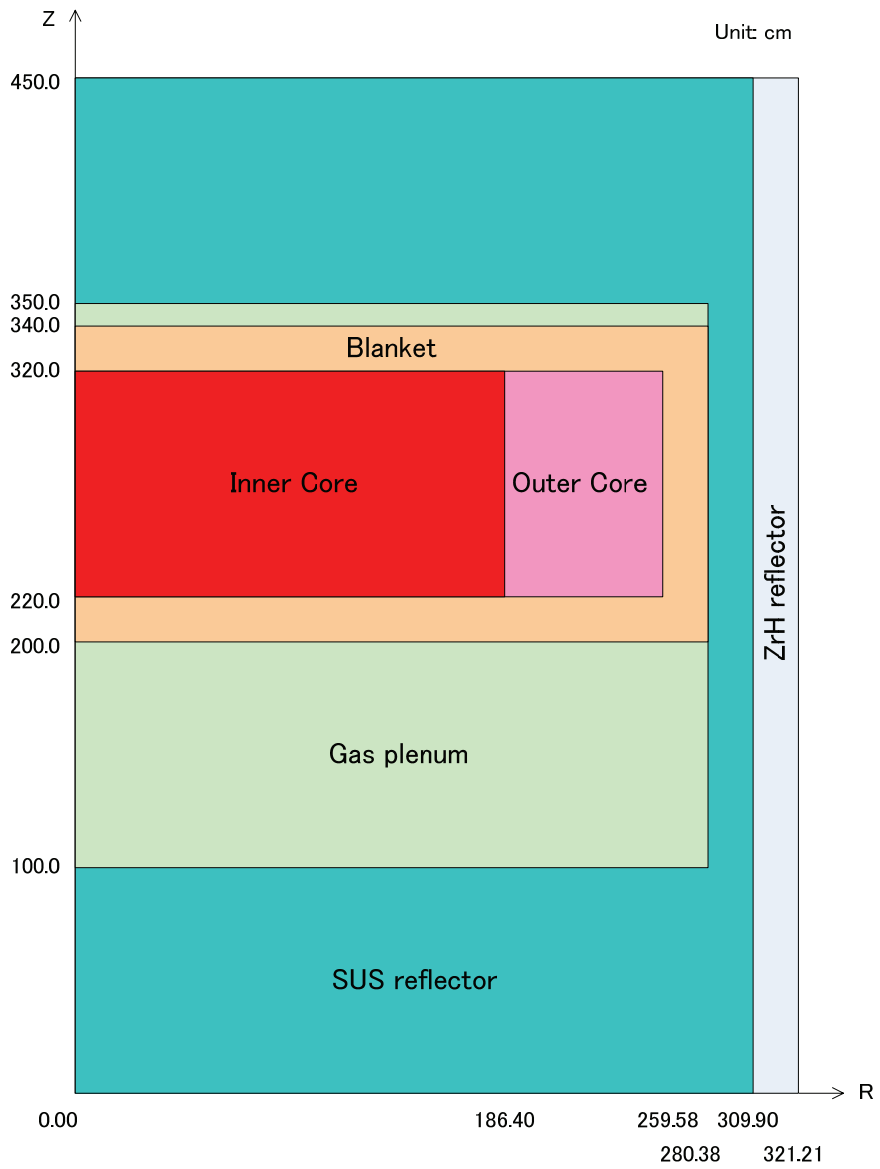


Fig. 3: RZ model of FR core

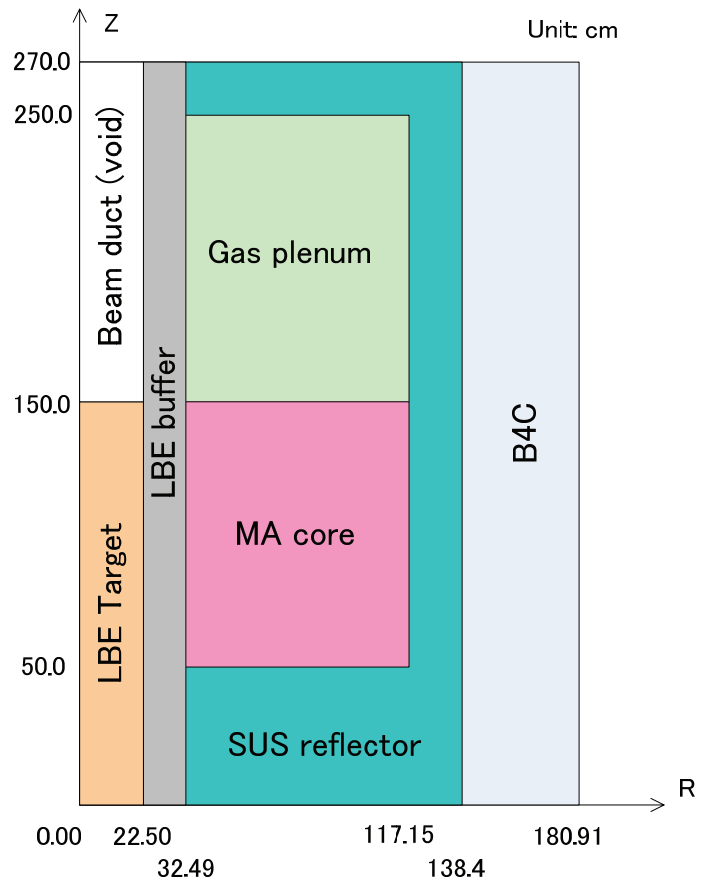


Fig. 4: RZ model of ADS core

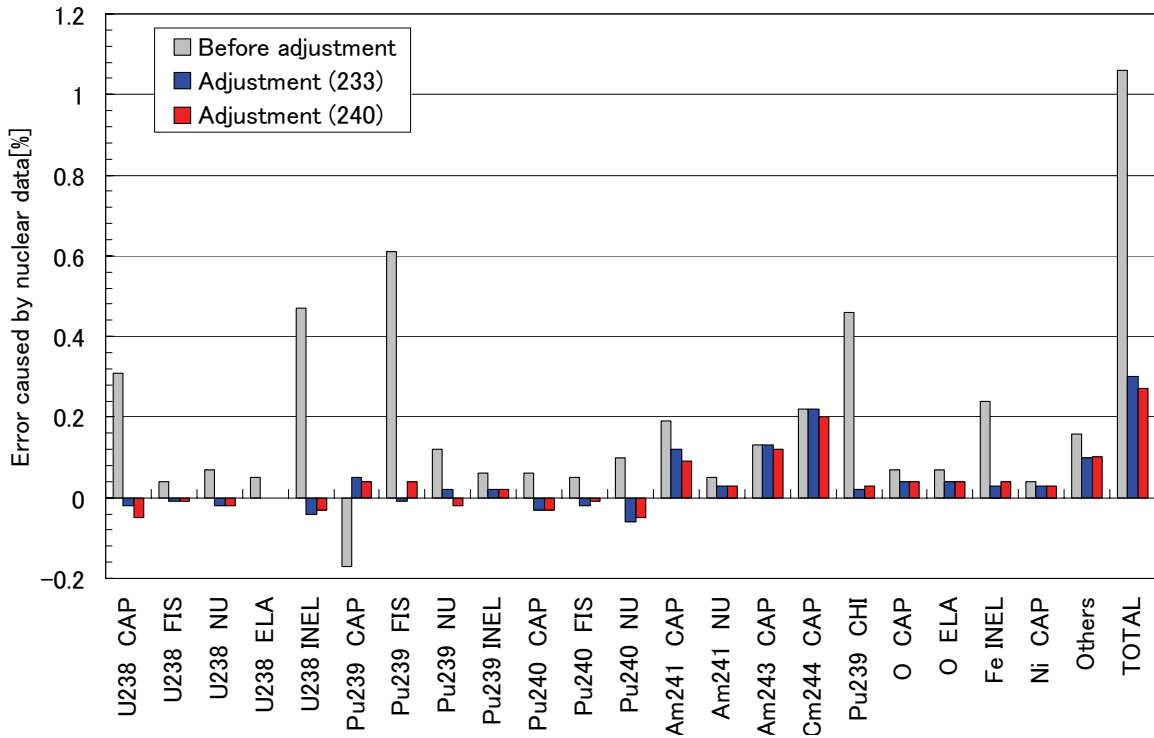


Fig. 5: Contribution of nuclides and reactions to errors caused by nuclear data (criticality, FR)

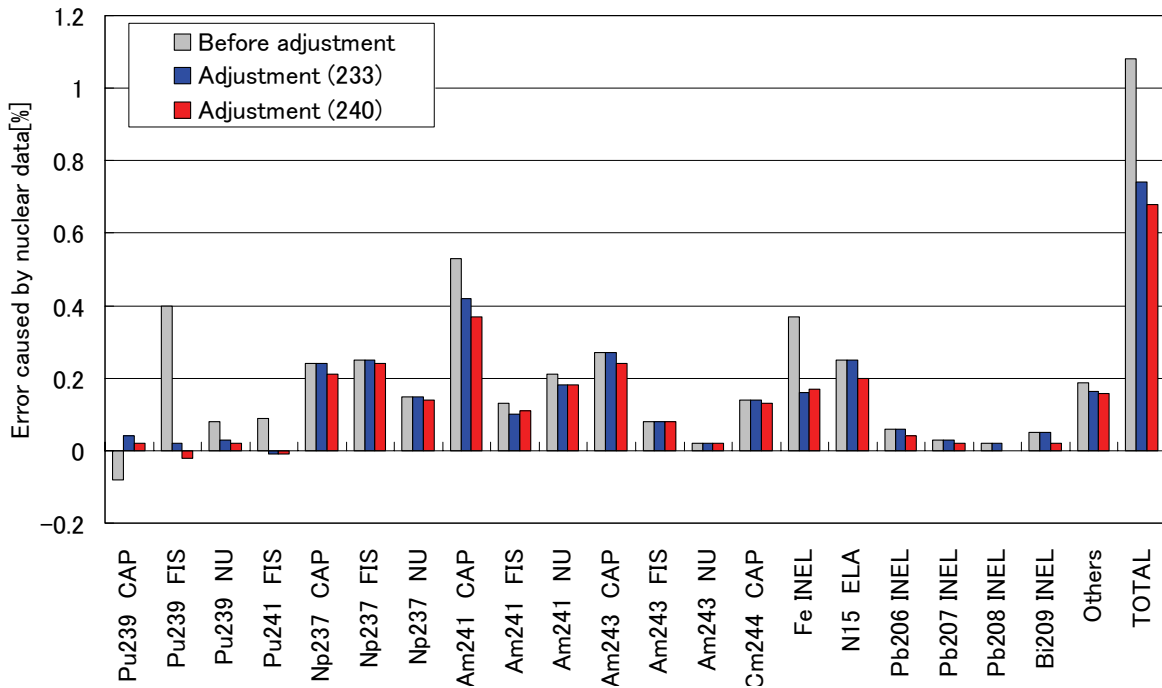


Fig. 6: Contribution of nuclides and reactions to errors caused by nuclear data (criticality, ADS)

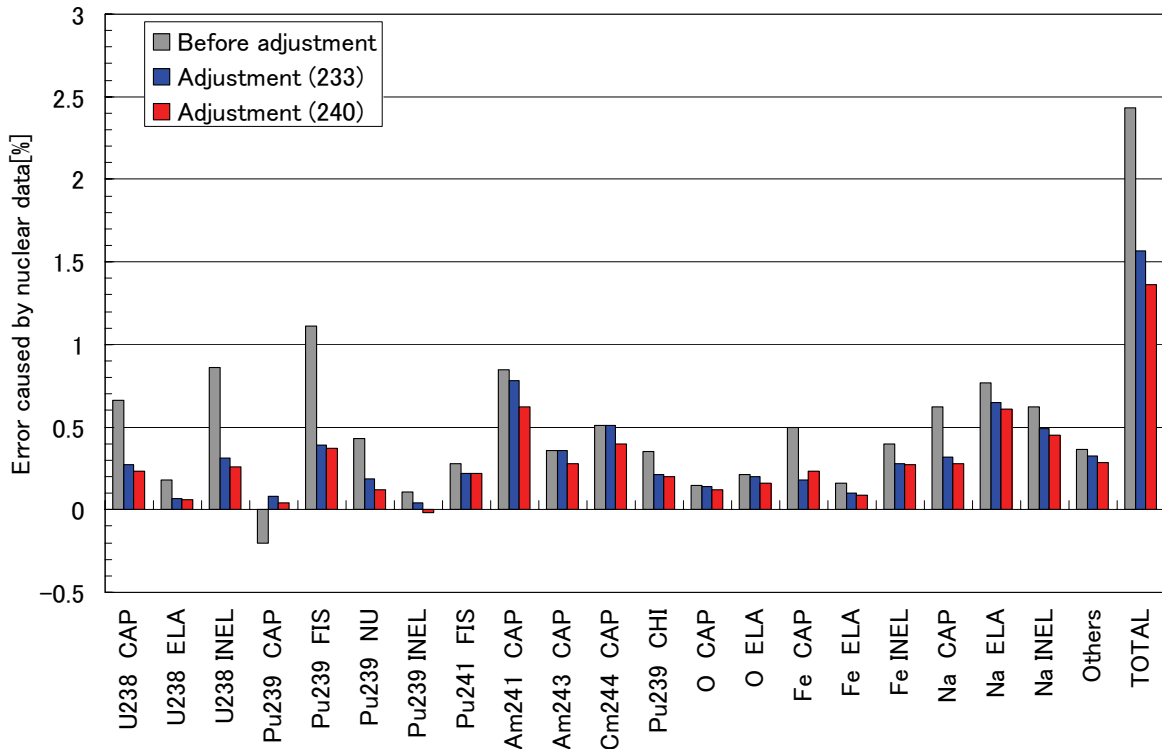


Fig. 7: Contribution of nuclides and reactions to errors caused by nuclear data (coolant void reactivity, FR)

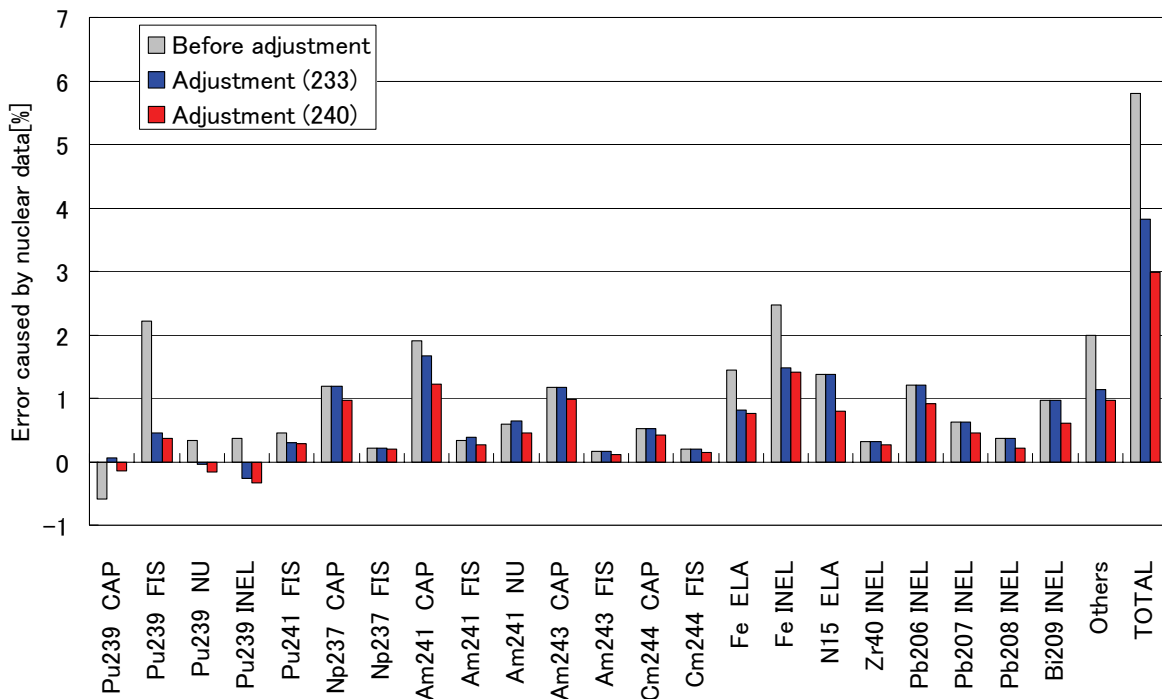


Fig. 8: Contribution of nuclides and reactions to errors caused by nuclear data (coolant void reactivity, ADS)

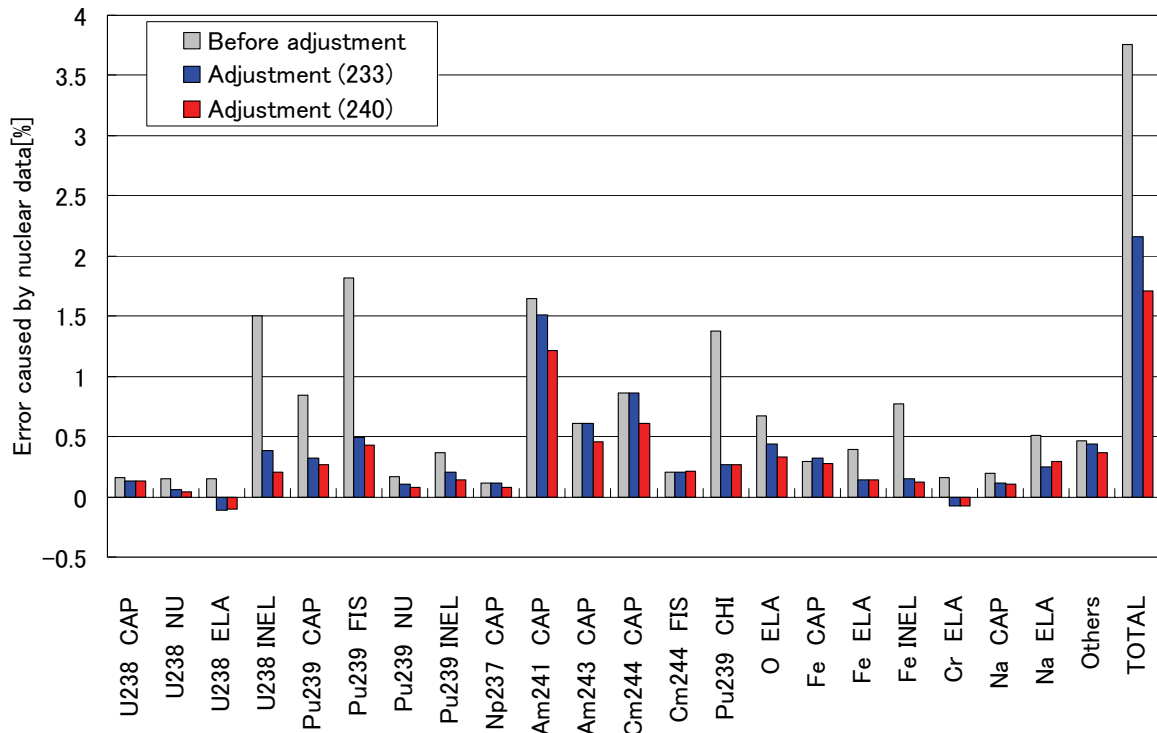


Fig. 9: Contribution of nuclides and reactions to errors caused by nuclear data (Doppler reactivity, FR)

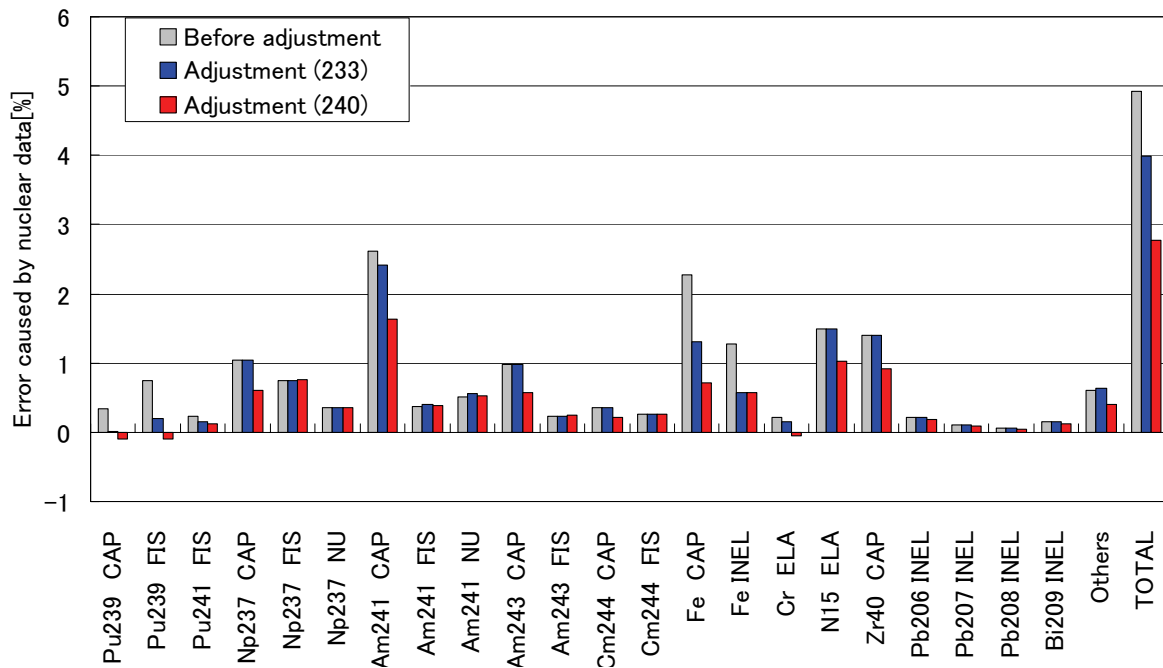


Fig. 10: Contribution of nuclides and reactions to errors caused by nuclear data (Doppler reactivity, ADS)

3.11 Analyses of Benchmark Experiments at FNS with Recent Nuclear Data Libraries

Kentaro Ochiai¹, Satoshi Sato¹, Masayuki Wada² and Chikara Konno¹

¹Fusion Research and Development Directorate, Japan Atomic Energy Agency
Tokai-mura, Naka-gun, Ibaraki-ken 319-1195 Japan
e-mail : ochiai.kentaro@jaea.go.jp

²Startcom Co., Ltd.
4-18-10, Hayamiya, Nerima-ku, Tokyo 179-0085 Japan

Integral benchmark experiments for nuclear data verification carried out at JAEA FNS have been analyzed with MCNP-4C and the recent nuclear data libraries; JENDL-3.3, FENDL-2.1, JEFF-3.1 and ENDF/B-VII.0. In this paper the results for the experiments for SiC and Iron were discussed and compared each other.

1. Introduction

For a few years several nuclear data libraries, JENDL-3.3 [1], FENDL-2.1 [2], JEFF-3.1 [3] and ENDF/B-VII.0 [4], have been newly released.

- JENDL-3.3 was released in May, 2002.
- FENDL-2.1 was released in December, 2004.
- JEFF-3.1 was released in May, 2005.
- ENDF/B-VII.0 was released in December, 2006.

It is essential to verify these libraries through analyses of integral benchmark experiments. Many integral benchmark experiments for nuclear data verification have been carried out at JAEA/FNS [5-7]. Thus we analyzed these experiments with JENDL-3.3, FENDL-2.1, JEFF-3.1 and ENDF/B-VII.0 and the results were compared each other.

2. Overview of integral benchmark experiments at JAEA/FNS

Two types of integral benchmark experiments for nuclear data verification with DT neutrons have been performed for long time at JAEA/FNS. One is a Time-of-flight (TOF) experiment, the other is an in-situ measurement experiment.

In the TOF experiments angular neutron spectra above ~ 50 keV leaking from slabs

were measured at several angles. So far they were done for lithium oxide, beryllium, graphite, nitrogen, oxygen, iron, copper and lead slabs changing the slab thickness.

In the in-situ measurement experiments neutron spectra over almost the whole energy region, reaction rates for several dosimetry reactions, fission rates, gamma-ray spectra, gamma-ray heating, etc. were measured inside slabs. So far they were done for lithium oxide, lithium aluminate, lithium titanate, lithium zirconate, beryllium, graphite, SiC, vanadium, iron, SS316, copper, tungsten.

3. Calculation method

The Monte Carlo code MCNP-4C [8] was used for this analysis. The following ACE files were adopted for the present analyses.

- JENDL-3.3 : ACE files supplied from JAEA Nuclear Data Center processed with NJOY99.67 [9] and local patch [10].
- FENDL-2.1 : ACE files supplied from IAEA Nuclear Data Services processed with NJOY99.90 and local patch [11].
- JEFF-3.1 and ENDF/B-VII.0 : ACE files processed with NJOY99.161 for ourselves.

4. Results and discussions

We have too many results of the analyses for integral benchmark experiments at JAEA/FNS to show all of them in this symposium. The results of the in-situ measurement experiments only for SiC and iron, where differences among the results with recent nuclear data libraries are rather large, are described here. All the results will be published in JAEA-Data/Code or so.

1) In-situ measurement experiment for SiC

Figure 1 shows ratios of calculation value to experimental one (C/E) for the reaction rate of $^{93}\text{Nb}(n,2n)^{92\text{m}}\text{Nb}$ which is sensitive to neutrons above 10 MeV. The calculations with JENDL-3.3 and ENDF/B-VII.0 agree with the measurement within 5 %, while that with JEFF-3.1 overestimates the measurement and that with FENDL-2.1 tends to underestimate the measurement slightly. Figure 2 plots C/E distributions for the gamma-ray heating rate. The calculation with FENDL-2.1 underestimates the measurement by around 30 % while those with the other libraries overestimate by 20 – 30 %.

2) In-situ measurement experiment for iron

Figures 3 and 4 show neutron spectra at the depths of 310 and 810 mm. Generally all the calculations agree with the measurements well. The calculation with JENDL-3.3

slightly overestimates the measurements below ~ 10 keV at the depth of 310 mm, if you check them in detail. This is clearly indicated in Fig. 5, which plots C/E distributions for the neutron flux from 0.1 keV to 1 keV. Figure 6 shows the C/E distribution for the reaction rate of $^{115}\text{In}(n,n')^{115\text{m}}\text{In}$, which is sensitive to neutrons above 300 keV. Note that the four calculations show a different tendency each other, though the difference is not so large.

5. Concluding remarks

We analyzed integral benchmark experiments at JAEA FNS with the recent nuclear data libraries (JENDL-3.3, FENDL-2.1, JEFF-3.1 and ENDF/B-VII.0) and MCNP-4C in order to verify these libraries. The results of the in-situ measurement experiments only for SiC and iron were discussed here. Differences among the results with recent nuclear data libraries were rather large. In the future we will investigate origins of the differences among the calculation results.

References

- [1] K. Shibata, et al. : J. Nucl. Sci. Tech. 39, 1125 (2002).
- [2] D. Lopez Al-dama and A. Trokov : "FENDL-2.1 Update of an evaluated nuclear data library for fusion applications," IAEA Report INDC(NDS)-467 (2004).
- [3] A. Koning, et al. (Ed.) : "The JEFF-3.1 Nuclear Data Library," JEFF Report 21, OECD Nuclear Energy Agency (2006).
- [4] M.B. Chadwick, et al. : Nuclear Data Sheets 107, 2931 (2006).
- [5] Sub working group of fusion reactor physics subcommittee (Ed.) : "Collection of Experimental Data for Fusion Neutronics Benchmark," JAERI-M 94-014 (1994).
- [6] F. Maekawa, et al. : "Data Collection of Fusion Neutronics Benchmark Experiment Conducted at FNS/JAEA," JAERI-Data/Code 98-021 (1998).
- [7] F. Maekawa, et al. : "Benchmark Experiments on Advanced Breeding Blanket Materials and SiC with 14-MeV Neutrons," JAERI-Conf 2001-006, p.311 (2001).
- [8] J.F. Briesmeister (Ed.) : "MCNP - A General Monte Carlo N-Particle Transport Code, Version 4C," LA-13709-M (2000).
- [9] R.E. MacFarlane and D.W. Muir : "The NJOY Nuclear Data Processing System, Version 91," LA-12740-M (1994).
- [10] K. Kosako, et al. : "The libraries FSXLIB and MATXSLIB based on JENDL-3.3," JAERI-Data/Code 2003-011 (2003).
- [11] <http://www-nds.iaea.org/fendl21/index.html>.

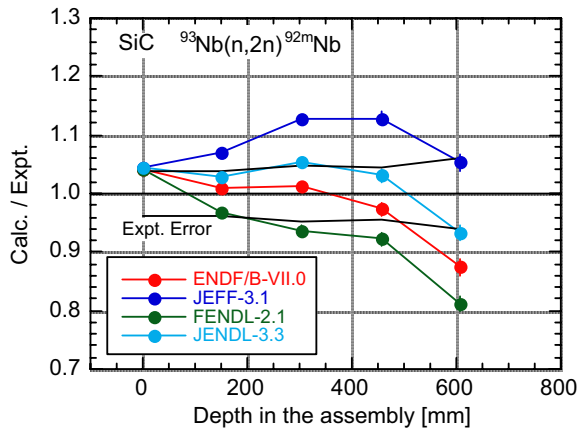


Fig. 1 C/E for reaction rate of $^{93}\text{Nb}(n,2n)^{92m}\text{Nb}$ in SiC experiment.

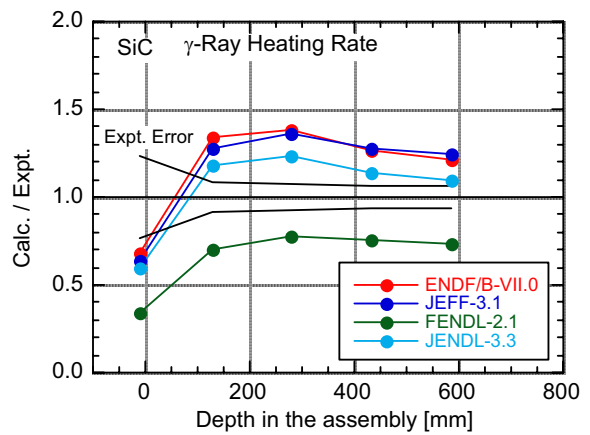


Fig. 2 C/E for gamma-heating rate in SiC experiment.

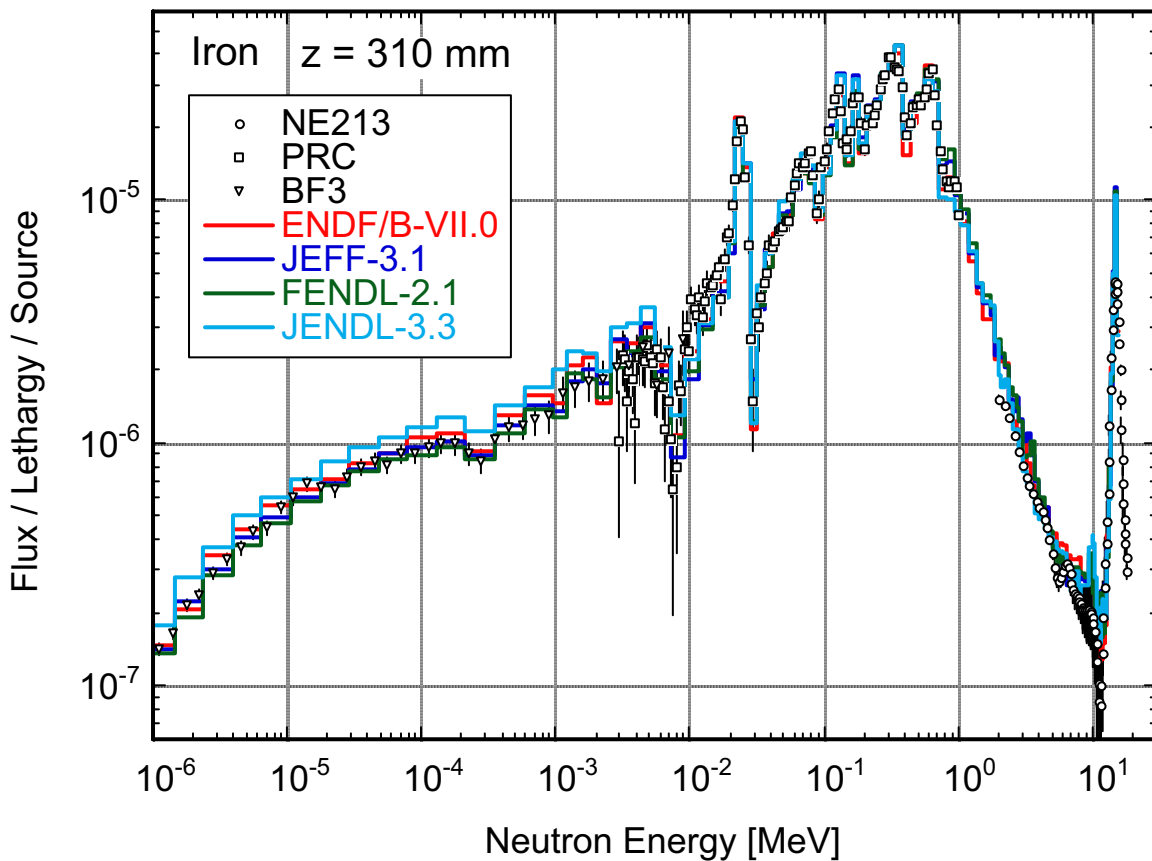


Fig. 3 Measured and calculated neutron spectra at depth of 310 mm in iron experiment.

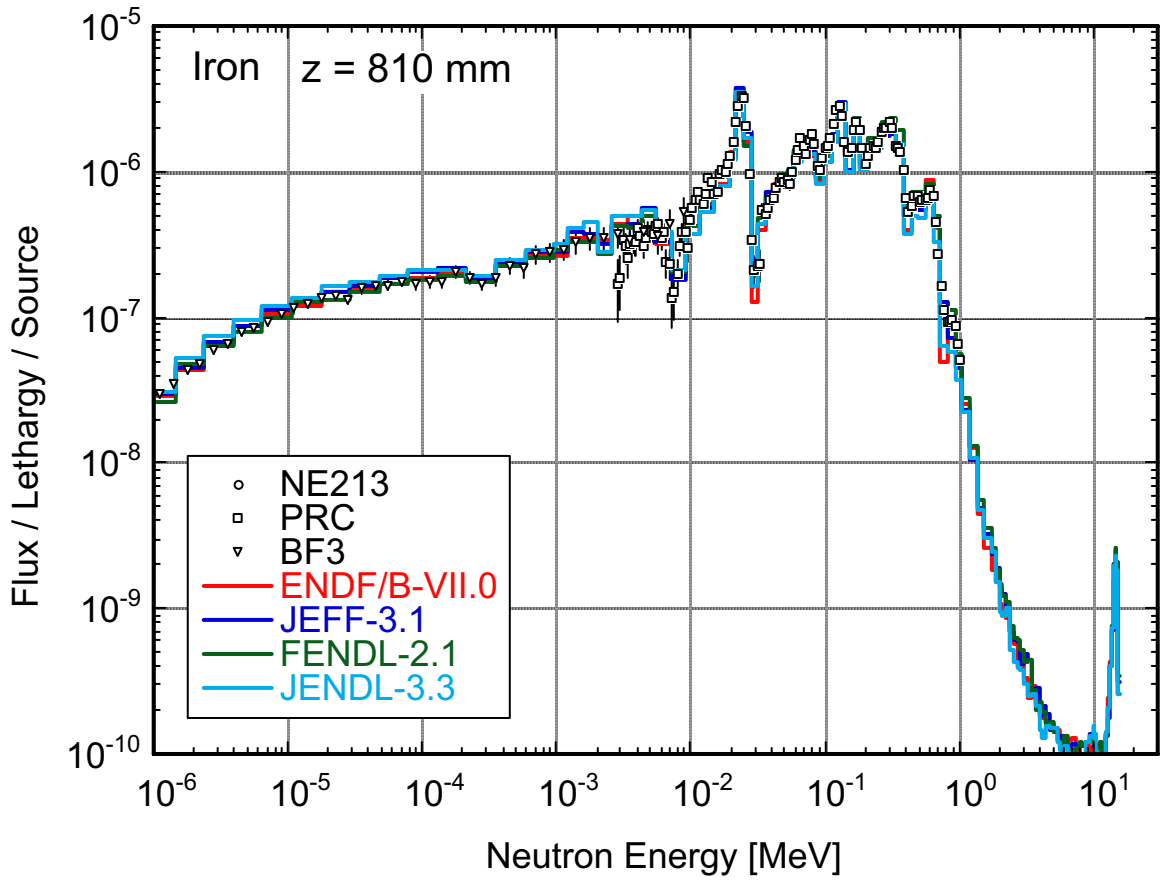


Fig. 4 Measured and calculated neutron spectra at depth of 810 mm in iron experiment.

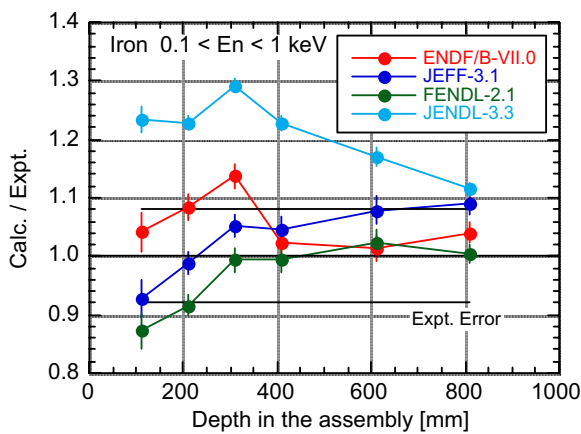


Fig. 5 C/E for neutron flux from 0.1 keV to 1 keV in iron experiment.

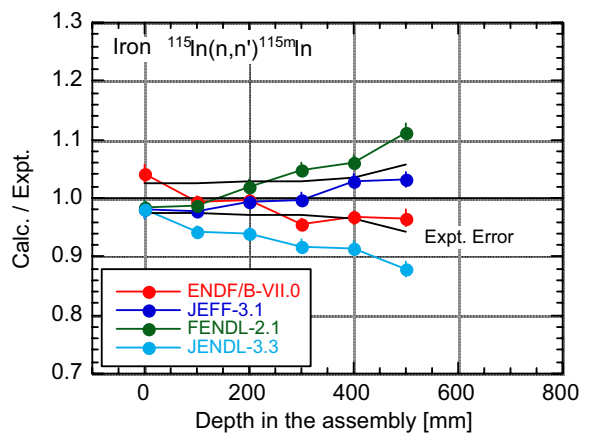


Fig. 6 C/E for reaction rate of $^{115}\text{In}(n,n')^{115\text{m}}\text{In}$ in iron experiment.

3.12 Development of Burn-up Calculation System for Fusion-Fission Hybrid Reactor

M. Matsunaka, S. Shido, K. Kondo, H. Miyamaru, I. Murata
Division of Electrical, Electronic and Information Engineering,
Graduate School of Engineering, Osaka University,
Yamada-oka 2-1, Suita, Osaka 565-0871, Japan

A fusion-fission hybrid reactor which is a fusion reactor with a blanket region containing nuclear fuel. In our group, a calculation system for analysis of fusion-fission hybrid reactor has been developed and transport and burnup calculations were carried out for various hybrid energy systems with three-dimensional ITER model. The burnup calculation system consists of a general-purpose Monte Carlo code MCNP-4B, a point burnup code ORIGEN2 and some other postprocessing codes developed by us, which process the calculated results. In order to evaluate collapsed cross section for burnup as precise as possible, making of collapsed cross section process was postprocessed using not tally function but neutron track length data of the MCNP calculation directly. We are using a modified version of MCNP-4B so as to output all neutron track length data in the blanket region. JENDL-3.3 pointwise data and JENDL Activation Cross Section File 96 were used as base cross section libraries. From the calculation results for a reactor type employing a water cooled uranium cycle, fusion-fission hybrid reactor is surely feasible from the standpoint of neutronics design. Further calculation and analysis are planned to improve hybrid reactor performance of LLFP transmutation and so on.

1 Introduction

A fusion-fission (FF) hybrid reactor system is a concept of combining nuclear fuel with fusion reactor. Neutrons can be well multiplied by fission in the nuclear fuel loaded in the fusion reactor blanket even for a relatively lower plasma condition. Tritium is thus bred so as to attain its self-sufficiency. Then enough energy multiplication is expected and moreover it is possible to transmute or to burn the nuclear waste such as long-lived fission products (LLFP) and minor actinides (MA) by surplus high energy neutrons.

In our group, a calculation system for the analysis had been developed to investigate the performance of FF hybrid reactor that is feasible at present. Such feasible FF hybrid reactor is expected to have the following characteristics, i.e., low plasma condition, subcriticality and tritium self-sufficiency. Target parameters considered are thus tritium breeding ratio (TBR), k_{eff} , power density, energy multiplication factor in accordance with the changes of material composition due to burnup. Transmutation ability of long-lived fission products and minor actinides is also evaluated. The author's group has performed a lot of neutronics analysis with the calculation system for various types of FF hybrid reactors¹⁾. Through a long experience to use the system, it was found that the system used previously had a problem in the making process of collapsed cross sections for burnup²⁾. The objectives of this work is to modify the burnup calculation system to make the cross section set for burnup very strictly with a special postprocess procedure. Also, as an example of the hybrid reactor analysis, the calculation results for a reactor type employing a water cooled uranium cycle is briefly described.

2 Calculation System

2.1 Development of Calculation System

Burnup calculations for FF hybrid reactor had been performed in the author's group so far with a calculation system combining general-purpose Monte Carlo code MCNP-4B³⁾ with point burnup code ORIGEN2⁴⁾. However, it was found from the experiences previously that the calculation system had a problem on making one-group cross sections for burnup calculation. The one-group cross section set was made by the tally function of MCNP. Tally function is known to be a useful function for users to estimate neutron flux, reaction rate, and so on. However the number of tallies available for users is too small to compute collapsed cross sections for all the nuclei included. Thus the calculation system was planned to be modified to improve making procedure of the one-group cross sections for burnup.

There were three options to improve the calculation system as follows. (1) Postprocessing to make one-group cross section using the calculated neutron spectrum by the MCNP tally. This option was very easy to apply and faster computation can be expected. But it would spoil continuous treatment of neutron energy. (2) Modification of MCNP to make one-group cross section directly or to remove the limit of the number of tallies available. But drastic modification of MCNP is actually unreal, and increase of the number of tallies will expand the computation time extremely. (3) Extracting neutron transport data and postprocessing of it. This is the most strict procedure and was finally adapted in the present study. This option required a little modification of MCNP with a slight increase of the computation time. But it takes a longer time required to make collapsed cross sections in the postprocessing.

Figure 1 shows the current burnup calculation procedure. One burnup cycle consists of the following four steps: 1) Criticality calculation by KCODE of MCNP, 2) Neutron transport calculation by modified MCNP, 3) Making of ORIGEN library from neutron track length data and evaluated nuclear data libraries, and 4) Burnup calculation by ORIGEN for each blanket cells. The whole burnup calculation of the FF hybrid system is completed by repeating this burnup cycle.

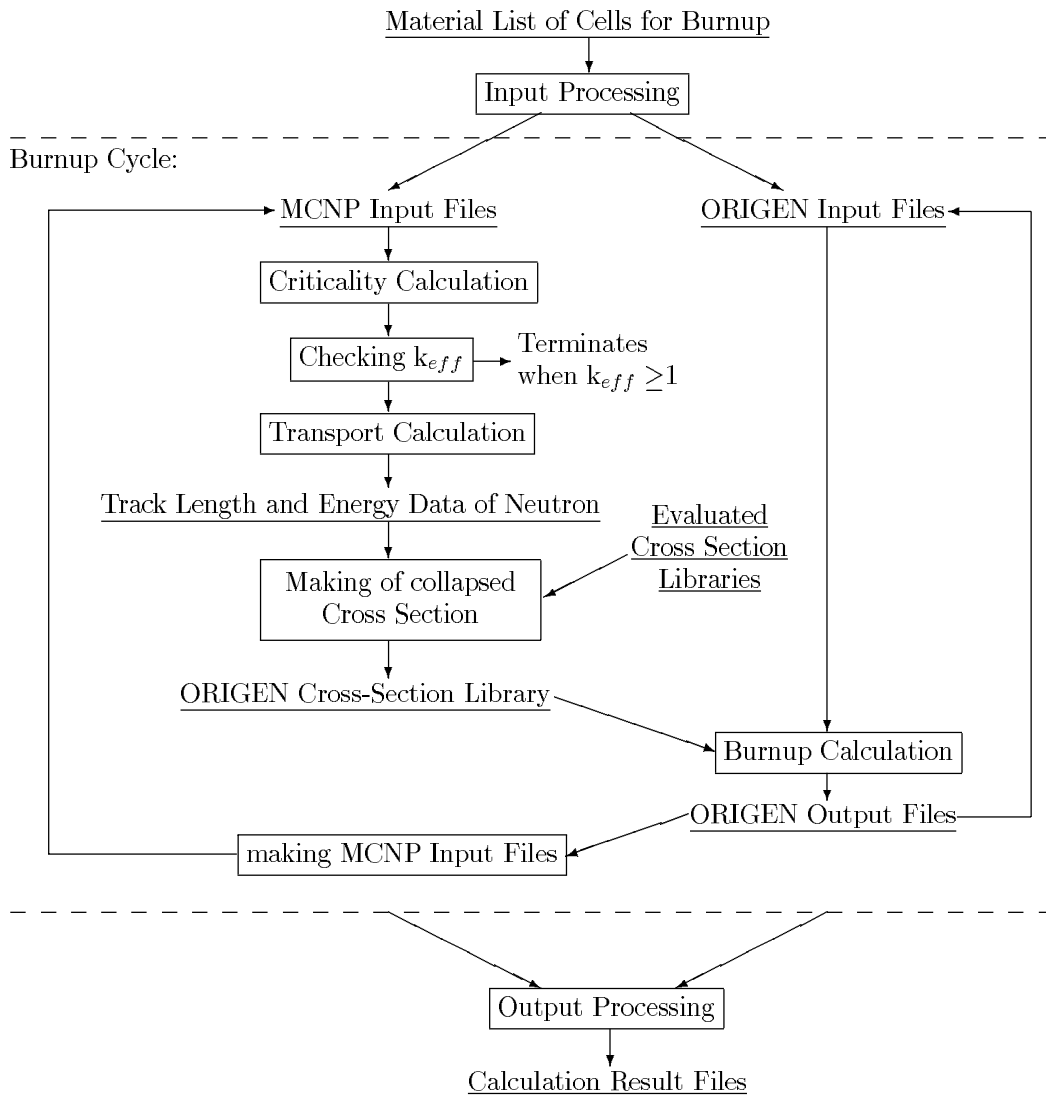


Figure 1: Flow Chart of Burnup Calculation

2.2 Making of Collapsed Cross Sections

In the ORIGEN code, cross section libraries for several types of nuclear reactor are prepared. However, those are not applicable to the present calculation, because FF hybrid reactor will be operated under subcritical condition and hence the energy spectrum varies depending on each configuration of nuclear fuel. It is thus needed to replace cross section values of the libraries attached in ORIGEN with the ones suitable for the present subcritical system. The ORIGEN code requires collapsed (one-group) cross-sections of (n,g), (n,2n), (n,α), (n,p), (n,gx) and (n,2nx) for activation products (including stable nuclei) and Fission products, and requires those of (n,g), (n,2n), (n,3n), (n,f), (n,gx) and (n,2nx) for actinides. (n,gx) and (n,2nx) mean cross sections of (n,g) and (n,2n) producing isomers.

As described above, in the present study, modified version of MCNP-4B was used to get all neutron transport data in the blanket cells. The data exported from a transport calculation and stored in a file are track-length (DLS), particle weight (WGT) and neutron energy (ERG). DLS, WGT and ERG are variable names of MCNP. Track-length is neutron flying distance between events, that is, reaching cell boundary and occurring of collision, as shown in Fig. 2.

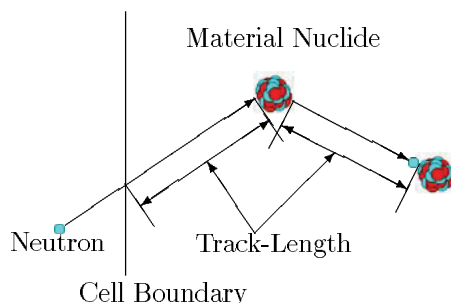


Figure 2: Neutron Track Length

The collapsed cross section is evaluated by the following equations.

$$\int \phi(E)dE = \frac{\sum_i DLS_i \cdot WGT_i}{NPS \cdot VOL}$$

$$\sigma^{coll} = \frac{\int \sigma(E) \cdot \phi(E)dE}{\int \phi(E)dE}$$

$$= \frac{\sum_i DLS_i \cdot WGT_i \cdot \sigma(ERG_i)}{\sum_i DLS_i \cdot WGT_i}$$

where:

σ^{coll}	Collapsed Cross-Section
E	Neutron Energy
$\sigma(E)$	Energy Dependent Cross-Section
$\phi(E)$	Energy Dependent Neutron Flux
DLS_i	Track-Length of Neutron Track i
WGT_i	Weight of Neutron Track i
ERG_i	Energy of Neutron Track i
NPS	History Number
VOL	Cell Volume

The cross sections of ORIGEN library are replaced by σ^{coll} . Point-wise data of $\sigma(E)$ is directly used from evaluated nuclear data libraries of JENDL-3.3 and JENDL Activation Cross Section File 96⁵⁾. The library for LMFBR contained in ORIGEN was also referred for minor nuclei as not contained in both of JENDL-3.3 and JENDL Activation Cross Section File 96.

3 Calculation Results

With the developed calculation system, various calculations have been carried out so far^{6, 7)}. In the present paper, as a typical example, brief results of a water cooled uranium cycle are described.

3.1 Calculation Model and Condition

Figure 3 shows cross sections of calculation geometry and tables 1 and 2 show calculation conditions. The 3-dimensional ITER⁸⁾ model (18 degree sector model) and physics parameters derived from the plasma conditions already achieved at JT-60 of JAEA⁹⁾ were employed.

The blanket was divided into 5 sections radially and each section was divided into 6 layers (30 cells total). The material composition of fuel cell and breeder cell are shown in table 3. Li_2ZrO_3 was selected as breeding material, and loaded into breeder cell with beryllium. ^6Li enrichment was 30 %. Fuel cell consists of structural material SS316, natural UO_2 and reprocessed PuO_2 as nuclear fuel and water as coolant.

There were two transmutation cells in second layer. 5 long-lived fission products (LLFP) of ^{93}Zr , ^{99}Tc , ^{107}Pd , ^{129}I and ^{135}Cs were loaded into transmutation cells with moderator.

In the present calculation, the period of burnup is 5 years and the plant factor is 70 %. Each year includes five burnup cycles and a cooling cycle of 100 days. Each burnup cycle lasts 53 days.

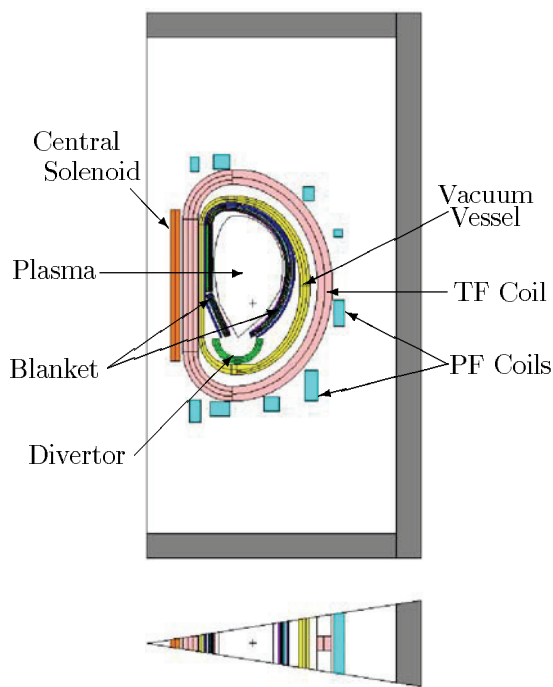


Figure 3: Cross Section of the Calculation Model

Table 1: Main parameters for calculations based on JT-60 and ITER

Plasma parameters	
Major radius (m)	6.2
Minor radius (m)	2.1
Plasma volume (m^3)	884
Plasma temperature (keV)	19
Confinement time (s)	1.1
Electron density (m^{-3})	4.8×10^{19}
Fusion power (MW)	646
neutron yield (n/s)	2.2×10^{20}
Neutron wall load (MW/m^2)	0.40 (average)
Blanket parameters	
Total thickness (m)	0.38
Total volume (m^3)	265

Table 2: Material loading arrangement

First Wall side	
1st layer	Breeder
2nd layer	Breeder*
3rd layer	Fuel
4th layer	Fuel
5th layer	Breeder
6th layer	Breeder
Vacuum Vessel side	

*two of five regions are replaced to FP transmutation cell

Table 3: Material composition

Composition of fuel (%)	
Reprocessed Pu	6.2
Natural UO ₂	40.6
Water	36.7
SS316	16.5
Composition of breeder (%)	
Li ₂ ZrO ₃	10
Be	90
⁶ Li enrichment (%)	30

3.2 Validation of Postprocessing

Table 4 shows validity confirmation result of the present making procedure of collapsed cross section. These 10 nuclei are especially significant when estimating the performance of FF hybrid reactor. The value in the table is the ratio of one-group cross section evaluated by the present procedure to FM option in MCNP. As shown in the table, present making procedure can be sufficiently trusted.

Table 4: Validity Confirmation Result of the Present Collapsed Cross-Section Making Procedure

	Ratio of Calculated Cross-Section (this method* / MCNP Tally**)			
	(n,g)	(n,2n)	(n,p)	(n,α)
⁹³ Zr	9.998E-01	1.000E+00	9.998E-01	1.000E+00
⁹⁹ Tc	1.000E+00	1.000E+00	1.000E+00	1.000E+00
¹⁰⁷ Pd	9.999E-01	9.997E-01	1.000E+00	1.000E+00
¹²⁹ I	9.998E-01	1.000E+00	1.000E+00	1.000E+00
¹³⁵ Cs	9.998E-01	1.000E+00	1.000E+00	1.000E+00
	(n,g)	(n,2n)	(n,3n)	(n,f)
²³² Th	9.999E-01	9.998E-01	9.999E-01	1.000E+00
²³³ U	9.977E-01	1.000E+00	1.000E+00	9.993E-01
²³⁵ U	1.000E+00	9.999E-01	9.998E-01	9.997E-01
²³⁸ U	1.000E+00	1.000E+00	1.000E+00	9.996E-01
²³⁹ Pu	9.998E-01	1.000E+00	9.999E-01	1.000E+00

*One-group cross-section estimated by the present procedure

**One-group cross-section estimated by dividing the calculated reaction rate by the calculated total flux

3.3 Burnup Calculation Results

The present burnup calculation system can estimate parameters such as effective multiplication factor (k_{eff}), power density in fuel cell, neutron flux and changes of nuclide number density. In the present paper, three most significant parameters on discussing feasibility of FF hybrid system are selected.

Figure 4 shows tritium breeding ratio (TBR) and energy multiplication factor and table 5 indicates transmutation performance of 5 LLFPs over the whole burnup period. The most important restriction is to ensure the TBR to be over 1.05 during the operation of fusion reactor. Figure 4 shows that the TBR is always over 1.2 throughout the burnup period of 5 years. The energy multiplication factor is about 10, however decreasing monotonously to around 8. These results indicate that this type of FF hybrid system is feasible. But the results for transmutation performance is not so excellent. Some of them show even a negative result, meaning increase of LLFP. Practically, transmutation ratios of ^{99}Tc , ^{107}Pd and ^{129}I are acceptable for performance in the transmutation cell and in the whole blanket as well. However, the amount of ^{93}Zr and ^{135}Cs are inversely increased compared to their initial inventory. This result suggests further investigation especially for LLFP transmutation performance.

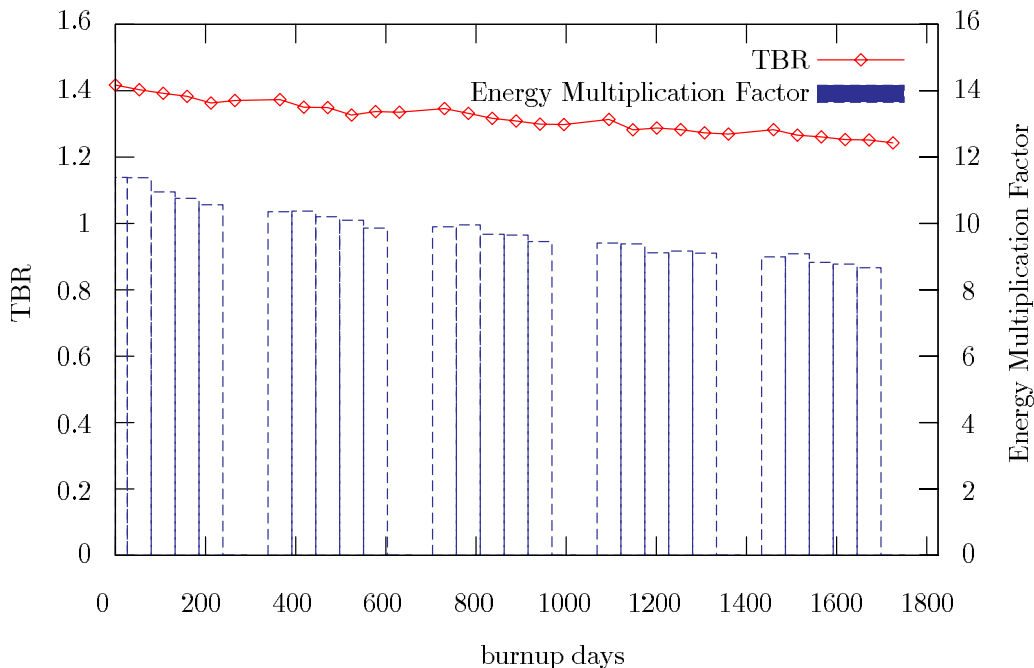


Figure 4: Burnup calculation results for TBR and Energy generation

Table 5: Transmutation Performance for LLFP (%)

(decreased percentage per initial load)

	^{93}Zr	^{99}Tc	^{107}Pd	^{129}I	^{135}Cs
transmutation cell	0.9	20	15	8	6
blanket total	-2	11	7	2	-19

4 Summary

A general-purpose transport and burnup code system for precise analysis of the fusion fission hybrid reactor has been developed. One group cross sections for burnup are updated in each burnup cycle, which is the most strict method to collapse cross sections. The present calculation system enables to perform precise neutronics analysis of subcritical systems such as a fusion fission hybrid reactor. However, at the moment, one difficult problem is still left, i.e., it takes a lot of computation time to calculate one-group cross section set.

From the present calculation results carried out with the newly developed calculation system, it is suggested that FF hybrid reactor is surely feasible from the standpoint of neutronics design. Further calculation and analysis are nevertheless needed to improve hybrid reactor performance including nuclear waste transmutation performance.

References

- 1) I. Murata, et. al., Fusion Eng. Des., 75-79 (2005) 871-875
- 2) I. Murata, et. al., to be published in the Proc. of the 24th Symposium on Fusion Technology, Warsaw, Poland, September 2006.
- 3) J. F. Briesmeister (Ed.), MCNP-A General Monte Carlo N-Particle Transport Code, Version 4B, LA-12625-M, 1997.
- 4) A. G. Croff, Nucl. Technol. 62 (1983) 335-352.
- 5) <http://wwwndc.tokai-sc.jaea.go.jp/nucldata/> .
- 6) S. Shido, et. al., Proc. of the 2005 Symposium on Nuclear Data, JAEA-Conf 2006-009, P.169.
- 7) M. Matsunaka, et. al., to be published in the Proc. of the 24th Symposium on Fusion Technology, Warsaw, Poland, September 2006.
- 8) <http://www.naka.jaea.go.jp/ITER/FDR/> .
- 9) <http://www.jaeri.go.jp/jpn/open/press/980625jt-60/index.html> (in Japanese).

3.13 Nuclear heating calculation for the high flux test module in IFMIF

Daisuke Kaku, Tao Ye, and Yukinobu Watanabe
Department of Advanced Energy Engineering Science, Kyushu University,
Kasuga, Fukuoka 816-8580, Japan
 Corresponding email: watanabe@aees.kyushu-u.ac.jp

The PHITS code is applied to neutronics calculations for the high flux test module in IFMIF. The calculated neutron energy spectrum and heating rate show reasonably good agreement with the previous result of the conceptual nuclear design. These physical quantities are calculated using different high-energy nuclear data libraries (LA150, NRG-2003, and JENDL/HE-2004), and the similarities and differences are discussed. The validity of the KERMA approximation and the sensitivity of the Li(d,xn) neutron source term to heat production calculation are examined.

1. Introduction

The International Fusion Materials Irradiation Facility (IFMIF)¹⁾ is composed of an accelerator-driven deuteron-lithium neutron source for irradiation tests of fusion reactor candidate materials. Neutrons up to about 55 MeV will be produced by two 125 mA beams of 40 MeV deuterons bombarding a thick target of flowing liquid lithium. So far, conceptual nuclear designs of the IFMIF have been performed mainly using a code M^cDelicious developed in Forschungszentrum Karlsruhe (FZK)^{2,3)}. In detailed design of the IFMIF, more accurate estimation will be required on behaviors of fast neutrons with energies up to 55 MeV in materials. Several high-energy particle transport codes such as MCNPX⁴⁾ and PHITS⁵⁾ are widely used for various accelerator applications in combination with the latest high energy nuclear data libraries. Therefore, it is worthwhile to test to what extent these codes and high energy nuclear data libraries are applicable to IFMIF neutronics calculations.

The PHITS code⁵⁾ is chosen for calculations of nuclear heating in the high flux test module (HFTM) in the IFMIF. The main purpose of this work is to examine the applicability of the PHITS code to IFMIF neutronics calculations. Neutron energy spectrum and nuclear heating over the HFTM are calculated and compared to FZK results. Furthermore, the sensitivity of three nuclear data libraries (LA150⁶⁾, NRG2003⁷⁾, and JENDL/HE-2004⁸⁾) to nuclear heating and the validity of KERMA approximation are discussed. Influence of the d-Li reaction source term is investigated on nuclear heating using differential thick target neutron yield data of the Li(d,n) reaction measured recently in Tohoku University⁹⁾.

2. Calculation procedure

The high flux test module (HFTM) is placed downstream behind the flowing liquid lithium target, forming the highest neutron radiation region. The HFTM consists of a steel container housing a number of irradiation rigs that contain encapsulated irradiation specimens.

The PHITS code is used for IFMIF-HFTM neutronics calculations. The details of the PHITS code are described in ref.⁵⁾.

In the present calculation, a simplified HFTM configuration is adopted as in the previous FZK work²⁾. The geometrical configuration is depicted in Fig.1. The HFTM part is composed of a rectangular block 20 x 5 x 5 cm³ filled with Eurofer with a mass density of 6.24 g/cm³, which is 80% of the normal density to take account of the space occupied by colling gas.

Each of two deuteron beams impinges on the lithium target with 10° declination angle in vertical direction. Fig.1 illustrates the lithium target (26 x 2.5 x 20 cm³) filled with lithium at 0.512 g/cm³ and its back plate (26 x 0.18 x 20 cm³) filled with Eurofer at 7.8 g/cm³ density. The PHITS code can calculate neutron production from the Li(d,xn) reaction in the lithium target using the QMD model¹⁰⁾ in principle, but a preliminary result does not show reasonable agreement with experimental results. Thus, the differential thick target neutron yields (TTY) calculated by the M^cDelicious code²⁾ are used as the source term in the present work. The source term is assumed to be a surface source placed at a distance corresponding to the range of deuteron in lithium, although it is a volume source in practice. The tilt angles of ±10° of incident deuteron beam are taken into account so that the direction of neutron emission at 0° coincides with that of

the incident deuteron beam. It should be noted that scattering of neutrons from lithium layer between the surface neutron source and the back plate is neglected because the calculated TTY data are used as the neutron source term.

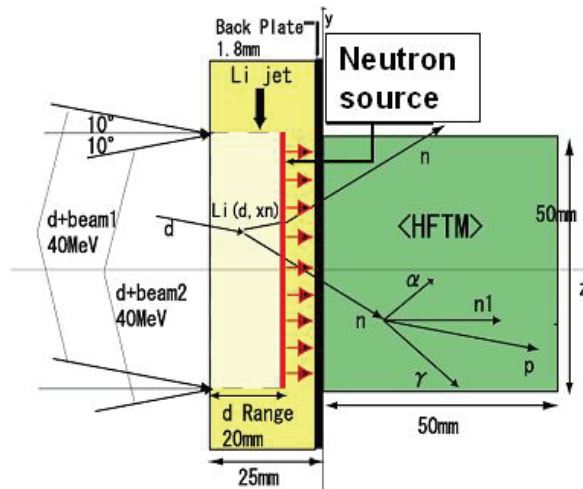


Fig.1 Geometrical configuration of the lithium target and HFTM

3. Results

3.1 Applicability test of the PHITS code to IFMIF neutronics calculation

Energy distribution of the average neutron flux in the HFTM calculated by the PHITS code is compared with the FZK result obtained by the M^cDelicious code²⁾ in Fig.2. The former reproduces the latter well, although there is a slight difference in the energy range between 10 and 25 MeV. The difference might be due to that in the neutron source term, because the surface neutron source is assumed in the present work as mentioned in sect. 2. Table 1 shows comparisons of the average neutron and gamma fluxes, the average dpa rate, the total heat production, and the average heat production density. The present calculation shows agreement with the FZK result within about 10 %. Thus, this benchmark test indicates that the PHITS code is applicable to neutronics calculations for thermal-hydraulic design of the HFTM.

3.2 Analysis of nuclear heating in the HFTM

The spatial distribution of nuclear heating rate in the HFTM is calculated for the case where each of two deuteron beams (2 x 125mA) impinges on the lithium target with 10° declination angle in horizontal direction. It should be noted that the beam incidence with horizontal declination is adopted in the latest IFMIF design³⁾. In fig.3, the result is presented as a three-dimensional plot sliced in half at x=0. The size of each boxel (i.e., an elementary cubic segment) is 0.5 x 0.5 x 0.5 cm³. The highest heating rate of 27 W/cm³ is obtained in the vicinity of the surface region. The spatial distribution is also plotted along the depth into HFTM (i.e., z-axis) in Fig.4. It is found that the total heating rate is attenuated linearly with the depth and the dependence of neutron and gamma heating upon the depth is different.

Nuclear heating for other fusion reactor candidate materials (F82H, V4Ti4Cr, SUS304, and SiC) is also calculated in the same way using the PHITS code. For the sake of simplicity, the geometrical model used consists of a rectangular block 20 x 5 x 5 cm³ filled with each material with the same mass density as the normal density, in order to see rough estimation of the dependence of nuclear heat production on materials. The result is shown in Table 2. The neutron and photo heat and their sum are almost same among three iron-based materials (Eurofer, F82H, and SUS304), while the total heat production for SiC, is much smaller than the other materials because the amount of photon heat released in the HFTM is considerably small.

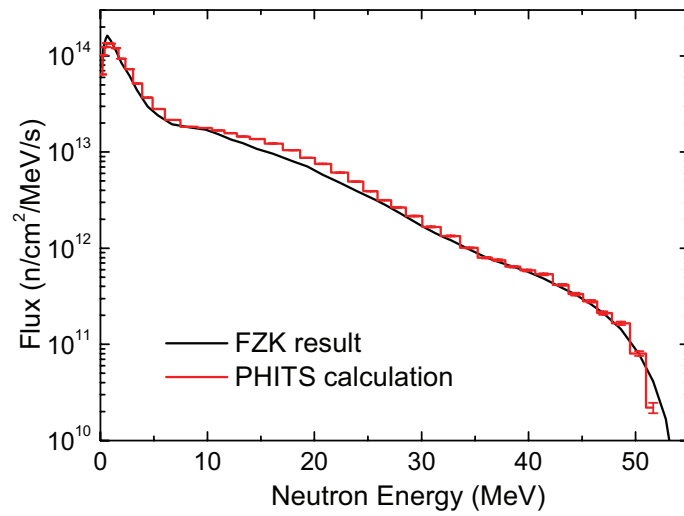


Fig.2. Comparison of neutron energy spectra in the HFTM between the present PHITS calculation and the FZK result²⁾

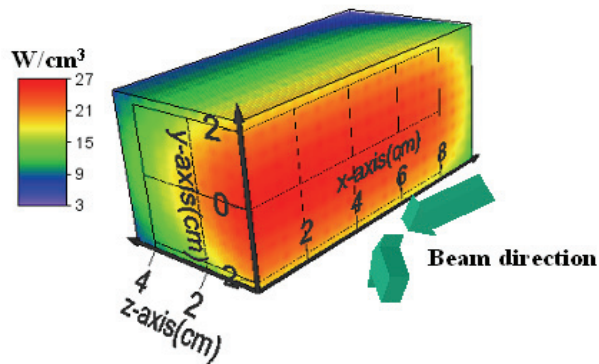


Fig.3. Three-dimensional spatial distribution of nuclear heating rate calculated by assuming deuteron beam incidence with horizontal declination

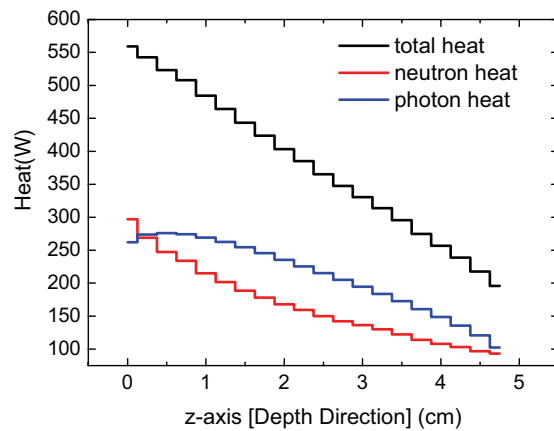


Fig.4. Spatial distribution of the heating rate produced in the HFTM along z-axis

Table 1. Physical parameters of the HFTM and results of neutronics calculations. The result of the FZK work is take from ref.²⁾ for comparison.

Parameter	FZK work	Present work
Size	20 x 5 x 0.18 cm ³	
Volume	500 cm ³	
Material	Eurofer (Fe-88.9%, Cr-9.6%, C-4.9%, ...)	
Material Density	6.24 g/cm ³	
Average Neutron Flux	5.86 x 10 ¹⁴ n/cm ² /s	6.40 x 10 ¹⁴ n/cm ² /s
Average Neutron Energy	7 MeV	7 MeV
Average Gamma-ray Flux	2.33 x 10 ¹⁴ γ/cm ² /s	2.63 x 10 ¹⁴ γ/cm ² /s
Average dpa rate	29 dpa/fpy	31 dpa/fpy
Total Heat Production	7.0 kW	7.5 kW
Average Heat Production Density	14 W/cm ³	15 W/cm ³

Table 2. Total heat production in the HFTM for different materials

material	Eurofer	F82H	V4Ti4Cr	SUS304	SiC
Total heating (kW)	9.94	9.50	9.70	10.70	6.10
Neutron (kW)	4.05	3.93	6.33	4.70	5.48
Photon (kW)	5.89	5.57	3.37	6.00	0.62

4. Discussion

4.1 Sensitivity of nuclear data library to calculation of nuclear heating and neutron flux

The neutronics calculations were performed using the PHITS code with three nuclear data libraries (LA150⁶⁾, NRG2003⁷⁾, and JENDL/HE-2004⁸⁾) in order to see how nuclear data libraries influence calculations of neutron flux and nuclear heating. As presented in Fig.5 and Table 3, the neutron fluxes are almost identical among three calculations, while the total heating rates are largely different (up to 50%). Table 3 indicates that the difference in the total heating rates is due to that in the heat generated by neutrons. This can be easily explained from the fact that the heating numbers of ⁵⁶Fe (i.e., kerma factors) included in the libraries are obviously different, particularly in the high energy range above 20 MeV, as seen in Fig.6.

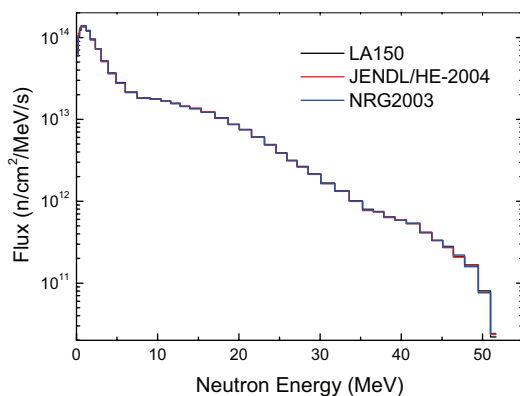


Fig.5. Comparison of the calculated neutron fluxes in the HFTM.

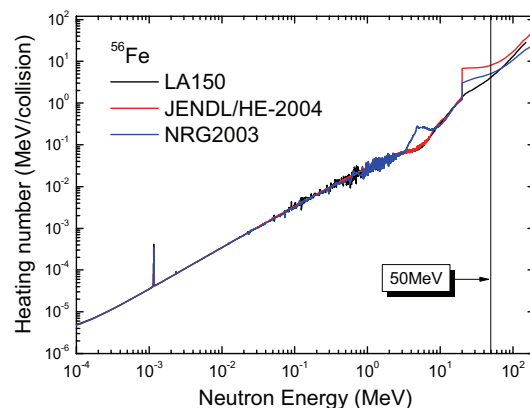


Fig.6. Total heating number of ⁵⁶Fe

Table 3. Comparison of calculated heating rates among three nuclear data libraries (LA150, JENDL/HE-2004, and NRG-2003)

Nuclear data library	LA150	JENDL/HE-2004	NRG-2003
Total heating rate (kW)	7.6	11.2	8.4
Neutron heating rate (kW)	3.4	6.7	4.4
Photo heating rate (kW)	4.2	4.5	4.0
Ratio to LA150	1	1.47	1.1

4.2. Validity of KERMA approximation

As neutron energy increases, production of light ions, such as protons and deuterons with relatively high kinetic energy, becomes prominent. With an increase in the kinetic energy, the range becomes long, e.g., the range of 50 MeV protons is 5.3 mm in Eurofer with the mass density 6.24 g/cm³. Therefore, it is expected that the KERMA approximation assuming local energy deposition becomes worse. The PHITS code has a feature to deal with transport of light ions in matter using the continuous slowing down approximation. This means that the spatial spreading of the energy deposited by light ions can be taken into account beyond the KERMA approximation in the present calculation. It should be noted that the KERMA approximation is adopted for heavy recoils because the range is quite short. In the preceding work in FZK²⁾, the KERMA approximation was used in calculations of heat production. Therefore, it is of interest to examine quantitatively the validity of the KERMA approximation in the HFTM design.

The calculation condition is same as mentioned in sect. 2, except that neutrons enter in the direction perpendicular to the surface xy-plane of the HFTM. The PHITS calculation is implemented under the full KERMA approximation with the total heating numbers included in the nuclear data library, which is called the PHITS-KERMA calculation hereafter, and compared with the normal PHITS calculation mentioned in sect. 3. First, the total heat production is calculated by varying the depth along the neutron incident direction. The result is shown in Fig.7. Both the results are in good agreement for thickness over 1 mm. The KERMA approximation tends to overestimate because the light ions generated by neutron-induced reactions are likely to escape from the HFTM volume. Next, the neutron energy dependence is examined. In the calculation, mono-energetic neutrons impinge on the HFTM with different thicknesses of 1, 5, and 10 mm, respectively. Fig.8 presents the ratios of the total heat production calculated under the full KERMA approximation to the normal PHITS calculation. The ratios increase with increasing neutron energy and reducing thickness, and thus the KERMA approximation becomes worse and worse. Since the maximum energy of the source neutron in the IFMIF is about 55 MeV and the thickness of the HFTM is 25mm, however, the KERMA approximation is found to be valid in the heat production calculation in the HFTM. Finally, the spatial distributions of total heat production are compared between the two cases in Fig. 9. It is found that the difference appears slightly in the vicinity of the surface because most of generated light ions are expected to escape from the front surface.

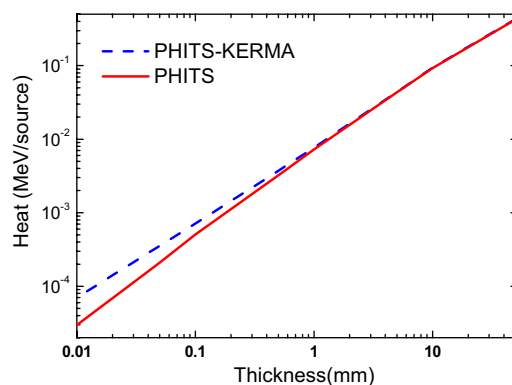


Fig. 7. Comparison of the total heat production between the full KERMA approximation and the normal PHITS calculation

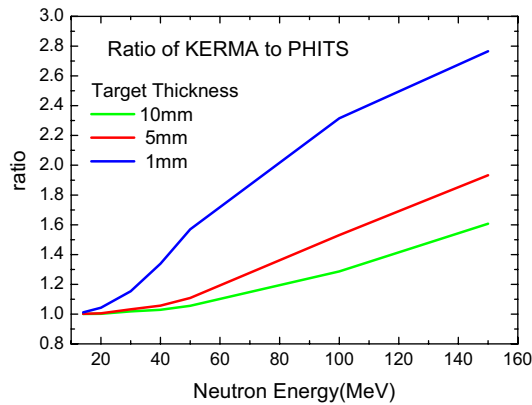


Fig.8. Ratio of the total heat production calculated under the full KERMA approximation to the normal PHITS calculation

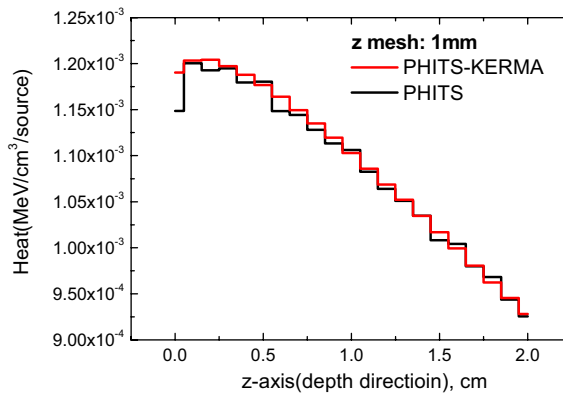


Fig. 9. Spatial distribution of total heat production

4.3. Sensitivity of the d-Li neutron source

The M^cDelicious neutron spectra used as input in the PHITS calculations mentioned early are compared with the recent experimental data of differential thick target neutron yields measured by Baba and co-workers⁹⁾ in Fig.10. It is shown that the M^cDelicious calculation overestimates the production of neutrons with energies below 5 MeV at 0° and the spectral shape is different from the observation at the high-energy end. Consequently, it is of interest to see how this difference affects the calculated neutron flux and heat production rate in the HFTM. In Fig.11, the PHITS result using the experimental data as the neutron source term is compared with that using the M^cDelicious neutron spectra. There is no appreciable difference between the two calculations. However, it will be necessary to improve the overestimation seen in Fig.10 by re-evaluating the cross section data for the d + ⁷Li reaction.

5. Summary

The PHITS code was first applied to neutronics calculations for the high flux test module (HFTM) in the IFMIF neutron source facility. The calculated neutron energy spectrum and nuclear heating were in good agreement within 10% with the previous result by the FZK group. This indicates the applicability of the PHITS code to neutronics calculations for the HFTM. The calculation using different nuclear data libraries, LA150, NRG-2003, and JENDL/HE-2004, showed that the neutron fluxes are almost identical, while the heating rates have a large discrepancy, reflecting the difference in the heating numbers included in these libraries. In addition, it was confirmed that the KERMA approximation is reasonably good in calculating the heating rates in the HFTM unless one discusses the heat generated within the small size less

than 1 mm. Finally, the sensitivity of the $\text{Li}(d,xn)$ neutron source term to nuclear heating in HFTM was examined, because there are some discrepancies between the M^cDelicious neutron spectra used in this work and the recent experimental data of differential thick target neutron yields. The heating calculation with the experimental data showed no remarkable difference from that with the M^cDelicious neutron spectra.

The PHITS code employs the quantum molecular dynamics (QMD) model¹⁰⁾ to describe nuclear reactions that may take place in heavy-ion transport processes in matter. Its application to deuteron transport calculation is not necessarily successful. In addition, there are some discrepancies between the M^cDelicious calculation and experimental data as mentioned in sect. 4. Thus, we plan to study deuteron-induced reactions with particular focus on neutron production, aiming at further upgrading of IFMIF neutronics calculations.

Finally, our IFMIF-HTFM neutronics calculation will be linked with thermal-hydraulic design that is being performed by the Kyushu University group^{11,12)} in the future.

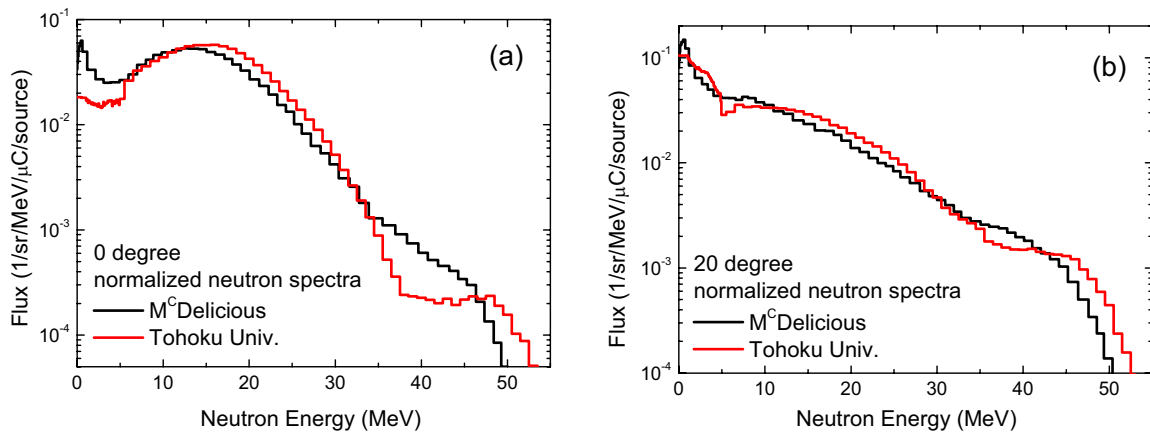


Fig. 10. Comparisons of calculated and measured thick target neutron yields from lithium at the deuteron incident energy of 40 MeV. The emission angles are 0 degree (a) and 20 degree (b), respectively. The experimental data are taken from ref.⁹⁾

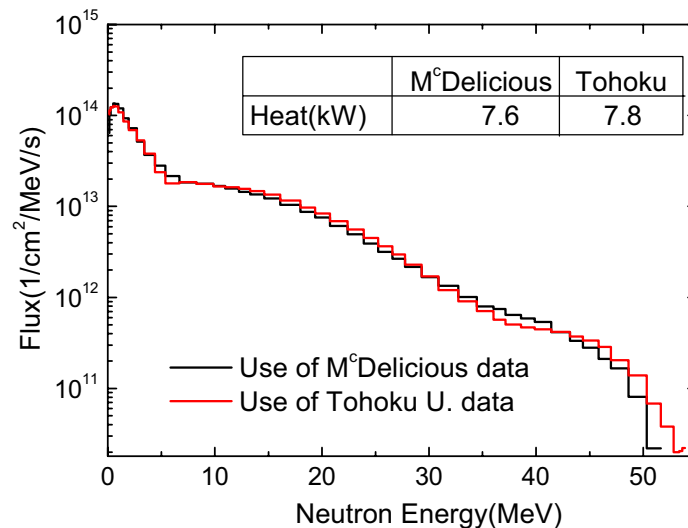


Fig.11. Comparison of average neutron fluxes and total heat production between the PHITS calculation with the M^cDelicious neutron source term²⁾ and that with the experimental data⁹⁾

Acknowledgements

The authors wish to thank K. Niita for his helpful instruction for use of the PHITS code. They acknowledge K. Kosako for his useful discussion on the heating numbers included in nuclear data libraries. They are also grateful to A. Shimizu, T. Yokomine, and S. Ebara for their cooperation and encouragement.

References

- [1] H. Matsui, "Present status and future prospects of the IFMIF project", in Proceedings of the 23rd Symposium on Fusion Technology, Sept. 20-24, 2004, Venice, Italy.
- [2] S.P. Simakov, et al., "IFMIF neutron source term simulation and neutronics analysis of the high flux test module", Report FZKA 6743, Karlsruhe (2002).
- [3] U. Fischer, et al., Fusion Eng. Des. **81**, 1195-1202 (2006).
- [4] L.S. Waters(Ed.), MCNPX Users's Manual, Version 2.3.0, LA-UR-02-2607 (2002).
- [5] H. Iwasa, K. Niita, and T. Nakamura, J. Nucl. Sci. and Technol., **39**, 1142-1151 (2002).
- [6] M.B.Chadwick, et al., Los Alamos National Laboratory report LA-UR-99-1222 (1999).
- [7] A. J. Koning, et al., in Proceedings of the International Conference on Nuclear Data for Science and Technology, Santa Fe, USA, September 26-October 1, pp.422-425 (2004).
- [8] Y. Watanabe, et al., in Proceedings of the International Conference on Nuclear Data for Science and Technology, Santa Fe, USA, September 26-October 1, pp. 326-331 (2004).
- [9] M. Hagiwara et al., J. Fusion Sci. & Technol., **48**, 1320 (2005).
- [10] K. Niita, et al., Phys. Rev. C **52**, 2620 (1995).
- [11] S. Ebara, S. Nagata, H. Irisa, T. Yokomine, and A. Shimizu, Fusion Eng. Des. **81**, 887-891 (2006).
- [12] S. Ebara, T. Yokomine, and A. Shimizu, Fusion Eng. Des. **82**, 61-72 (2007).

3.14 Sensitivity Analysis of Actinide Decay Heat Focused on Mixed Oxide Fuel

Naoto HAGURA, Tadashi YOSHIDA

Musashi Institute of Technology, Tamazutsumi 1-28-1, Setagaya-ku, Tokyo 158-8557, Japan

E-mail: g0567014@sc.musashi-tech.ac.jp

Nuclear power plants in the world accumulate a vast amount of spent fuels. In Japan, the spent fuel is reprocessed and is not disposed directly. Therefore utilization of this reprocessed fuel, i.e. Mixed Oxide (MOX) Fuel, will eventually expand. Under this background, hereafter, the MOX fuel will play a role of greater importance. It is, then, essential to understand the characteristics of the spent MOX fuel. In this work, the uncertainty of the fission-product and actinide decay heats was studied introducing the uncertainty of the nuclear data and the prediction accuracy of isotopic generation. At 100 year after discharge, for example, 7% error of the decay heat will be introduced by 10% uncertainty of Pu-241 generation calculation through Am-241 production.

1. Introduction

There are 440 nuclear power plants in the world. They hold a vast amount of spent fuels. In Japan, the spent fuel is reprocessed and is not disposed directly. Therefore utilization of this reprocessed fuel, i.e. Mixed Oxide (MOX) Fuel, will eventually expand.

Under this background, hereafter, the MOX fuel will play a role of greater importance. It is, then, essential to understand the characteristics of the spent MOX fuel. Above all, the radioactivity and decay power of spent MOX fuel are very crucial in storage or disposal terms. In this work, the uncertainty of the fission-product and actinide decay heats was studied introducing the uncertainty of the nuclear data and the prediction accuracy of isotopic generation.

2. Procedure of Analyses

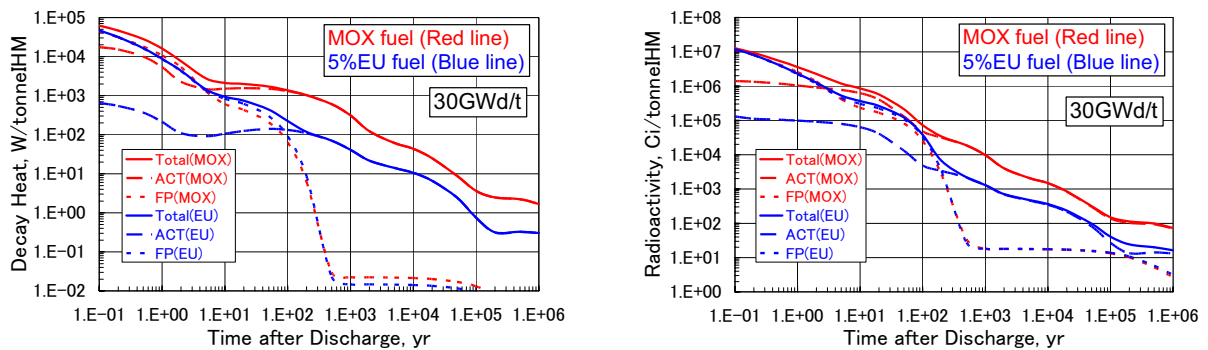
In this study, we made use of SWAT code system¹ developed by Japan Atomic Energy Research Institute (JAERI) and ORIGEN2 code² developed by Oak Ridge National Laboratory (ORNL). Burnup calculation is performed by SWAT code, and decay heat calculation is carried out by ORIGEN2 code. In SWAT, typical PWR pin cell model is selected as calculation model. Component of MOX fuel is specified as PWR33G-MOX³ (enrichment of 0.22% depleted uranium and 5.3% Pu). Calculation conditions are as follows: Thermal power is 37.9MW/t, normal discharged burnup is 30GWd/t, and library is JENDL3.3. Isotopic inventory calculated by SWAT is translated into the input of ORIGEN2 code.

3. Calculation Results

3.1 Spent fuel characteristics in perspective

For keeping the decay heat and radioactivity of spent fuel in perspective, Fig.1 shows the results of standard calculation of this study. On these figures, red line means MOX fuel, while blue line means 5% enriched uranium (EU) fuel. We should pay attention to the Actinide component. The difference that exceeds one decade is seen between MOX fuel and EU fuel in the actinide component. As a result, total decay heat (ACT and FP) has been raised. In each cooling time, the nuclides that mainly show

contribution are as follows: Cm-242 (~1yr), Pu-238 (~100yr), Am-241 (~500yr), Pu-240 (~10⁴yr), Pu-239 (~10⁵yr), and nuclides of neptunium series (>10⁵). Characteristics of radioactivity also indicate similarity between MOX fuel and EU fuel (Fig.1 (b)).



(a) Absolute of Decay heat of spent fuel (b) Absolute of Radioactivity of spent fuel
 Fig.1 Characteristics of spent fuel at 30 GWd/t

Figure 2 shows each decay heat by deference of discharged burnup per unit amount of power generation⁴. The representation of decay heat per unit amount of power generation is appropriate for the viewpoint of the economy. On MOX fuel the curve per unit amount of power generation of this figure leads the advantage of higher burnup approach clarify.

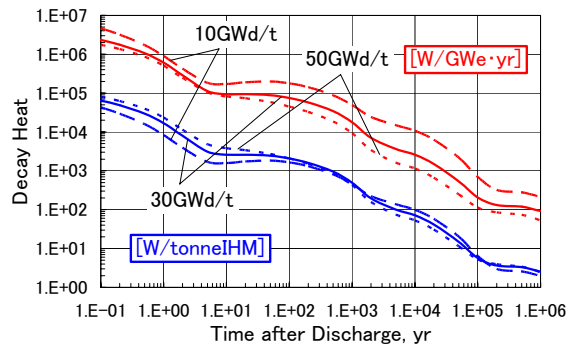


Fig.2 Decay heat per gigawatt (electric) year versus time after discharge

3.2 Impact of uncertainty of prediction accuracy of isotopic generation

Figure 3 indicates an example⁵ of discrepancy of C/E ratio for Pu vector and MAs. These figures means that Pu isotopes have a few percent disagreement and that miner actinide isotopes have tens of percent disagreement. Therefore, evaluation of decay heat containing their uncertainty is required. On Pu-238, -239, -240, -241, Am-241, Cm-242, the ratio to the standard calculation result is shown about decay heat when the combustion calculation result contains the uncertainty from 2 to 20 percent as follows (Fig.4 (a) - (d)).

These figures show the variations of decay-heat behavior with respect to the intentional charge in the discharge amount of each isotope, for example ²³⁹Pu in Fig.4 (a). The peak in Fig.4 (c), is not coming directly from Pu-241 itself but through Am-241. Pu-241 decays into Am-241 with the half-life of 14.35 years. It is Pu-241 that dominates the amount of Am-241 long after discharge. Am-241 is an important nuclide for decay heat for an important period for storing spent fuels from ten-odd years to thousands of years. According to this figure, at 100 year after discharge, 7% error of the decay heat will be introduced by 10% uncertainty of Pu-241 generation calculation through Am-241 production.

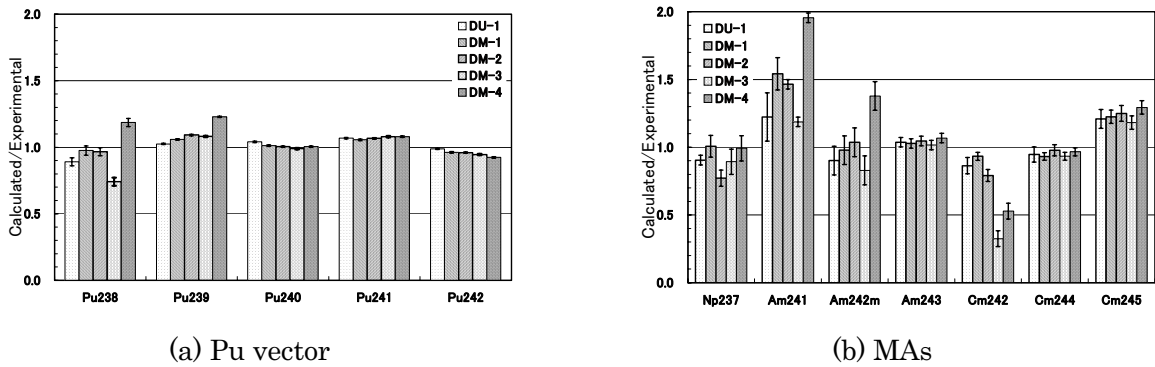


Fig.3 C/E ratio for Pu-isotopes and minor actinides⁵

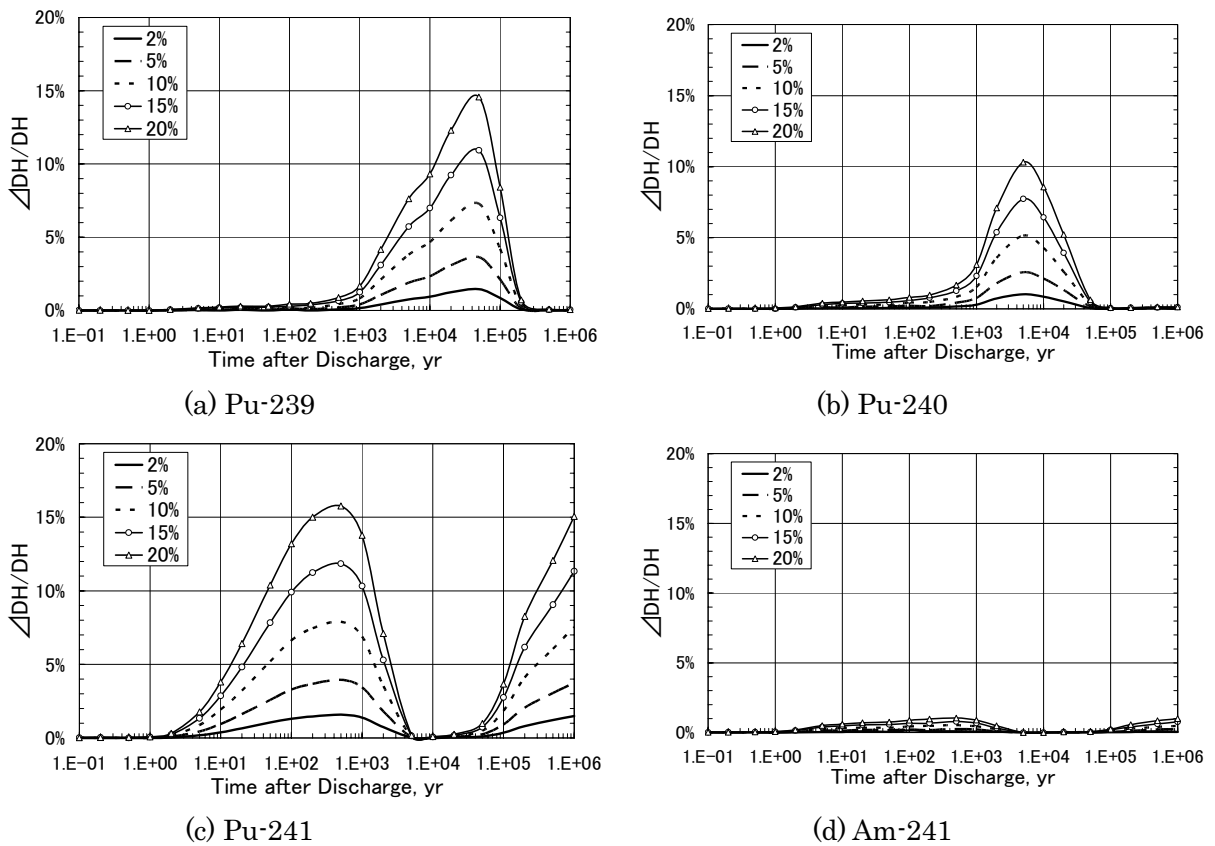


Fig.4 Uncertainty of the FP and actinide decay heats introduced by uncertainty of the prediction accuracy of isotopic generation of each nuclide

3.3 Impact of uncertainty of one-group cross section

On the spent fuel storage term (several 100 years from 10 years), Am-241 is dominant nuclide. Importance of the amount of Pu-241 has already been described. In a reactor in operation, generation of Pu-241 is remarkable. Evaluation value⁶ of uncertainty of Pu-240 capture cross sections is shown in Figure 5. In this figure, capture cross section of Pu-240 has 20% from 10% uncertainty in whole energy range. Then the influence on decay heat when capture cross sections of Pu-240 and Pu-239 were changed from 10 to 50 percent was examined.

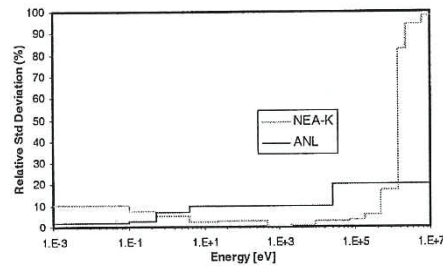


Fig.5 Evaluation value of uncertainty of Pu-240 capture cross sections⁶

Figure 6 shows the peak caused by Am-241 around 500 year cooling. Fig.6 (a) indicates that decay heat increases by 3% when the capture cross section of Pu-239 is increased by 10%. Fig.6 (b) shows that decay heat increases by 5% when the capture cross section of Pu-240 is increased by 20%. The dip of about 10⁴ year results from reduction of Pu-239 and Pu-240, respectively.

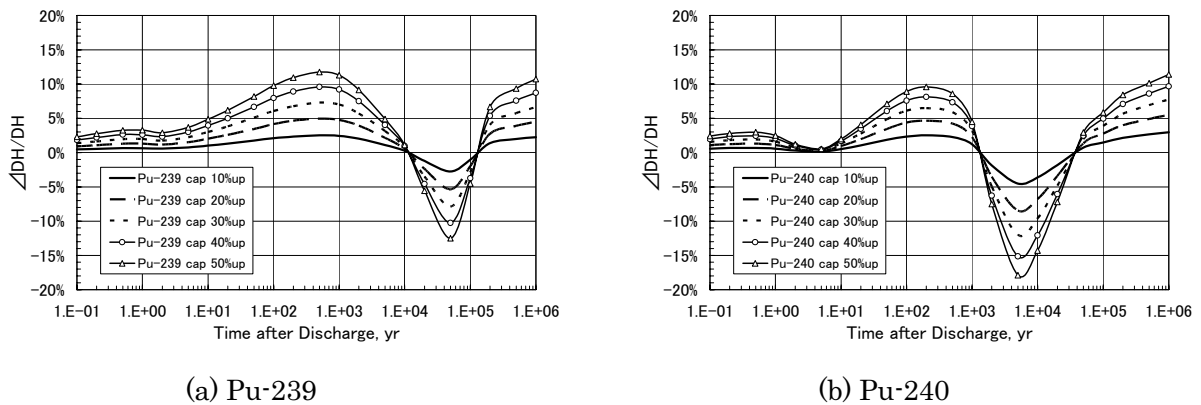


Fig.6 Uncertainty of the total decay heats introduced by uncertainty of the one-group capture cross section

4. Summary and Future Plan

It is important to evaluate the characteristics of spent MOX fuel, especially decay heat, appropriately. In this study, sensitivity analyses of prediction accuracy of isotopic generation and uncertainty of one-group cross section were performed. Between 100 and 1,000 years after discharge of the spent MOX fuel, the total decay heat is dominated by Am-241. We should pay attention to the generation of Pu-241 which decays into Am-241. The amount of Pu-241 has a close relation to the capture cross section of Pu-239 and -240. The uncertainty of the burnup calculation is discussed. At 100 year after discharge, for example, 7% error of the decay heat will be introduced by 10% uncertainty of Pu-241 generation calculation through Am-241 production.

We will make sensitivity analyses of capture cross section of notable isotopes on each energy group.

Reference

1. K. Suyama, T. Kiyosumi and H. Mochizuki, JAERI-Data/Code 2000-027, JAERI (2000).
2. A.G.croff, ORNL/TM-7175, Oak Ridge National Laboratory (1980).
3. Y. Ando, H. Takano, JAERI-Research 99-004, JAERI (1999).
4. Zhiwen Xu, Mujid S. Kazimi, and Michael J. Driscoll, Nucl. sci. Eng., **151**, 261(2005).
5. Y. Ando, K. Yoshioka, I. Mitsuhashi, K. Sakurada and S. Sakurai, Proc. of the 7-th International Conference on Nuclear Criticality Safety, Tokai, Japan, Oct.20-24, 2003, pp494-499 (2003).
6. G. Aliberti, et. al., Proc. of the Int. Workshop on Nucl. Data Needs For Gen. IV Nucl. Energy Systems, Antwerp, Belgium, Apr.5-7, 2005 (2005).

3.15 Neutron Multigroup Constant Sets of Moderator Materials for Design of Low-Energy Neutron Sources

Yutaka Abe and Nobuhiro Morishima

Department of Nuclear Engineering, Kyoto University
 Yoshida, Sakyo-ku, Kyoto 606-8501, Japan
 e-mail: yutaka_abe@nucleng.kyoto-u.ac.jp (Yutaka Abe)

For design assessment of low-energy neutron sources, neutron multigroup constant sets (energy-averaged cross sections) are developed, which consist of 36 sets of multigroup constants for liquid ^4He , H_2 , D_2 , CH_4 , H_2O and D_2O and solid CH_4 at many different temperatures. The neutron energy range between $0.1 \mu\text{eV}$ and 10 MeV are divided into 140 energy groups at equal logarithmic intervals. The angular distribution of scattered neutrons is represented by the expansion in Legendre polynomials up to order 3. The multigroup constants at energies below 10 eV are generated using physical models of a double-differential scattering cross section for the moderator materials, which are newly developed for describing low-energy neutron scattering in terms of the general considerations of molecular dynamics and structures inherent in liquid and solid phases.

Most of the calculated cross-section results are compared with many experimental measurements, both double-differential and total, at various material temperatures and neutron energies. Availability of the constant sets are demonstrated by the multigroup neutron transport analyses for production of ultra-cold ($\sim 0.3 \mu\text{eV}$), cold ($\sim 2 \text{ meV}$) and thermal ($\sim 25 \text{ meV}$) neutrons. Features of the multigroup constant sets for each moderator material and typical results of low-energy neutron production are reported in the present study.

1 Introduction

Although a variety of moderators have been actually used for low-energy neutron sources, most of them are hydrogenous liquids because of the following advantages: large scattering cross section leading to rapid moderation and small source volume; good removal of neutron kinetic energy by excitation of molecular motions; favorable refrigeration requirements due, in some liquids, to low melting and boiling points; and much less technical problems as compared with solid moderators at the time of heat dissipation and radiation damage. Hence, moderator materials to be taken up below are liquid H_2 , D_2 , CH_4 , H_2O and D_2O , together with solid CH_4 and liquid ^4He . The last two materials are selected from the viewpoints of an efficient solid moderator for production of an intense cold neutron beam and a specific liquid moderator for an ultracold neutron source.

At present, available experimental data for the moderator materials are very limited in comprehensive tabulations and interpolations. Consequently, scattering cross section models are newly developed to describe major features of neutron scattering in the liquid and solid moderators for neutron energies E between $0.1 \mu\text{eV}$ and 10 eV [1, 2]. This aims at generating a cross section library available for research and development of advanced neutron sources to produce ultracold ($\sim 0.3 \mu\text{eV}$), very cold ($\sim 10 \mu\text{eV}$) and cold ($\sim 2 \text{ meV}$) neutrons. By use of the cross section models, together with an evaluated nuclear data file for $E \geq 10 \text{ eV}$, a total of 36 sets of 140-group constants (averaged cross sections over the energies of each group) are systematically generated in the energy range between $0.1 \mu\text{eV}$ and 10 MeV . Accordingly, it becomes possible to evaluate slowing-down of fission/spallation neutrons and thermalization to thermal and cold neutrons, including the production and storage of ultracold neutrons.

Table 1. Group constant sets for moderator materials at temperatures.

Material	N_s	T	N_m in order of T	$\sigma_{a,th}$	σ_{fr}
Liquid ^4He	11	0.1,0.3,0.5,0.6	2.189 in common	2.34×10^{-7}	0.760
		0.7,0.8,0.9,1.0	2.189 in common		
		1.5,2.0,2.5	2.190,2.197,2.180		
Liquid para- H_2	2	14.0,20.4	2.30,2.11	0.665	41.0
Liquid ortho- H_2	2	14.0,20.4	2.31,2.12	0.665	41.0
Liquid normal- H_2	2	14.0,20.4	2.31,2.12	0.665	41.0
Liquid para- D_2	2	18.7,23.6	2.61,2.45	1.04×10^{-3}	6.80
Liquid ortho- D_2	2	18.7,23.6	2.61,2.45	1.04×10^{-3}	6.80
Liquid normal- D_2	2	18.7,23.6	2.61,2.45	1.04×10^{-3}	6.80
Solid CH_4	3	20.4,50.0,90.7	1.99,1.92,1.83	1.33	86.8
Liquid CH_4	2	90.7,111.7	1.70,1.59	1.33	86.8
Liquid H_2O	4	278,300,325,350	3.35,3.33,3.30,3.26	0.665	44.8
Liquid D_2O	4	278,300,325,350	3.35,3.33,3.30,3.26	1.04×10^{-3}	10.6

where N_s (number of sets), T (K), N_m ($\times 10^{22}$ molecules cm^{-3}), $\sigma_{a,th}$ (b molecule $^{-1}$) at $E_{th} = 25$ meV and σ_{fr} (b molecule $^{-1}$) at $E = 10$ eV.

2 Generation of Multigroup Constant Sets

The high-energy part for $E \geq 1$ eV (energy group $g \leq 70$) and the low-energy part for $E \leq 10$ eV ($g \geq 61$) are made up separately and then combined into one set. The overlapping energy region between 1 and 10 eV is prepared to make a gradual transition between the two parts: this is made using the expression of $W \times (\text{the high-energy part}) + (1 - W) \times (\text{the low-energy part})$ with the weight $W = (E - 1)/9$ for $E = 1 - 10$ eV. The resulting group constants are examined with total scattering cross sections, integral quantities (e.g., averaged scattering angle and averaged energy transfer) and neutron energy spectra. The high-energy part is produced using the Japanese evaluated nuclear data library JENDL-3.3[3] and the nuclear data processing program NJOY[4]. The low-energy part is created by use of double-differential scattering cross section models developed theoretically for liquid and solid moderator materials. Low-energy neutron scattering by molecular dynamics inherent in each material is generally described and the calculated cross-section results are compared with many experimental measurements, both double-differential and total, at many different temperatures and neutron energies. Slowing-down and thermalization properties are analyzed by calculating neutron energy spectra for moderator models in relatively simple geometries such as an infinite slab and a finite slab surrounded by a vacuum. All the results are reported in research papers on scientific journal: liquid ^4He [5, 6, 7, 8], liquid H_2 [9, 10, 11], liquid D_2 [12, 13, 14], solid CH_4 [15, 16, 17], liquid CH_4 [15, 16, 17], liquid H_2O [18, 19], and liquid D_2O [19, 20].

Table 1 summarizes the group constant sets generated for the seven different materials at various temperatures, mostly between melting and boiling points. For liquid H_2 and D_2 , two sorts of sets, distinguished by the spin states of para and ortho, are prepared in order to make up a mixture with an arbitrary-chosen para:ortho ratio. In Table 1, σ_{fr} is the free atom cross section (b molecule $^{-1}$) at $E = 10$ eV and $\sigma_{a,th}$ is the absorption cross section (b molecule $^{-1}$) at a thermal neutron energy $E_{th} = 25$ meV. By use of $\sigma_{a,th}$, an absorption (radiative capture) cross section $\sigma_a(E)$ as a function of E is defined by $\sigma_a(E) = \sigma_{a,th} \sqrt{E_{th}/E}$. One exception is $\sigma_a(E)$ of liquid ^4He which is given by $\sigma_a(E) = 1/(N_m \tau_\beta v)$ due to the neutron β -decay with a lifetime $\tau_\beta = 885.7$ s, together with the number density N_m of molecules (molecules cm^{-3}) and a neutron speed $v = 2.20 \times 10^5 \sqrt{E/E_{th}}$ cm s $^{-1}$. For reference, the value of N_m for each

material is also presented as an equilibrium or theoretical value at given temperature since it is required for making up macroscopic cross section tables for neutron transport analyses. The group constant sets have the following structure and property:

1. Neutron energy range between $0.1 \mu\text{eV}$ and 10 MeV ,
2. A total of 140 energy groups at equal logarithmic energy intervals(i.e. 10 groups per energy decade),
3. Expansion of the angular distribution of scattered neutrons in Legendre polynomials up to order 3,
4. Weighting energy spectrum of a neutron flux by a combination of Maxwellian, $1/E$ and fission spectra as a function of E ,
5. Microscopic cross sections(b molecule^{-1}) in ANISN-type cross section tables (text form, length IHM=282, position IHT=3, groups IGM=140) though not multiplied by the Legendre factor $(2l + 1)$.

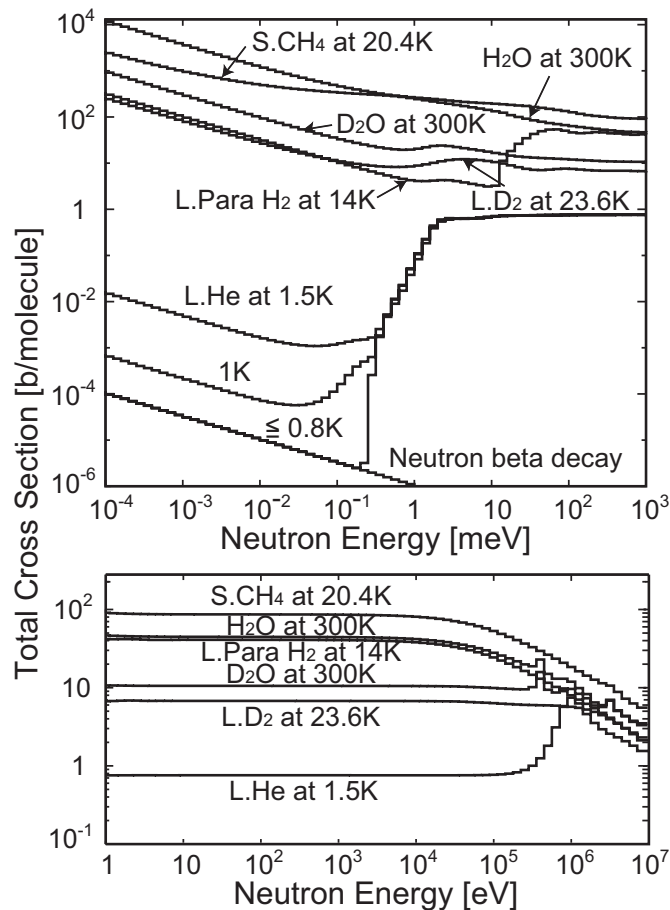


Figure 1: Total cross sections of various moderator materials at temperatures shown, together with an effective absorption cross section due to the neutron β -decay.

In addition, it is worth noting the definition of the group constants, i.e. energy-averaged scattering cross sections associated with the change of neutron energies from group g to g' ,

$$\sigma_s^l(g \rightarrow g') = 2\pi \int_{-1}^1 d \cos \theta \int_{E_g}^{E_{g-1}} dE \int_{E_{g'}}^{E_{g'-1}} dE' w_g(E) \sigma_s(E \rightarrow E', \theta) P_l(\cos \theta) \quad (l = 0, 1, \dots, L; g \text{ and } g' = 1, 2, \dots, G) \quad (1)$$

where $\sigma_s(E \rightarrow E', \theta)$ is the double-differential scattering cross section for initial and final energies, E and E' respectively, at scattering angle θ , $w_g(E)$ is the intergroup weighting spectrum, $P_l(\cos \theta)$ is the Legendre polynomial of order l , and E_{g-1} and E_g are, respectively, the upper and lower energy boundaries of energy group g and given by

$$E_g = E_0 \exp \left[-\frac{g}{G} \ln \frac{E_0}{E_G} \right] \quad (2)$$

with $E_0 = 10$ MeV, $E_G = 0.1$ μ eV, $L = 3$ and $G = 140$. Numerical methods for calculation of $\sigma_s(E \rightarrow E', \theta)$ and $\sigma_s^l(g \rightarrow g')$ are described in detail and illustrated with physical cross section models[1, 2]. The total cross sections of scattering and absorption in group g are defined as, respectively,

$$\sigma_{s,g} = \sum_{g'=1}^G \sigma_s^0(g \rightarrow g') \quad (3)$$

$$\sigma_{a,g} = \int_{E_g}^{E_{g-1}} w_g(E) \sigma_a(E) dE. \quad (4)$$

Then the total cross section for any type of neutron reaction is given by

$$\sigma_{t,g} = \sigma_{s,g} + \sigma_{a,g}. \quad (5)$$

Figure 1 shows $\sigma_{t,g}$ for various moderator materials at specified temperatures in the whole energy range from 0.1 μ eV (group 140) to 10 MeV (group 1), together with $\sigma_{a,g}$ of liquid ^4He due to the neutron β -decay.

3 Demonstration of Low-energy Neutron Production

3.1 Production and Storage of Ultracold Neutrons in Liquid ^4He

Multigroup constants of liquid ^4He are generated by using the cross-section model[6] developed for neutron scattering in liquid ^4He at temperatures between 0.1 and 4.2 K. The model describes some fundamental excitations in superfluid and normal ^4He in terms of phonon-roton (quasi-particle) excitation at temperatures below $T_\lambda = 2.172$ K and density mode (non-condensate component) excitation at all temperatures[21], together with an elastic scattering collision with a ^4He nucleus for incident energies above about 10 meV. The temperature dependence of these excitations is verified by comparison with the experimental results of scattering cross sections, both double-differential and total [5, 6]. Figure 2 shows the scattering cross section $\sigma_s^0(g \rightarrow g')$ of liquid ^4He at 0.1 and 1.5 K. The production of ultracold neutron (UCN) in liquid ^4He occurs by a single down-scattering event for a cold neutron with an incident energy of about 1 meV, because neutron with an energy of 1 meV transfers its almost entire energy and momentum to a phonon in liquid ^4He at the intersection of the free neutron dispersion curve with the phonon-roton one. The UCN production is found in Fig. 2 as a peak near the incident energy of 1.0 meV and final energy of 0.1 μ eV.

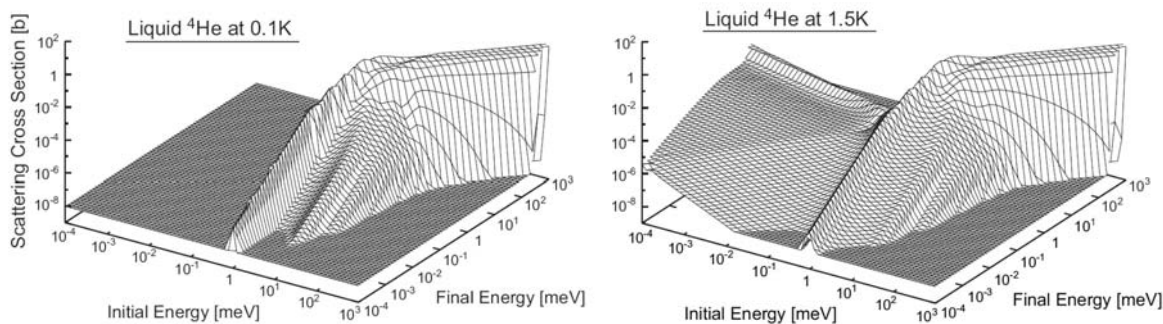


Figure 2: Scattering cross sections $\sigma_s^0(g \rightarrow g')$ of liquid ^4He at 0.1 K (left) and 1.5 K (right).

To demonstrate UCN production in liquid ^4He , an UCN source is modeled as an infinite-slab geometry with a thickness of 3 m. An isotropic plane neutron source with an intensity of $2 \times 10^{10} \text{ cm}^{-2}\text{s}^{-1}$, emitting cold neutrons with a Maxwellian spectrum at 20 K, is located at left boundary of the slab, so that one half of the source neutrons enters into the slab. Boundary conditions particular to UCNs are considered, that is, there are no incoming neutrons with energies above $0.316 \mu\text{eV}$ ($1 \leq g \leq 135$) at both boundaries (i.e. vacuum boundary condition), while UCNs with energies below $0.316 \mu\text{eV}$ ($136 \leq g \leq 140$) are totally reflected at the surfaces. Neutron energy spectra calculated at an opposite side to the cold-neutron source are shown in Fig. 3, together with the Maxwellian spectrum of the cold neutron source with a neutron temperature of 20 K. Storage of UCNs is obvious especially at lower temperatures, thus yielding the UCN density of $7.7 \times 10^4 \text{ cm}^{-3}$ below 0.5 K. It is to be noted that the UCN production by down-scattering of a 1-meV neutron is almost independent of liquid temperature. On the contrary, as temperature is raised, up-scattering of an UCN becomes significant instead of disappearance by the neutron β -decay. This is due to an increase in the number of thermally-excited phonons in liquid ^4He at higher temperatures.

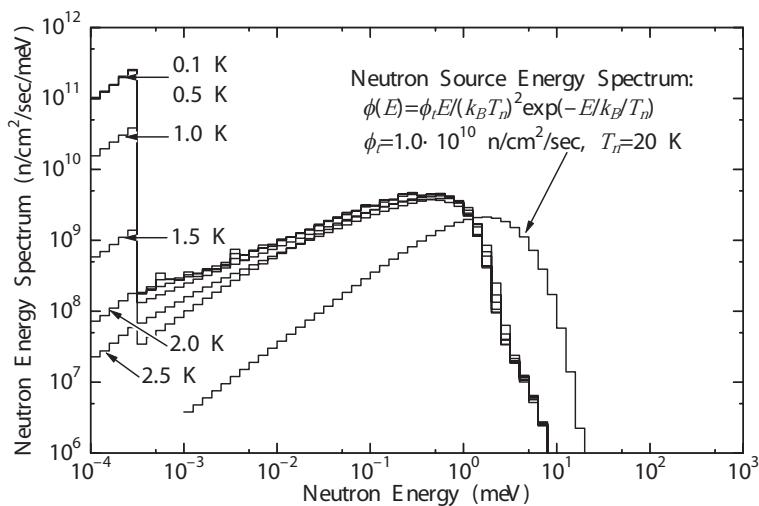


Figure 3: Neutron energy spectra for a liquid- ^4He source model at temperatures shown, together with a cold-neutron source spectrum having a Maxwellian distribution at 20 K.

3.2 Converter Characteristics of Liquid H₂ and D₂

Liquid H₂, both in the para state(anti-parallel spins of two protons) and in the ortho state(parallel spins), is efficient for producing high-density cold neutrons. This is due to the following properties: (a)a large scattering cross section, (b)a para-to-ortho(e.g. $J = 0 \rightarrow 1$) transition for free molecular rotations with energy levels $E_J = 15 \times J(J + 1)/2$ meV ($J = 0, 1, 2, \dots$) and (c)a thermal translational motion of a molecule with kinetic energies around $k_B T \sim 2$ meV where k_B is the Boltzmann constant. In order to describe low-energy neutron scattering in liquid H₂, the cross section model[9] has been developed as a generalization of the Young-Koppel model for gaseous H₂[22]. Various intermolecular motions are fully taken into account: a very short-time free-gas like translation, a short-lived vibration of about 5.3 meV due to molecular interaction, and a long-time diffusive motion with a temperature dependent diffusion coefficient. Coherent scattering in liquid para-H₂ is also included in a convolution approximation based on the experimental static structure factor. Besides, the following intramolecular motions are considered: nuclear-spin correlations, free quantized rotations of a molecule and harmonic stretching vibrations (~ 0.546 eV) of an atomic bond. A satisfactory agreement with the experimental cross section results, both double-differential and total has been found for various neutron energies and liquid temperatures [9, 11, 12]. In Fig. 4, $\sigma_s^0(g \rightarrow g')$ for liquid normal-H₂ at 14 K is shown. Since liquid normal-H₂ with a para:ortho ratio of 1:3 is mainly incoherent scatterer, it has a large scattering cross section to indicate neutron slowing down at $E >$ about 10 meV and a quasi-elastic scattering cross section at lower E , together with a up-scattering component for lower-energy neutrons to gain a kinetic energy of 15 meV by the $J = 1 \rightarrow 0$ transition. The cross-section model of liquid D₂ is also described in common with liquid H₂ except for the following points: the energy levels $E_J = 7.5 \times J(J + 1)/2$ meV from the rotation of a D₂ molecule, the vibrational energies of about 2.6 meV from an intermolecular vibration and the intramolecular vibrational energy of 386 meV, together with a very small absorption cross section for pure liquid D₂. The cross-section model of liquid D₂ is found to be in good agreement with the experimental results of cold neutron scattering cross sections, both double-differential and total [9, 12, 13, 14].

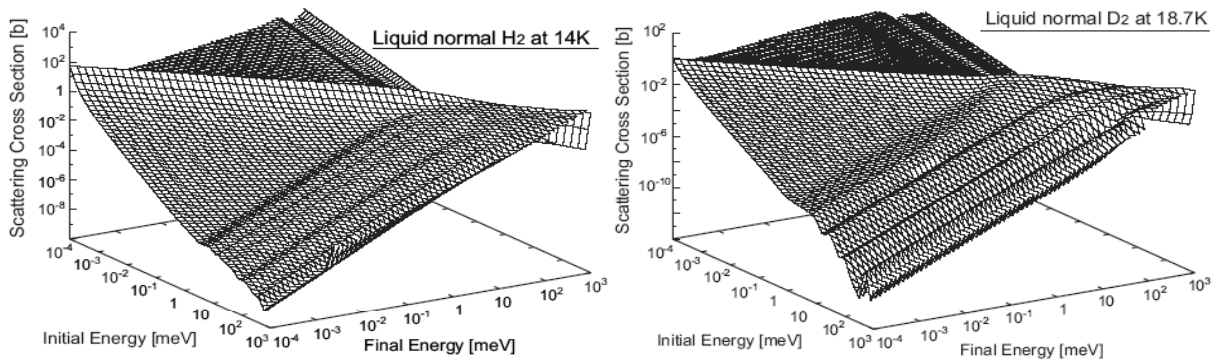


Figure 4: Scattering cross sections $\sigma_s^0(g \rightarrow g')$ of normal-H₂ at 14 K (left) and liquid normal-D₂ at 18.7 K (right).

To see converter characteristics of liquid normal-, para- and ortho-H₂ at 20.4 K, a cold-neutron source is modeled as a bare-slab geometry with a thickness a to be varied, An isotropic plane neutron source with an intensity of 2×10^{10} cm⁻²s⁻¹, emitting thermal neutrons with a Maxwellian spectrum at 300 K, is located at the left boundary. Neutron energy spectra at the right boundary are calculated by varying a so that a cold neutron flux for $E \sim 2$ meV may be maximized. The selected values of a are about 3, 2 and 2 cm for liquid para-, normal- and

ortho-H₂, respectively. The energy spectra obtained are shown in Fig. 5. A para-H₂ converter is superior in producing cold neutrons on account of the para-to-ortho transition of a H₂ molecule (i.e. an efficient down-scattering of a thermal neutron) and a small total cross section for cold neutrons below about 15 meV (i.e. a good penetrating property). It is to be noted that up-scattering of cold and lower-energy neutrons is caused by an ortho-to-para transition with an energy transfer of 15 meV and a de-excitation of intermolecular vibration with a characteristic energy of about 6 meV. This behavior may be slightly seen from Fig. 5 in terms of the shoulders of energy spectra for liquid normal- and ortho-H₂ at energies around 15 meV.

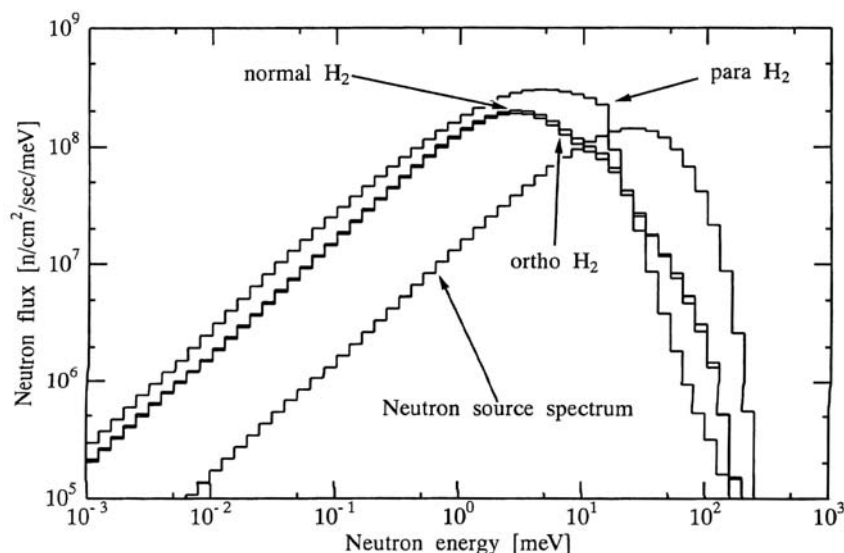


Figure 5: Neutron energy spectra for slab moderators of liquid para-, normal- and ortho-H₂ at 20.4 K, together with the Maxwellian neutron-source spectrum at 300 K.

3.3 Cold Neutron Source of Solid and Liquid CH₄ in a Thermal Neutron Field

Among various realistic hydrogenous moderators, solid CH₄ has a relatively high hydrogen-atom density that is advantageous to fast-neutron slowing-down in a narrow region with a small time spread. For thermal neutrons thus produced, there are some low-energy exchange modes, both intra- and intermolecular, for cold neutron production. A typical one is nearly free rotation of a CH₄ molecule in solid and liquid phases. By the excitation of rotational motions with energy levels $E_J = 1.3 \times J(J + 1)/2$ meV ($J = 0, 1, 2, \dots$), most of thermal neutrons are downscattered to yield cold neutrons. For intermolecular motions, low-frequency lattice vibrations in solid phase and translational vibrations in liquid phase may possibly contribute to the moderation of thermal neutrons. On the basis of these viewpoints, neutron scattering cross sections for solid CH₄ in the temperature range from 20.4 to 90.7 K and for liquid CH₄ at temperatures between 90.7 and 111.7 K are evaluated theoretically as cross-section models[15]. Major features of the cross-section models are as follows: short-time free rotation of a CH₄ molecule and long-time isotropic rotational diffusion with a temperature-dependent relaxation constant. The former is very efficient for cold neutron production by successive inelastic scatterings, while the latter gives rise to quasi-elastic scattering accompanied with very small energy transfer. The other features are the inclusion of molecular translations such as very short-time free-gas like motion, short-lived vibration of about 6.45 meV and longtime diffusion(only in the liquid phase). The intramolecular vibrations with two characteristic energies of 0.170 and 0.387 eV are also

considered. A good agreement with the experimentally-measured cross-sections, both double-differential and total, at many different temperatures is found [15]. Figure 6 shows scattering cross sections $\sigma_s^0(g \rightarrow g')$ of solid and liquid CH_4 . At low temperatures quasi-elastic scattering by the molecular rotational diffusion becomes dominant while up-scattering at low energies below 1 meV is relatively suppressed. This is shown in Fig. 1 in terms of a gradual increase in $\sigma_{t,g}$ with decreasing neutron energies below 1 meV.

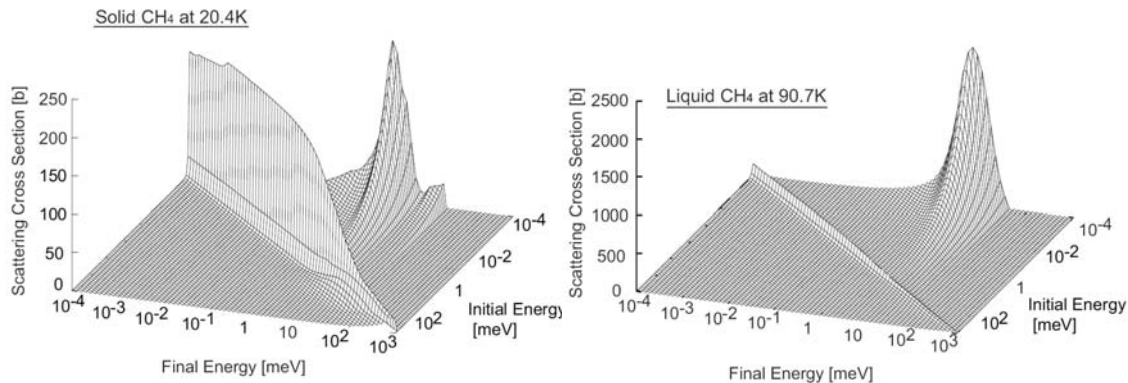


Figure 6: Scattering cross sections $\sigma_s^0(g \rightarrow g')$ of solid CH_4 at 20.4 K (left) and liquid CH_4 at 90.7 K (right).

A cold-neutron source is modeled as a slab geometry with a thickness of $D = 15$ cm. A uniformly distributed source of an intensity of $1 \text{ n cm}^{-3}\text{s}^{-1}$ is located throughout the moderator, emitting epithermal neutrons with energies of group 61 ($7.94 \text{ eV} \leq E \leq 10 \text{ eV}$). A set of neutron energy spectra at the slab center is shown in Fig. 7 in which the magnitudes are normalized in the energy region of a $1/E$ component. It is ascertained that, with increasing D more than 15 cm, there is little change of an energy spectrum in magnitude and shape. This means that almost equilibrium spectra characterizing each of the moderators are obtained for $D = 15$ cm. Since a Maxwellian plus $1/E$ spectrum is well fitted, a neutron temperature T_N and a cold-neutron gain can be determined systematically as a function of moderator temperature. Consequently, good moderating properties of solid CH_4 at 20.4 K are found especially in terms of a variation of T_N in direct proportion to moderator temperature and a good agreement of T_N with experimental results [16, 17].

3.4 Thermalization of Fission Neutrons in Liquid H_2O and D_2O

Cold and thermal neutron scattering in liquid H_2O has been described in terms of the physical cross section model[18]. The microscopic dynamics of water molecules is fully represented from very general consideration of jump diffusion, intermolecular vibration, hindered rotation and intramolecular vibration at temperatures between melting and boiling points. Furthermore, the cross-section model has been employed to treat neutron scattering by liquid D_2O [20]. Coherent neutron scattering is expressed in a convolution approximation based on the partial static structure factors for pairs of DD, DO and OO. For the double-differential and total cross sections of liquid H_2O and D_2O , satisfactory agreement with the neutron scattering experiments has been found [18, 19, 20]. It is shown that the inclusion of water molecule dynamics is essential for proper understanding and reproduction of the experimentally-observed behavior of low-energy neutron scattering. This is in marked contrast to the molecular-gas models for H_2O [23] and D_2O [24]. Figure 8 shows $\sigma_s^0(g \rightarrow g')$ for liquid H_2O and D_2O at 300 K. The following features are observed: quasi-elastic scattering components centered around initial energies below

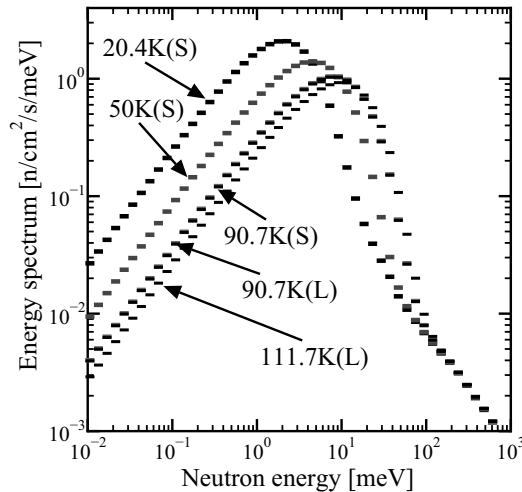


Figure 7: Neutron energy spectra for slab moderators of solid and liquid CH₄ at temperatures shown. The characters S and L, respectively, mean solid and liquid phases.

about 10 meV and up-scattering peaks for final energies \sim 5-60 meV by the de-excitation of intermolecular vibration and hindered rotation.

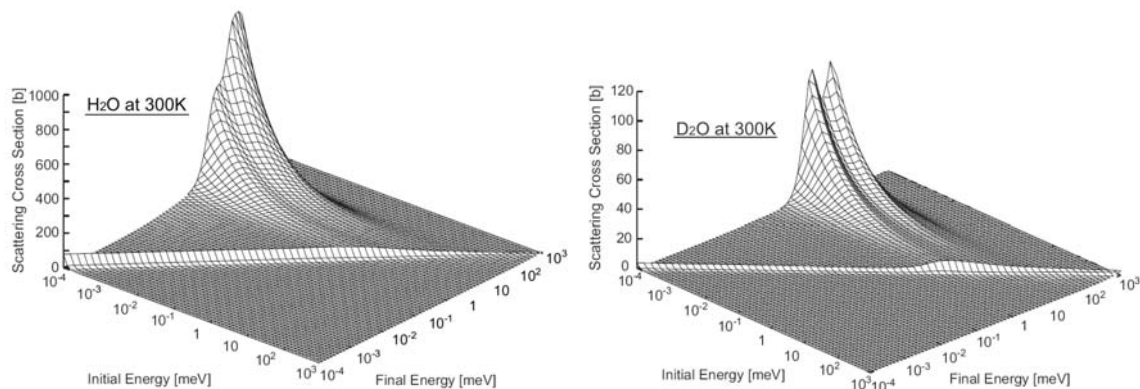


Figure 8: Scattering cross sections $\sigma_s^0(g \rightarrow g')$ of liquid H₂O at 300 K (left) and D₂O at 300 K (right).

To demonstrate thermalization of fast neutrons, infinite homogeneous mediums such as pure liquid H₂O and D₂O at 300 K, liquid D₂O containing slightly liquid H₂O (0.25, 1, 3 and 10 %), and liquid H₂O poisoned with a $1/v$ absorber (3.15 and 6.04 b H⁻¹ at E_{th} , instead of 0.333 b H⁻¹ for pure liquid H₂O) are prepared. Spatially-uniform neutron sources emitting fission neutrons with an average energy of 2 MeV are located in the medium. Neutron energy spectra in the whole energy range 0.1 μ eV to 10 MeV are shown in Fig. 9, though normalized to the $1/E$ component around 10 eV. Moderating properties to thermal neutrons vary systematically according to the H₂O content in liquid D₂O and the poison concentration in liquid H₂O. This may also be characterized in terms of a neutron temperature and a thermal neutron gain to be estimated by a least-square fitting of a Maxwellian plus $1/E$ spectrum. A notable feature of the infinite-medium energy spectra is that there are significant non-Maxwellian deviations at varying temperatures, caused by water molecular dynamics, i.e. a jump diffusion process

with translational diffusion and intermolecular vibration, and a hindered rotation with a broad distribution of energies around 80 meV [19]. This spectral behavior is essentially in contrast to the corresponding energy spectra by molecular gas models.

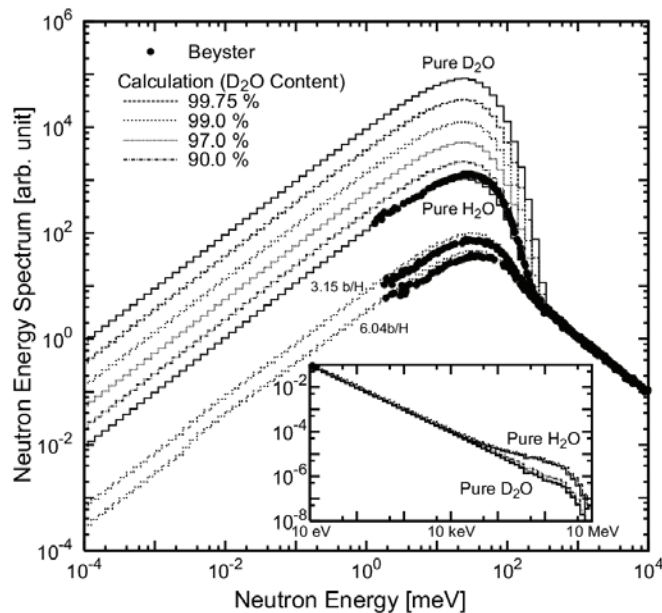


Figure 9: Infinite medium energy spectra of neutron fluxes in liquid H₂O, liquid D₂O and their mixtures at 300 K. The experimental data by Beyster [25] are shown by full circles.

4 Concluding Remarks

A total of 36 sets of multigroup constants for 6 moderator materials are developed and confirmed to be applicable in the wide range of neutron energies from 0.1 μ eV (UCN) to 10 MeV (fission neutron) by the neutron multigroup transport analysis. The cross section library has been released at OECD/NEA Data Bank and RIST NUCIS [26]. The authors expect it to serve for research and development of advanced low-energy neutron sources. Optimum design of pulsed spallation neutron sources may be made in terms of low-energy neutron intensity and pulse characteristics.

Since the present multigroup library is developed as the ANISN type of 140-group constant sets, it is also necessary to generate scattering-law files for continuous energy Monte Carlo calculations. For further research, it is desirable to treat other moderating materials such as, for instance, solid CH₄ in phase II below 20.4 K, solid D₂ and solid CD₄, together with reflector and structure materials.

Acknowledgment

The authors are grateful to Mr. Y. Nagaya of JAEA for making available group-constant generation codes and Dr. Y. Edura for generating high-energy group constants.

References

- [1] N. Morishima and S. Ito: *Nucl. Instr. and Method*, **A572**, 1071 (2007).

- [2] N. Morishima: *J. Neutron Res.*, **13**, 225 (2005).
- [3] K. Shibata et al.: *J. Nucl. Sci. Technol.*, **39**, 1125 (2002).
- [4] R. E. MacFarlane and D. W. Muir: “*The NJOY Nuclear Data Processing System, Version 91*,” LA-12740-M, Los Alamos National Laboratory (1994).
- [5] N. Morishima and Y. Abe: *Nucl. Instr. and Method*, **A397**, 354 (1997).
- [6] Y. Abe and N. Morishima: *Nucl. Instr. and Method* **A459**, 256 (2001).
- [7] N. Morishima and M. Sakakibara: *J. of Neutron Res.*, **8**, 233 (2000).
- [8] Y. Abe and N. Morishima: *Nucl. Instr. and Method*, **A481**, 414 (2002).
- [9] N. Morishima and D. Mizobuchi: *Nucl. Instr. and Method*, **A350**, 275 (1994).
- [10] N. Morishima and A. Nishimura: *Nucl. Instr. and Method*, **A426**, 638 (1999).
- [11] N. Morishima and Y. Matsuo: *Nucl. Instr. and Method*, **A490**, 308 (2002).
- [12] N. Morishima: *Ann. Nucl. Energy*, **27**, 505 (2000).
- [13] N. Morishima and Y. Nishikawa: *Ann. Nucl. Energy*, **31**, 737 (2004).
- [14] Y. Matsuo, N. Morishima and Y. Nagaya: *Nucl. Instr. and Method*, **A496**, 446 (2003).
- [15] N. Morishima and Y. Sakurai: *Nucl. Instr. and Method*, **A490**, 527 (2002).
- [16] N. Morishima and T. Mitsuyasu: *Nucl. Instr. and Method*, **A517**, 295 (2004).
- [17] T. Mitsuyasu, N. Morishima and Y. Nagaya: *Nucl. Instr. and Method*, **A537**, 610 (2005).
- [18] Y. Edura and N. Morishima: *Nucl. Instr. and Method*, **A534**, 531 (2004).
- [19] Y. Edura and N. Morishima: *Nucl. Instr. and Method*, **A560**, 485 (2006).
- [20] Y. Edura and N. Morishima: *Nucl. Instr. and Method*, **A545**, 309 (2005).
- [21] H. R. Glyde: *J. Low Temp. Phys.*, **87**, 407 (1992); also *Phys. Rev.*, **B45**, 7321 (1992).
- [22] J. A. Young and J. U. Koppel: *Phys. Rev.*, **135**, A603 (1964).
- [23] M. Nelkin: *Phys. Rev.*, **119**, 741 (1960).
- [24] H. C. Honeck: *Trans. Am. Nucl. Soc.*, **5**, 47 (1962).
- [25] J. R. Beyster: *Nucl. Sci. Eng.*, **31**, 254 (1968).
- [26] N. Morishima: “*ZZ-CLES, Cross section library of moderator materials for low-energy neutron sources*,” NEA Data Bank, NEA-1775 (2006).

This is a blank page.

Appendix: Participants Lists

ABE Yutaka	Kyoto Univ.	KOSAKA Shinya	TEPSYS
AKINO Fujiyoshi		KOSAKO Kazuaki	Shimizu co.
ANDO Yoshihira	Toshiba Co.	KOURA Hiroyuki	JAEA
ARAKAWA Hiroyuki	Kyushu Univ.	KUGO Teruhiko	JAEA
CHAKI Masao	Hitachi Ltd.	KUNIEDA Satoshi	JAEA
CHIBA Gou	JAEA	Liem Peng Hong	NAIS
CHIBA Satoshi	JAEA	MAEBARA Sunao	JAEA
Dimitre N. Kadrev	Kyushu Univ.	MAKII Hiroyuki	JAEA
FUKAHORI Tokio	JAEA	MARUYAMA Hiromi	GNF-J
FURUTAKA Kazuyoshi	JAEA	MATSUNAKA Masayuki	Osaka Univ.
HAGURA Hiroyuki	KEK	MITSUYASU Takesi	Hitachi Ltd.
HAGURA Naoto	Musashi Inst. of Tech.	MIYAZAKI Itaru	Nagoya Univ.
HARA Kaoru-Yamasaki	JAEA	MIYOSHI Yoshinori	JAEA
HARADA Masahide	JAEA	MIZUMOTO Motoharu	Tokyo Inst. of Tech.
HAYASHI Hiroaki	Nagoya Univ.	MORI Takamasa	JAEA
HIRANO Go	TEPSYS	MURATA Isao	Osaka Univ.
ICHIHARA Akira	JAEA	MURATA Toru	
IGARASHI Kenji	Toshiba Co.	NAGAI Yasuki	Osaka Univ.
IGASHIRA Masayuki	Tokyo Inst. of Tech.	NAGAYA Yasunobu	JAEA
ISHII Kazuya	Hitachi Ltd.	NAKAGAWA Tsuneo	JAEA
ISHIKAWA Makoto	JAEA	NAKAJIMA Ken	Kyoto Univ.
IWAMOTO Nobuyuki	JAEA	NAKAMURA Shoji	JAEA
IWAMOTO Osamu	JAEA	NEMOTO M.	Ibaraki Univ.
IWAMOTO Yosuke	JAEA	NIITA Koji	RIST
IWANAGA K.	JAEA	NISHIO B.	CNIC
IWASHITA Daiki	KEK	OCHIAI Kentaro	JAEA
KAJIMOTO Tsuyoshi	Kyushu Univ.	OGAWA Sakae	
KAKU Daisuke	Kyushu Univ.	OHNISHI Seiki	NMRI
KATAKURA Jun-ichi	JAEA	OHTA Masayuki	JAEA
KIMURA Atsushi	JAEA	OIGAWA Hiroyuki	JAEA
KIN Tadahiro	JAEA	OKADA Koichi	JAEA
KOBAYASHI Katsutoshi		OKUMURA Keisuke	JAEA
KOJIMA Kensuke	JAEA	OSHIMA Masumi	JAEA
KONDO Keitaro	JAEA	OTSUKA Naohiko	JAEA
KONNO Chikara	JAEA	SATO Tatsuhiko	JAEA

SEGAWA Mariko	JAEA
SHIBATA Keiichi	JAEA
SHIGYO Nobuhiro	Kyushu Univ.
SUGAWARA Takanori	JAEA
TAKADA Hiroshi	JAEA
TAKAKURA Kosuke	JAEA
TOH Yosuke	JAEA
TOISHIGAWA Akiko	GNF-J
WATANABE Yukinobu	Kyushu Univ.
YAMANO Naoki	Tokyo Inst. of Tech.
YANAGISAWA Masaru	JNFL
Ye Tao	Kyushu Univ.
YOSHIDA Tadashi	Musashi Inst. of Tech.
ZUKERAN Atsushi	NAIS

国際単位系 (SI)

表1. SI 基本単位

基本量	SI 基本単位	
	名称	記号
長さ	メートル	m
質量	キログラム	kg
時間	秒	s
電流	アンペア	A
熱力学温度	ケルビン	K
物質の量	モル	mol
光度	カンデラ	cd

表2. 基本単位を用いて表されるSI組立単位の例

組立量	SI 基本単位	
	名称	記号
面積	平方メートル	m ²
体積	立方メートル	m ³
速度	メートル毎秒	m/s
加速度	メートル毎秒毎秒	m/s ²
波数	毎メートル	m ⁻¹
密度 (質量密度)	キログラム毎立方メートル	kg/m ³
質量体積 (比体積)	立法メートル毎キログラム	m ³ /kg
電流密度	アンペア毎平方メートル	A/m ²
磁界の強さ	アンペア毎メートル	A/m
(物質量の) 濃度	モル毎立方メートル	mol/m ³
輝度	カンデラ毎平方メートル	cd/m ²
屈折率	(数の) 1	1

表5. SI 接頭語

乗数	接頭語	記号	乗数	接頭語	記号
10 ²⁴	ヨタ	Y	10 ⁻¹	デシ	d
10 ²¹	ゼタ	Z	10 ⁻²	センチ	c
10 ¹⁸	エクサ	E	10 ⁻³	ミリ	m
10 ¹⁵	ペタ	P	10 ⁻⁶	マイクロ	μ
10 ¹²	テラ	T	10 ⁻⁹	ナノ	n
10 ⁹	ギガ	G	10 ⁻¹²	ピコ	p
10 ⁶	メガ	M	10 ⁻¹⁵	フェムト	f
10 ³	キロ	k	10 ⁻¹⁸	アト	a
10 ²	ヘクト	h	10 ⁻²¹	ゼプト	z
10 ¹	デカ	da	10 ⁻²⁴	ヨクト	y

表3. 固有の名称とその独自の記号で表されるSI組立単位

組立量	SI 組立単位			
	名称	記号	他のSI単位による表し方	SI基本単位による表し方
平面角	ラジアン ^(a)	rad		m ⁻¹ ・m ¹ =1 ^(b)
立体角	ステラジアン ^(a)	sr ^(c)		m ² ・m ⁻² =1 ^(b)
周波数	ヘルツ	Hz		s ⁻¹
力	ニュートン	N		m ¹ ・kg ¹ ・s ⁻²
圧力, 応力	パスカル	Pa	N/m ²	m ⁻¹ ・kg ¹ ・s ⁻²
エネルギー, 仕事, 熱量	ジュール	J	N・m	m ² ・kg ¹ ・s ⁻²
工率, 放射束	ワット	W	J/s	m ² ・kg ¹ ・s ⁻³
電荷, 電気量	クーロン	C		s ¹ ・A
電位差 (電圧), 起電力	ボルト	V	W/A	m ² ・kg ¹ ・s ⁻³ ・A ⁻¹
静電容量	ファラド	F	C/V	m ⁻² ・kg ⁻¹ ・s ⁴ ・A ²
電気抵抗	オーム	Ω	V/A	m ² ・kg ¹ ・s ⁻³ ・A ⁻²
コンダクタンス	ジーメン	S	A/V	m ⁻² ・kg ⁻¹ ・s ³ ・A ²
磁束	ウェーバ	Wb	V・s	m ² ・kg ¹ ・s ⁻² ・A ⁻¹
磁束密度	テスラ	T	Wb/m ²	kg ¹ ・s ⁻² ・A ⁻¹
インダクタンス	ヘンリー	H	Wb/A	m ² ・kg ¹ ・s ⁻² ・A ⁻²
セルシウス温度	セルシウス度 ^(d)	°C		K
光束度	ルーメン	lm	cd・sr ^(c)	m ² ・m ⁻² ・cd=cd
照射 (放射性核種の) 放射能	ベクレル	Bq	lm/m ²	m ² ・m ⁻⁴ ・cd=m ⁻² ・cd
吸収線量, 質量エネルギー分与, カーマ線量当量, 周辺線量当量, 方向性線量当量, 個人線量当量, 組織線量当量	グレイ	Gy	J/kg	m ² ・s ⁻²
	シーベルト	Sv	J/kg	m ² ・s ⁻²

- (a) ラジアン及びステラジアンの使用は、同じ次元であっても異なった性質をもった量を区別するときの組立単位の表し方として利点がある。組立単位を形作るときにいくつかの用例は表4に示されている。
 (b) 実際には、使用する時には記号rad及びsrが用いられるが、習慣として組立単位としての記号“1”は明示されない。
 (c) 測光学では、ステラジアンの名称と記号srを単位の表し方の中にそのまま維持している。
 (d) この単位は、例としてミリセルシウス度m°CのようにSI接頭語を伴って用いても良い。

表4. 単位の中に固有の名称とその独自の記号を含むSI組立単位の例

組立量	SI 組立単位		
	名称	記号	SI 基本単位による表し方
粘力のモーメント	ニュートンメートル	N・m	m ² ・kg ¹ ・s ⁻²
表面張力	ニュートン毎メートル	N/m	kg ¹ ・s ⁻²
表角速度	ラジアン毎秒	rad/s	m ¹ ・m ⁻¹ ・s ⁻¹ =s ⁻¹
角加速度	ラジアン毎平方秒	rad/s ²	m ¹ ・m ⁻¹ ・s ⁻² =s ⁻²
熱流密度, 放射照度	ワット毎平方メートル	W/m ²	kg ¹ ・s ⁻³
熱容量, エントロピー	ジュール毎キログラム	J/kg	m ² ・kg ¹ ・s ⁻² ・K ⁻¹
質量熱容量 (比熱容量), 質量エントロピー	ジュール毎キログラム	J/(kg・K)	m ² ・s ⁻² ・K ⁻¹
質量エネルギー (比エネルギー)	ジュール毎キログラム	J/kg	m ² ・s ⁻² ・K ⁻¹
熱伝導率	ワット毎メートル毎ケルビン	W/(m・K)	m ¹ ・kg ¹ ・s ⁻³ ・K ⁻¹
体積エネルギー	ジュール毎立方メートル	J/m ³	m ⁻¹ ・kg ¹ ・s ⁻²
電界の強さ	ボルト毎メートル	V/m	m ¹ ・kg ¹ ・s ⁻³ ・A ⁻¹
体積電荷	クーロン毎立方メートル	C/m ³	m ⁻³ ・s ¹ ・A
電気変位	クーロン毎平方メートル	C/m ²	m ⁻² ・s ¹ ・A
誘電率	ファラド毎メートル	F/m	m ⁻³ ・kg ⁻¹ ・s ⁴ ・A ²
透磁率	ヘンリー毎メートル	H/m	m ¹ ・kg ¹ ・s ⁻² ・A ⁻²
モルエネルギー	ジュール毎モル	J/mol	m ² ・kg ¹ ・s ⁻² ・mol ⁻¹
モルエントロピー	ジュール毎モル毎ケルビン	J/(mol・K)	m ² ・kg ¹ ・s ⁻² ・K ⁻¹ ・mol ⁻¹
モル熱容量	ジュール毎モル毎ケルビン	J/(mol・K)	m ² ・kg ¹ ・s ⁻² ・K ⁻¹ ・mol ⁻¹
照射線量 (X線及びγ線)	クーロン毎キログラム	C/kg	kg ⁻¹ ・s ¹ ・A
吸収線量	グレイ毎秒	Gy/s	m ² ・s ⁻³
放射強度	ワット毎ステラジアン	W/sr	m ⁴ ・m ⁻² ・kg ¹ ・s ⁻³ =m ² ・kg ¹ ・s ⁻³
放射輝度	ワット毎平方メートル毎ステラジアン	W/(m ² ・sr)	m ² ・m ⁻² ・kg ¹ ・s ⁻³ =kg ¹ ・s ⁻³

表6. 国際単位系と併用されるが国際単位系に属さない単位

名称	記号	SI 単位による値
分	min	1 min=60s
時	h	1 h=60 min=3600 s
日	d	1 d=24 h=86400 s
度	°	1°=(π/180) rad
分	'	1'=(1/60)°=(π/10800) rad
秒	''	1''=(1/60)'=(π/648000) rad
リットル	l, L	1 l=1 dm ³ =10 ⁻³ m ³
トン	t	1 t=10 ³ kg
ネーパ	Np	1 Np=1
ベル	B	1 B=(1/2) ln10 (Np)

表7. 国際単位系と併用されこれに属さない単位でSI単位で表される数値が実験的に得られるもの

名称	記号	SI 単位であらわされる数値
電子ボルト	eV	1 eV=1.60217733(49)×10 ⁻¹⁹ J
統一原子質量単位	u	1 u=1.6605402(10)×10 ⁻²⁷ kg
天文単位	ua	1 ua=1.49597870691(30)×10 ¹¹ m

表8. 国際単位系に属さないが国際単位系と併用されるその他の単位

名称	記号	SI 単位であらわされる数値
海里	海里	1 海里=1852m
ノット	ノット	1 ノット=1 海里毎時=(1852/3600)m/s
アール	a	1 a=1 dam ² =10 ² m ²
ヘクタール	ha	1 ha=1 hm ² =10 ⁴ m ²
バル	bar	1 bar=0.1MPa=100kPa=1000hPa=10 ⁵ Pa
オングストローム	Å	1 Å=0.1nm=10 ⁻¹⁰ m
バーン	b	1 b=100fm ² =10 ⁻²⁸ m ²

表9. 固有の名称を含むCGS組立単位

名称	記号	SI 単位であらわされる数値
エルグ	erg	1 erg=10 ⁻⁷ J
ダイン	dyn	1 dyn=10 ⁻⁵ N
ポアズ	P	1 P=1 dyn・s/cm ² =0.1Pa・s
ストークス	St	1 St=1cm ² /s=10 ⁻⁴ m ² /s
ガウス	G	1 G ≅10 ⁴ T
エルステッド	Oe	1 Oe ≅(1000/4π) A/m
マクスウェル	Mx	1 Mx ≅10 ⁻⁸ Wb
スチルブ	sb	1 sb=1cd/cm ² =10 ⁴ cd/m ²
ホト	ph	1 ph=10 ⁴ lx
ガリ	Gal	1 Gal=1cm/s ² =10 ⁻² m/s ²

表10. 国際単位に属さないその他の単位の例

名称	記号	SI 単位であらわされる数値
キュリー	Ci	1 Ci=3.7×10 ¹⁰ Bq
レントゲン	R	1 R=2.58×10 ⁻⁴ C/kg
ラド	rad	1 rad=1cGy=10 ⁻² Gy
レム	rem	1 rem=1 cSv=10 ⁻² Sv
X線単位	X	1 X unit=1.002×10 ⁻⁴ nm
ガンマ	γ	1 γ=1 nT=10 ⁻⁹ T
ジャンスキー	Jy	1 Jy=10 ⁻²⁶ W・m ⁻² ・Hz ⁻¹
フェルミ	fm	1 fermi=1 fm=10 ⁻¹⁵ m
メートル系カラット		1 metric carat = 200 mg = 2×10 ⁻⁴ kg
トル	Torr	1 Torr = (101 325/760) Pa
標準大気圧	atm	1 atm = 101 325 Pa
カロリ	cal	
マイクロン	μ	1 μ=1μm=10 ⁻⁶ m

